Risø–R–1180(EN)

RISØ

Aspects of Quantum Magnetism in One, Two and Three Dimensions

Henrik Moodysson Rønnow

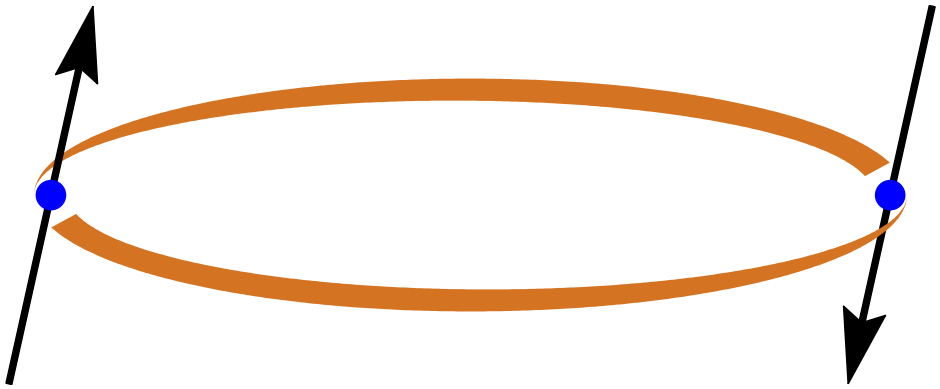

Risø National Laboratory, Roskilde, Denmark
April 2000

Abstract The study of *quantum magnetism* remains at the forefront of condensed matter physics. Spin models provide a large class of many-body systems, in which cooperative quantum phenomena can be studied in a controlled way. In addition, the *neutron scattering* technique offers a near-ideal tool to probe the state of magnetic materials. This thesis presents neutron scattering studies of three selected materials, each representing an important aspect of quantum magnetism.

- $CuGeO_3$ is a quasi one-dimensional $S = 1/2$ spin–Peierls material. This is an example of a system that has a *quantum ground state* with no classical analogue. The spins dimerize to form a coherent non-magnetic singlet, where the expectation value of each individual spin is zero, as if they were 'hidden'. As a consequence, the *excitations* (called solitons) are different from the spin waves of a classical system. In a high magnetic field, the solitons can be condensed to form a periodic lattice. Through neutron scattering measurements, the structure of this soliton lattice has been determined, and the excitations in the soliton phase have been identified.

- $Cu(DCOO)_2{\cdot}4D_2O$ is a two-dimensional $S = 1/2$ Heisenberg antiferromagnet on a square lattice. The $T = 0$ ground state of this system has long range order similar to the classical system. But the order parameter is reduced by *quantum fluctuations*, and the physical observables are *renormalized*. In particular, it was found that the spin wave dispersion is non-uniformly renormalized. At finite temperatures long range order is destroyed by thermal and quantum fluctuations, which act together. Still, there are strong *correlations*, which on short length and time scales resembles the long range order. The temperature dependence of the correlation length and the excitation spectrum has been measured using two specialized neutron scattering methods.

- $LiHoF_4$ is a three-dimensional Ising ferromagnet, in which the magnetic order can be destroyed even at $T = 0$ by applying a large magnetic field transverse to the Ising axis. Ordinary phase transitions occur as a function of temperature, when the thermal fluctuations become strong enough to destroy the order. At $T = 0$ there are no thermal fluctuations and the transition is driven by quantum fluctuations, which are controlled by some external parameter,in this case the magnetic field. It is important to understand the universal behaviour of such *quantum phase transitions*, as several novel phenomena in solid state physics may be related to the proximity of a *quantum critical point*. Using inelastic neutron scattering the behaviour of the excitations around the quantum critical point in $LiHoF_4$ has been investigated.

This thesis was submitted in partial fulfillment of the requirements for a Ph.D. in physics at the University of Copenhagen. The work presented was carried out in the Department of Condensed Matter Physics and Chemistry at Risø National Laboratory, Denmark. The supervisors were Des McMowrrow from Risø and Jens Jensen from the University of Copenhagen.

ISBN 87–550–2693–1
ISBN 87–550–2695–8 (internet)
ISSN 0106–2840

Information Service Department · Risø · 2000

Preface

The goals of this thesis are manifold. The main objective is to report on some specific research results obtained during the last three years. At the same time, it is my intention to make a review of the general progress/status of the fields studied. In addition, I will take the opportunity to pass on some technical ideas and experience that I have developed in the course of my experiments. As a result, there may be passages that appear irrelevant to the individual reader. If so, I refer the readers looking for specific results to the articles that we have or will publish, the readers looking for a general review to the articles written by other scientists in the field and the people looking for experimental tips to the old-proven technique of learning by doing.

It is always difficult to decide in which order a subject should be presented. A chronological description will show the relevance of each contribution, but inevitably also reflect the staggering path to sagacity. In this thesis, theoretical developments and experimental results will be presented separately. This may be unfair to the experimental contributions, as their importance as guide to the theoretical development will be neglected. But this will be compensated for explicitly, by showing in the following how in some directions the experimental results are in fact 'ahead of theory'.

The structure of the thesis is the following: The first chapter motivates the title, the second the technique. The subjects of the project are covered in each of the three remaining chapters.

Risø, April 12, 2000

Contents

Chapter 1

Quantum Magnetism

It could be argued that the term *quantum magnetism* in the title of this thesis is superfluous. Magnetism, defined as the properties of magnetic materials, is after all a quantum mechanical phenomena. The magnetic moments are built from the spin and the orbital motion of the electrons in magnetic materials and coupled through the so-called exchange interactions, which arises from the Pauli exclusion principle for identical Fermi particles. However, this is not what is meant by quantum magnetism in this thesis, which is devoted to the study of quantum effects in many-body physics.

Since the discovery of quantum mechanics, magnetic systems have been recognized as suitably complex applications of the theoretical developments. Their historically proven role as an arena in which quantum many-body methods can be developed and tested relies on the wide variety of models that can be built from some well defined basic ingredients. By placing a number of quantum mechanical objects (Ising, XY or Heisenberg spins) in certain spatial arrangements, and defining the means of interactions among them, there is an almost unlimited source of model systems to work with. In other words,

quantum magnetism is the LEGO of many-body physics.

It is in this sense that quantum magnetism is discussed in the present thesis. Experimental results on physical realizations of three such model systems will be presented, each illustrating different quantum effects of many-body physics.

1.1 Quantum effects of coupled angular momenta

The building blocks of quantum magnetism are electronic spins, which are the quantized version of angular momenta. The quantum mechanical treatment of angular momentum has three important consequences:

- The size of a spin $\boldsymbol{S}$ is quantized in units of $\hbar$. The total length is $\sqrt{S(S+1)}$, where S is either an integer or a half integer.
- Like any object in quantum mechanics, it is not possible to specify simultaneously all three components of $\boldsymbol{S}$. Instead, the spin is described by states $|\psi\rangle$, which carry the probability that an observable has a certain value. In particular, the eigenstates of an operator, say $S_z|m\rangle = m|m\rangle$, are characterized by having probability 1 that the spin has a z component of m. The probability that a spin in any other state $|\psi\rangle$ has a z component of m is given by $\langle m|\psi\rangle$ and the *expectation value* of S_z in that state is given by $\langle\psi|S_z|\psi\rangle$.
- For a given size of the spin, S, the largest possible eigenvalue of S_z is S with the corresponding eigenstate denoted $|S\rangle$. But the total length of the spin is

given by $\langle S|\boldsymbol{S}^2|S\rangle = S(S+1)$, which means that a fraction of the spin remains undetermined. This is a consequence of Heisenberg's uncertainty principle, that the commutator of two conjugate variables is at least equal to $\hbar$. It is said that the remainder of the spin is 'hidden' by quantum fluctuations

To illustrate these points, we first consider the simplest possible spin system, which is a spin 1/2 dimer (*i.e.* a pair of spin 1/2) with rotationally invariant Heisenberg coupling J, expressed by the Hamiltonian

$$\mathcal{H} = J\boldsymbol{S}_1 \cdot \boldsymbol{S}_2 \ . \tag{1.1}$$

The corresponding classical system is two unit vectors coupled by $JS(S+1)$. The ground state is one in which the spins point in opposite directions, giving a ground state energy of $-3J/4$. The ground state is highly degenerate since the spins can align along any direction. Once a given direction has been chosen, the rotational symmetry is broken, but it costs no energy to rotate the two spins into another direction as long as they are kept anti-parallel. In infinite systems, where a continuous symmetry is broken, the corresponding zero energy shift of the entire system is called a Goldstone mode.

The quantum mechanical system can be described in terms of product states of the individual spins. Choosing the eigenstates of S_z as a basis, each spin can point either up ($|\uparrow\rangle$) or down ($|\downarrow\rangle$), and the combined system is described by the four states $\{|\uparrow\uparrow\rangle, |\downarrow\downarrow\rangle, |\uparrow\downarrow\rangle, |\downarrow\uparrow\rangle\}$. The ground state is found to be the linear combination $\frac{1}{\sqrt{2}}(|\uparrow\downarrow\rangle - |\downarrow\uparrow\rangle)$ with energy $-3J/4$, while the three remaining eigenstates of the Hamiltonian are $\{|\uparrow\uparrow\rangle, |\downarrow\downarrow\rangle, \frac{1}{\sqrt{2}}(|\uparrow\downarrow\rangle + |\downarrow\uparrow\rangle)\}$ with the degenerate energy $J/4$. The ground state is a singlet with total spin zero, while the excited states form a triplet with total spin 1.

There are important differences between the classical and the quantum system. The quantum ground state does not break the rotational symmetry, and therefore no Goldstone modes exist. The expectation value of any single spin operator is zero, which means that the ground state is non-magnetic. Classically, it appears as if the orientations of the spins were random so that they averaged to zero. This is however not true – the two spins are perfectly coherent.

In quantum magnetism, the quantization of S means that there exist different types of spins. As evident from the ratio $S/\sqrt{S(S+1)}(\simeq 1 - \frac{1}{2S}$ for large $S)$, the largest quantum effects occur for $S = 1/2$. When an assembly of many spins are coupled, the entire system is described by states that mix the states of the individual spins. And the notion of quantum fluctuations is transferred to the many-spin states of the coupled system. These quantum properties lead to profound effects that cannot be visualized by a classical analogue. In the remainder of this chapter, three aspects of quantum many-body spin systems will be introduced.

1.1.1 Ground states and excitations

An important consequence of quantum mechanics in many-body physics is the possibility for *quantum ground states*. That is a state with no classical analogue, like the ground state of the dimer pair considered above. Let us again consider a classical spin system (*i.e.* an assembly of interacting vectors of fixed length). The ground state is the spin arrangement that minimizes the total energy of the system. In this state each spin points in a specified direction. This could, for instance, be an antiferromagnetic arrangement, where neighbouring spins point in opposite directions, which is called the Néel state.

A quantum spin system with antiferromagnetic interactions will still have a tendency towards antiferromagnetic alignment of the spins. But due to the quantum fluctuations, the staggered moment (the expectation value $m = \langle(-1)^n S_n^z\rangle$) will be reduced (renormalized) from its classical value. This is the case in the $S = 1/2$

Heisenberg antiferromagnet on a square lattice, where $m = 0.3$ is reduced to 60% of its classical value. But the ground state of this system is still analogous to the classical Néel state, which can be treated as a basis for perturbative calculations of the quantum renormalizations.

This situation is changed in one dimension, where the quantum fluctuations are so strong that they destroy the Néel order all together. The ground state of the 1D $S = 1/2$ spin chain is *quantum disordered*. In some sense, a classical analogue can still be imagined by assimilating the quantum fluctuations with thermal fluctuations at finite temperatures. But there is another posibility for having a ground state without magnetic order. As seen for the dimer system, the description by a wave function rather than the orientation of each spin, makes it possible to have a ground state in which the expectation value of each individual spin operator is zero, while the spins are still coherent.

One such quantum ground state is realized in the 1D $S = 1/2$ spin–Peierls system. This is a spin chain, where spin-lattice interactions allow the lattice to dimerize, hence causing an alternation of the coupling parameter. The ground state of this system can be visualized as pairs of spins coupling to singlets, but in fact the entire spin system is described by one coherent singlet ground state. It is as if the order is 'hidden' when considering the expectation value of single spins, and is only revealed when the entire system is considered.

The excitations in a system are collective fluctuations relative to the ground state. When the nature of the ground state changes, so does the nature of the excitations. In magnetically ordered materials, the excitations are pressesions of the moments around their equilibrium position. Such excitations are known as spin waves, and have been subject of intense studies in decades (see *e.g.* Borovik-Romanov and Sinha, 1988). Quantum ground states in general have different types of excitations. For instance, the excitations of the spin–Peierls state are pairs of domain walls (solitons) that shift the phase of the dimer order by π. Such a soliton pair corresponds to a delocalized broken dimer, by which each soliton carries spin 1/2. Therefore solitons can be stabilised in a sufficiently high field to form a regular soliton lattice.

Chapter 3 describes a neutron scattering determination of this soliton structure in $CuGeO_3$. In a field of 14.5 T, the soliton structure has a staggered component with an amplitude of just 10% of the classical moment. The rest of the expectation value is still 'buried' in the singlet pairs. Concomitant with the soliton structure is a new set of excitations, which have been identified using inelastic neutron scattering.

1.1.2 Correlations and fluctuations

In an ordered system, thermal and quantum fluctuations in the order parameter will decrease its average value, and eventually destroy the order all together. In the disordered phase that arise, there will however still be correlations, that on short length and time scales resemble the ordered state.

One example of a system, with strong correlations is the 2D Heisenberg antiferromagnet. Mermin and Wagner (1966) have proved that at any finite temperature the long ranged order will be destroyed by fluctuations — even in the classical system. It is therefore interesting to understand how the correlations evolve in a system with both thermal and quantum fluctuations.

Chapter 4 will present results from $Cu(DCOO)_2{\cdot}4D_2O$, which is an excellent physical realization of the 2D $S = 1/2$ Heisenberg antiferromagnet on a square lattice. The temperature dependence of the correlation length, ξ, in the classical system would diverge towards $T = 0$ as $\frac{J}{T}e^{J/T}$, where J is the coupling constant. When quantum fluctuations are added, the leading exponential behaviour persists,

but the divergence is slowed down by the disappearance of the prefactor.

The excitations of the system remain qualitatively the same as in the ordered phase, but they are damped due to the finite correlation length. As seen above, an excitation is an eigenstate of the system relative to the order parameter. As an excitation propagates outside the correlated region of size ξ the order parameter changes and the excitation is no longer an eigenstate, which means that it will decay. Thus the life time of excitations at finite temperatures is approximately given by $\tau = \xi/v_s$, where v_s is the group velocity of the collective mode. Within some prefactors, this simple relation is true both for the classical and the quantum system.

1.1.3 Quantum phase transitions

In the previous sections, it was mentioned how quantum fluctuations lowered the staggered magnetization in the ground state of the 2DQHAFSL to about 60% of its classical value. In the 1D $S = 1/2$ Heisenberg antiferromagnet, quantum fluctuations prevent ordering at $T = 0$ all together. If it was possible somehow to go in a continuous manner from the chain system to the 2D system, there would be a point at which the ground state would start to build long range order. Such a point is quite similar to ordinary thermally driven phase transitions, in that there is an order parameter, which is zero on one side and finite on the other side of the critical point. But ordinary phase transitions are driven by thermal fluctuations in the order parameter, which as temperature is increased disorder the system. This particular kind of phase transition take place even at zero temperature, where there are no thermal fluctuations. Instead the transition is driven by the zero point fluctuations that exist in quantum mechanical systems due to Heisenberg's uncertainty principle. Therefore such a transition that takes place even at zero temperature is denoted a *quantum phase transition* (QPT). It occurs as a function of some parameter which controls the strength of the quantum fluctuations. The point in parameter space at which the transition takes place is called the *quantum critical point* (QCP).

Just as studies of thermal phase transitions have been of continuing importance, both in the development of new theoretical methods and in the understanding of problems in all areas of physics, there has recently been a considerable interest into the properties of QPTs. Apart from the challenge it is to develop new theoretical tools, it has become clear that the properties of many of the novel phenomena in correlated electron systems are in fact significantly influenced by the proximity to nearby QCPs. In these materials, however, the QPT is only one ingredient in complicated and far from well characterized problems. It is therefore of interest to find simple realizations of QCPs, which can be studied with the aim of developing a general understanding of QPTs.

One candidate for a simple QCP is $LiHoF_4$, in which the lowest crystal field level is doubly degenerate. This makes the system equivalent to an Ising ferromagnet, which can be driven to a QPT with an external transverse magnetic field as the controlling parameter. Chapter 5 describes inelastic neutron scattering measurements of the excitations around this QCP. It is found that hyperfine coupling of the electronic moments to the nuclear moments split the two crystal field levels, thereby dramatically influencing the excitations. Instead of a softening of the excitation at the QPT, as predicted by mean-field theory, the excitations remain at a finite energy, and strong quasi-elastic scattering occur. Still, the system is well described by a rare-earth Hamiltonian, which makes it a good starting point for quantitative investigations of quantum critical behaviour.

Chapter 2

Neutron scattering

Though there exist a range of experimental techniques that probe the properties of magnetic systems, the neutron scattering method holds a special position. This is because neutron scattering directly probes the correlation functions that are used to describe the systems of interest. In part, t is the existence of the neutron scattering probe that makes magnetic systems attractive to study. The combination of the ability to custom design the system with a powerful tool to measure its behaviour provides a unique playground for studies of many-body physics.

The theory of neutron scattering has been described by amongst others Bacon (1975), Squires (1978) and Lovesey (1984), but the main lines will briefly be presented below. Small sections are also devoted to explain the two ways of implementing the technique used in the work of this thesis.

2.1 The scattering cross-section

The formalism of neutron scattering is built upon the definition of the *scattering cross-section*, σ, as the rate of scattered neutrons per incident flux Ψ_0. In a neutron scattering experiment, a collimated beam of monochromatic neutrons with initial energy E_i is directed to a target. The rate of neutrons scattered into the solid angle element $\Delta\Omega$ with final energy $E_f < E < E_f + \Delta E_f$ is

$$I = \Psi_0 \frac{d^2\sigma}{d\Omega dE_f} \Delta\Omega \Delta E_f \ , \tag{2.1}$$

where $\frac{d^2\sigma}{d\Omega dE_f}$ is the partial differential scattering cross-section. In the following, it will first be shown how it is related to the physics of the system under study, then demonstrated how the above mentioned situation is realised experimentally. For clarity, only unpolarized neutron scattering will be considered, as used throughout this work. The formalism is straightforwardly extendable to polarized neutron scattering. Current developments of ^{3}He filters and 3D polarization analysis, will probably make polarization analysis much more widely used within the next decade.

We first consider a single scattering process in which a neutron changes wave vector from $\boldsymbol{k}_i$ to $\boldsymbol{k}_f$, while concomitantly the target changes state from λ_i to λ_f. Owing to the weakness of the interaction between neutron and matter, the transition probability per unit time can be evaluated through Fermi's golden rule

$$W_{i\to f} = \frac{2\pi}{\hbar} |\langle \lambda_f \boldsymbol{k}_f | V | \lambda_i \boldsymbol{k}_i \rangle|^2 \ , \tag{2.2}$$

where V is the interaction potential between the neutron and the sample. Taking the neutron wave functions to be plane waves and assuming the interaction potential to be independent of the neutron momentum, the matrix element can be

reduced to

$$\langle \lambda_f \boldsymbol{k}_f | V | \lambda_i \boldsymbol{k}_i \rangle = \langle \lambda_f | \int e^{i(\boldsymbol{k}_i - \boldsymbol{k}_f)\cdot \boldsymbol{r}} V(\boldsymbol{r}) d\boldsymbol{r} | \lambda_i \rangle = \langle \lambda_f | V(\boldsymbol{q}) | \lambda_i \rangle \ , \tag{2.3}$$

where $V(\boldsymbol{q})$ is the Fourier transform of the scattering potential and the scattering wave vector $\boldsymbol{q} = \boldsymbol{k}_i - \boldsymbol{k}_f$ is given by the neutron momentum transfer.

To obtain the partial differential scattering cross-section, we average over all initial states with distribution p_{λ_i} and sum over all final states λ_f that fulfill energy conservation

$$\frac{d^2\sigma}{d\Omega dE_f} = \frac{k_f}{k_i} \left(\frac{m}{2\pi\hbar^2} \right)^2 \sum_{\lambda_i \lambda_f} p_{\lambda_i} |\langle \lambda_f | V(\boldsymbol{q}) | \lambda_i \rangle|^2 \delta(\hbar\omega + E_{\lambda_i} - E_{\lambda_f}) \ , \tag{2.4}$$

where the energy transfer is $\hbar\omega = \frac{\hbar^2}{2m}(k_i^2 - k_f^2)$ with m being the neutron mass. By using the integral representation $\delta(\hbar\omega + E_{\lambda_i} - E_{\lambda_f}) = \frac{1}{2\pi\hbar} \int e^{-i\omega t} e^{i(E_{\lambda_f} - E_{\lambda_i})t/\hbar} dt$, the identity $|\langle \lambda_f | V | \lambda_i \rangle|^2 = \langle \lambda_i | V^\dagger | \lambda_f \rangle \langle \lambda_f | V | \lambda_i \rangle$ and the completeness relation $1 = \sum_{\lambda_f} |\lambda_f\rangle\langle\lambda_f|$, the scattering cross-section can be rewritten as

$$\frac{d^2\sigma}{d\Omega dE_f} = \frac{k_f}{k_i} \left(\frac{m}{2\pi\hbar^2} \right)^2 \frac{1}{2\pi\hbar} \int dt \, e^{-i\omega t} \langle V^\dagger(\boldsymbol{q}, 0) V(\boldsymbol{q}, t) \rangle \ , \tag{2.5}$$

where in the Heisenberg-picture, the time-dependent interaction potential operator is given by $V(\boldsymbol{q}, t) \equiv e^{iHt/\hbar} V(\boldsymbol{q}) e^{-iHt/\hbar}$ and $\langle O \rangle \equiv \sum_\lambda p_\lambda \langle \lambda | O | \lambda \rangle$ denotes the average over initial states.

2.1.1 Nuclear scattering

The neutron interacts with the nuclei in the sample via the nuclear forces, which are very short ranged ($\sim$fm$= 10^{-15}$ m) compared to the neutron wavelength ($\sim$Å$= 10^{-10}$ m). The interaction potential between a neutron at position $\boldsymbol{r}$ and a nuclei at position $\boldsymbol{R}$ can therefore be approximated by the Fermi pseudo-potential

$$V(\boldsymbol{r}) = \frac{2\pi\hbar^2}{m} b_{\boldsymbol{R}} \delta(\boldsymbol{r} - \boldsymbol{R}) \qquad \Rightarrow \qquad V(\boldsymbol{q}) = \frac{2\pi\hbar^2}{m} b_{\boldsymbol{R}} e^{-i\boldsymbol{q}\cdot\boldsymbol{R}} \tag{2.6}$$

$$\left(\frac{m}{2\pi\hbar^2} \right)^2 \langle V^\dagger(\boldsymbol{q}, 0) V(\boldsymbol{q}, t) \rangle = \sum_{RR'} b_R b_{R'} \langle e^{i\boldsymbol{q}\cdot(\boldsymbol{R}(t) - \boldsymbol{R}(0))} \rangle \ , \tag{2.7}$$

where the scattering length $b_{\boldsymbol{R}}$ of the element at position $\boldsymbol{R}$ is determined by the isotope and orientation of the nuclear spin relative to that of the neutron.

The nuclei on each site can have a distribution f_α of scattering lengths b^α due to different isotopes and non-ordered nuclear spins, where $\sum_\alpha f_\alpha = 1$. We define the average scattering length $\overline{b} = \sum_\alpha f_\alpha b^\alpha$ and $\overline{b^2} = \sum_\alpha f_\alpha (b^\alpha)^2$. If there are no correlations between the α distribution on different sites, the product $b_R b_{R'}$ is replaced by $\overline{b}_R \overline{b}_{R'}$ for $R \neq R'$ and by $\overline{b_R^2}$ for $R = R'$.

The scattering cross-section then becomes the sum of a coherent and an incoherent part

$$\left(\frac{d^2\sigma}{d\Omega dE_f} \right)_{\text{coh}} = \frac{k_f}{k_i} \frac{1}{2\pi\hbar} \int dt \, e^{-i\omega t} \sum_{RR'} \overline{b}_R \overline{b}_{R'} \langle e^{i\boldsymbol{q}\cdot(\boldsymbol{R}(t) - \boldsymbol{R}'(0))} \rangle \tag{2.8}$$

$$\left(\frac{d^2\sigma}{d\Omega dE_f} \right)_{\text{inc}} = \frac{k_f}{k_i} \frac{1}{2\pi\hbar} \int dt \, e^{-i\omega t} \sum_{R} (\overline{b_R^2} - \overline{b}_{R'}^2) \langle e^{i\boldsymbol{q}\cdot(\boldsymbol{R}(t) - \boldsymbol{R}(0))} \rangle \ . \tag{2.9}$$

The coherent scattering is given by the average scattering length on each site and produces interference effects, while the incoherent scattering is due to the random distribution of deviations in the scattering lengths from their mean value.

The nuclear interactions that determine b are too complicated for *ab initio* calculations hereof. Instead, the values of b have been determined experimentally for each element and have been tabulated by Stehn *et al.* (1964), Koester *et al.* (1991) and Sears (1992).

2.1.2 Magnetic scattering

The interaction between the magnetic moment of the neutron and the electronic moments in the sample can on the other hand be calculated directly from Maxwell's equations. The neutron dipole moment $\boldsymbol{\mu}_n = -\gamma \times \mu_N \boldsymbol{\sigma}$, with the gyromagnetic ratio $\gamma = 1.913$ and the nuclear magneton $\mu_N = \frac{e\hbar}{2m}$, creates a vector potential $\boldsymbol{A_n} = \boldsymbol{\mu}_n \times \boldsymbol{r}/r^3$ felt by the electron at position $\boldsymbol{r}$. The interaction potential is then given by the difference between the electron energy in the presence and in the absence of the neutron.

$$V(r) = 2\mu_B \left[\frac{1}{\hbar} \boldsymbol{A}_n \cdot \boldsymbol{p} + \boldsymbol{s} \cdot (\boldsymbol{\nabla} \times \boldsymbol{A}_n) \right] \ , \tag{2.10}$$

where $\boldsymbol{s}$ is the electronic spin. An external magnetic field is included by adding its vector potential to $\boldsymbol{p} + \frac{e}{c}\boldsymbol{A}_e$. The Fourier transformed interaction potential for a single electron becomes

$$V(q) = 8\pi\mu_B \boldsymbol{\mu}_n \cdot (\frac{i}{\hbar q} \hat{\boldsymbol{q}} \times \boldsymbol{p} + \hat{\boldsymbol{q}} \times \boldsymbol{s} \times \hat{\boldsymbol{q}}) e^{-i\boldsymbol{q}\cdot\boldsymbol{r}} \ . \tag{2.11}$$

The total interaction potential is then obtained by integrating over the spin- and orbit distribution in the sample. For moment distributions formed by individual moments $\mu_j = \int_j d^3r \mu(r)$ that are located around ions in the material, the spatial distribution around each ion can be integrated to give the magnetic form factor

$$f_j(q) = \int_j d^3r \frac{\mu(r)}{\mu_j} e^{i\boldsymbol{q}\cdot\boldsymbol{r}} \ , \tag{2.12}$$

where the integral runs over the moment distribution belonging to the jth magnetic ion. The interaction potential is then reduced to a sum over ionic moments

$$V(q) = 8\pi\mu_B \sum_j f_j(q) e^{-i\boldsymbol{q}\cdot\boldsymbol{r}_j} \boldsymbol{\mu}_n \cdot (\hat{\boldsymbol{q}} \times \boldsymbol{\mu}_j \times \hat{\boldsymbol{q}}) e^{-i\boldsymbol{q}\cdot\boldsymbol{r}} \ . \tag{2.13}$$

The expression consists of an orbital part and a spin part. In half-filled shell configurations (like the $4s$ electron in Cu^{2+}) or if the total angular momentum is quenched by the crystal field, only the spin component contributes so that $\boldsymbol{\mu}_j = g\boldsymbol{S}_j$ with $g \simeq 2$. In the rare earths, for example, the orbital contribution is significant, and $\boldsymbol{\mu}_j = g_L \boldsymbol{J} = \boldsymbol{L} + 2\boldsymbol{S}$, where $g_L = \frac{3}{2} + \frac{S(S+1)-L(L+1)}{2J(J+1)}$ is the Landé factor.

In the spherical approximation, the form factor can be approximated by

$$f(q) \simeq \int_0^\infty R(r) r^2 \sin(qr) dr + \left(\frac{2}{g} - 1 \right) \int_0^\infty R(r) r^2 j_2(qr) dr \ , \tag{2.14}$$

where $R(r)$ is the normalized radial wave function. The spherical Bessel functions $j_0(z) = \sin(z)$ and $j_2(z) = (3z^{-2} - 1)\sin(z) - 3z^{-1}\cos(z)$ are the lowest order terms in an expansion of the phase factor e^{iqr}. Parameterizations of the form factors have been given by Brown (1992). In figure 2.1 the form factors for Cu^{2+} and Ho^{3+} which are the subject of this thesis have been shown.

Inserting the scattering potential into Fermi's golden rule and following the same procedure as for the nuclear scattering, the magnetic scattering cross section becomes

$$\frac{d^2\sigma_{\mathrm{mag}}}{d\Omega dE_f} = \frac{k_f}{k_i} \left(\frac{\hbar\gamma e^2}{mc^2} \right)^2 \left| \tfrac{1}{2} g f(q) \right|^2 \sum_{\alpha\beta} (\delta_{\alpha\beta} - \hat{q}_\alpha \hat{q}_\beta)$$
$$\times \frac{1}{2\pi\hbar} \int dt \, e^{-i\omega t} \sum_{RR'} \left\langle S_R^\alpha(t) e^{-i\boldsymbol{q}\cdot\boldsymbol{R}(t)} S_{R'}^\beta(0) e^{i\boldsymbol{q}\cdot\boldsymbol{R}'(0)} \right\rangle \ , \tag{2.15}$$

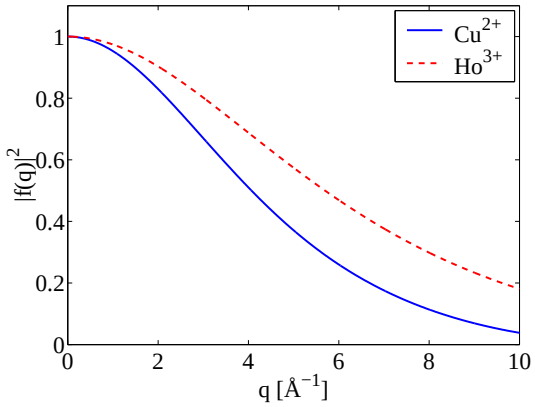

Figure 2.1. Squared form factors for Cu^{2+} and Ho^{3+} as a function of q up to 10 Å. The wider extent of the form factor for Ho^{3+} reflects that the holmium 4f shell is more localized than the 4s shell of copper.

where for simplicity, only one type of magnetic ions has been assumed and the symbol $\boldsymbol{S}$ is used for the angular momentum operator. If there is an orbital contribution, $\boldsymbol{S}$ should be replaced by $\boldsymbol{J}$. It is possible to have interference between the motion $\boldsymbol{R}(t)$ of the ions and the dynamics of the spins $\boldsymbol{S}(t)$, but for the following purposes such magneto-elastic scattering effects will be neglected. In this case, the fluctuations in $\boldsymbol{R}(t)$ transfer some of the coherent scattering into incoherent scattering as contained in the Debye–Waller reduction factor $e^{-2W(q)}$. Having decoupled the lattice motion, the remaining spin-expectation value is recognised as the dynamic structure factor.

$$\frac{d^2\sigma_{\mathrm{mag}}}{d\Omega dE_f} = \frac{k_f}{k_i}\left(\frac{\hbar\gamma e^2}{mc^2}\right)^2 e^{-2W(q)}\left|\tfrac{1}{2}gF(q)\right|^2 \sum_{\alpha\beta}(\delta_{\alpha\beta}-\hat{q}_\alpha\hat{q}_\beta)S_{\alpha\beta}(q,\omega)\ , \quad (2.16)$$

where the dynamic structure factor is the space and Fourier transform of the time dependent spin–spin correlation function

$$S_{\alpha\beta}(q,\omega))\frac{1}{2\pi\hbar}\int\sum_{RR'} e^{i\omega t - iq\cdot(R-R')}\langle S^\alpha_R(t)S^\beta_{R'}(0)\rangle\ . \quad (2.17)$$

Thus apart from the geometric factor $\delta_{\alpha\beta}-\hat{q}_\alpha\hat{q}_\beta$ the magnetic scattering cross section is directly proportional to the dynamic structure factor. In fact, the geometric factor can often be exploited to separate the longitudinal and transverse components of $S(q,\omega)$.

2.2 Neutron scattering instruments

In practice, the realization of the formulated scattering geometry with a perfectly collimated and monochromated neutron beam is not achievable. There exist a number of ways to realize an approximation of the scattering geometry, and the two perhaps most common will be presented below. The two major complications for neutron scattering experiments are that neutrons are difficult to produce and that they interact weakly with matter. In combination, they make neutron scattering a technique, which in many cases is limited by counting statistics.

There are two ways of producing neutrons for scattering purposes. At a nuclear reactor, the flux of neutrons in the core can be guided out through the shielding to perform experiments. Alternatively, neutrons can be produced by bombarding highly accelerated particles onto a target of some heavy element, which is spallated

with a burst of particles — including neutrons — as a result. These two source types are denoted reactor and spallation sources, respectively. When created, the neutrons have energies much higher than the 1 meV to 1 eV range which is interesting to neutron scattering. Therefore the neutrons are sent through a moderator material, where through elastic collisions the neutrons are thermalised to the desired energy range. The outcome is a neutron beam with a broad distribution of energies and with a broad directional distribution.

In order to obtain sufficient statistics in a measurement, it is necessary to abandon the ideal monochromatic collimated beam used in the theory, and accept a finite distribution in both energy and divergence. The result is that the measured intensity is given by the scattering cross-section folded with the experimental resolution. Depending on the information required, the count rates versus resolution must be balanced.

Thus in a nominal scattering condition specified by q and ω, there is a finite probability $R(q,\omega;\Delta q,\Delta\omega)$ that a neutron with slightly deviating momentum $q' = q+\Delta q$ and energy $\omega' = \omega+\Delta\omega$ transfers is detected. The function R is denoted the resolution function and the count rate in an experiment is given by the convolution

$$I(q,\omega) = \int \left.\frac{d^2\sigma}{d\Omega dE_f}\right|_{q',\omega'} R(q,\omega;q'-q,\omega'-\omega)dq'd\omega' \ . \tag{2.18}$$

The resolution volume $R_0 = \int R(q,\omega;q'-q,\omega'-\omega)dq'd\omega'$ expresses the total acceptance of the experiment.

2.2.1 The triple axis spectrometer

One well-proven way to realize the scattering condition is to use a so called triple axis spectrometer (TAS). The key ingredient is that the energy selection both before and after the sample is achieved by Bragg scattering from well defined crystals. If a white beam of neutrons is shined onto a set of scattering planes with spacing d at an angle of θ, most neutrons will not satisfy the Bragg scattering condition and will travel through the crystal. But those neutrons that have a wavelength $\lambda = 2d\sin\theta$ will be scattered and leave the crystal with an angle of 2θ relative to the incident beam direction. Thus, a single energy $E = \frac{h^2}{2m\lambda^2}$ has been separated out. In reality, the divergence of the incoming beam and the mosaicity (distribution in crystal-plane orientations) of the crystal will result in a finite energy band rather than a truly monochromatic beam.

In addition to the collimating effect due to the distance to the source and a finite size of the crystal, the divergence of the beam can be controlled by using a collimator, which is an assembly of thin neutron absorbing sheets. The largest divergence by which a neutron can travel through the collimator is given by the sheet separation divided by their length.

By placing such energy selecting crystals both before and after the sample (denoting them respectively monochromator and analyser), the scattering situation with well defined $\boldsymbol{k}_i$ and $\boldsymbol{k}_f$ is realised. Since each crystal and the sample represents an axis of rotation, the instrument is called a triple axis spectrometer (TAS). Figure 2.2 shows the schematics of the RITA spectrometer at Risø National Laboratory, Denmark. This instrument was used for studying the finite temperature correlations in $Cu(DCOO)_2{\cdot}4D_2O$ as presented in section 4.3.

The traditional elements of a TAS are: source, monochromator, sample, analyser and detector, each separated by collimators to enable flexibility over the resolution volume. The 're-invented triple axis spectrometer' (RITA) is one in a series of newly designed spectrometers, where the overall design goal has been to gain intensity on the account of resolution along directions in reciprocal and energy space that can be afforded (Mason *et al.*, 1995, Broholm, 1996, Hiess, 1999,

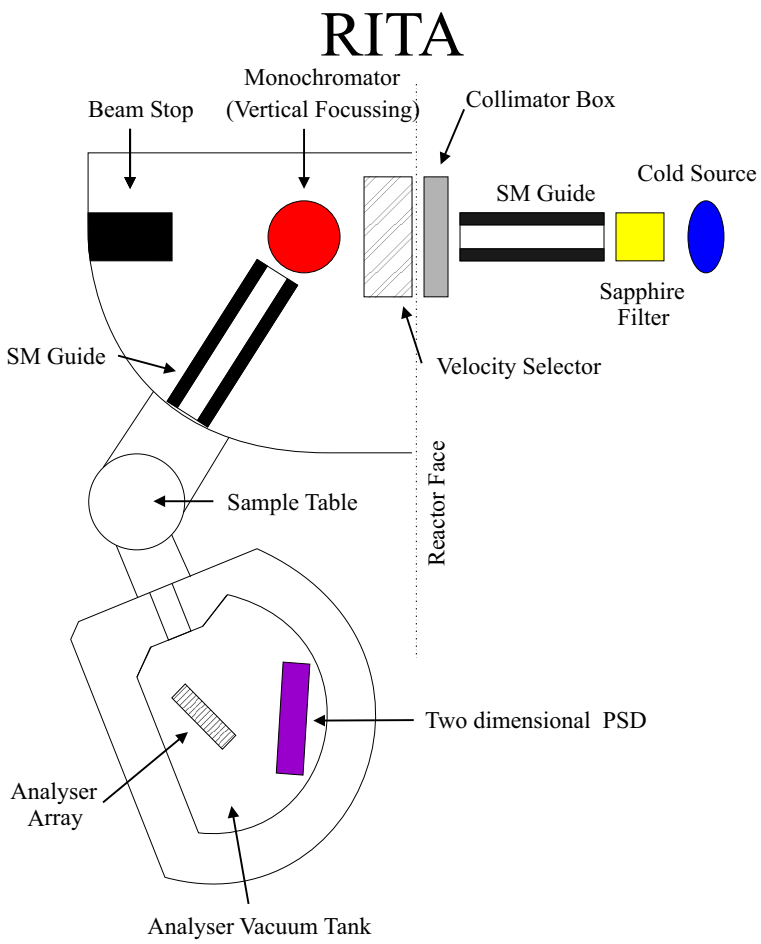

Figure 2.2. Schematic representation of the RITA spectrometer. The front end is constructed to optimise the flux at the sample position by using neutron mirrors and focusing monochromator. The back end with 7 individually turnable analyser blades and a position sensitive detector (all in one detector tank) is designed to enable flexible shaping of the resolution function.

FRM-II, 2000). On RITA, this is achieved by introducing new features, such as a velocity selector, neutron guides, a focusing monochromator, a multi-blade analyser assembly and a position sensitive detector. A new RITA-II is currently under construction at Risø. For this instrument, care has been taken to create a flexible modular design that will allow easy customisation of the instrument for each individual experiment (Lefmann *et al.*, 2000).

2.2.2 Time of flight neutron scattering

An alternative to the triple axis spectrometers, where the incident and final energies of the neutrons are filtered by Bragg reflection, is the time-of-flight (TOF) technique. This method becomes particularly useful at spallation sources, where the neutrons are created in well defined time-pulses by bombarding atoms with a high-energetic beam of particles. Knowing the time it takes a neutron to reach the detector, the velocity and hence energy can be calculated. The advantage is that one energy-filter can be removed, thus exploiting a larger fraction of the available neutrons.

The method of finding the energy of the neutrons by measuring their time of flight has been implemented in different ways. In *diffraction* experiments, the in-

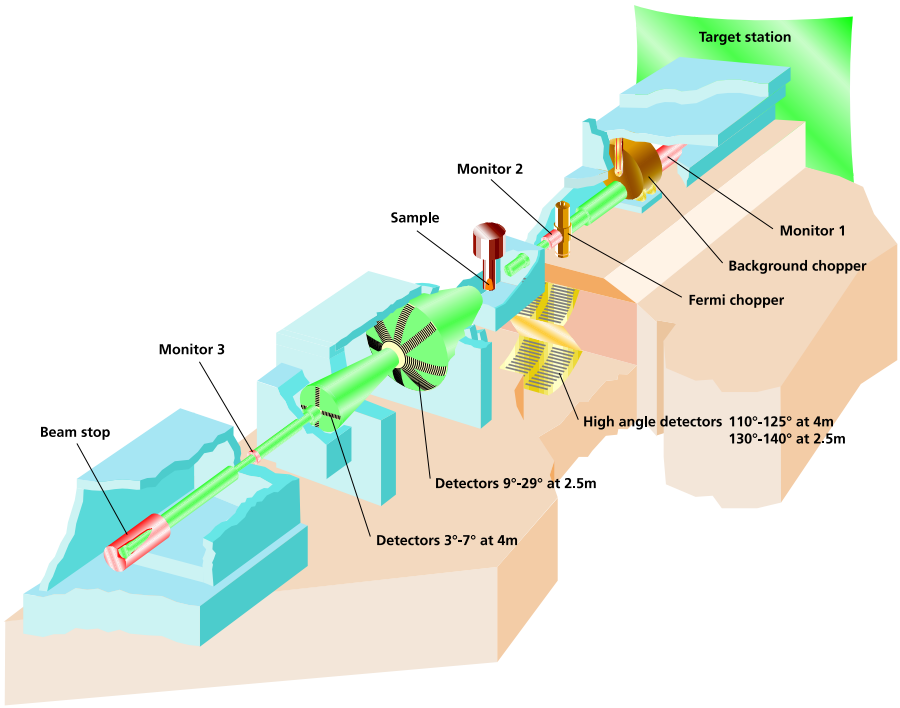

Figure 2.3. The HET spectrometer. Figure is adapted from (Eccleston et al.*, 1998)*

elastic scattering contribution is neglected. The sample is illuminated by a white beam pulse of neutrons, that are scattered into detectors at different scattering angles. From the time of arrival, the wave length and hence momentum transfer of the neutrons is deduced. Detectors in the same scattering plane contain essentially the same information but can be combined to supply better statistics. If the detector assembly could be made to cover all solid angle around the sample, all neutrons would be exploited. The corresponding two-axis spectrometer inevitably wastes the neutrons discarded at the monochromator.

For inelastic scattering, the velocity of the scattered neutrons depends on the energy transfer, and it is not sufficient to measure the time of flight. Therefore the energy of the neutrons is monochromated before the sample (*direct geometry*) or analysed after the sample (*indirect geometry*). In both cases, one filtering stage discards neutrons. In comparison, the triple axis spectrometer discards neutrons both at the monochromator and at the analyser.

The dynamics of $Cu(DCOO)_2 \cdot 4D_2O$ was investigated at the HET direct geometry spectrometer at ISIS, UK (Eccleston *et al.*, 1998), as described in section 3.5. A schematic drawing of the instrument is presented in figure 2.3. The pulse of neutrons created at the target is thermalised by a 22 K hydrogen moderator. A nimonic chopper blocks the incident neutron path during the pulse creation, thereby removing γ and fast neutron background. The incident energy is determined by a Fermi-chopper, which is a rotating drum with thin absorbing sheets. By varying the phase of the drum to the pulse, the desired incident energy is obtained. The resolution and flux requirements can be accommodated by choosing between drums with different sheet-separation and spinning them at multiples of the pulse-frequency.

Finally, it should be mentioned that even reactor based sources host time of flight instruments. Here, the constant flux beam is chopped into pulses of desired duration and interval. Though the main advantage of saving a filtering stage is lost, reactor based TOF instruments are relevant when an energy resolution of 3 μeV to 200 μeV is required (NIST and ILL, 2000). They thereby fill the gap

between the resolution of triple axis and neutron-spin-echo spectrometers, having the advantage over the later that TOF still works in frequency space.

A note on units Out of practicality, most experimental techniques have a special set of units associated with it. In neutron scattering, it is customary to use the units of Å, $Å^{-1}$ and meV. For neutrons $E = \frac{\hbar^2 k^2}{2m} = \frac{h^2}{2m\lambda^2}$ leads to the following useful numerical relations E [meV]= $2.072k^2$ [meVÅ^2]= $81.8/\lambda^2$ [meVÅ^2]. Other methods use different units for energy based on for instance the frequency of light. The conversion between a number of frequently used energy units is defined by $E = eU = k_B T = \mu_B H = h\nu = hc/\lambda$. Throughout this thesis the defining constants will often be set equal to unity in theoretical expressions. And when quoting experimental results, the units that are traditionally used in different experimental techniques are used interchangeably according to 1 meV $\leftrightarrow$ 11.60 K $\leftrightarrow$ 17.28 T $\leftrightarrow$ 0.2418 THz $\leftrightarrow$ 8.065 cm^{-1} $\leftrightarrow$ 1.602×10^{-22} J.

Similarly will reciprocal space vectors often be measured in units of the lattice constant so that a reciprocal lattice point is a multiple of 2π. And the inner field H which is formally in units of A/m will be given in tesla, corresponding to setting μ_0 equal to unity.

Chapter 3

$CuGeO_3$ — a spin–Peierls material

Structure and excitations in the soliton phase

The domain wall pair excitations in dimerised spin–Peierls systems can be stabilized to form a static soliton lattice by application of a magnetic field. Neutron scattering studies of the spin–Peierls system $CuGeO_3$ have led to the determination of the magnetic soliton structure with a periodicity of more than 66 lattice spacings. The maximum amplitude of the magnetic structure reaches only one tenth of the ordered moment, the rest being 'buried' in a coherent quantum ground state. Still, the soliton structure completely changes the excitation spectrum which has also been examined by inelastic neutron scattering.

The ground state of the pure one-dimensional spin 1/2 Heisenberg antiferromagnet is disordered due to quantum fluctuations, which raise the ground state energy. This makes it susceptible to perturbations that can suppress the quantum fluctuations. If embedded in a non-rigid three-dimensional lattice, the system will below a certain temperature undergo a so-called spin–Peierls transition, below which the chain distorts so that spins are paired to form a non-magnetic singlet ground state. The alternating lattice distortion and the concomitant pairing of the spins is known as dimerization.

There are two degenerate ways in which the system can dimerize. A given spin can pair up with either the left or the right neighbour. The elementary excitations of a dimerized system are therefore domain walls, which separate the two types of domains. The domain walls are also called *solitons* and in order to affect only a finite number of sites, they have to appear in (soliton–anti-soliton) pairs. In the ideal 1D system, they can be infinitely separated, but if there is any coupling (magnetic or elastic), the region of a chain spanned by a soliton pair will be in the 'wrong' state relative to the surrounding chains. The interchain energy cost will bind the soliton pairs.

A soliton pair can be imagined as a broken dimer, creating two free spins which then repel each other, leaving a region of the 'wrong' domain between them. Because each soliton carries spin $\frac{1}{2}$, it will be favored by a magnetic field, and at a critical field H_c they are stabilized to form a static lattice of solitons. This provides a unique opportunity to study a macroscopic quantum ground state in which the magnetic system and the lattice system are delicately balanced.

This chapter reports on neutron scattering studies of the soliton-phase. As neutrons probe both the magnetic and structural correlations with sufficient energy

resolution, a rather complete description of both the statics and dynamics of the soliton-phase in $CuGeO_3$ has been obtained. Quite remarkably, the soliton structure is well described by a continuum field theory with only two parameters that have been fixed by measurements in the spin–Peierls phase at zero magnetic field. The theoretical expectations for the excitation spectrum are less settled, but the experimentally observed excitations are qualitatively understood and a quantitative description is anticipated in the near future (Enderle *et al.*, 2000).

The chapter is organized as follows: Section 3.1 and 3.2 give an introduction to the spin–Peierls phenomena and in particular the soliton solution. The present understanding of $CuGeO_3$ as a physical realization of a spin–Peierls system is summarized in section 3.3. The neutron scattering results are presented in sections 3.4 and 3.5 for the statics and the dynamics respectively.

3.1 The spin–Peierls transition

The ground state of the classical Heisenberg antiferromagnetic chain is the Néel state with a ground state energy of $E_g^{\rm cl} = -JS^2$ per spin, where it is appropriate to use $S^2 \equiv S(S+1)$, giving $E_g^{\rm cl} = -\frac{3}{4}J$ for $S = 1/2$. In the quantum mechanical case, quantum fluctuations populate the lowest lying excited states, which is known as zero-point motion. In fact, they do it to an extent where long ranged antiferromagnetic order is destroyed, but what is important in this context is that the quantum fluctuations raise the ground state energy to $E_g^{\rm qm} = (\frac{1}{4} - \ln 2)J$ (Hulthén, 1938). Thus quantum fluctuations 'cost' energy and the system is therefore susceptible to any perturbation that can act to reduce the quantum fluctuations.

One such perturbation would be an alternation $J(1\pm\delta)$ of the coupling strength, where $\delta = 0$ is the uniform chain and $\delta = 1$ corresponds to isolated spin pairs. The alternation breaks the translational symmetry by doubling the unit cell, thereby opening a gap in the excitation spectrum as illustrated in figures 3.1 and 3.2. The size of this gap is proportional to $\delta^{2/3}$ and hence the ground state energy is reduced to

$$E_g^{qm} = \left(\frac{1}{4} - \ln 2 - \frac{\delta^{4/3}}{c_1}\right) J \ , \tag{3.1}$$

where $c_1 \simeq \pi^{2/3}4/3$ (Cross and Fisher, 1979, Barnes *et al.*, 1999). What is happening can be realized by going to the extreme alternation limit $\delta = 1$, where one of the coupling parameters vanishes. In this case the system becomes an assembly of isolated spin-pairs (*dimers*). The ground state of one dimer can be described as $\frac{1}{\sqrt{2}}(|\uparrow\downarrow\rangle - |\downarrow\uparrow\rangle)$ with a ground state energy of $-\frac{3}{4}J$ per spin. The excited states form a degenerate triplet $\{|\uparrow\uparrow\rangle, |\downarrow\downarrow\rangle, \frac{1}{\sqrt{2}}(|\uparrow\downarrow\rangle + |\downarrow\uparrow\rangle)\}$ with energy $\frac{1}{4}J$ per spin.

One way to realize an alternating coupling would be to exploit a spatial dependence of the coupling $J(r_n - r_{n+1}) \simeq J + (u_n - u_{n+1})\nabla J$, where u_n measures the deviation of r_n from the equilibrium position and ∇J is the derivative of J in this position. By shifting adjacent spins in opposite directions along the chain ($u_n = (-1)^n u_0$), an alternating exchange is realized $J_{n,n+1} = J + (-1)^n 2u_0\nabla J$ with $\delta = 2u_0(\nabla J)/J$. In the following, the term dimerisation is used both for the alternating lattice distortion and for the concomitant formation of spin singlet states as described above in the $\delta = 1$ case.

A distortion of the lattice will have an elastic energy cost that can be assumed to be quadratic in the displacement and hence also in δ

$$E_{\rm elast} = 2Ku_0^2 = \frac{KJ^2}{2(\nabla J)^2}\delta^2 \ , \tag{3.2}$$

where K is the elastic constant. Since the decrease in magnetic energy is proportional to $\delta^{4/3}$ and the elastic energy only increases as δ^2, the total energy is minimized by

$$\delta \simeq \pi \left(\frac{(\nabla J)^2}{KJ}\right)^{3/2} \ . \tag{3.3}$$

Hence any finite amount of *magneto-elastic coupling* (∇J) will lead to dimerization.

At finite temperature, thermal fluctuations will affect not only the spins, but also the lattice. Fluctuations in the lattice will reduce the effect of dimerization thus leading to an increase in the quantum fluctuations. Eventually, this will destroy the dimerization at a characteristic temperature $T_{sp} \sim \frac{(\nabla J)^2}{K}$ called the spin–Peierls temperature. In the uniform phase above T_{sp}, translational symmetry is recovered.

3.1.1 The uniform Heisenberg chain

Before embarking upon a quantitative description of the spin–Peierls transition, it is useful to summarize the properties of the uniform $S = 1/2$ antiferromagnetic Heisenberg chain (on a rigid lattice) described by

$$\mathcal{H} = J \sum_i \boldsymbol{S}_i \cdot \boldsymbol{S}_{i+1} \ . \tag{3.4}$$

This very simple model has a remarkably rich behaviour. Even though an exact solution for the ground state has been found using the Bethe ansatz (Bethe, 1931, Hulthén, 1938, des Cloizeaux and Pearson, 1962, Bonner and Fisher, 1964), many aspects of the system remain to be fully understood. The ground state does not exhibit long range order, but the staggered spin–spin correlation function $(-1)^r \langle \boldsymbol{S}_0 \cdot \boldsymbol{S}_r \rangle$ decays algebraically with the distance r (Müller *et al.*, 1981, Schulz, 1986, Nomura and Yamada, 1991, Lin and Cambell, 1991). However, also the 'dimer'-correlation function $(-1)^r [\langle (\boldsymbol{S}_0 \cdot \boldsymbol{S}_1)(\boldsymbol{S}_r \cdot \boldsymbol{S}_{r+1}) \rangle - \langle \boldsymbol{S}_0 \cdot \boldsymbol{S}_1 \rangle^2]$ has a similar slow decay with r (Deisz, 1992).

The excitation spectrum is dominated by a quasi-particle mode with dispersion

$$\omega_q = \frac{\pi}{2} J |\sin q| \ , \tag{3.5}$$

with a spin wave velocity $v_s = \lim_{q \to 0} E_q/q = \frac{\pi}{2} J$. The term spin-wave velocity is used even though the elementary excitations are spinons and not spin waves. At finite temperatures, the susceptibility $\chi(T)$ increases from its $T = 0$ value of $\frac{g^2 \mu_B^2}{\pi^2 J}$, passes through a broad maximum at $T \sim 0.6J$, after which it decreases as described by a high temperature expansion (see figure 3.12 and Griffiths, 1964, Eggert *et al.*, 1994).

The quasi-particle mode is the lower bound of a spinon continuum extending the region up to $\pi J |\sin q/2|$, for which the dynamic structure factor has been calculated numerically (Müller *et al.*, 1981, Lefmann and Rischel, 1996).

The Jordan–Wigner transformation

A spin-wave calculation of the reduction in the staggered moment due to zero-point fluctuations diverges in one dimension, thus signaling the breakdown of the spin wave approximation (Broholm *et al.*, 1998). Instead, considerable insight has been obtained by performing a Jordan–Wigner (JW) transformation, by which the system is equivalent to one of interacting fermion particles (Luther and Peschel, 1975).

$$S_n^+ = (-1)^{\sum_m^{n-1} a_m^\dagger a_m} a_n^\dagger = (S_n^-)^\dagger \tag{3.6}$$

$$S_n^z = -\frac{1}{2} + a_n^\dagger a_n \tag{3.7}$$

$$S_n^+ S_{n+1}^- = a_n^\dagger a_{n+1} \tag{3.8}$$

Inserted in the spin part of the Hamiltonian, the Jordan–Wigner transformation turns the x, y part into a kinetic energy term, while the z part introduces a two-particle interaction operator

$$\mathcal{H}_s = \sum_k \epsilon_k a_k^\dagger a + \frac{1}{N} \sum_{kk'q} v(q) a_{k+q}^\dagger a_{k'+q}^\dagger a_{k'} a_k \ , \tag{3.9}$$

where $\epsilon_k = J(\cos k - 1)$ and $v(q) = J \cos q$. (In the following $\hbar$ is set equal to unity and the momentum is in units of the reciprocal lattice constant.) In the Hartree mean field approximation (MF) the two-particle terms are treated by using $\langle a_k^\dagger a_{k'} \rangle \simeq n_k \delta_{kk'}$, where $n_k = (e^{\beta E_k} + 1)^{-1}$. The resulting fermion energy

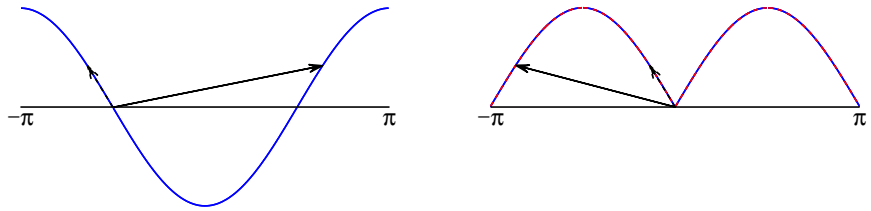

Figure 3.1. Left: The fermion particle energy, which is filled to the Fermi-level indicated by the horizontal line. Two representative excitation processes are demonstrated with arrows. Right: The corresponding collective excitation dispersion, where the two processes are again illustrated with arrows.

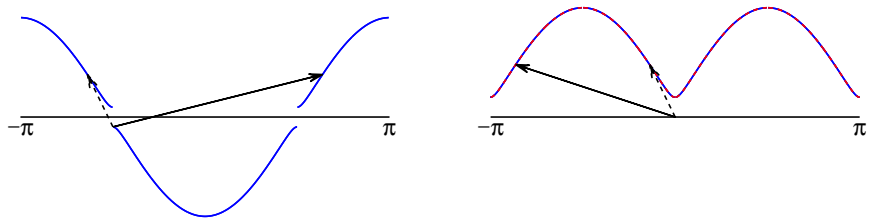

Figure 3.2. Left: An alternating coupling parameter opens a gap in the fermion bands. Right: This gap is transferred to the dispersion of the collective excitations, thereby suppressing the quantum fluctuations. The arrows illustrate two possible processes.

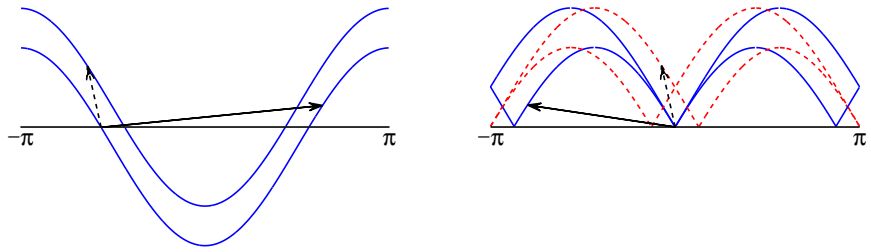

Figure 3.3. Left: Splitting by $g\mu_B H$ of the two fermion bands, causing to different kinds of collective excitations: The inter band (solid arrow) excitations correspond to longitudinal spin fluctuations, while the band crossing (dashed arrow) excitations corresponds to transverse spin fluctuations. Right: The longitudinal (solid) and transverse(dashed) dispersion relations with soft modes both at commensurate positions and at incommensurate positions.

$E_k = pJ\cos k$ is renormalized due to the z component of the interaction. The value $p = 1 - 2/N\sum_k n_k \cos k \simeq 1.64$ is quite close to the exact result $\frac{\pi}{2}$.

The relation between the single fermion particle energy and the dispersion of the collective excitations is visualized graphically in figure 3.1. The degenerate fermion band is filled to the Fermi level which is indicated by a horizontal line. Excitations of the system brings particles on the Fermi-brink to unoccupied states at higher energies. The resulting excitation spectrum has a dispersion relation as illustrated to the right. An alternating exchange interaction opens a gap in the single particle band, which is transferred to the collective dispersion relation as shown in figure 3.2.

For later purposes it is also instructive to see how the system is influenced by application of an external magnetic field. By inspecting the JW transformation, it is seen that the Zeeman term splits the two fermion bands by $g\mu_B H$ as depicted in figure 3.3 (Pytte, 1974, Müller *et al.*, 1981, Dender *et al.*, 1997). As a result the inter band and the band-crossing excitation processes acquire different dispersion relations with soft modes at respectively the zone center and at the incommensurate positions given by $g\mu_B H/v_s$.

3.1.2 Spin–phonon treatment

The coupling between the spin-system and the vibrations in the lattice is through the dependence of the coupling $J_{n,n+1}\boldsymbol{S}_n \cdot \boldsymbol{S}_{n+1}$ on the atomic positions. This section explains how the phonons are affected by the coupling to the spin system. In the simplest form, this coupling is given by the distance between the two magnetic ions and can be approximated by the constant and linear terms in a Taylor expansion around the equilibrium positions $J(r_{n+1} - r_n) \simeq J + (\boldsymbol{u}_{n+1} - \boldsymbol{u}_n) \cdot \boldsymbol{\nabla} J(r_{n+1} - r_n)$, where u_n is the displacement of r_n from its equilibrium position. It is seen that the coupling depends on the difference between two displacements and it is therefore denoted *difference coupling*. It is characterized by the fact that one displacement u_n influences two adjacent bonds.

If the magnetic interaction is mediated by super exchange through some non-magnetic atom in the crystal structure, then a displacement $\boldsymbol{u}_{n,d}$ of that atom will influence only one bond. This type of coupling is called *local coupling*. A general linear approximation for the spin–lattice coupling is

$$\begin{aligned} \mathcal{H}_{sp} &= \sum_{nd} \boldsymbol{u}_{nd} \cdot (\boldsymbol{\nabla}_{n,d} J_{n-1,n} \boldsymbol{S}_{n-1} \cdot \boldsymbol{S}_n + \boldsymbol{\nabla}_{n,d} J_{n,n+1} \boldsymbol{S}_n \cdot \boldsymbol{S}_{n+1}) \\ &= \sum_{nd} (\boldsymbol{u}_{nd} \cdot \boldsymbol{\nabla}_{n,d} J_{n,n+1} + \boldsymbol{u}_{n+1d} \cdot \boldsymbol{\nabla}_{n+1,d} J_{n,n+1}) \boldsymbol{S}_n \cdot \boldsymbol{S}_{n+1} \ , \end{aligned} \quad (3.10)$$

where n refers to the unit cell and d to the (magnetic and mediating) atoms within the unit cell. The above mentioned cases are realized as $\nabla_{n+1,d} J_{n,n+1} = 0$ for *local coupling* and $\nabla_{n,d} J_{n,n+1} = -\nabla_{n+1,d} J_{n,n+1}$ for *difference coupling*. In $CuGeO_3$, the motion of the Cu ions results in difference coupling, while motion of the connecting oxygen results in local coupling. As the lowest SP active phonon involves negligible motion of Cu, it corresponds to local coupling. The next mode is a mixture of the two. (See section 3.3.1)

The kinetic and potential energy of the lattice is treated in the standard way of transforming to normal modes and quantizing to phonon operators (Ashcroft and Mermin, 1976, Kittel, 1996)

$$\boldsymbol{u}_{nd} = \frac{1}{\sqrt{N}} \sum_{q\alpha} e^{iq\cdot r_n} \frac{\boldsymbol{e}_d(q\alpha)}{\sqrt{2m_d \Omega_0(q\alpha)}} (b^\dagger_{-q\alpha} + b_{q\alpha}) \ , \quad (3.11)$$

where $\boldsymbol{e}_d(q\alpha)$ is the polarization vector of ion d for mode α with dispersion $\Omega_0(q,\alpha)$. Though it is straight forward to include several phonon modes (Werner

et al., 1999), for simplicity, only one is kept here, and hence the index α is dropped. Using this transformation, the phonon part of the Hamiltonian is diagonalised:

$$\mathcal{H}_p = \sum_q \Omega_0(q)(b_q^\dagger b_q + \frac{1}{2}) \ . \tag{3.12}$$

The spin-phonon coupling term becomes

$$\mathcal{H}_{sp} = \frac{1}{\sqrt{N}} \sum_q g_q (b_{-q}^\dagger + b_q) \sum_n e^{iq\cdot r_n} \boldsymbol{S}_n \cdot \boldsymbol{S}_{n+1} \ , \tag{3.13}$$

where

$$g_q = \sum_d \boldsymbol{e}_d(q) \cdot (\boldsymbol{\nabla}_{n,d} + e^{iq} \boldsymbol{\nabla}_{n+1,d}) J(n, n+1) / \sqrt{2 m_d \Omega_0(q)} \ . \tag{3.14}$$

First, the effect on the phonon system is considered. The renormalised phonon frequency $\Omega(q)$ is given by the poles in the phonon Green's function

$$D(q,\omega) = \frac{-i}{2\pi} \int dt e^{i\omega t} \langle \Theta(t) b_q(t) b_q^\dagger + \Theta(-t) b_q^\dagger b_q(t) \rangle \ , \tag{3.15}$$

which is calculated through Dyson's equation $D = D_0 + D_0 \Pi D$, where $D_0(q,\omega) = 2\Omega_0(q)[\omega^2 - \Omega_0^2(q) + i\eta]^{-1}$ is the noninteracting phonon propagator (η is a positive infinitesimal) and $\Pi(q,\omega)$ the phonon self energy. Rewriting gives $D(q,\omega) = 2\Omega_0(q)[\omega^2 - \Omega_0(q)^2 - 2\Omega_0(q)\Pi(q,\omega)]^{-1}$ with the poles Ω_q determined as selfconsistent solutions to

$$\Omega_q^2 = \Omega_0^2(q) + 2\Omega_0(q)\Pi(q,\Omega_q) \ . \tag{3.16}$$

In the random-phase approximation (RPA) the phonon self energy is given by the susceptibility $\Pi(q,\omega) = |g_q|^2 \chi_d(q,\omega)$. The dimer–dimer susceptibility $\chi_d(q,\omega)$ is the space and time Fourier transform of the response function $-i\Theta(t)\langle [S_n(t) \cdot S_{n+1}(t), S_0 \cdot S_1] \rangle$.

In the JW–MF approximation the spin–phonon term becomes

$$\mathcal{H} = \sum_{kq} g(q,k) a_k^\dagger a_{k-q} (b_{-q}^\dagger + b_q) \ , \tag{3.17}$$

where $g(q,k) = -ip(\sin k - \sin(k-q)) g_q$. This gives for the phonon self energy

$$\Pi(q,\omega) = \frac{1}{N} \sum_k \frac{|g(k,q)|^2 (n_k - n_{k-q})}{\omega - E_{k-q} + E_k} \ . \tag{3.18}$$

Using $E_{k-\pi} = -E_k$ so that $n_k - n_{k-\pi} = -\tanh \frac{1}{2}\beta E_k$ and $\sin(k-\pi) = -\sin k$, the assumption of a softening $\Omega_\pi = 0$ at a critical temperature T_{sp} gives the self consistency equation

$$\Omega_0(\pi) = \frac{4}{N} p^2 |g_\pi|^2 \sum_k \frac{|\sin k|^2 \tanh \frac{1}{2}\beta_{sp} E_k}{E_k} \ , \tag{3.19}$$

which is turned into an integral using $\frac{1}{N}\sum_k \longrightarrow \frac{1}{2\pi}\int dk \longrightarrow \frac{1}{\pi}\int_{-pJ}^{pJ} g E (dE_k/dk)^{-1}$ and $pJ|\sin k| = \sqrt{p^2J^2 - E_k^2}$ so that

$$\Omega_0(\pi) = \frac{4}{\pi} \frac{|g_\pi|^2}{J^2} \int_{-pJ}^{pJ} dE \frac{\sqrt{p^2J^2 - E^2}}{E} \tanh \tfrac{1}{2}\beta_{sp} E \ . \tag{3.20}$$

For $T_c \ll J$, the integral can be solved by introducing a cutoff $T_c \ll X \ll pJ$ and integrating $E < X$ and $E > X$ separately. This determines the transition temperature

$$T_c = 0.8343 \times pJ \exp\left(-\frac{\pi \Omega_0(\pi) J}{4p|g_\pi|^2} \right) \ . \tag{3.21}$$

Below this temperature, the lattice dimerizes, thus producing a magnetic excitation gap $\Delta(T=0) = 1.765T_c$ and an alternating exchange coupling $J(1 \pm \delta)$, where $\delta = \Delta/pJ$.

The MF approximation neglects spin-fluctuations, which a priori must be expected to be significant in a 1D antiferromagnet. This is partially justified by the 3D nature of the phonons, but a more careful treatment leads to quantitatively different results for the parameters like T_{sp}. Cross and Fisher circumvented the MF approximation by calculating the susceptibility from a bosonized version of the spin system.

$$T\chi_q(\omega) = -2dI_1\left(\frac{\omega - v_s|q-\pi|}{2\pi T}\right) I_1\left(\frac{\omega + v_s|q-\pi|}{2\pi T}\right) \ , \tag{3.22}$$

with

$$I_1(x) = \frac{1}{2\pi}\int_0^\infty \frac{e^{ixy}}{\sqrt{\sinh y}}dy = \frac{1}{\sqrt{8\pi}}\frac{\Gamma(\frac{1}{4}+\frac{i}{2}x)}{\Gamma(\frac{3}{4}+\frac{i}{2}x)} \ , \tag{3.23}$$

where $d = \frac{9}{4}(1+\alpha^2)^{-3/4} \simeq 0.38$ and $\alpha \simeq \pi$ is the momentum cutoff. For a quantum critical system such as the uniform Heisenberg chain $T\chi_q(\omega)$ is a scale invariant function of $\omega/2\pi T$, which justifies an expansion $T\chi_\pi(\omega) = -\sum_n \chi_n(\omega/2\pi T)^n$. For $q=\pi$ the coefficients are $\chi_0 = 0.26$, $\chi_1 = -0.81i$, $\chi_2 = -2.22$, $\chi_3 = 5.63i$ and $\chi_4 = 13.7$. However, numerical calculations predict a significant dependence of the parameters on temperature and also on possible next-nearest-neighbour coupling, giving values at T_{sp} for χ_0 between 0.28 and 1 for the range of parameters that are likely to be relevant for $CuGeO_3$ (Werner *et al.*, 1999, Klümper *et al.*, 1999).

The renormalised phonon frequency at $q=\pi$ is given by the location of the poles of the Green's function

$$\frac{\omega^2 - \Omega_0^2(\pi)}{2\Omega_0(\pi)|g_\pi|^2} = \mathrm{Re}\chi_\pi(\omega) = -\frac{\chi_0}{T} - \frac{\chi_2}{T}\left(\frac{\omega}{2\pi T}\right)^2 - \frac{\chi_4}{T}\left(\frac{\omega}{2\pi T}\right)^4 - \cdots \ . \tag{3.24}$$

This determines the transition temperature as $T_{sp} = 2|g_\pi|^2\chi_0/\Omega_0(\pi)$. Looking for solutions with $\omega > 0$ at T_{sp} gives the equation

$$\left(\frac{1}{2\Omega_0(\pi)|g_\pi|^2} + \frac{\chi_2}{(2\pi T_{sp})^2}\right) = -\frac{\chi_4}{T_{sp}(2\pi T_{sp})^4}\omega^2 \ . \tag{3.25}$$

Since $\chi_4 > 0$, the right-hand-side is a parabola with the branches pointing down, there is a solution with $\omega > 0$ when the left-hand-side is positive. Thus for $\Omega_0(\pi) < 2\pi\sqrt{\chi_0/\chi_2}T_{sp} \simeq 2.15 \times T_{sp}$ there is only the $\omega = 0$ solution, which is the result of a continuous softening from $\Omega_0(\pi)$ at high temperatures. But for $\Omega_0(\pi) > 2.15 \times T_{sp}$, the phonon energy remains finite at the transition, where a central peak (the new $\omega = 0$ mode) develops. In fact, for large enough $\Omega_0(\pi)$, the renormalised phonon frequency hardens at the transition.

The important conclusion is that a spin–Peierls transition can occur for any value of the unrenormalized phonon frequency.

3.1.3 Effective magnetic model

Having understood the renormalization of the phonon modes and the spin–Peierls transition itself, the spin-system can be examined. Naturally, the true ground state and excited states of the system are composite spin- and phonon-states, but until the task of solving the combined system has been accomplished, it is useful to consider the effective magnetic Hamiltonian.

As realized above, both the soft and the hard phonon regions lead to a static ($\Omega = 0$) lattice displacement. Treating this displacement classically, neglecting the phonon dynamics is known as the adiabatic approximation, which leads to an effective Hamiltonian given by

$$\mathcal{H}_{sp} = \sum_n J(1+\lambda u_n)S_n \cdot S_{n+1} + \frac{K}{2}u_n^2 \ , \tag{3.26}$$

where $\delta_n = \lambda u_n$ and the displacement parameter u_n is adjusted to minimize the ground state energy. But as will be seen below, in the case of hard phonons, an additional renormalization of the magnetic coupling parameters takes place. Of particular importance is that an effective second nearest neighbour interaction is induced. The problem has been treated using flow equations (Uhrig, 1998), unitary transformations (Zheng, 1997, Weiße and Fehske, 1998, Weiße *et al.*, 1999) and DMRG calculations (Bursill *et al.*, 1999).

Zheng (1997), Weiße and Fehske (1998) and Weiße *et al.* (1999) used unitary transformations of the spin–Peierls Hamiltonian to reach an effective spin-only Hamiltonian. They used two sequential unitary transformations $\tilde{\mathcal{H}} = e^{U_1}\mathcal{H}e^{-U_1}$ and $\bar{\mathcal{H}} = e^{U_2}\tilde{\mathcal{H}}e^{-U_2}$ with

$$U_1 = -\frac{\Delta_\pi}{2g_\pi}\sum_r (-1)^r (b_r^\dagger - b_r) \ , \tag{3.27}$$

$$U_2^{\mathrm{loc}} = f\frac{g_\pi}{\Omega_0(\pi)}\sum_r (b_r^\dagger - b_r)\boldsymbol{S}_r \cdot \boldsymbol{S}_{r+1} \ , \tag{3.28}$$

$$U_2^{\mathrm{diff}} = f\frac{g_\pi}{\Omega_0(\pi)}\sum_r (b_r^\dagger - b_r)(\boldsymbol{S}_r \cdot \boldsymbol{S}_{r+1} - \boldsymbol{S}_{r-1} \cdot \boldsymbol{S}_r) \ , \tag{3.29}$$

where Δ_π and f are variational parameters that are fixed self-consistently. The first transformation shifts the equilibrium position of the oscillators, thereby describing the static lattice dimerization. The second transformation decouples the hard phonons from the spin-system for respectively local and difference coupling. By averaging over the phonon subsystem $\mathcal{H}_{\mathrm{eff}} = \langle\bar{\mathcal{H}}\rangle$ an effective spin-Hamiltonian is reached

$$\mathcal{H}_{\mathrm{eff}} = J_0 + \sum_r (J_1 + (-1)^r \lambda u_0) S_r \cdot S_{r+1} + \sum_{n\leq 2} J_n \sum_r S_r \cdot S_{r+n} \ , \tag{3.30}$$

where u_0 and J_n are determined by J, g_π and $\Omega_0(\pi)$. For small $\Omega_0(\pi)/J \lesssim 1/10$, f is close to zero and the second transformation vanishes. In this situation, $\lambda u_0 = \Delta_\pi$ and $J_1 = J$, while there are no longer ranging effective interactions. At large phonon energies ($\Omega_0(\pi)/J \gtrsim 10$), f approaches 1. In this case, $J_1 = J + |g_\pi|^2/\Omega_0(\pi) - 3|g_\pi|^2 J/2\Omega_0(\pi)^2 Y$ and $J_2 = |g_\pi|^2/2\Omega_0(\pi) + 3|g_\pi|^2 J/2\Omega_0(\pi)^2 Y$ for the difference coupling (Weiße *et al.*, 1999) in agreement with the flow-equation approach (Uhrig, 1998), DMRG calculations (Bursill *et al.*, 1999) and a simple second order perturbation calculation similar to the electron–phonon treatment in BCS theory (Kuboki and Fukuyama, 1987). The parameter $Y = \coth\Omega_0(\pi)/2T$ makes the effective magnetic coupling temperature dependent. Weiße *et al.* (1999) included an intrinsic NNN coupling αJ and report J_n up to $n = 4$ for both local and difference coupling.

If the phonon frequencies are not much higher than, but just comparable to the magnetic coupling strength $\Omega_0(\pi) \sim J$, the elimination of the phonon dynamics may neglect important spin-lattice quasi-particles. In a numerical Lanczos diagonalisation on finite chains, it was found that for $\Omega_0(\pi) \sim g_\pi \sim J$ the magnetic excitations indeed involve a local lattice distortion (Wellein *et al.*, 1998). By quantum Monte Carlo calculations for the specific choice $\Omega_0(\pi) = J/4$ a $T = 0$ transition to spontaneous dimerization was found only for sufficiently large spin-phonon coupling $g_\pi > g_\pi^c = (0.225 \pm 0.015)J$ (Sandvik and Campbell, 1999).

Alternating and next-nearest neighbour coupling

As seen above, the soft and hard phonon limits of the spin–Peierls model can (at least for low applied fields) be transformed to a purely magnetic model with alternating nearest neighbour (NN) coupling $J(1 \pm \delta)$ and antiferromagnetic next-nearest neighbour (NNN) coupling αJ. In addition, there is of course the possibility that physical realizations of the spin–Peierls model may have intrinsic NNN

exchange coupling. It is therefore important to understand the behaviour of such a magnetic model system, but even in the absence of phonons this poses a considerable challenge.

Classically, there is no spin arrangement that can satisfy both NN and NNN antiferromagnetic coupling. This is called frustration and tends to destabilize magnetic order on behalf of dimer-correlations. In fact, at a critical value $\alpha_c = 0.2412$ translational symmetry is spontaneously broken and the dimer correlator $O_D = |\langle S_{n-1} \cdot S_n - S_n \cdot S_{n+1} \rangle|$ becomes non-zero (Chitra *et al.*, 1995). Obviously, the alternation directly breaks the translational symmetry and causes a finite value of O_D for any non-zero value of δ. In combination, NNN coupling serves to enhance the dimerization effects due to alternation.

Only for $\delta = 0$ and $\alpha < \alpha_c$ does the system resemble the pure NN $S = 1/2$ chain. The ground state has algebraically decaying antiferromagnetic correlations $(-1)^r \langle S_0 \cdot S_r \rangle$, and there is no long ranged dimer order. The excitation spectrum remains gapless with the same features as for the NN chain (Sørensen *et al.*, 1998). The spin-wave velocity is decreased by the NNN coupling. A numerical study (Fledderjohann and Gros, 1997) gives $v_s(\alpha) = \frac{\pi}{2} Ja(1 - 1.12\alpha)$, while a non-linear σ model approach (Affleck, 1990) gives $v_s(\alpha) = \frac{\pi}{2} J(1 - 4\alpha)^{1/2}$. A MF calculation gives $v_s(\alpha) = \frac{\pi}{2} J(1 - 0.8\alpha)$ and suggests that J and α can be determined independently from the temperature dependence of v_s (Muthukumar *et al.*, 1997).

Above α_c or for non-zero alternation, the dimer correlator O_D becomes finite and the long-distance behaviour of the antiferromagnetic correlation function crosses over from algebraic to (faster) exponential decay. A gap $\Delta \propto e^{-1/(\alpha - \alpha_c)}$ opens in the excitation spectrum, which is constituted by solitons with respect to the dimer order.

3.2 The field induced soliton phase

There are two degenerate dimerised ground states corresponding to respectively positive and negative u_0. The excitations from such a dimerised state are so-called solitons, which at a certain point along the chain change the sign of the dimerization. In one dimension, such solitons will destroy the dimer order, and therefore the MF and RPA theories presented above implicitly rely on the three-dimensionality of the phonons to stabilize the dimerization. Through this 3D coupling, solitons in adjacent chains attract each other, tending to line up perpendicular to the chain direction. Such arrays of solitons are called domain walls.

The energy cost of forming solitons is decreased by application of an external field. In the following it will be derived how above a critical field a static lattice of solitons is formed.

Effect of a magnetic field

The effect of a magnetic field is easily described within the fermion description. By Jordan–Wigner transformation, the Zeeman term becomes

$$-g\mu_B H \sum_n S_n^z = -\frac{1}{2} g\mu_B HN + g\mu_B H \sum_n a_n^\dagger a_n \ , \tag{3.31}$$

which merely changes the single particle energy by a chemical potential $-g\mu_B H$, thereby changing the fermion occupation and the Fermi wave vector

$$\delta k_F = \frac{g\mu_B H}{v_s} = \frac{2g\mu_B H}{\pi J} \ . \tag{3.32}$$

Since $\chi_d(\omega)$ was calculated in a continuum linear band model, the result should be corrected for Umklapp processes according to $\Pi_u(\pi + Q) = \frac{1}{2}[\Pi(\pi + Q) + \Pi(\pi - Q)]$, where Q is the deviation of q from π. For $2k_F = \pi$, this makes no difference since Π is quadratic in the deviation from $2k_F$. Defining $\xi = \frac{v_s}{4\pi T}$ and $f(\xi Q) = \Pi(\pi + Q)/\Pi(\pi)$, the soft mode condition can be written as

$$\frac{T_c(H,Q)}{T_c(0)} = \frac{1}{2}[f(\xi(Q - \delta k_F)) + f(\xi(Q + \delta k_F))] \ . \tag{3.33}$$

The transition temperature $T_c(H)$ and $Q(H)$ are found by maximizing $T_c(H,Q)$ with respect to Q. As long as $f''(x) < 0$, the maximum remains commensurate at $Q = 0$. In this region

$$\frac{T_c(H)}{T_c(0)} = f\left(\frac{g\mu_B H}{T_c}\right) \simeq 1 - 0.091 \times \left(\frac{g\mu_B H}{T_c(0)}\right)^2 \ , \tag{3.34}$$

which means that a small field suppresses the stability of the spin–Peierls phase. This is because the field suppresses the quantum fluctuations, thereby decreasing the energy gain of the spin–Peierls transition. This is opposite to antiferromagnetic order, which is destabilized by quantum fluctuations, where $T_N(H)$ increases with the field.

At $x = \frac{g\mu_B H}{4\pi T_c(H)} = 0.145$, $f''(x) = 0$ and Q becomes non-zero, indicating that the system enters a modulated phase. This nonzero solution for Q gives the modulation of the system and will be called δk_{sp} in the following. Neglecting the possibility of weak pinning to the lattice periodicity, the modulation is in general incommensurate (IC). This corresponds to $T_C(H) = 0.77 \times T_c(0)$ and $g\mu_B H = 1.38 \times T_c(0)$. Above this field, δk_{sp} rapidly evolves from 0 to δk_F, but it is worth noticing that $\delta k_{sp} \neq \delta k_F$. Contrary to the general saying, Cross and Fisher theory does predict a continuous evolution from $\delta k_{sp} = 0$ with $g\mu_B H/v_s$ as the asymptotic value.

Though correctly predicting the transition to a phase, where the lattice dimerization (the static $\Omega_Q = 0$ phonon) is incommensurately modulated, the approach does not provide insight into the nature of this modulated phase.

3.2.1 Soliton solutions

A quantitative description of the IC phase was developed by transforming the boson fields to conjugated phase variables $\theta(x)$ and $p(x)$ (Nakano and Fukuyama, 1980, 1981, Inagaki and Fukuyama, 1983a,b, 1984, Zang *et al.*, 1995, 1997, Dobry and Riera, 1995). The thereby obtained *phase Hamiltonian* has the form

$$\mathcal{H} = \int dx[A(\nabla\theta)^2 + Cp^2 - Bu(x)\cos\theta + \frac{2K}{a}u(x)^2] \ , \tag{3.35}$$

where $u(x)$ is the adiabatic lattice distortion, which is found by minimising the free energy. For clarity, the lattice constant a is re-introduced explicitly. The parameters $A = \frac{Ja}{8\pi}(1+\frac{3}{\pi}) \to \frac{v_s}{8}$ and $C = 2Ja(\pi-1) \to \frac{\pi^2 v_s}{2}$ have been adjusted to reproduce the correct spin-wave dispersion and correlation function exponents. The spin-lattice coupling is contained in $B = \frac{J\lambda}{a^2}$.

Writing $\theta = \theta_{\rm cl} + \hat{\theta}$, where $\theta_{\rm cl}$ is a classical field, the quantum fluctuations are treated in the self-consistent harmonic approximation (SCHA)

$$\cos\theta \simeq e^{-\frac{\langle\hat{\theta}^2\rangle}{2}}\left(1 - \frac{\hat{\theta}^2 - \langle\hat{\theta}^2\rangle}{2}\right)\cos\theta_{\rm cl} \ . \tag{3.36}$$

The original spin-operator is given by $S^z_n = \frac{(-1)^n}{a}\cos\theta(na) + \frac{1}{2\pi}\nabla\theta(na)$, where the magnetization $m = \langle S^z\rangle$ is obtained by inserting the classical field $\theta_{\rm cl}$.

Assuming the fluctuation average $\langle\hat{\theta}^2\rangle$ to be constant, leads to the following two differential equations for the semiclassical field

$$2A\nabla^2\theta_{\rm cl} = u(x)\frac{\lambda J}{a^2}e^{-\langle\hat{\theta}^2\rangle/2}\cos\theta_{\rm cl} \tag{3.37}$$

$$\frac{4K}{a}u(x) = \frac{\lambda J}{a^2}e^{-\langle\hat{\theta}^2\rangle/2}\sin\theta_{\rm cl} \tag{3.38}$$

$$\Downarrow$$

$$\nabla^2 2\theta_{\rm cl} = \frac{1}{\Gamma^2}\sin 2\theta_{\rm cl} \ , \tag{3.39}$$

where $\Gamma = v_s/\Delta_0$. This equation has two homogeneous solutions $\theta_{\rm cl} = 0, \frac{\pi}{2}$. For $\theta_{\rm cl} = 0$ the Néel state is realized with $u(x) = 0$, while for $\theta_{\rm cl} = \frac{\pi}{2}$ the magnetization vanishes and $u(x) = u_0 = \frac{\lambda J}{4Ka}e^{-\langle\hat{\theta}^2\rangle/2}$. This is the spin–Peierls state.

The fluctuation average is determined by inserting $\theta_{\rm cl} = \frac{\pi}{2}$ into the Hamiltonian, which becomes quadratic in $\hat{\theta}$, giving the following dispersion relation

$$\omega_q = \sqrt{\Delta_0^2 + v_s^2 q^2}, \quad \Delta_0^2 = 4\pi B e^{-\frac{\langle\hat{\theta}^2\rangle}{2}}, \quad \langle\hat{\theta}^2\rangle = \ln\frac{2\pi v_s}{a\Delta_0} \ . \tag{3.40}$$

The energy gap is determined selfconsistently

$$\Delta_0 = \frac{2v_s}{a}\left(\frac{\lambda^2}{\pi}\right)^{1/3}\left(\frac{u_0}{a}\right)^{2/3} \ . \tag{3.41}$$

The change in free energy due to dimerization is

$$\Delta E = -\frac{3}{4}\left(\frac{\lambda^2}{\pi}\right)^{2/3}\frac{J}{a}\left(\frac{u_0}{a}\right)^{4/3} + \frac{2K}{a}u_0^2 \ , \tag{3.42}$$

where the fluctuation term is proportional to $u_0^{4/3}$ and the elastic energy to u_0^2, which leads to a non-zero value at minimum energy

$$u_0 = a\frac{\lambda^2}{\pi}\left(\frac{J}{4Ka^2}\right)^{3/2} \ , \tag{3.43}$$

giving the excitation gap

$$\Delta_0 = \frac{\lambda^2 J^2}{Ka^2} \ . \tag{3.44}$$

Allowing $\theta_{\rm cl}(x)$ and $u(x)$ to vary but keeping $\langle\hat{\theta}^2\rangle$ fixed at the value derived in the uniform case, inhomogeneous solutions can be found. Two such solutions are

$$\cos\theta_{\rm cl} = \pm\tanh\frac{x}{\Gamma} \tag{3.45}$$

$$u(x) = \pm u_0\tanh\frac{x}{\Gamma} \tag{3.46}$$

$$m(x) = \pm\frac{1}{\Gamma\cosh\frac{x}{\Gamma}} \pm (-1)^{x/a}\frac{1}{\cosh\frac{x}{\Gamma}} \ . \tag{3.47}$$

These two solutions correspond to solitons which over a length scale of the soliton width Γ shift the phase of the lattice distortion. By integration of $m(x)$ it is seen that the two types of solitons carry a total spin of respectively $\frac{1}{2}$ and $-\frac{1}{2}$. The energy of the soliton solutions is given by the energy of the dimerised solution plus a soliton creation energy $E_s \simeq 0.279\times\Delta_0$.

The influence of a magnetic field is to replace $A(\nabla\theta)^2$ in the Hamiltonian with $A(\nabla\theta - h)^2$ where $h = \frac{g\mu_B H}{v_s}$. Neglecting the influence on the shape of the solutions, the presence of a magnetic field will lower the soliton formation energy by the Zeeman energy $g\mu_B H/2$, which leads to spontaneous formation of solitons at a critical field of $H_c = 0.279\times 2\Delta_0/g\mu_B$.

The local spin density is given by $m(x) = \frac{1}{2\pi}\nabla\theta$, which in the absence of lattice distortions satisfies $m(x) = \frac{1}{2\pi}h = \frac{g\mu_B H}{\pi^2 Ja}$, reproducing the exact result for a uniform HAF chain (Griffiths, 1964).

In this incommensurate phase the solitons will repel each other to form a regular lattice. A periodic generalization of the $\tanh(x)$ solution is found in the Jacobi elliptic function $\mathrm{sn}(x/\Gamma k, k)$ of modulus k (It should be noted that some prefer to use the definition $\mathrm{sn}(x/\Gamma k, k^2)$.) The periodicity of this function is $L = 4\Gamma k K(k)$, where $K(k)$ is the complete elliptic integral of the first kind. The shape and amplitude of the soliton lattice can be estimated from the above, under the assumption that the soliton lattice does not influence the differential equations. But in order to determine the distance $L/2$, the interaction between solitons has to be included. This was achieved in a slightly different approach where the fermion operators of the MF approximated Jordan–Wigner transformed Hamiltonian were written as complex fields $\psi(x) = u(x)e^{i\pi x/2a} - iv(x)e^{-i\pi x/2a}$, where $u(x)$ and $v(x)$ are slowly varying functions satisfying the self consistency equations

$$(\omega - g\mu_B H)u = iv_s\nabla u + \Delta(x)v \tag{3.48}$$

$$(\omega - g\mu_B H)v = -iv_s\nabla v + \Delta(x)u \tag{3.49}$$

$$\Delta(x) = \lambda\langle u^*(x)v(x) + v^*(x)u(x)\rangle \ . \tag{3.50}$$

When the dispersion is linearized around the Fermi wave vector, these equations have the previously found Jacobi elliptic function $\Delta(x) = \Delta_1\mathrm{sn}(x\Delta_1/v_s k, k)$ as an exact solution. The difference between the free energy of the uniform solution and the soliton lattice solution is

$$\Delta E = 2\Delta_0^2 N(0)(-\frac{1}{4} - \frac{\delta}{\ln 4/k'} + \frac{k'^2}{4\ln 4/k'} - \frac{\delta^2}{2\ln(4/k')^2}) \ , \tag{3.51}$$

where $k' = \sqrt{1-k^2}$ and $\delta = (H - H_c)/H_c$. Minimization of the energy gives $\delta = k'^2\ln(4/k')/2$, which is approximately equivalent to $k = \sqrt{1 - 2\delta/\ln(1/\delta)}$ from which the periodicity is found according to $L = 4\Gamma k K(k)$.

Writing $m(x) = m_u(x) + (-1)^{x/a}m_s(x)$ in terms of a staggered (antiferromag-

netic) and a uniform (ferromagnetic) part, the periodic solution becomes

$$u(l) = u_0(-1)^l \mathrm{sn}(lc/\Gamma k, k), \quad u_0 = a\frac{\lambda^2}{\pi}\left(\frac{J}{4Ka^2}\right)^{3/2} \tag{3.52}$$

$$m_s(x) = m_s(-1)^l \mathrm{cn}(lc/\Gamma k, k), \quad m_s = \frac{1}{\sqrt{2\pi\Gamma}} \tag{3.53}$$

$$m_u(x) = m_u \mathrm{dn}(lc/\Gamma k, k), \quad m_u = \frac{1}{2\pi k\Gamma}\ . \tag{3.54}$$

Apart from being the exact solutions to an approximate model, these functions provide a continuous basis going from a sinusoidal to a sharp (square) soliton lattice with just two parameters Γ and k, one being fixed by the periodicity. This makes them much more suitable than the standard Fourier series for which an infinite number of parameters are needed to produce a sharp soliton lattice. But, for instance when using diffraction methods to investigate the soliton structure, it is useful to know the Fourier series of the Jacobi elliptic functions.

$$\mathrm{sn}(u,k) = \frac{2\pi}{kK(k)}\sum_{n=1}^{\infty}\frac{q^{n-\frac{1}{2}}}{1-q^{2n-1}}\sin\frac{(2n-1)\pi u}{2K(k)} \tag{3.55}$$

$$\mathrm{cn}(u,k) = \frac{2\pi}{kK(k)}\sum_{n=1}^{\infty}\frac{q^{n-\frac{1}{2}}}{1+q^{2n-1}}\cos\frac{(2n-1)\pi u}{2K(k)} \tag{3.56}$$

$$\mathrm{dn}(u,k) = \frac{\pi}{2K(k)} + \frac{2\pi}{K(k)}\sum_{n=1}^{\infty}\frac{q^n}{1-q^{2n}}\cos\frac{n\pi u}{K(k)}\ , \tag{3.57}$$

where $\kappa = e^{-\pi K(1-k^2)/K(k)}$.

The Fourier components are given by

$$a_n^{\mathrm{sn}} = \frac{\pi}{kK(k)}\frac{q^{n-\frac{1}{2}}}{1-q^{2n-1}}, \qquad n \text{ odd} \tag{3.58}$$

$$a_n^{\mathrm{cn}} = \frac{\pi}{kK(k)}\frac{q^{n-\frac{1}{2}}}{1+q^{2n-1}}, \qquad n \text{ odd} \tag{3.59}$$

$$a_n^{\mathrm{dn}} = \begin{cases} \frac{\pi}{2K(k)}, & n=0 \\ \frac{\pi}{K(k)}\frac{q^n}{1-q^{2n}}, & n>0 \end{cases}\ . \tag{3.60}$$

So the distortive and the staggered magnetic components give reflections at odd harmonics away from half order positions. The uniform magnetic component gives even harmonics.

Once the first harmonic of either the structural or the magnetic component has been measured, the amplitude can be found

$$u_0 = \frac{kK(k)}{\pi}\frac{1-\kappa}{\sqrt{\kappa}}u(q=\delta k_{sp}) \tag{3.61}$$

$$m_s = \frac{kK(k)}{\pi}\frac{1+\kappa}{\sqrt{\kappa}}m_s(q=\delta k_{sp}) \tag{3.62}$$

$$m_u = \frac{K(k)}{\pi}\frac{1+\kappa^2}{\kappa}m_u(q=2\delta k_{sp})\ . \tag{3.63}$$

Effect of NNN and interchain coupling

For treating the hard phonon case and for comparison with physical realizations of the soliton phase, it is important to investigate how the soliton-structure is affected by NNN and interchain coupling.

The effect of NNN coupling is easily realized by remembering that the starting point of the field theory was to adjust the parameters so that the correct spin-wave velocity v_s was reproduced. The dispersion relation in the dimerised phase was $\epsilon(q) = \sqrt{\Delta^2 + q^2 v_s^2}$ and the results depended only on v_s and Δ. The NNN coupling will decrease v_s but leave the form of the soliton solution unaltered. As $\Gamma = v_s/\Delta$, NNN coupling will decrease the soliton width (for fixed J) (Dobry and Riera, 1995). But it should be noted that often (including the case of $CuGeO_3$), the coupling constant J is determined by measuring the dispersion relation (*i.e.* determining v_s and Δ), in which case the value of α is irrelevant.

An interchain coupling $J_\perp$ can be included in a MF way (Zang *et al.*, 1997) by adding a classical field $h(x) = \langle S^z_{n,m+1}\rangle = \frac{\tilde{Z}}{Z}\langle S^z_{n,m}\rangle$ to the Hamiltonian

$$\mathcal{H}_\perp = -J \int \tilde{Z} h(x) \cos\theta - \frac{Z}{2} h(x)^2 dx \ , \tag{3.64}$$

where Z is the coordination number and $\tilde{Z} \neq Z$ accounts for the possibility that a soliton (finite $\langle S^z_{n,m}\rangle$) in chain m is not fully transferred to the neighbouring chains.

Considering the ground state energy for $\theta = 0$ (Néel order) and $\theta = \frac{\pi}{2}$ (dimerized), the two are seen to be favored for

$$C_K \equiv \frac{J_\perp Z}{\Delta} \ , \tag{3.65}$$

respectively larger and smaller than 1. It should be noted that NNN coupling changes C_K slightly. For $C_K < 1$ the soliton width is decreased by $\Gamma = \frac{v_s}{\Delta}(1 - (\tilde{Z}/Z)^2 C_K)^{1/2}$ by magnetic interchain interactions.

The effect of interchain elastic coupling (still in the adiabatic approximation) was considered by Dobry and Riera (1995), who reached $\Gamma = \Gamma_0/B(0)$, where

$$B(\boldsymbol{n}) = \int\int \frac{d\boldsymbol{k}}{(2\pi)^2} \frac{\cos \boldsymbol{k}\cdot\boldsymbol{n}}{1 + \frac{K_x}{K_{||}} \sin^2 \frac{k_x}{2} + \frac{K_y}{K_{||}} \sin^2 \frac{k_y}{2}} \ , \tag{3.66}$$

where $\boldsymbol{n} = (n_x, n_y)$ and $K_{||}$, K_x and K_y are the effective elastic constants along the chains and in the two perpendicular directions respectively. However, this result concerned a soliton excitation in a single chain, while the other chains remained dimerized. For the case of a static soliton lattice, where all chains share the same modulation, the soliton width becomes $\Gamma = \Gamma_0 / \sum_{\boldsymbol{n}} B(\boldsymbol{n})$. Since $\sum_{\boldsymbol{n}} B(\boldsymbol{n}) = 1$, it is seen that the static soliton width is unaltered by elastic interchain coupling.

3.2.2 Numerical calculations

The field theoretical results for the dimerization δk_{sp}, energy gap Δ and soliton width Γ have been supplemented by numerical calculations based directly on the microscopic parameters J, α and K. Though both direct diagonalization and Monte Carlo techniques have been applied (Feiguin *et al.*, 1997), the most successful approach has been the density-matrix renormalization-group (DMRG) calculations (White, 1992, 1993, 1998).

The numerical results for the dimerization and the energy gap in the dimerized phase have been found to be in good agreement with the field theoretical prediction (Feiguin *et al.*, 1997, Meurdesoif and Buzdin, 1999).

In the soliton phase, the shapes of both the structural and the magnetic soliton components were found to be well described by the predicted Jacobi elliptic functions. This is not surprising, as the Jacobi elliptic functions form a parameterization of periodic functions. However, also the parameters such as the soliton width, the distortion amplitude and the amplitudes of the staggered and uniform parts of the magnetic soliton structure are in generally good agreement with the

field theoretical predictions (Meurdesoif and Buzdin, 1999, Schönfeld *et al.*, 1998, Uhrig *et al.*, 1998, 1999a,b, Uhrig, 1999, Klümper *et al.*, 1999).

Some quantitative differences have been reported though (Uhrig *et al.*, 1999a). The amplitudes of the magnetic soliton structure are reported to deviate between the field theoretical prediction and the DMRG calculations. Here it is however important to be consistent in the choice of the parameters when comparing. More important, the DMRG calculations suggest that the structural soliton width is about 35% higher than the magnetic soliton width, and that they both increase slowly with the applied field.

While numerical calculations have the possibility of providing quantitative descriptions of experimental data with fewer approximations and easier inclusion of the parameters specific to the physical realizations on which the measurements are performed, they suffer from the difficulty in establishing the functional dependence of the results on the individual parameters of the model.

3.2.3 Excitations in the soliton phase

The understanding of the dynamics in the soliton phase is far from settled. The focus has been on two types of excitations: excitations of the magnetic soliton structure and fluctuations in the positions of the solitons. In the adiabatic (static lattice) approach, magnetic excitations with total spin of respectively ± 1 have been treated both in the field theory approach (Machida and Fujita, 1984, Fujita and Machida, 1984, 1988) and through numerical calculations (Poilblanc *et al.*, 1997, Uhrig *et al.*, 1998, Schönfeld *et al.*, 1998, Yu and Haas, 1999).

Based on the fermion model, a qualitative expectation for the excitation spectrum can be established. Figure 3.4 shows how respectively the fermion particle energy and the dispersion relation evolves upon increasing magnetic field. In the upper panels, below H_c, the field splits the two fermion bands, resulting in three Zeeman split triplet excitations. At H_c in the middle panel, the branches of the two different fermion band join at the Fermi level, resulting in a softening of the lower triplet excitation. Above H_c the incommensurate lattice modulation shifts the gap positions (and hence k_F) in the fermion bands away from $\pm\pi/2$. The resulting excitation spectrum resembles that of the uniform spin chain in a magnetic field (see figure 3.3), except that the soft modes acquire gaps. In general, the two degenerate modes at the zone center will be split because of the finite magnetization. Thus around the zone center ($q = 0$), a total of four modes are expected: two commensurate longitudinal modes and two transverse modes at the incommensurate position to either side of the zone center. The same scenario is present around the antiferromagnetic zone center ($q = \pi$) but with the longitudinal and transverse modes interchanged. A quantitative calculation of the excitation spectrum within the JW–MF theory based on the Bogoliubov equations for the fermion particles is in progress (Mortensen and Rønnow, 2000).

In numerical studies on finite chain lengths, a subset of eigenstates corresponding to different values of the total spin S_z are calculated. The magnetization is then given by $m = S_z/L$, where L is the chain length. Hence the $S_z = 1$ state with the lowest energy is the ground state at a field in the incommensurate phase corresponding to a magnetization of $1/L$.

The modulated coupling is included either as $\delta_n = \cos qr_n$, or allowed to vary individually. In each case either q or the series of numbers δ_n are determined self-consistently by minimizing the ground state energy. In the former case, the ground state energy is minimized by $q = \pi \pm 2\pi/L$ in agreement with the expectation. In the later case, δ_n is found to be described by the Jacobi elliptic function sn with parameters that are in good accord with the field theoretical prediction.

The magnetic excitations can then be determined by keeping the δ_n at the

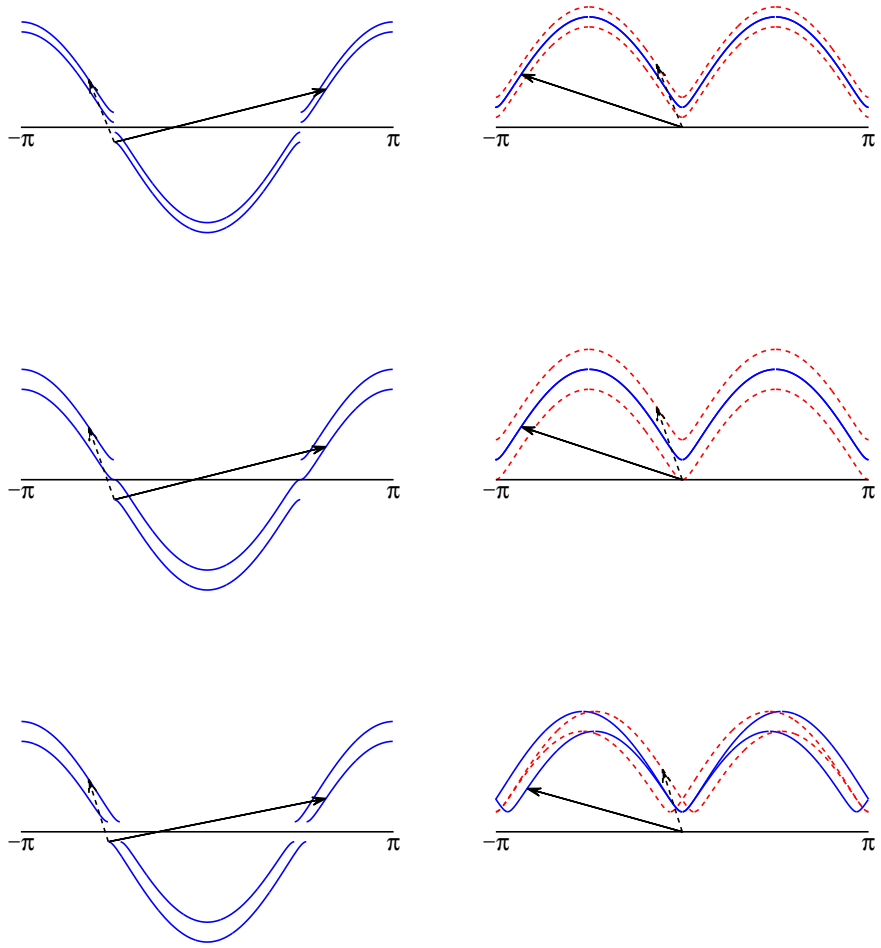

Figure 3.4. Schematic illustration of how the excitation spectrum changes as the field is increased from below H_c (upper), at H_c (middle) to above H_c (lower). The left panels show the fermion energy with the Fermi level indicated by the horizontal line. The arrows illustrate respectively an inter band (solid) and a band crossing excitation. The right panels show the corresponding excitation dispersions where the inter band processes (solid) correspond to longitudinal excitations, while the band crossing processes (dashed) correspond to transverse spin fluctuations.

selfconsistent values for $S_z = 1$ and then calculating the eigenstates with $S_z = 1 \pm 1$. Once the ground state and excited states are known, the excitation spectrum can be calculated (Yu and Haas, 1999). As a special case the excitation gaps are given as the difference between the lowest eigen energy and the ground state energy (Schönfeld *et al.*, 1998).

One drawback of numerical approaches is that the dependence on the parameters like the amplitude δ of the exchange alternation, the amount of NNN coupling α and the elastic constant K is difficult to infer. Therefore these calculations have to be redone each time a new set of parameters become relevant in the study of a given physical realization of a spin–Peierls system. The excitation spectrum has been treated in a sinusoidal approach with different values for $(\delta, \alpha) = (0.014, 0.36)$ (Poilblanc *et al.*, 1997), (0.12,0) (Uhrig *et al.*, 1998), (0.4,0) (Yu and Haas, 1999) and for an adaptive modulation with $\alpha = 0.35$ and $K = 2.38$. This later choice

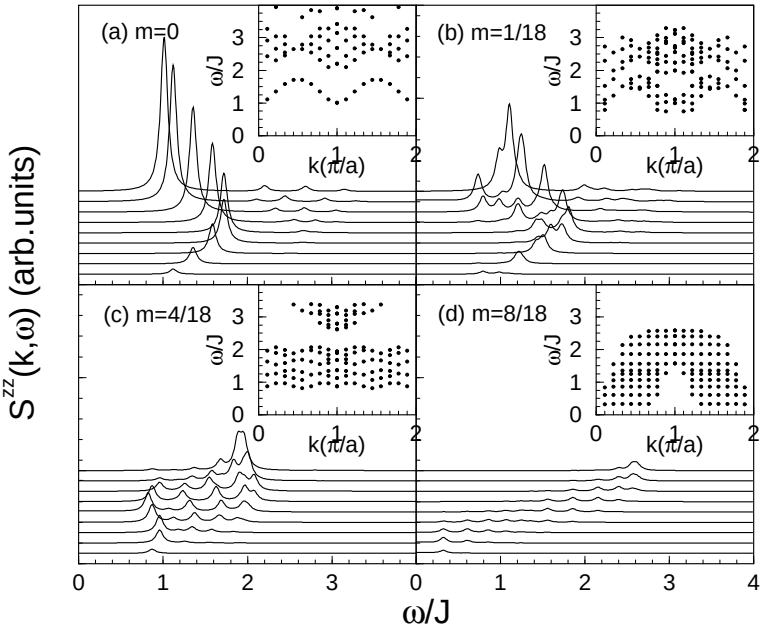

Figure 3.5. Dynamic structure factor $S_{zz}(q,\omega)$ obtained from exact diagonalization of a $L = 18$ chain with a sinusoidal modulation of δ_n. The figure is adapted from Yu and Haas (1999).

corresponds to $\delta = 0.14$ in the modulated phase.

In figure 3.5b the excitation spectrum at a magnetization of $m = 1/18$ is shown. It is seen that the energy minima are located at $q = 0$ and at $q = \pi - 2\pi m$ in consistency with the field theoretical expectation. However, as is the case in zero field (figure 3.5a), the spectral weight is concentrated at $q = \pi$, where a double peak is observed at an energy slightly higher than the minimum.

Unfortunately, the numerical calculations are limited to magnetizations higher than $1/L_{\max}$, where $L_{\max}$ is the highest number of spins the given method can be extended to. Due to the low degree of translational symmetry of the coupling $J(1+\delta_n)$, exact diagonalization via the Lanczos algorithm is limited to $L \leq 24$. DMRG calculations have been extended to $L = 200$ but the energy gaps have only been reported for $m \geq 0.02$. These results are shown in figure 3.6.

Phasons

In the incommensurate phase, the translational symmetry is broken by the formation of a soliton lattice. This soliton lattice can be shifted along the chain with relatively ease. This is a general feature of systems where a continuous symmetry is broken and the mode connected with the specific phase or position at which it is broken is called a Goldstone mode.

In the soliton phase, these longitudinal domain wall oscillations can be considered as fluctuations in the phase of the soliton lattice and have therefore been denoted phasons. The dispersion relation for the phasons has been related to the correlation lengths in the critical region around the spin–Peierls transition (Bhattacharjee *et al.*, 1998, Schoeffel *et al.*, 1996)

$$\omega_{\text{phason}}(q) = \Delta_0 \sqrt{\xi_x^2 q_x^2 + \xi_y^2 q_y^2 + \xi_z^2 q_z^2}\ , \tag{3.67}$$

with rough estimates $\xi_x = 0.25$, $\xi_y = 0.43$ and $\xi_z = 2.35$.

If, as predicted from field theory, the phasons are gapless, there will be zero point oscillations around the equilibrium positions. This will lead to an averaging

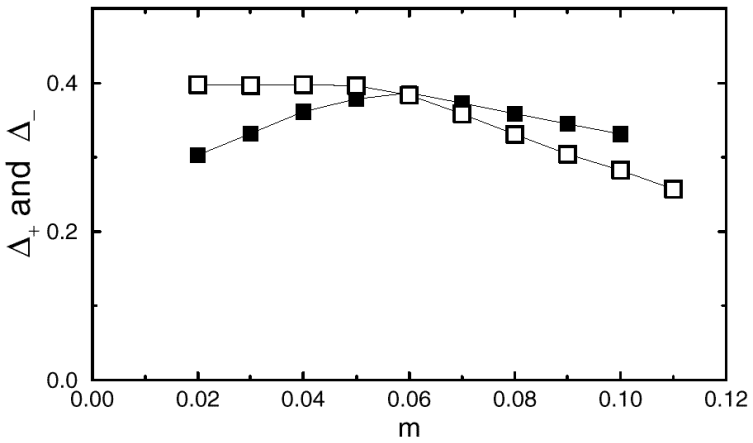

Figure 3.6. The development of the two adiabatic gaps $\Delta_\pm$ as a function of magnetization for $\alpha = 0.35$ and $K = 2.38$ corresponding to an alternation of $\delta = 0.14$. The figure is adapted from Schönfeld et al. *(1998).*

of the magnetic soliton lattice as obtained through the expectation value of S_n^z. A quantitative treatment within the field theory leads to

$$m_n^{\mathrm{av}} \simeq (1-2\gamma)m_n + \gamma(m_{n-1} + m_{n+1}) \ , \tag{3.68}$$

where γ was determined by the phason dispersion. This averaging has little effect on the slowly varying uniform component of the magnetic structure, but significantly reduces the staggered component by a factor of approximately $1 - 4\gamma$. If on the other hand the discreteness of the lattice (which means that there is only quasi-translational symmetry) induces a gap in the phason dispersion, then such an averaging of the magnetic structure will not take place.

3.2.4 Physical realizations of Spin–Peierls systems

The first spin–Peierls transition was discovered in the organic metal-complex compound tetra-thiofulvalene-copper-bisdithiolene (TTF-CuBDT) (Bray *et al.*, 1975, Jacobs *et al.*, 1976), and subsequently in the related compounds TTF-CuBDSe and TTF-AuBDT. A review on the spin-Peierls transition and the experimental results from these materials is given by Bray *et al.* (1983).

The signature of the spin–Peierls transition is a susceptibility $\chi(T)$ that follows the Bonner and Fisher (1964) prediction for an $S = 1/2$ chain down to a temperature T_{sp}, below which $\chi(T)$ rapidly decreases to zero. In the organic spin–Peierls systems $\chi(T)$ is perfectly described by the combination of Bonner–Fisher theory and an alternating chain model, where $\delta(T)$ follows the self-consistent solution for the gap with T_c, J and $\delta(0)$ as fitting parameters. The obtained $\delta(0)$ was in reasonable agreement with the prediction $\delta(0) = 1.076T_c/J$.

The expected BCS-like jump in the specific heat was confirmed experimentally (Wei *et al.*, 1977). The lattice distortion in TTF-CuBDT was observed as satellite reflections in X-ray diffraction (Moncton *et al.*, 1977). The gradual development of these reflections was described by the square of the BCS-like gap. Diffuse scattering was observed far above the transition (up to 225 K$\sim 20T_{sp}$), which is interpreted as the existence of a low energy phonon mode, thereby explaining the good overall agreement with the MF and RPA approaches.

The (T, H) phase diagram was derived using a series of techniques. The expected behaviour was observed with $T_c(H)$ decreasing with field until a tricritical point $T_c(H_c)$, above which a new phase is realized. The incommensurability of the high-field phase was observed as a splitting of the satellite reflections in X-ray diffraction

in TTF-CuBDT (Kiryukhin *et al.*, 1995), and as a broadening of the NMR signal above H_c in TTF-AuBDT (Hijmans *et al.*, 1985).

A number of other materials have been proposed to exhibit spin–Peierls transitions. There are other transition-metal-complexes like (3MAP)$CuCl_3$ and (6MAP)-$CuCl_3$ (Liu *et al.*, 1995), but also truly organic materials like MEM$(TCQN)_2$, $(TMTTF)_2PF_6$ and *p*-CyDOV (Mukai *et al.*, 1996, Jamali *et al.*, 1998), where the spins are constituted by localized spin densities at certain parts of the organic molecules. The compound MEM$(TCQN)_2$ undergoes first an electronic Peierls metal-insulator transition at 335 K, below which each dimer contains a localized spin 1/2 (Huizinga *et al.*, 1979). At 17.1 K, a second dimerization occurs, which has been ascribed to a spin–Peierls transition (van Bodegom *et al.*, 1981, Blundell *et al.*, 1997, Lumsden and Gaulin, 1999). In $(TMTTF)_2PF_6$, the ambient pressure spin–Peierls ground state below 18 K can be turned into ordinary antiferromagnetic order above 1 GPa (Chow *et al.*, 1998).

There are materials like TMPD-perchlorate where a lattice distortion is accompanied by a sharp decrease in the susceptibility. In this case, however, it is a structural phase transition, in which the magnetic system plays little if any role (Terauchi *et al.*, 1976).

However, the inability to grow large single crystals of these organic spin-Peierls materials, precluded the use of techniques like inelastic neutron scattering. Therefore the interest in the spin–Peierls transition stagnated until the discovery of the inorganic spin–Peierls material $CuGeO_3$. In the meantime, there has been a significant development in neutron scattering instruments. It may therefore prove interesting to resurrect one of the best characterized organic spin–Peierls systems.

Recently, it has been suggested that the inorganic α'-NaV_2O_5 should display a spin–Peierls transition (Isobe and Ueda, 1996). Subsequently it has been realized that the behaviour of NaV_2O_5 is more complex due to charge ordering effects and mixed V^{4+}/V^{5+} valence states (Poirier *et al.*, 1999, Fudamoto *et al.*, 1999). For this reason, NaV_2O_5 is a highly interesting system but inadequate for studies of the spin–Peierls model, which is the subject of this chapter.

3.3 Characterization of $CuGeO_3$

The spin–Peierls transition in $CuGeO_3$ was first conjectured from susceptibility measurements by Hase *et al.* (1993a). The concomitant lattice distortion was observed in diffraction experiments (Kamimura *et al.*, 1994, Pouget *et al.*, 1994), thereby verifying the spin–Peierls nature of $CuGeO_3$. With this, the number of experimental results on the SP transition has been much increased. Because $CuGeO_3$ is an inorganic compound of which large single crystals can be grown, it has enabled measurements that have not been possible on the previously studied SP materials. But at the same time, it has been realized that $CuGeO_3$ is not an ideal physical realization of the simple spin–Peierls model. Therefore considerable work, both experimental and theoretical has been devoted to the understanding of $CuGeO_3$ (For reviews see Boucher and Regnault, 1996, van Loosdrecht, 1998, Enderle, 1999). Following an intense effort in the last few years, it seems like there is now a sufficient basis available for understanding $CuGeO_3$. It is therefore useful to review the present facts.

3.3.1 Crystal structure

$CuGeO_3$ crystallizes in the orthorombic $Pbmm$ structure with room temperature lattice parameters $a = 4.80$ Å, $b = 8.47$ Å and $c = 2.94$ Å (Völlenkle *et al.*, 1967, Braden *et al.*, 1996). As illustrated in figure 3.7, one unit cell contains 2 formula units. There are two inequivalent oxygen sites that will be denoted O1 and O2.

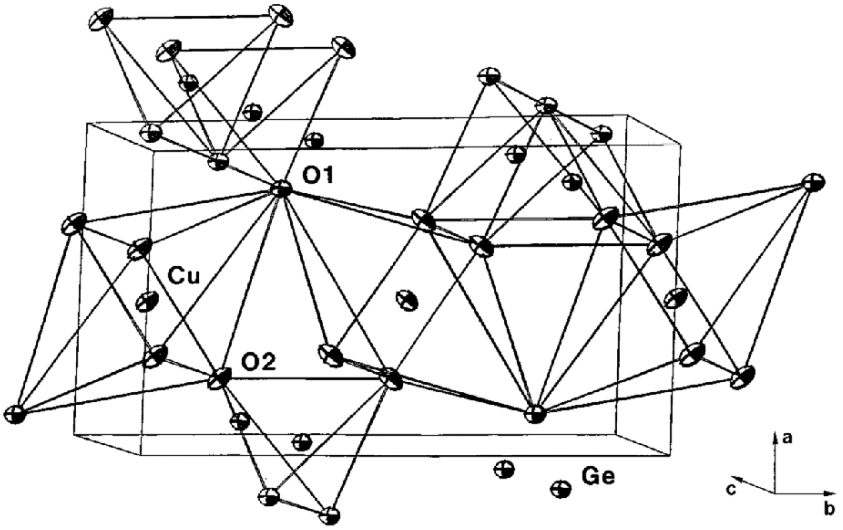

Figure 3.7. The crystal structure of $CuGeO_3$ with the arrangement of the CuO_6 octahedra and the GeO_4 tetrahedra indicated. The figure is an ORTEP *plot adapted from Braden* et al. *(1996).*

Each Cu ion is contained in a CuO_6 octahedron with 1.93 Å to the closest oxygen (type 2). Along c, adjacent octahedra share edges and two oxygen ions, so that they form a ribbon of oxygen rectangles with face centered Cu ions as shown in figure 3.8.

Each O2 is also part of a GeO_4 tetrahedron, where the other three oxygen come from neighboring CuO_6 octahedra in the b (one O2) and a (two O1) directions. Along b, adjacent CuO_6 octahedra are related by a glide mirror plane perpendicular to the a axis, giving two formula units per unit cell.

The crystal structure of $CuGeO_3$ is remarkably simple, and in particular the arrangement of the GeO_4 tetrahedra with a period of just one along the chain

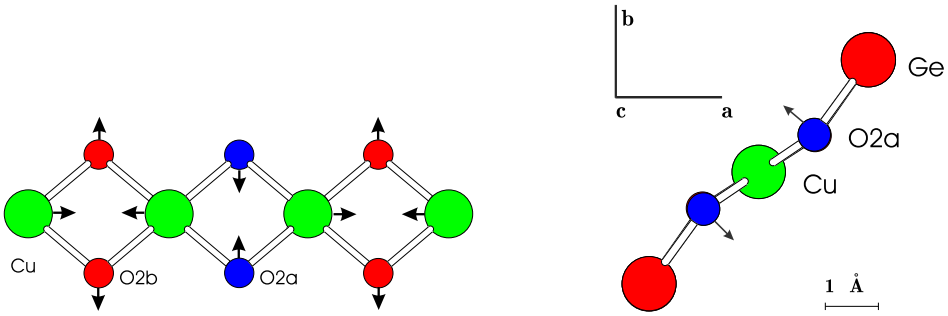

Figure 3.8. The local crystal structure of the Cu chains in $CuGeO_3$. To the left, the CuO_2 ribbons are viewed with c horizontal. To the right, the structure is viewed along c, showing how the O2 are spanned between the Cu chains and the Ge chains. The displacement pattern in the dimerised phase is indicated by arrows.

is rather exceptional for germanates and silicates. Motivated by indications from electron spin resonance (ESR) measurements for an anisotropic Dzyaloshinskii–Moriya (DM) exchange interaction (Yamada *et al.*, 1996), this structure has in fact recently been questioned. An X-ray investigation on a crystal, that had been annealed in oxygen atmosphere at 1150°C, showed super-lattice reflections that correspond to a larger unit cell ($2a\times b\times 4c$; $P2_12_12$) in which the 4 GeO_4 tetrahedra along the chain are twisted with respect to each other. The authors postulate that in non-annealed samples, these twists are still present but only short range ordered. A thorough neutron scattering investigation (Braden *et al.*, 1998b) on a non-annealed sample excluded such reflections and hence long ranged ordered distortions of the octahedra. Analysis of the Debye–Waller factors also excluded a short range ordered twisting of the octahedra. It could be that the signal seen in the X-ray diffraction is from phonons with a significant spectral weight, which would not be observed in neutron scattering studies. Until this controversy has been settled, and through the rest of this thesis, the originally proposed structure will be used.

Structure of dimerised phase

The distortion of the lattice, which accompanies the spin–Peierls dimerisation was detected in electron (Kamimura *et al.*, 1994) and X-ray (Pouget *et al.*, 1994) diffraction experiments as satellite reflections at $(\frac{h}{2}, k, \frac{l}{2})$, where h, k, l are all odd. This corresponds to a doubling of the unit cell along a and c.

The crystal structure of the SP phase has been determined by neutron scattering (Hirota *et al.*, 1994, Braden *et al.*, 1996). By measuring 14 satellite reflections, Hirota *et al.* (1994) determined the space group to be *Bbcm*, which can be derived from the room temperature (RT) structure by allowing shifts $u_z^{\mathrm{Cu}} \equiv (z_{\mathrm{RT}}^{\mathrm{Cu}} - z_{\mathrm{SP}}^{\mathrm{Cu}})/c_{\mathrm{RT}}$, $u_{x,y}^{\mathrm{O2}}$ and u_y^{Ge}. Along a and c, the shifts have alternating direction, which causes the doubling of the unit cell in these directions, whereas the unit cell is already double along b. In fact, due to the loss of mirror-symmetry, the O2 sites divide into two inequivalent sets O2a and O2b. Hirota *et al.* (1994) found that the satellites intensities were well described by constraining the refinement to just three displacements u_z^{Cu}, u_x^{O2} and u_y^{O2}.

This was confirmed in a thorough crystallographic study by Braden *et al.* (1996), who indexed between 100 and 400 independent reflections at temperatures 295 K, 20 K and 4 K. The 20 K data showed that although there are significant changes in the unit cell volume and the free positional parameters between RT and 20 K, the doubling of the unit cell does not appear before T_{sp}. Refinement of the 4 K data gave the following displacement parameters $u_z^{\mathrm{Cu}} = 0.00192(6)$, $u_x^{\mathrm{O2}} = 0.00199(11)$,

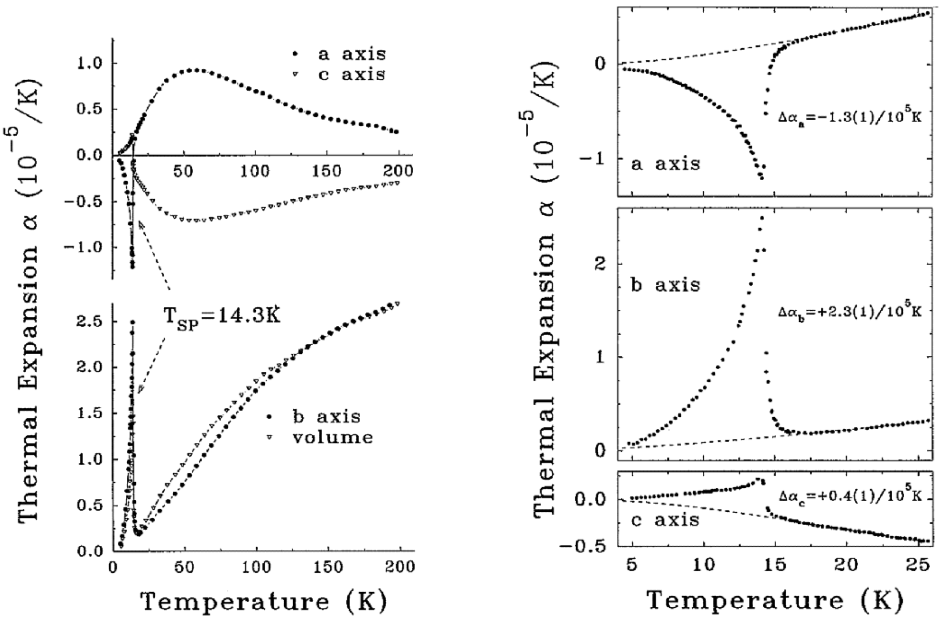

Figure 3.9. The linear thermal expansion coefficients α_a, α_b and α_c as a function of temperature from Winkelmann et al. *(1995).*

$u_y^{O2} = 0.00077(6)$ and $u_y^{Ge} = 0.00009(3)$. The three first are comparable, while the shift of Ge is an order of magnitude smaller and therefore negligible. The distortion is easily understood as driven by a dimerisation of the Cu along the chain as illustrated in figure 3.8. In order to conserve bond-length energy, the O2 is then pushed in the *ab* plane between the two Cu ions and one Ge ion.

Lattice dynamics

The linear thermal expansion coefficients α_a, α_b and α_c as shown in figure 3.9 display not only a sharp anomaly at the spin–Peierls transition, but even above T_{sp} they show considerable temperature dependence (Winkelmann *et al.*, 1995). In particular the non-monotonic behaviour of α_a and α_c with respectively a maximum and a minimum around 60 K resembles the broad maximum in the susceptibility. This suggests that already at high temperatures, the magnetic fluctuations influence the lattice through spin-phonon coupling.

A comparison between the thermal expansion coefficients and measurements of the magnetostriction was interpreted as evidence that the spin–Peierls transition is assisted by NNN interactions (Büchner *et al.*, 1996).

Despite thorough searches, the soft phonon expected in the simple theory for the spin–Peierls transition has not been found in $CuGeO_3$. With 10 atoms in the unit cell, there are in total 30 phonon branches, of which three are acoustic. Experimentally, some attention has been focused on the existence of an anomalously low longitudinal acoustic (LA) phonon branch along the b^* direction (Lorenzo *et al.*, 1994, Nishi *et al.*, 1995, Hirota *et al.*, 1995, Nishi *et al.*, 1999) as shown in figure 3.10. In initial experiments, the mode appeared quite broad, but recently it has been shown that it is in fact constituted of two sharp modes (Nishi *et al.*, 1999). Despite the unusual feature that along b^* the longitudinal mode lies below the transverse, it is difficult to imagine which influence this has on the spin–Peierls transition. On the other hand, it naturally explains the large thermal expansion coefficient along b as shown in figure 3.9.

In the original theory, the spin–Peierls active phonon would be expected to become soft at k_{sp}. In the right panel of figure 3.10, the phonon spectrum along

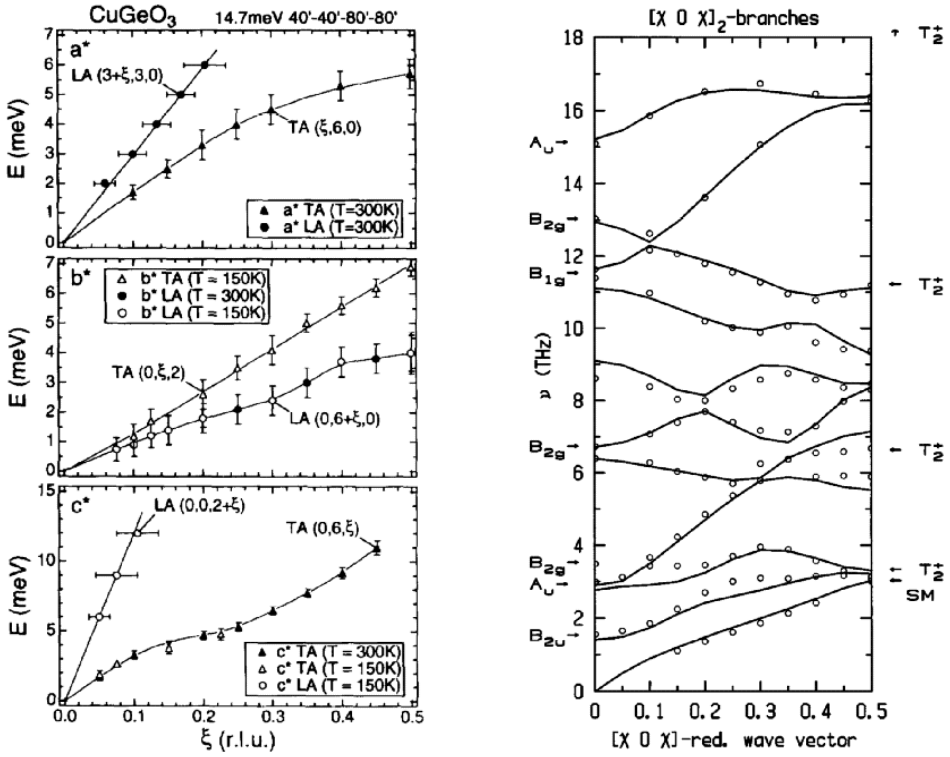

Figure 3.10. Phonon dispersions of respectively the acoustic phonons along a^*, b^* and c^* (Hirota et al.*, 1995, left,) and the phonon spectrum along [1,0,1] (Braden* et al.*, 1998a, right,). For comparison, 1* THz *corresponds to 4.136* meV.

[1,0,1] at room temperature is reproduced from Braden *et al.* (1998a). The phonon dispersion and intensities were modeled by a shell model calculation as shown by the solid lines. From this calculation, the polarization-scheme of each mode was determined. The modes that correspond to the SP distortion from *Pbmm* to *Bbcm* are marked by T_2^+. No single mode has a polarization-scheme matching the static lattice distortion of the SP phase, but reasonable matching is achieved by taking the two lowest modes in a ratio of 2 to 3. These two modes have energies 14 meV and 28 meV respectively, which is considerably larger than the gap $\Delta_0 =$ 2 meV. In addition, they do not soften at the SP transition. On the contrary, they continuously stiffen by respectively 6% and 4% as the temperature is decreased from room temperature. This has now been understood by the extended RPA calculation described in section 3.1.2.

In fact, only the oxygen displacement contributes to the $(\frac{h}{2}, k, \frac{l}{2})$ reflections with k even, while for k odd also the copper displacement is in effect. It would therefore be interesting to see the phonon spectrum along [1,2,1], but no such results have been published yet. From far infrared absorption (FIR) experiments it has been found that the lowest spin–Peierls active phonon is split symmetrically in the incommensurate soliton phase (Takehana *et al.*, 1998, 1999). The splitting was found to be proportional to the inverse period δk_{sp}.

3.3.2 Magnetic properties

The magnetic moments in $CuGeO_3$ are localized as $S = 1/2$ spins on the Cu^{2+} ions, although recent neutron scattering results suggest that there might be a small spin-density on the oxygen sites. The large elongation of the CuO_6 octahedron gives rise to an ellipsoidal g-tensor that is staggered between adjacent Cu sites along b. By electron spin resonance (ESR), the principal axes $g_{||} = 2.348 \pm 0.005$

and $q_\perp = 2.063 \pm 0.005$ respectively parallel and perpendicular to the Cu–O1 direction have been determined (Honda *et al.*, 1996, Pilawa, 1997). The average values along the three crystallographic axes are $g_a = 2.154(3)$, $g_b = 2.256(4)$ and $g_c = 2.064(3)$

From the crystal structure, it is often possible to guess the type and relative size of the magnetic interactions, although there exist examples where the original guesses have been proved wrong (See *e. g.* Johnston *et al.*, 1987, Eccleston *et al.*, 1994, Tennant *et al.*, 1997). In $CuGeO_3$, already the short Cu–Cu distance along c (2.94 Å compared to 4.80 Å along a and 4.22 Å along b) hints that the magnetic interaction will be strongest along this direction. This assumption is strengthened by considering the possible exchange paths. While there is a quite short Cu–O–Cu exchange path along the chain with a total length of 3.86 Å, the exchange paths along the a and b directions involve at least 2 oxygen with total path lengths of 7.53 Å and 6.69 Å respectively.

Electronic origin of magnetic interactions

More quantitative considerations based on electron orbitals and band structure calculations have been performed. From simple considerations of the orbital symmetries, it can be deduced that a straight Cu–O–Cu bond should provide a strong antiferromagnetic coupling, while a 90° bond should give vanishing magnetic coupling (Goodenough, 1963). Improving this argument leads to a small ferromagnetic coupling for 90°.

In $CuGeO_3$, the difference between the rectangle sides (2.51 Å and 2.94 Å) gives the double Cu–O–Cu bonds an angle of 99°. To make a smooth transition between the weak ferromagnetic coupling at 90° and the strong antiferromagnetic coupling at 180°, the deviation from 90° in $CuGeO_3$ will favor antiferromagnetic coupling. But in addition the existence of Ge side groups also aids to forming an antiferromagnetic coupling (Eskes and Jefferson, 1993, Geertsma and Khomskii, 1996, Braden *et al.*, 1996). One, perhaps, counterintuitive fact is that since it is the deviation from 90° bonding that causes the antiferromagnetic interactions, the strong magnetic coupling is in fact between the two Cu ions that move away from each other.

It has been shown that the binding energy of the oxygen p orbitals is almost the same for the orbitals pointing along the chain as if they point perpendicular to the chain (within the plane of the CuO_2 ribbon) (Mattheiss, 1994). From this, it is argued that if the p orbitals dynamically switch between the two orientations, they could provide a NNN coupling of the Cu-spins (Castilla *et al.*, 1995). In a three-band calculation, including the two $p_{x,y}$ orbitals of oxygen and the d_{xy} orbital of copper, an antiferromagnetic NN coupling of $J = 140$ K and a NNN coupling of $\alpha = 0.13$ were reached (Mizuno *et al.*, 1998). Such calculations have been extended to include more bands, but then the number of electronic exchange parameters that need to be determined grows considerably (Tornow *et al.*, 1999).

A slightly different approach of applying standard band structure calculations (Skriver, 1984) using the known crystal structure also gives quite good values for the coupling parameters (Khomskii *et al.*, 1996, Zagoulaev and Tupitsyn, 1997, Šljivančanin *et al.*, 1997).

In summary, attempts to determine the magnetic coupling parameters from electronic calculations are surprisingly successful. Though not reliable enough to give the accurate absolute values of the parameters, one important application of these calculations is the ability to investigate the relative change of the parameters upon changes in the crystal structure due to phonons or applied pressure.

The crystal structure has recently been measured for a number of applied pressures up to 6.16 GPa corresponding to a reduction of the unit cell volume by 10%

(Braden *et al.*, 1999). Combined with measurements of the magnetic properties like susceptibility, this provides an excellent way to test the dependence of the magnetic interactions on changes in the structural parameters (the distances and angles between the ions) (Raupach *et al.*, 1999).

Magneto-elastic coupling

The magneto-elastic coupling parameters have been determined from the experimentally measured phonons (Werner *et al.*, 1999). Using the observed phonon frequencies and displacement schemes for the four active spin–Peierls phonons, both the effective spin–phonon coupling constants and the individual derivatives of J with respect to each of the structural parameters were derived. These coupling parameters can to some extend be reproduced by an electronic calculation, although there are several large discrepancies (Feldkemper and Weber, 1998, 1999).

Phase diagram

The observation that there is a lattice dimerization at the same temperature as where the susceptibility starts to decrease rapidly could also be interpreted as alternating chain behaviour as a result of a structural phase transition. The first evidence that the phase transition at 14 K is in fact a spin–Peierls transition driven by the magnetic instability towards forming singlet pairs was provided by the sensitivity of the transition temperature to the application of a magnetic field. The initial dependence $T_{sp}(H) = T_{sp}(0)[1 - t(g\mu_B H/2k_B T_{sp}^2)]$ was in agreement with the finding from organic spin–Peierls materials and the theory of Cross and Fisher (1979), Cross (1979). The experimental values $t = 0.39$ (Hase *et al.*, 1993b) and $t = 0.52 \pm 0.05$ (Regnault *et al.*, 1996) for the prefactor are roughly consistent with the predictions $t = 0.365$ (Cross and Fisher, 1979, Cross, 1979) and $t = 0.44$ (Bulaevskii *et al.*, 1978, Bray, 1978, Bray *et al.*, 1983). This is illustrated in figure 3.11, where also the boundary to the soliton-phase is visible.

There has been considerable interest in the order of the C–IC phase transition(Brill *et al.*, 1994, Rémenyi *et al.*, 1997, Schönfeld *et al.*, 1998). It is believed to change from second order at $T = 0$ to first order at finite T, although different experiments are not completely consistent and theoretically the order depends sensitively on the model that is used. In this context, it should be noted that experimentally it has been observed that the entire IC phase has tendency to hysteresis, as for instance observed in the present neutron scattering experiments.

Uniform susceptibility

While the susceptibility curve of Hase *et al.* (1993a) rather uniquely established the spin–Peierls transition, it proved more complicated to obtain a quantitative description of the susceptibility in the uniform phase above the spin–Peierls transition. As illustrated in figure 3.12 the susceptibility curve is more flat than the Bonner-Fisher shape for a $S = 1/2$ nearest neighbour chain.

It has been pointed out (Castilla *et al.*, 1995, Riera and Dobry, 1995) that a much better description can be obtained by introducing considerable NNN interactions $J_{NNN} = \alpha J$. In fact, the best description of the susceptibility is obtained by using $\alpha = 0.354$ (Fabricius *et al.*, 1998) which is above the critical value $\alpha_c = 0.241$ for spontaneous dimerization. With this value, perfect account is made for the susceptibility from 40 K and upwards.

Inclusion of inter-chain interactions, which are definitely present, also lower the susceptibility from the Bonner–Fisher curve (Uhrig, 1997, Bouzerar *et al.*, 1999). A high temperature expansion gives $\chi(T) = \frac{N_A(g\mu_B)^2}{4T}(1 - \frac{J(1+\alpha+J_\perp/J)}{2T})$, were $N_A\mu_B^2/k_B = 0.375$ emu K/mole. To reproduce the same high-temperature

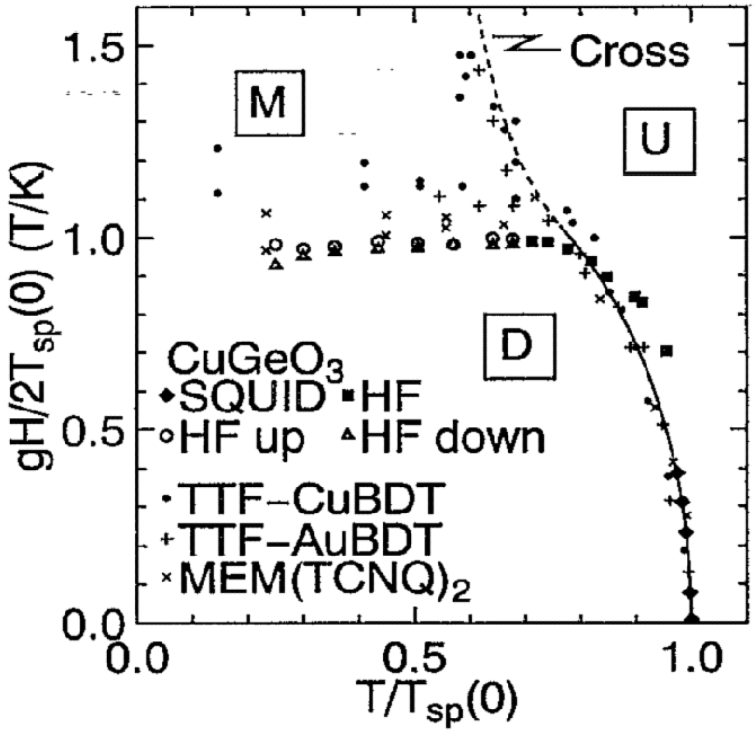

Figure 3.11. The phase diagram of $CuGeO_3$ showing the uniform (U) phase, the dimerized (D) spin–Peierls phase and the incommensurate (IC) magnetic soliton-phase taken from Hase et al. *(1993b). The field dependence of $T_{sp}(H)$ is in agreement with the theory of Cross and Fisher (1979), Cross (1979) shown by the solid line.*

susceptibility as in the 1D treatment, the NNN coupling is reduced to $\alpha_{2D} = \alpha_{1D} - J_\perp/J$.

In figure 3.12 the susceptibility is compared to the high-temperature expansion (1) for $(J, \alpha, J_\perp/J) = (180\text{ K}, 0, 0)$ and to results from exact diagonalization. Systems of up to 18 spins were diagonalized using the code RLexact by Lefmann and Rischel (1996, 1998). The parameters were from (2) to (6): (180 K,0,0), (146 K,0.2,0.15), (160 K,0.354,0), (88 K,0,0.15), (88 K,0,0). For finite interchain coupling, systems of sizes 2×6 and 2×8 were used. For the curve (6), $J = 88$ K has been chosen so that the maximum occurs at the right temperature. This demonstrates the inability of the pure NN chain to model the measured susceptibility. The effect of interchain coupling alone is illustrated as the difference between (5) and (6). It is seen how the 1D chain with NNN interaction (4) makes perfect account for the data down to about 30 K. The apparent ability of the calculation to model the drop to zero below T_{sp} is an artifact of the gap that exist in finite sized systems. The gap decreases as N^{-1} which has been illustrated by each curve shading the region between the result for respectively 12 and 16 spins. As could be expected, the interchain curves are more affected by the finite size effect, and it is inconclusive whether parameter set (3) would actually give an equally good description of the data as (4) if the system size was increased. It is seen that the finite size only affects the low temperature part of the susceptibility.

At low temperatures, the susceptibility can be calculated by retaining only single quasi-particle excitations. Since the excited states form a triplet, the susceptibility is given by $\chi(T) = \frac{N_A}{T}(g\mu_B)^2 \frac{z(T)}{1+3z(T)}$, where $z(T) = \frac{1}{(2\pi)^2}\int e^{-\omega(\boldsymbol{k})/T} d\boldsymbol{k}$ (Troyer *et al.*, 1994). This has been evaluated for a dispersion obtained using the lowest order dimer expansion with the dispersion along the chains replaced by exact diag-

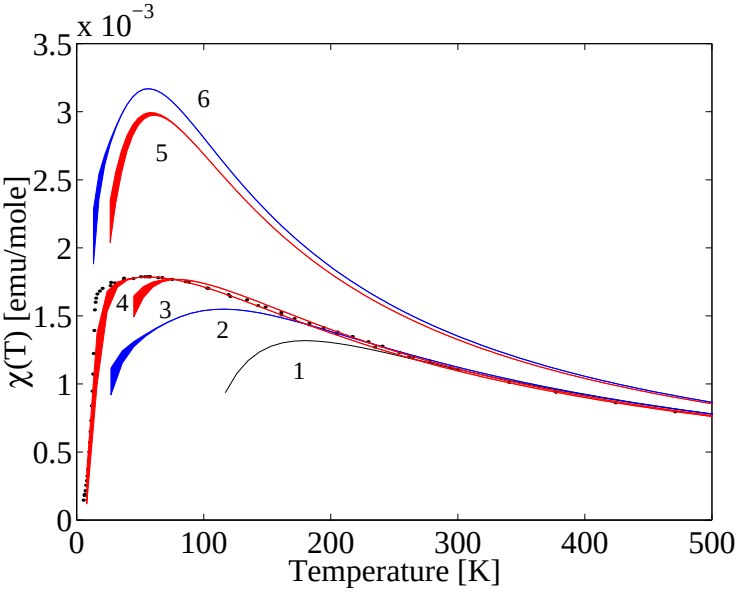

Figure 3.12. The uniform susceptibility of $CuGeO_3$ with the field along **b**, *where* $g = 2.25$ *(Hase* et al.*, 1993a, Fabricius* et al.*, 1998). It is compared to calculations for different choices of* $(J, \alpha, J_\perp/J)$ *as explained in the text.*

onalization results. With $(J, \alpha, J_\perp/J) = (146\text{ K}, 0.2, 0.15)$ a reasonable agreement was obtained for low temperatures in the dimerised phase (Bouzerar *et al.*, 1999).

Magnetization measurements

For all directions of the applied field, the magnetization remains very small until the critical field H_c is reached (Ohta *et al.*, 1994, Hori *et al.*, 1995). Above H_c the magnetization increases quickly, approaching asymptotically $m = g\mu_B H/(2\pi v_s)$ as predicted by Cross and Fisher. The reason that there is any magnetization at all in the dimerized phase is that the staggered g-tensor produces a small polarization which is antiferromagnetic along b but can be canted to give a uniform contribution along a and c.

Magnetic excitation spectrum

Perhaps the most important feature of the magnetic excitation spectrum is the existence of an energy gap Δ_0. For all momentum transfers k, the excitation spectrum is bound towards lower energies by a sharp dispersion branch, which has been mapped out along a^*, b^* and c^* by neutron scattering (Nishi *et al.*, 1994, Regnault *et al.*, 1996). As shown in figure 3.13, the minimum gap $\Delta_0 = 2$ meV is found at $k_{AF} = (0, 1, \frac{1}{2})$.

The expected triplet nature of this excitation branch was proven by applying a magnetic field. As shown in figure 3.14, the excitation is split in three according to the Zeeman energy $g\mu_B H$. While originally reported to be around 2.15 meV (Nishi *et al.*, 1994), subsequent measurements with higher resolution have established that $\Delta_0 = 1.93 \pm 0.01$ meV (Lussier *et al.*, 1996, Lorenzo *et al.*, 1997). The determination of v_s is somewhat less precise, as it requires the determination of ω_q for a number of q values around $(0, 1, \frac{1}{2})$. Due to the changing slope of the dispersion around $q = (0, 1, \frac{1}{2})$, focusing effects in the experimental resolution can lead to a q-dependent shift of ω_q towards higher or lower energies, which has a dramatic effect on the estimate of v_s. Fitting the low-q data to $\omega_q = \sqrt{\Delta_0^2 + v_s^2 q^2}$ leads to $v_s/c \simeq 13.2 \pm 0.8$ meV, while the limiting value of the dispersion obtained

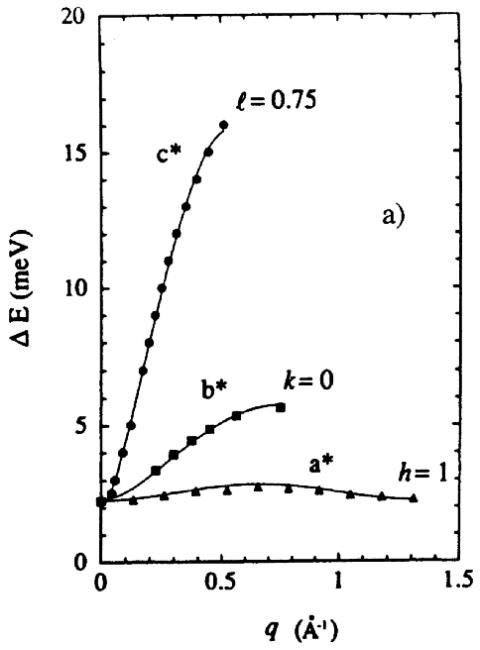

Figure 3.13. The dispersion of the magnetic excitations in the spin–Peierls phase of $CuGeO_3$ along a^*, b^* and c^* as found by neutron scattering. The minimum energy gap $\Delta_0 = 1.93 \pm 0.02$ meV is found at $k_{AF} = (0, 1, \frac{1}{2})$. The zone boundary energies are 2.8 meV, 5.7 ± 0.2 meV *and* 15.7 meV *along each of the three directions.*

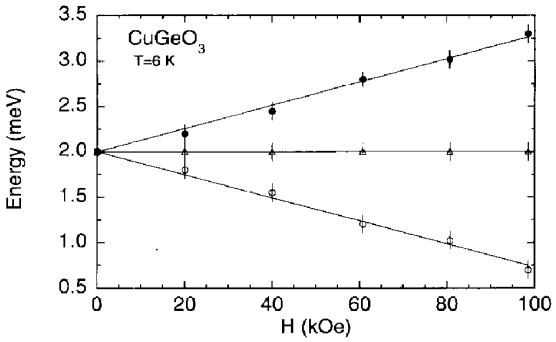

Figure 3.14. The field dependence of the energy gap Δ at $(0, 1, \frac{1}{2})$ as measured by neutron scattering (Regnault et al.*, 1996). It is seen how the triplet excitation is Zeeman split according to $g\mu_B H$.*

by fitting equation 3.69 to the entire experimental data leads to $v_s/c = 15.3$ meV (Regnault *et al.*, 1996). While the former value is probably the most appropriate, the later indicates the uncertainty in the value.

Triplet dispersion relation

In section 3.1 it was found that for very low and for very high phonon frequencies, the phonons could be integrated out to yield an effective magnetic model. In $CuGeO_3$ the lowest spin–Peierls phonon has an energy approximately equal to J, for which it is not clear that such an effective magnetic model is valid. But in the absence of results for the full spin–phonon excitations, it is probably the best approximation to make.

The easiest interpretable part of the excitation spectrum is the q dependence of the triplet excitation, but upon inclusion of alternation, NNN and interchain

coupling there exists no unique result for the dispersion relation. Starting from the effective magnetic model, a number of different approaches have been taken, including standard spin-wave theory, expansion from the isolated dimer limit and Jordan–Wigner mean field approximation (Cowley *et al.*, 1996, Brenig, 1997, Fan and Gong, 1999, Bouzerar *et al.*, 1999).

In principle, the excitation spectrum can be modeled by the linear spin-wave result for a 3D antiferromagnet with a single-site anisotropy to reproduce the gap. Though hardly justifiable, this illustrates the generic problem that the dispersion relation alone is insufficient to uniquely determine the magnetic coupling parameters.

A physically more appealing approach is an expansion from the dimer ground state (Cowley *et al.*, 1996). The ground state is assumed to be composed by spin singlets, which can be excited by one of three operators that create each of the three triplet states. Keeping terms up to second order in the dimer operators, the Hamiltonian can be diagonalised to give

$$\omega_q = \sqrt{J_0[J_0 - J_1\cos(2q_c) - 2\cos(q_c)(J_a\cos(q_a) - J_b\cos(q_b/2))]} \qquad (3.69)$$

where $J_0 = J(1+\delta)$ and $J_1 = J(1-\delta)$. Using the measured dispersion relation gives the magnetic coupling parameters $J_0 = 9.8$ meV, $J_1 = 11.4$ meV, $J_b = 0.62$ meV and $J_a = -0.08$ meV (where I have included the subsequently measured dispersion along a in the fits). Neglecting the coupling along a, but including NNN coupling, the same dispersion is found but with J_1 replaced by $J_1 - 2J_{NNN}$ (Brenig, 1997, Lake, 1999). It is therefore not possible from this dispersion relation alone to determine J_1 and J_{NNN} independently.

In a slightly different approach, the dispersion was calculated to third order with no qualitative differences except that the square root in equation 3.69 is expanded (Uhrig and Schulz, 1996, Uhrig, 1997). For the higher order terms, there is a distinction of J_1 and J_{NNN}. Supposedly, the best fit to the neutron scattering data is obtained using frustrating interchain interactions along the diagonal of the 2D rectangles rather than intrachain NNN coupling. But without a clear understanding of the precision of the calculation, small differences in the quality of the fits should be treated with great care.

Equation 3.69 can be written as $\omega_q = \sqrt{\omega_{1D}^2(q_c) - 2J_0J_\perp\cos(q_c)\cos(q_\perp)}$, where $\omega_{1D}(q_c)$ is the dispersion in the absence of interchain coupling. It has been proposed to use a more exact result for $\omega_{1D}(q_c)$ based on exact diagonalization (Bouzerar *et al.*, 1999). But in this approach, the square root is expanded around the dimer limit, which is hardly valid. This leads to a prediction for $J_\perp$ which is a factor of 3 larger than what is obtained by keeping the square root.

In addition to the neutron data for the dispersion, the interchain coupling has also been estimated from exchange induced splitting of the EPR signal in very high magnetic fields (up to 180 T) (Nojiri *et al.*, 1998b, Kokado *et al.*, 1998). The value $J_b \simeq 0.75 - 0.9$ meV is roughly consistent with the result from the dispersion relation, but it is unclear how it depends on the presence of NNN coupling.

Excitation continuum

In addition to the sharp triplet mode discussed so far, neutron scattering experiments have revealed a continuum of scattering above it (Arai *et al.*, 1996). By polarized neutron scattering, both these features have been shown to be magnetic of origin (Lorenzo *et al.*, 1997). The uniform Heisenberg antiferromagnet also shows such a continuum, which is due to two-particle processes. It therefore extends from the single particle dispersion $\frac{\pi}{2}J|\sin q|$ to twice the zone boundary energy as $\pi J|\sin q/2|$. In $CuGeO_3$ there are some differences compared to the uniform model. The sharp triplet mode and the continuum is actually separated by

a second gap (Aïn *et al.*, 1997). This is because the triplet is formed by a bound soliton–anti-soliton pair, while the continuum is constituted of free soliton–anti-soliton pairs (Sørensen *et al.*, 1998, Dobry and Ibaceta, 1998, Augier *et al.*, 1998, 1999). The continuum is found to have lower intensity than expected from the uniform model. Instead, the intensity seems to be condensed in the boundaries $\frac{\pi}{2}J|\sin q|$ and $\pi J|\sin q/2|$ (Braden *et al.*, 1999).

Other features in the excitation spectrum

Recently, another low energy magnetic excitation branch was discovered, whose dispersion is given by the already known triplet branch shifted by $b^* + c^*/2$ (Lorenzo *et al.*, 1999). This is interpreted as a small exchange anisotropy, which had in fact already been proposed on the basis of electron spin resonance (ESR) measurements (Pilawa, 1997).

3.3.3 Model parameters for $CuGeO_3$

As described above, the experimental findings on both the uniform and the dimerized phases of $CuGeO_3$ are qualitatively understood within an effective magnetic model. However, as precise calculations are still missing, the parameters cannot be determined uniquely. On top of this difficulty, there is the question about whether the phonons can actually be integrated out and whether the effective magnetic parameters are in fact temperature dependent.

Rather than trying to select one specific choice of parameters, it is important that there is consistency between the way the parameters were determined and how they are used. If for example some physical observable is calculated by neglecting the interchain coupling, it is most appropriate to use the parameters determined by fitting the previous experimental data to the predictions for the 1D system.

In this context it should be realized, that although the field theoretical treatment of the soliton phase was derived by Jordan–Wigner transformation of the microscopic Hamiltonian, the parameters were adjusted to yield the correct dispersion relation (at low q) $\omega_q = \sqrt{\Delta_0^2 + v_s^2 q^2}$. The results for the soliton phase depend only on these two parameters, which are directly inferable from the neutron scattering data in the spin–Peierls phase. The prospect of a parameter free test of the predictions for the soliton phase motivates the neutron scattering study reported in the following sections.

3.3.4 Doped $CuGeO_3$

There exist various means of doping $CuGeO_3$ by replacing either Cu with Zn, Mg or Ni and Ge with Si. A vast amount of work has been reported on doping, which has profound effects (Sasago *et al.*, 1996, Grenier *et al.*, 1999, Shirane, 1999, Büchner *et al.*, 1999, Masuda *et al.*, 1999, Wang *et al.*, 1999). For instance substitution of just 1.5% Ni or 4% Zn causes normal antiferromagnetic order on behalf of the spin–Peierls phase (Lussier *et al.*, 1995, Regnault *et al.*, 1995). Most of these effects can be understood by considering the impurities as randomly distributed broken dimer bonds and hence pinning centers for solitons. If enough such impurity bound solitons exist, the system becomes antiferromagnetic. Though broken dimer bonds provide a very interesting mean to study the competition between dimer and antiferromagnetic order, it will not be discussed further in this thesis.

3.4 Statics of the high field phase

As described in section 3.2 there exist precise predictions for the soliton structure in the high-field phase. As these depend on just two parameters Δ_0 and v_s, which have been determined experimentally for $CuGeO_3$, this allows for a parameter free test of the theoretical approach. This section describes a neutron scattering investigation of the magnetic soliton structure, but starts by reviewing what has already been found.

3.4.1 Previous experiments

The incommensurate nature of the high-field phase was demonstrated in X-ray diffraction measurements (Harris *et al.*, 1994, Kiryukhin and Keimer, 1995, Kiryukhin *et al.*, 1996a,b). Above H_c the satellite reflections were split into $(\frac{h}{2}, k, \frac{l}{2} \pm \delta k_{sp})$ where $\delta k_{sp} = 1/L$. The appearance of third harmonics showed the non-sinusoidal shape of the modulation, and the relative intensity was used to estimate the soliton width $\Gamma/c = 13.6 \pm 0.3$.

In a 0.5 T region around H_c the commensurate and incommensurate peaks were found to coexist, without showing any sign of broadening. This is in accord with the hysteresis observed in magnetization measurements. From ESR measurements, it was found that not just the transition, but the IC phase itself exhibits hysteresis (Palme *et al.*, 1996).

The spontaneous strain $\epsilon(H)/\epsilon(0)$ has been derived from thermal expansion and magnetostriction measurements (Lorenz *et al.*, 1998). This number is proportional to the average square displacement parameter $\langle u^2 \rangle$. Only in a narrow region just above H_c is the experimental result in agreement with the average $\langle u^2 \rangle$ calculated from the field theoretical Jacobi elliptic function. A considerably better agreement was reached in a DMRG calculation using $J = 160$ K, $\alpha = 0.35$, $K = 18J$ and $\delta = 0.014$. A similar agreement could be obtained by allowing a field dependent Γ.

The elastic constants C_{bb} and C_{cc} have been found to behave differently above the IC transition (Saint-Paul *et al.*, 1997). While C_{bb} jumps to a lower value above H_c, C_{cc} increases in a continuous manner. This is interpreted as gradual filling of solitons with decreasing regions of the remaining dimerised regions. The volume fraction of the solitons relative to the dimerised regions was extracted and found to increase to 1 at about 14 T. This picture is certainly true, but the relation between C_{cc} and the soliton structure is probably too complicated to give accurate handles on the extent of the solitons as a function of the field.

Copper NMR has been measured up to 26 T (Fagot-Revurat *et al.*, 1996, 1997, Horvatić *et al.*, 1999). Above H_c a broad lineshape develops, signaling a continuous distribution of the local magnetization. The line-shape was analysed using the Jacobi elliptic functional form with the amplitudes m_u, m_s and the soliton width Γ_m as free parameters. From H_c to 26 T the uniform magnetization amplitude varies from $m_u = 0.016$ to 0.030, while the staggered magnetization varied from $m_s = 0.023$ to 0.029. The soliton width was found to decrease from 10 to 6.3. The modulus k decreased according to $k' = \sqrt{1-k^2} \simeq 0.56(H/H_c - 1)^{0.35}$. These observations are generally in good accord with the field theoretical prediction expect for the staggered amplitude, which is 4 to 8 times lower than the prediction. It has been proposed that the reason for such a low result in the NMR experiment is that the zero point motion of the phason mode introduced an effective averaging of the magnetic structure compared to the field theoretical prediction. While the averaging would have little effect on the slowly varying uniform component, it would significantly reduce the staggered component.

3.4.2 Experimental details

The static behaviour of the high field phase was investigated using three different spectrometers, each providing a different range of resolution versus reciprocal space coverage. In a preliminary experiment on the thermal triple axis spectrometer E1, the development of 5 satellite reflections was investigated. The existence a magnetic structure was proven at the thermal two-axis instrument E4. The detailed structure of the magnetic soliton lattice was determined in a high resolution experiment on the cold triple axis spectrometer V2.

The sample

Samples for the investigation were grown by Revcolevschi and Dhalenne 1999 using the floating zone method.

For the first two experiments, a sample of size $3 \times 7 \times 16$ mm^3 was used. $CuGeO_3$, apparently, has a tendency towards growing as twinned crystals, and so also our first sample was in fact twinned. A rocking curve in the *bc*-plane revealed two peaks separated by 2.8° and of equal peak intensity. However, one twin had almost the double mosaicity and hence composed about two thirds of the sample weight. During the first experiment each of the two twins were used depending on whether the specific measurement required resolution or intensity. In the first inelastic experiment, the second twin constituted a continuous uncertainty of the origin of double peaks and possible continua observed in the energy scans.

For the two next experiments we used another crystal which was borrowed from Michel Aïn 1997. This crystal was slightly larger ($4 \times 8 \times 17$ mm^3) and had the advantage of not being twinned.

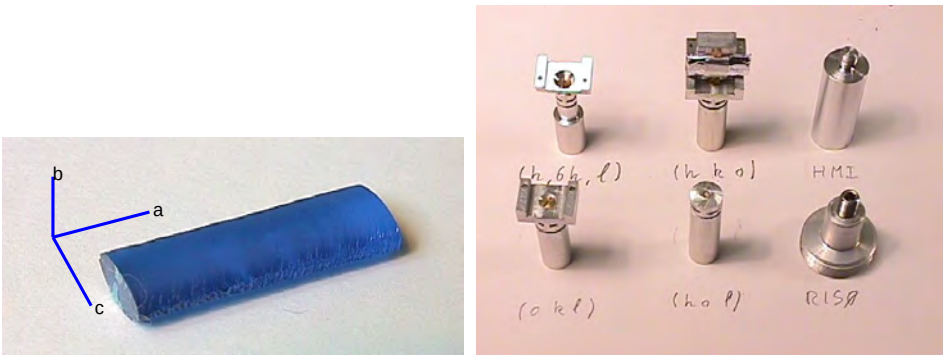

Figure 3.15. Pictures of the crystal which was grown by the floating zone method (left), and of the sample mounts that were designed to allow changing between different pre-aligned scattering planes (right).

Crystal mounting

The occurrence of satellite reflections at the $(\frac{h}{2}, l, \frac{l}{2})$ positions, incommensurability along l and an expected magnetic ordering at the $(0, 1, \frac{1}{2})$-type positions made it necessary to invoke several different orientations of the crystal. Combined with the restriction that the cryomagnet used did not allow for any post mounting adjustment of the scattering plane made it necessary to design a set of sample holders allowing us to change scattering plane without the need to realign the sample. The crystal was embedded in a small aluminum block equipped with several threads for mounting in different sample pins, each realizing a given scattering plane. The sample pins were equipped with two perpendicular 'weak links', which allowed each pin to be aligned. Once a pin had been bent into alignment, the aluminum block

with the crystal could be removed and replaced, keeping the alignment within less than half a degree, which is sufficient for the vertical resolution of the neutron spectrometers that were used.

The VM1 14.5 T vertical field cryomagnet

The high-field phase was accessed using a 14.5 T vertical field cryomagnet from Oxford Instruments. The coils provide an opening of 20 mm at the sample position and a divergence of ±2°. The total width of the aluminum shields is 2 × 34 mm with a dark angle of only 25°. The core provides a sample space of Ø19 mm and a base temperature of 1.6 K. With a dilution insert, a sample space of Ø15 mm and a base temperature of 40 mK is possible. Recently, a pair of dysprosium pole-shoe-boosters have been designed, enabling fields of 17 T in a limited sample space of Ø6.5 mm×4 mm.

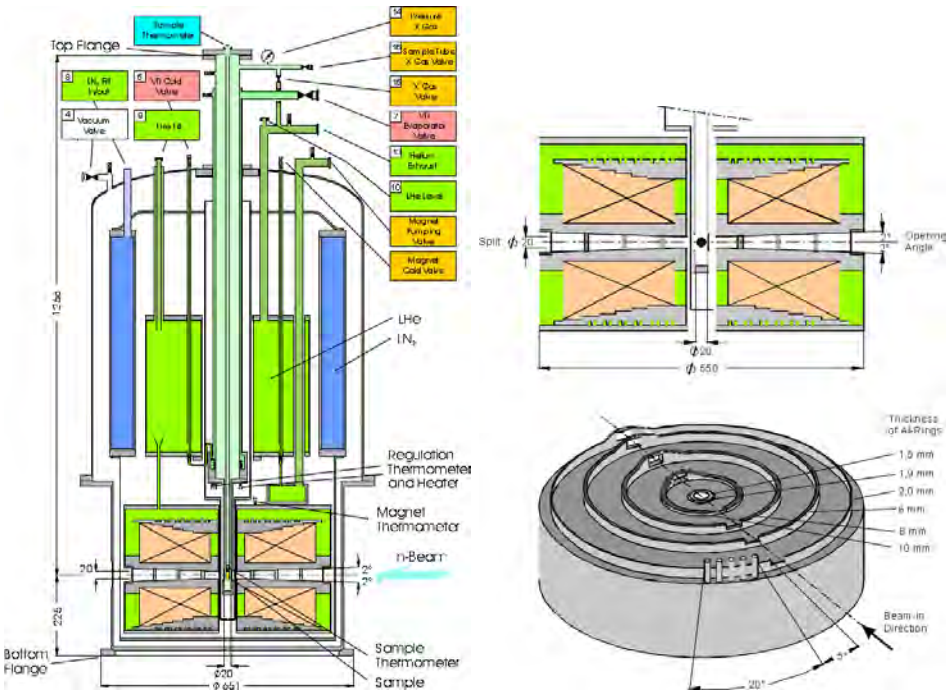

Figure 3.16. Schematics of the 14.5 T vertical field cryomagnet VM1 at HMI, Berlin.

Field dependence on the E1 thermal triple axis experiment

With the wave-length set to 2.4226 Å and a collimation of 20'-80'-20'-40', a resolution of typically 0.02 $Å^{-1}$ was achieved. The rather unconventional collimation configuration was found to perform best in terms of signal to background ratio. The need for a low background made it important to stop the 'unwanted' neutrons as early as possible, be it before hitting the monochromator or the analyser.

The experiment consisted of two parts. The development of five different satellite reflections upon entering the high field phase was investigated. In addition, a search was conducted in an attempt to locate scattering due to the proposed magnetic order of the high field phase, but no elastic signal other than the $(\frac{h}{2}, k, \frac{l}{2})$ satellite reflections was found.

Two different crystal orientations with respectively $(h, 2h, l)$ and $(h, 6h, l)$ in the scattering plane made a total of five satellite reflections $(\frac{1}{2}, 1, \frac{1}{2})$, $(\frac{3}{2}, 3, \frac{1}{2})$, $(\frac{3}{2}, 3, \frac{3}{2})$, $(\frac{1}{2}, 3, \frac{1}{2})$ and $(\frac{1}{2}, 3, \frac{3}{2})$ accessible.

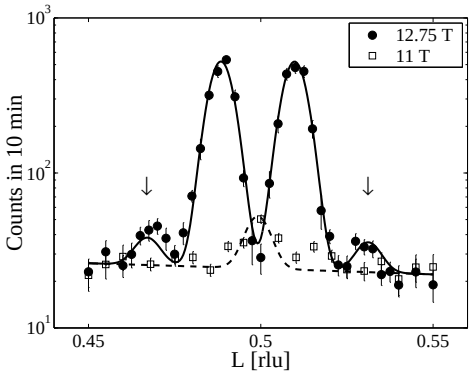

Figure 3.17. Scans along c^* through the $(\frac{1}{2}, 1, \frac{1}{2})$ satellite reflection at respectively 11 T$< H_c$ and 12.75 T$> H_c$. At 12.75 T the third harmonics have been marked with arrows.

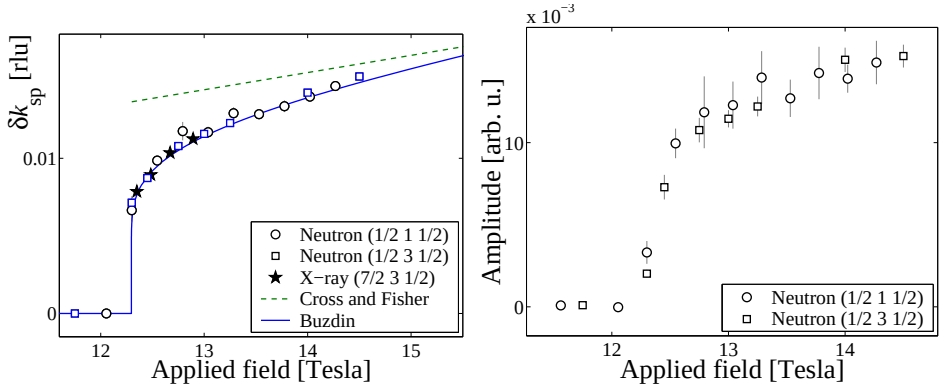

Figure 3.18. Left: The incommensurability δk_{sp} measured with neutrons as the splitting of the $(\frac{1}{2}, 1, \frac{1}{2})$ and $(\frac{1}{2}, 3, \frac{1}{2})$ satellite reflections. A representative selection of the X-ray data for $(\frac{7}{2}, 3, \frac{1}{2})$ is shown. The data are compared to the theories by Cross and Fisher 1979a, 1979b (dashed line) and by Buzdin et al. *(1983) (solid line) using the value $\Delta_0/v_s = 0.13$. Right: The field dependence of the amplitude of the two reflections scaled to each other.*

Figure 3.17 shows scans through the $(\frac{1}{2}, 1, \frac{1}{2})$ satellite reflection respectively below and above the transition. Apart from the expected splitting into $(\frac{1}{2}, 1, \frac{1}{2} \pm \delta k_{sp})$, a tremendous increase in intensity was observed. The data were analysed by fitting the peaks to simple Gaussian line shapes. The splitting of the two strongest reflections $(\frac{1}{2}, 1, \frac{1}{2})$ and $(\frac{1}{2}, 3, \frac{1}{2})$ was recorded as a function of magnetic field and is shown in figure 3.18. Through the slightly anisotropic g-tensor, the critical field depends on the orientation of the sample. Throughout this text, we scale to the average g-value, which makes the results for different orientations collapse on one curve. This is also the case for the splitting $\delta k_{sp}(H)$, where we obtain perfect agreement with both the previous X-ray results (Kiryukhin *et al.*, 1996a,b) and the field theory based predictions by Cross and Fisher 1979a, 1979b $\delta k_{sp} = g\mu_B H/(2\pi v_s)$ and by Buzdin *et al.* (1983) $1/\delta k_{sp} = \frac{2v_s}{\Delta_0} \ln \frac{8H_c}{H - H_c}$. The best agreement with field theory is reached by using the upper limit value 0.13 for the experimentally determined ratio $\Delta_0/v_s = 0.12 \pm 0.01$. In fact, the $\delta k_{sp}(H)$ data can be used to determine $\Delta_0/v_s = 0.130 \pm 0.002$ quite precisely.

At the maximum field of 14.5 T, the $(\frac{1}{2}, 1, \frac{1}{2})$ satellite reflection was recorded as a function of temperature until the uniform phase was reached at 10 K. The splitting and intensity as a function of temperature is plotted in figure 3.19. It

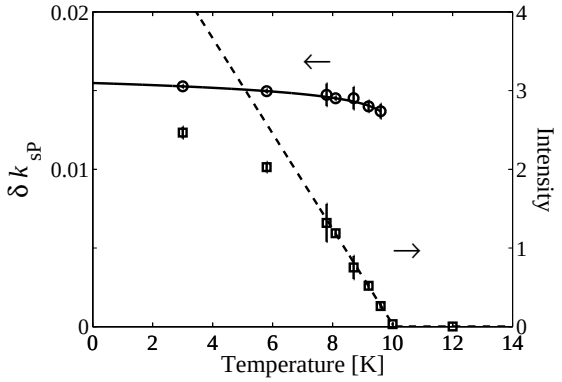

Figure 3.19. The incommensurability δk_{sp} and amplitude of the $(\frac{1}{2}, 1, \frac{1}{2})$ satellite reflection as a function of temperature in a field of 14.5 T.

is seen how the intensity decreases continuously towards the transition, while the splitting remains finite and almost constant. This reflects the fact that even the uniform phase is susceptible to incommensurability when subject to an applied field. The slight decrease of $\delta k_{sp}(T_c)/\delta k_{sp}(0) = 0.86$ with increasing temperature is in accord with the field theoretical calculations by Machida and Fujita (1984) who calculated $\delta k_{sp}(T_c)/\delta k_{sp}(0) = 0.82$ numerically for a field corresponding to 16 T in $CuGeO_3$.

The surprising observation of large increases in intensity of in particular the $(\frac{1}{2}, 1, \frac{1}{2})$ satellite reflection made a quantitative analysis of the peak intensities interesting. The peak widths were in good accordance with a resolution calculation with the rescal program based on the Popovici method (Cooper and Nathans, 1967, Tucciarone *et al.*, 1971, Popovici, 1975, Tennant and McMorrow, 1996). From these calculations, the normalization constants R_0 which converts peak-intensities to structure factors were determined. A priori, five structure factors are insufficient to allow a determination of the distortion scheme, but in this case, the well known zero field distortion pattern served as a good starting point. Still, it was not possible to obtain a reasonable fit without using unphysical distortion parameters. The reason was that the large intensity at low Q-values could not be modeled by a structural distortion, for which the intensity scales like Q^2.

This in combination with the absence of magnetic scattering at other places in the reciprocal space caused the speculation that the increased intensity is due to a contribution from the magnetic soliton structure.

Structural distortion and magnetic order on the E4 thermal two-axis instrument

To verify the hypothesis of a magnetic contribution to the low-Q satellites, the structure factors of 14 satellite reflections were collected.

The experiment was performed on the two-axis spectrometer E4 at HMI, Berlin. The pyrolytic-graphite (PG) monochromator was tuned to a scattering angle of 42.65° giving a diachromatic beam of neutrons with wavelengths 2.441 Å for PG(002) and 1.2205 Å for PG(004). To reach sufficiently far out in reciprocal space, $\lambda = 1.2205$ Å was used. Without any filter there was a weak contamination of $\lambda/2$ in the order of 1%.

The untwinned crystal number 2 was mounted with $(0, 0, l)$ and $(h, 2h, 0)$ in the scattering plane in order to reach satellite reflections of the form $(h+\frac{1}{2}, 2h+1, l+\frac{1}{2})$. With a maximum scattering angle of $2\theta = 117°$ a total of 14 non-equivalent reflections were accessible. The neutrons with wavelength $\lambda/2$ will scatter from Bragg peaks at the same instrument position as the satellite reflections. For each

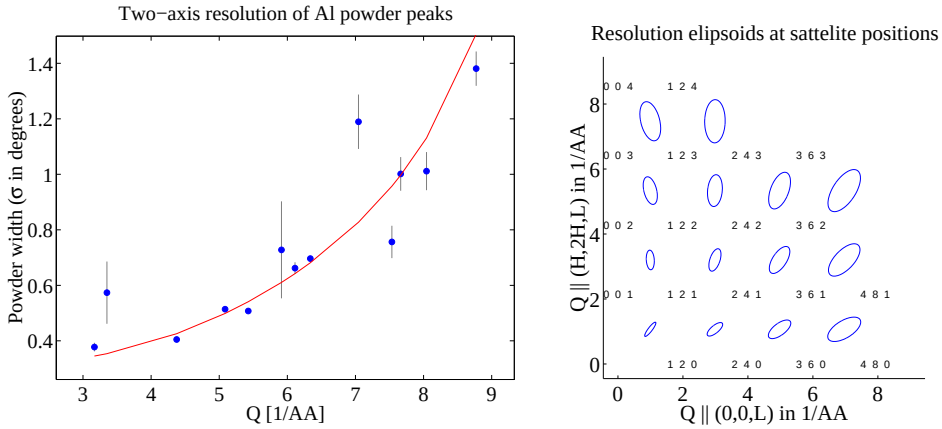

Figure 3.20. Left: The Gaussian width of a number of powder reflections from the aluminum sample holder as a function of scattering vector Q. The solid line indicates the calculated resolution, which gives very good account for the observed widths. Right: The resolution ellipses defined as the HWHM of the resolution function for each of the satellite reflections in the $(h, 2h, l)$ plane. For clarity, the resolution ellipses have been scaled by a factor of 10 in both directions.

of the 14 reflections, rocking scans were performed in order to obtain the integrated intensity at $(T, B) = (2\text{ K}, 14.5\text{ T})$, (2 K,0 T) and (20 K,0 T). The latter in order to correct for the $\lambda/2$ background.

In order to extract the structure factors, it is necessary to carefully consider the resolution of the instrument, which for both 2- and 3-axis spectrometers is derived as the sequential convolution of the transmission function for each part of the spectrometer. If all distribution functions are assumed Gaussian, the convolutions correspond to adding the resolution widths in quadrature. However, as the resolution function is multi-dimensional, appropriate coordinate transformations are necessary before each component can be added (Lebech and Nielsen, 1975).

The calculated resolution was verified by comparing the calculated and measured widths of a number of powder reflections from the aluminum sample holder. The good agreement as depicted in figure 3.20a show that the resolution calculation is reliable. In figure 3.20b the resolution ellipsoid for each of the 14 satellite reflections is shown. In addition to the resolution widths, also the resolution volumes R_0, to which the measured intensities were normalized, were calculated and are listed in table 3.1.

The first part of the experiment aimed to reproduce the zero field results of Hirota *et al.* (1994) and Braden *et al.* (1996). In figure 3.21 rocking scans of the $(\frac{1}{2}1\frac{1}{2})$ reflection at 2 K and at 20 K are shown. The integrated intensity was found by fitting resolution-determined lineshapes to the data. The solid lines in figure 3.21 are the result of such fits. It should be noticed how the resolution calculation gives perfect account for the measured width. At 20 K, there is no dimerisation, so the only intensity at the satellite positions is due to $\lambda/2$ scattering from Bragg peaks. At 2 K, additional intensity from the lattice distortion is observed. The intensity of the satellite reflection was taken as the difference in integrated intensity between the 2 K data dn the 20 K data. Since the two 0 T scans were performed at the same scattering angle 2θ, an alternative means of analysis was to subtract the measured intensities at 20 K from the 2 K intensities point by point. This procedure gave identical intensities, thereby consolidating our confidence in the resolution treatment.

The fitted integrated intensities were corrected for the resolution volume R_0 to give the structure factors listed in table 3.1. The structure factor for the distortion

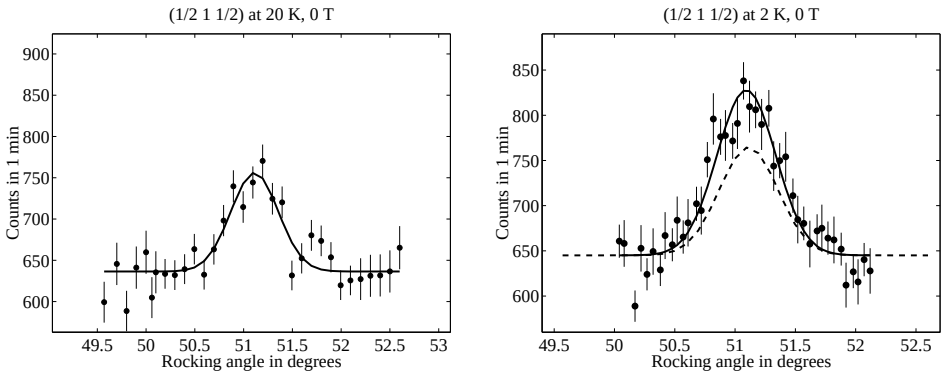

Figure 3.21. Rocking curves of the $(\frac{1}{2}, 1, \frac{1}{2})$ satellite reflections at 20 K and at 2 K. The solid line is the result of a fit to a peak with the width given by the experimental resolution. The dashed line in the 2 K graph is the fit to the 20 K data.

h	k	l	q [Å^{-1}]	2θ	$1/R_0$	$I(0\mathrm{T})$	$I(14.5\mathrm{T})$	$\frac{I(0\mathrm{T})}{R_0}$	$\frac{I(14.5\mathrm{T})}{R_0}$
1/2	1	1/2	1.46	16.3	0.28	65 ± 17	664 ± 18	18 ± 5	186 ± 5
3/2	3	1/2	3.17	35.9	0.57	25 ± 20	257 ± 11	14 ± 12	147 ± 6
1/2	1	3/2	3.35	38.0	0.60	199 ± 42	259 ± 10	120 ± 25	156 ± 6
3/2	3	3/2	4.38	50.3	0.79	217 ± 18	170 ± 16	171 ± 14	134 ± 12
5/2	5	1/2	5.09	59.2	0.96	149 ± 20	81 ± 7	142 ± 19	77 ± 7
1/2	1	5/2	5.43	63.6	1.06	153 ± 48	62 ± 22	162 ± 51	66 ± 23
5/2	5	3/2	5.91	70.1	1.24	315 ± 16	114 ± 7	389 ± 19	141 ± 9
3/2	3	5/2	6.11	72.8	1.32	62 ± 20	43 ± 7	82 ± 26	57 ± 9
7/2	7	1/2	7.04	86.3	1.88	215 ± 20	61 ± 11	404 ± 37	115 ± 22
5/2	5	5/2	7.29	90.2	2.08	29 ± 18	22 ± 3	61 ± 37	45 ± 7
1/2	1	7/2	7.53	94.1	2.30	183 ± 20	32 ± 4	419 ± 47	74 ± 8
7/2	7	3/2	7.66	96.2	2.43	423 ± 27	168 ± 14	1026 ± 65	408 ± 34
3/2	3	7/2	8.04	102.7	2.85	141 ± 27	46 ± 4	401 ± 78	131 ± 12
7/2	7	5/2	8.77	116.8	3.92	30 ± 38	0 ± 9	117 ± 149	0 ± 34

Table 3.1. Integrated intensities in degrees/min of the 14 measured satellite reflections at zero and at maximum field.

satellites is given by $F(q) = \sum_d b_d q \cdot u_d(q) e^{-iq\cdot d}$, where $u_d(q) = \sum_r u_d(r) e^{-iq\cdot r}$ is the Fourier component of the displacement of atom d. We adopt the distortion parameter choice of Hirota *et al.* (1994) and Braden *et al.* (1996) where only $u_z^{\mathrm{Cu}} \times 1000 = 1.92$, $u_x^{\mathrm{O2}} \times 1000 = 1.98$ and $u_y^{\mathrm{O2}} \times 1000 = 0.77$ are non-zero. Fitting the 0 T intensities to $|F|^2$ gave distortion parameters that are proportional to the square root of the overall normalization factor for the intensities. This parameter could be determined by scaling the satellite intensities to the main Bragg peak intensities, but as the latter are highly extinction affected, this is an inaccurate method. Instead, the normalization factor was chosen such that the sum of the fitted displacement parameters was equal to the sum of the displacement parameters reported by Braden *et al.* (1996). The resulting displacement parameters are $u_z^{\mathrm{Cu}} \times 1000 = 2.04 \pm 0.14$, $u_x^{\mathrm{O2}} \times 1000 = 1.82 \pm 0.10$ and $u_y^{\mathrm{O2}} \times 1000 = 0.79 \pm 0.09$. The fact that the relative sizes of the displacement parameters of Braden *et al.* (1996) were well reproduced shows that the method for the experiment and the analysis is reliable.

The second part of the experiment proceeded by measuring rocking curves of the satellite reflections in the high field phase at 14.5 T. Figure 3.22 shows scans of $(\frac{1}{2}, 1, \frac{1}{2} + \delta)$ and $(\frac{3}{2}, 3, \frac{1}{2} + \delta)$, where it is seen that the resolution picks up both satellite reflections and the $\lambda/2$ peak. The data were fitted to the two satellite reflections at $\pm\delta$ and the $\lambda/2$ peak. All three contributions had the shape given by the instrumental resolution, and the satellite amplitude was the only free parame-

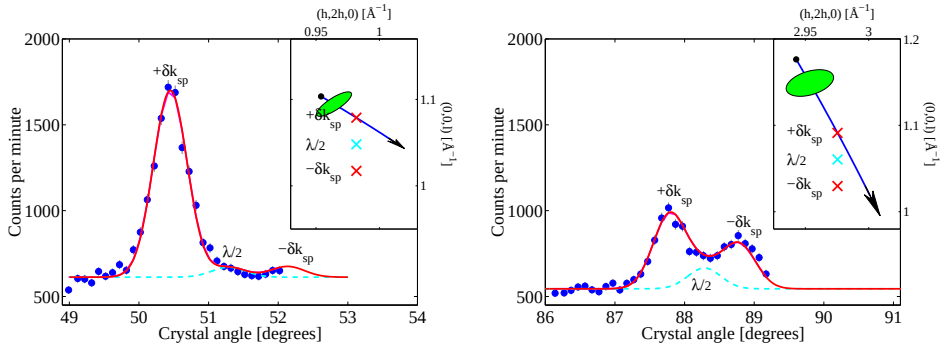

Figure 3.22. Rocking scan through the $(\frac{1}{2}, 1, \frac{1}{2} + \delta k_{sp})$ *and* $(\frac{3}{2}, 3, \frac{1}{2} + \delta k_{sp})$ *satellite reflections at 14.5* T. *The insert displays the reciprocal space trajectory of the scan. Both satellites and also the (3,6,1) Bragg peak due to* $\lambda/2$ *contamination are picked up by the resolution which is indicated by the half-height ellipse. The* $\lambda/2$ *contribution determined at 20* K *is shown by the dashed line. With the satellite intensity as the only fitting parameter, perfect account is made for the data (solid line).*

ter. The amplitude of the $\lambda/2$ peak was kept fixed at the value obtained at 20 K, 0 T as shown with the dashed line. For $(\frac{3}{2}, 3, \frac{1}{2})$, both the $\lambda/2$ peak and the second satellite contribute to the measured intensities, but the resolution treatment gives full account for this. The inserts show the trajectory of the rocking scans in the reciprocal plane. The resolution is illustrated with a half-height contour.

The satellite intensities were normalised to the resolution volume and the overall scale factor determined from the 0 T data. The resulting 14.5 T structure factors are listed in table 3.1. One immediately notices the drastic increase in intensity at low q. As the nuclear satellite intensity scales with q^2, it is not possible to account for this by changing the distortion parameters.

Instead, a magnetic contribution which scales with the square of the form factor $f(q)$ for free Cu^{2+} (Watson and Freeman, 1961) was introduced. The magnetic intensity also depends on the direction of the magnetic moment. The best fit is obtained with the moment parallel/antiparallel to the field and hence perpendicular to the scattering plane. A Fourier component with amplitude $0.098 \pm 0.003 \mu_B$ accounts well for the low q part of the intensities.

At higher q, the form factor reduces the magnetic contribution, and the intensities are mainly nuclear of origin. A fit gives Fourier components, which are roughly halved compared to the spin–Peierls phase. When the lattice distortion becomes incommensurate, the Fourier component of the lattice distortion is split into two components each of half the size of the original. So, when the Fourier components are halved, it means that the amplitude of the lattice distortion remains more or less unchanged: $u_z^{\mathrm{Cu}} \times 1000 = 1.58 \pm 0.26$, $u_x^{\mathrm{O2}} \times 1000 = 1.96 \pm 0.36$ and $u_y^{\mathrm{O2}} \times 1000 = 0.61 \pm 0.25$. In the incommensurate phase, there is the possibility that u_z^{O2} becomes non-zero, but it is expected to scale with $\delta \ll 1$. Indeed if included in the fit, we get a small value. It should be noted that u_z^{O2} is modulated out of phase with the remaining u's and should therefore be imaginary (Grenier *et al.*, 1998).

A further illustration of the magnetic origin of the low-Q intensity is given in figure 3.23, where the calculated nuclear scattering has been subtracted from the measured structure factors. The excess contribution is seen to follow nicely the formfactor for free Cu^{2+} (Watson and Freeman, 1961).

				0 T		14.5 T	
h	k	l	q [Å^{-1}]	$\lvert F\rvert^2_{\rm exp}$	$\lvert F\rvert^2_{\rm fit}$	$\lvert F\rvert^2_{\rm exp}$	$\lvert F\rvert^2_{\rm fit}$
1/2	1	1/2	1.46	4 ± 1	1	40 ± 1	41
3/2	3	1/2	3.17	3 ± 2	1	31 ± 1	29
1/2	1	3/2	3.35	26 ± 5	16	33 ± 1	30
3/2	3	3/2	4.38	36 ± 3	34	29 ± 3	26
5/2	5	1/2	5.09	30 ± 4	20	16 ± 1	21
1/2	1	5/2	5.43	35 ± 11	34	14 ± 5	20
5/2	5	3/2	5.91	83 ± 4	89	30 ± 2	28
3/2	3	5/2	6.11	18 ± 6	16	12 ± 2	15
7/2	7	1/2	7.04	86 ± 8	90	25 ± 5	37
5/2	5	5/2	7.29	13 ± 8	0	10 ± 1	9
1/2	1	7/2	7.53	89 ± 10	81	16 ± 2	21
7/2	7	3/2	7.66	218 ± 14	208	87 ± 7	59
3/2	3	7/2	8.04	85 ± 17	116	28 ± 3	25
7/2	7	5/2	8.77	25 ± 32	21	0 ± 7	17

Table 3.2. Structure factors and fitted structure factors in 1000×10^{-24} cm^{-2}.

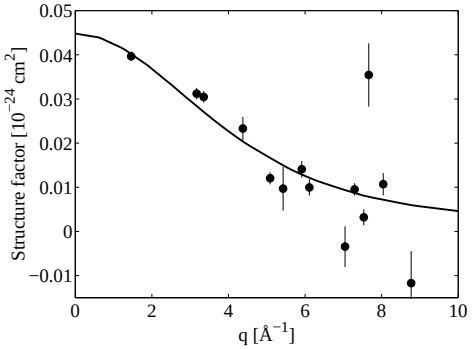

Figure 3.23. The excess intensity $|F_{exp}|^2 - |F_{nuc}|^2$ *after subtraction of the calculated nuclear scattering follows the formfactor for a free* Cu^{2+} *ion (solid line).*

Magnetic soliton structure on the V2 cold triple axis instrument

The $(\frac{1}{2}, 1, \frac{1}{2})$ reflection is almost completely magnetic in origin (40:1 *c.f.* table 3.2), and can therefore be used to investigate the detailed structure of the magnetic soliton. This was done using the cold triple axis spectrometer V2, HMI, Berlin. V2 is located on a ^{58}Ni neutron guide, and can therefore not be equipped with collimation before the vertically focusing 24' PG monochromator. The remaining three beam-paths were collimated to 20'. With a neutron energy of 3 meV ($\lambda = 5.236$ Å), a resolution FWHM of 0.009 Å^{-1} along l through $(\frac{1}{2}, 1, \frac{1}{2})$ was achieved.

The increased resolution and lower background compared to th E1 experiment made it possible to quantitatively follow the evolution of the third harmonics $(\frac{1}{2}, 1, \frac{1}{2} \pm 3\delta k_{sp})$ as depicted in figure 3.24. The intensity of the higher harmonics is proportional to the overall intensity, which increases monotonically with the field as shown in figure 3.18. But at the same time the soliton shape develops more and more towards a sinusoidal form, which cause a reduction in the relative intensity of the higher harmonics. Therefore the third harmonics go through a maximum in intensity just above the transition.

In figure 3.25 scans through $(\frac{1}{2}, 1, \frac{1}{2})$ at respectively 12.25 T and 13 T are shown (In both cases compared to the 0 T scan). At 12.25 T, the IC and the C peaks are seen to coexist, while at 13 T the C peak has completely disappeared. But the 13 T scan reveal third and even very weak fifth order harmonics.

The data were fitted to resolution limited Gaussian lineshapes with a relative intensity given by equation 3.60, with the overall amplitude, δk_{sp} and Γ as fitting parameters. The amplitude and δk_{sp} were completely determined by the first har-

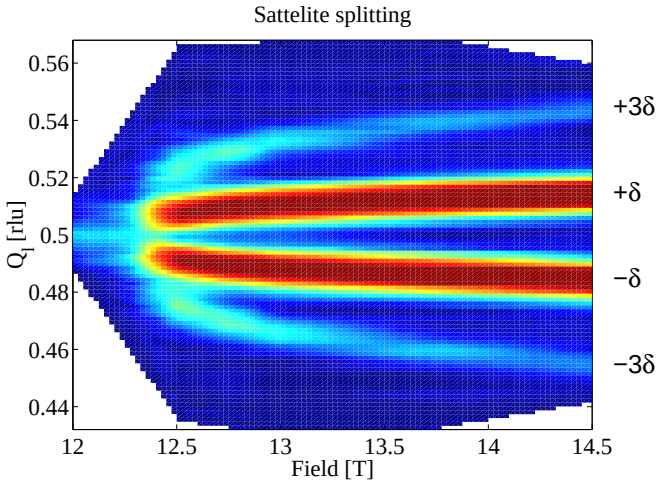

Figure 3.24. Pseudo-color map of the $(\frac{1}{2},1,\frac{1}{2})$ *satellite reflection as a function of applied magnetic field. The weak nuclear peak below* H_c *is seen to split by* δk_{sp} *into the two strong reflections* $(\frac{1}{2},1,\frac{1}{2}\pm\delta k_{sp})$*. The third harmonics* $(\frac{1}{2},1,\frac{1}{2}\pm 3\delta k_{sp})$ *are seen to undergo a maximum just above the transition and then decay due to the gradually more sinusoidal soliton shape.*

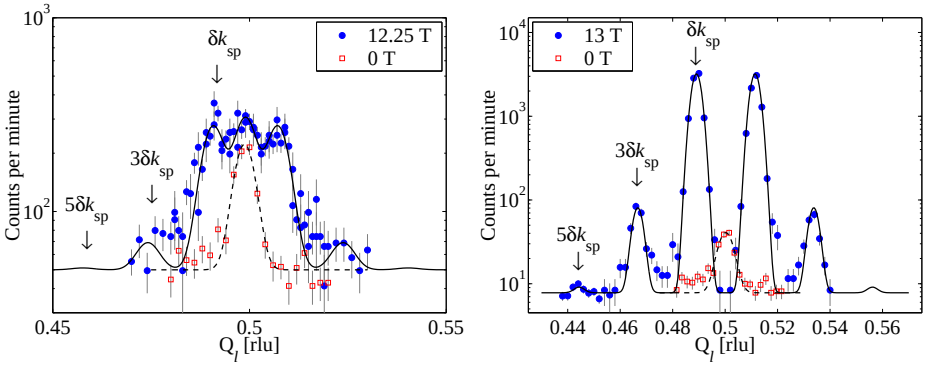

Figure 3.25. Scan along c^* *through the* $(\frac{1}{2},1,\frac{1}{2})$ *satellite reflection at respectively 12.25 T (left) and 13 T (right). At both fields, the zero field scan is shown for comparison. The peaks were fitted to resolution limited Gaussian line shapes with the relative intensity given by equation 3.60. With the overall amplitude, the incommensurability* δk_{sp} *and the soliton width* Γ *as variable parameters, good fits were obtained as shown by the solid line.*

monics, while Γ is determined by the relative intensity of the third harmonics. The fifth harmonics have no influence on the fits, but the fact that their amplitudes are correctly reproduced validates the Jacobian elliptic soliton shape. In principle, any line-shape with a Γ like parameterization could reproduce the first and third harmonics, but in general not the fifth.

The result for Γ as a function of the field is shown in figure 3.26, where it is compared to the result from earlier X-ray measurements (Harris *et al.*, 1994, Kiryukhin *et al.*, 1996a,b) and to DMRG calculations (Uhrig *et al.*, 1999a) as discussed below. The X-ray data were originally analysed by fitting the ratios I_3/I_1 to one constant value $\Gamma/c = 13.6\pm0.3$. The data in figure 3.26 were obtained by digitizing the data for I_3/I_1 and δk_{sp} in reference (Kiryukhin *et al.*, 1996b).

The apparent discrepancy between the neutron and the X-ray data can be understood by realizing that while the neutron result measures the magnetic soliton

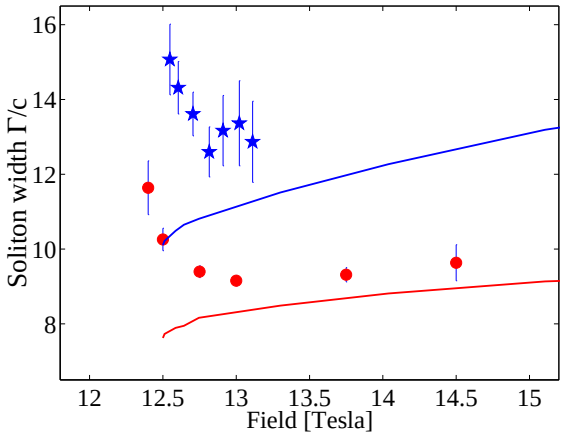

Figure 3.26. Respectively the magnetic and distortive soliton width as extracted from the neutron (circles) and X-ray (start) measurements. The result of DMRG calculations shown with the solid lines was digitized from reference (Uhrig et al.*, 1999a) and converte from m to H using $1/m = \frac{2v_s}{\Delta_0} \ln \frac{8H_c}{H-H_c}$.*

width, X-rays probe the distortive soliton width. It has been predicted theoretically (Zang *et al.*, 1997, Uhrig *et al.*, 1999a) that such a difference is possible when detailed interactions in $CuGeO_3$ are taken into account.

Both widths exhibit the same field dependence with a rapid decrease just above H_c. Thanks to the wider field range in the present data, it is possible to see a slow increase at fields above 13 T, which can be described by $\Gamma/c = 0.26 \pm 0.11 + (5.74 \pm 1.46)H/[\mathrm{T}]$.

Apart from the rapid decrease just above H, both widths are in quite good agreement with the DMRG calculations of Uhrig *et al.* (1999a) shown by the solid line in figure 3.26. These calculations used $\Delta_0/v_s = 0.157$, while the present $\delta k_{sp}(H)$ data lead to 0.130 ± 0.002. As $\Gamma \sim v_s/\Delta_0$, the DMRG calculations under estimates Γ, and can most likely be brought to complete agreement above 13 T by using $\Delta_0/v_s = 0.13$.

The behaviour just above H_c must be related to the coexistence of the C and IC peaks, as described above. This coexistence was also seen in the X-ray experiment, which employed slightly better resolution. In neither experiments was any broadening of the peaks observed, which excludes a random distribution of the solitons. This behaviour is often seen in first order transitions, where domains of the old phase are gradually reduced in volume until the transition is complete. The extend of the coexistence is in good accord with the hysteresis observed in the magnetization curves.

Amplitudes of the magnetic soliton structure

Knowing the soliton shape as determined by δk_{sp} and Γ, the amplitudes m_s and m_u of the magnetic soliton structure can be determined. At 14.5 T, the high resolution V2 data give $\delta = 0.01494 \pm 0.00003$, $\Gamma = 9.75 \pm 0.35$, $k = 0.8313$, $K(k) = 2.0624$, $\kappa = 0.0729$ and $kK(k)/\pi \times (1+\kappa)/\sqrt{\kappa} = 2.17$.

The Fourier component of the magnetic moment is $\mu(q = \delta) = 0.098 \pm 0.003 \mu_B$ corresponding to a Fourier component of the magnetic structure of $m_s(q = \delta) = \frac{1}{g}\mu(q = \delta) = 0.045 \pm 0.002$, where $g = 2.19$ when the field is perpendicular to $(k/2, k, l)$ (Pilawa, 1997). The amplitude m_s of the magnetic structure is then given by $m_s = \frac{kK(k)}{\pi} \frac{1+\kappa}{\sqrt{\kappa}} m_s(q = \delta) = 0.097 \pm 0.004$.

This value is about 30% lower than the field theoretical prediction $m_s = \frac{1}{\sqrt{2\pi\Gamma}} =$

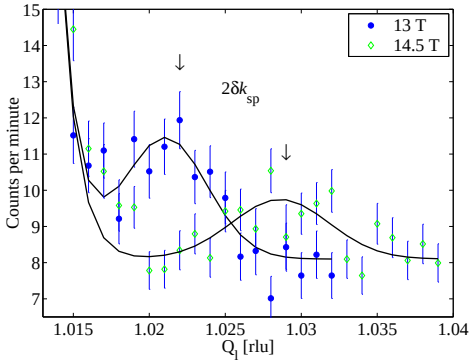

Figure 3.27. Scan along c through* $(0,0,1+2\delta k_{sp})$ *at respectively 13* T *and 14.5* T. *At the low-*Q_l *side, the strong nuclear (0,0,1) Bragg peak shoots up, but the amplitude of the second harmonics could still be accurately determined by the fits shown with the solid lines.*

$0.12 - 0.14$ depending on whether the value $\Gamma = v_s/\Delta_0 = 7.9$ or the measured value of 9.5 is used. This is in sharp contrast to the NMR measurements, which led to a value of $m_s = 0.026$ at 14.5 T. If the magnetic structure was affected by zero point motion of phasons, then also the neutron scattering experiment should find a reduced staggered moment. One possible explanation for this discrepancy would be if the phasons had a finite frequency fast compared to the NMR time scale ($\sim$170 MHz) but slow compared to that probed by the neutron scattering ($\sim 2 \times 10^4$ MHz). This will be further discussed in section 3.5.

In addition to the staggered component of the local magnetization, which has been described so far, theory also predicts a uniform component. Being uniform, it will be superimposed on the nuclear Brag peaks, and therefore impossible to observe directly. However, the main peak is accompanied by even harmonics, which can be detected with sufficiently tight resolution.

In figure 3.27, scans in the tail of the strong (0,0,1) nuclear Bragg peak reveal the second harmonics $(0,0,1+2\delta k_{sp})$ at both 13 T and 14.5 T. The structure factor was extracted by scaling to the $(\frac{1}{2},1,\frac{1}{2}\pm\delta k_{sp})$ reflections measured in the same configuration and correcting for the different resolution volumes as calculated by rescal. The corresponding Fourier components $\mu(0,0,1+2\delta)$ of the magnetic structure are $0.0062\pm0.0008\,\mu_B$ and $0.0047\pm0.0010\,\mu_B$ at respectively 13 T and 14.5 T. The amplitude of the uniform component is given by $m_{\rm u} = \frac{K(k)}{\pi}\frac{1+\kappa^2}{\kappa}\frac{\mu(q=2\delta k_{sp})}{g}$ which becomes respectively $m_u = 0.017 \pm 0.002$ and $m_u = 0.019 \pm 0.004$. The extracted values of m_u are again about 25% lower than those predicted by theory and those measured by NMR, but are roughly within a standard error from those. The self consistency of the entire description can be tested by calculating the incommensurability $\delta k_{sp} = \pi m_u/2K(k)$ from m_u. The values 0.0105 ± 0.0013 and 0.0145 ± 0.0032 are in good agreement with those measured directly as the splitting of $(\frac{1}{2},1,\frac{1}{2}\pm\delta k_{sp})$, giving 0.0112 and 0.0149 respectively.

Finally it should be noted that there is potentially a systematic error connected with the overall normalization from scattering intensities to structure factors, that could well explain the 30% disagreement between the extracted amplitudes and the field theory. But the ratio $m_s/m_u = 5.1\pm1.1$ does not depend on this normalization and compares well to the field theoretical prediction.

3.4.3 The magnetic soliton structure

In summary, the three neutron scattering experiments reported have provided a rather complete description of the magnetic soliton structure. The amplitudes m_s

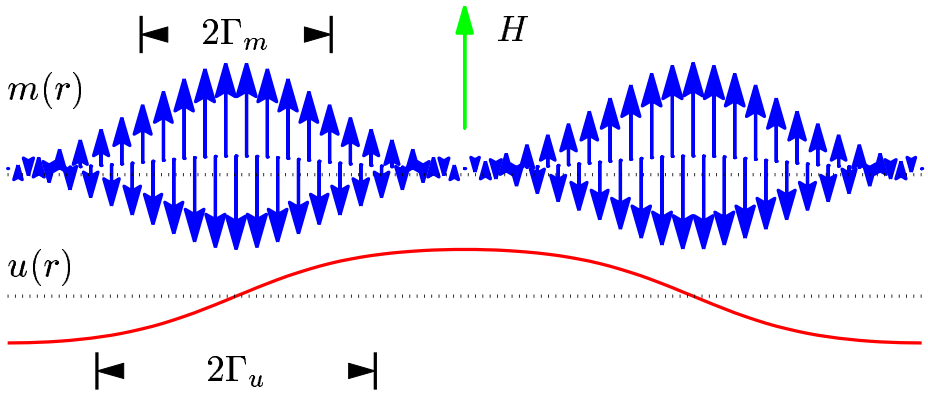

Figure 3.28. One period L of the soliton lattice showing the modulation of the magnetic moment $m(r)$ and the structural displacement $(-1)^r u(r)$, with widths Γ_m and Γ_u respectively. The length of the arrows illustrate the staggered part of $m(r)$, and the tails are displaced from the base-line by the small ferromagnetic part. The present soliton is drawn according to the parameters determined at 13 T.

and m_u of both the staggered and uniform parts and the incommensurability δk_{sp} are without any free parameters well described by the field theoretical predictions. Above 13 T, both the magnetic and distortive soliton widths are well described by the DMRG calculations of Uhrig *et al.* (1999a). Just above the transition, the C and IC peaks coexist and the soliton widths exhibit a rapid decrease with field, which remains to be explained theoretically. Nevertheless, it is fair to say that the magnetic soliton structure in $CuGeO_3$ has been solved and is depicted for 13 T in figure 3.28.

3.5 Dynamics of the high field phase

Having solved the soliton structure and found it to be well described by theory, it is interesting to see if a similar success can be reached for the dynamics in the soliton phase. The present section reports the results of inelastic neutron scattering measurements in the soliton phase. The theoretical expectations are much less settled in this case, which prevents a quantitative analysis of the findings. Instead, it is hoped that the experimental findings will stimulate a convergence of the theoretical description.

3.5.1 Previous experiments

Several experiments in the soliton phase have shown that the excitation spectrum is significantly changed in comparison to the spin–Peierls phase. But so far it has not been possible to interpret the experimental results to reach a general picture of the dynamics.

In addition to the acoustic phonon, there is another contribution to the specific heat in the IC phase, which has been ascribed to the phason mode. Gapped phasons would give rise to an exponential temperature dependence, and therefore the observed T^3 law (Lorenz *et al.*, 1998) in principle excludes gapped phasons. However, upon close inspection, the C/T v.s. T^2 curve does show a tiny hump at 0.3 meV, which could be due to a gapped phason.

Several optical spectroscopy experiments have probed the soliton-phase (Loa *et al.*, 1996, 1999, van Loosdrecht *et al.*, 1996a,b, van Loosdrecht, 1998, Nojiri *et al.*, 1998a,c). The soliton-assisted Raman-excitation peak at 17 cm^{-1} corresponding to 2.1 meV in the spin–Peierls phase (Loa *et al.*, 1996, Els *et al.*, 1998) is replaced by two close lying modes with energies matching $g\mu_B H + 0.29$ meV and $g\mu_B H + \delta k_{sp} \times 44.9$ meV (Loa *et al.*, 1999). Similarly, most of the low energy features observed in the spin–Peierls phase disappear above H_c, while new features appear. In particular, Loa *et al.* (1999) observed a peak at 2.7 cm^{-1} $\sim$0.4 meV, which could be the incommensurate phason. However, optical resonance processes often involves two or more quasi-particles, with no handles on their individual wave-vector, which turns the interpretation into a process of qualified guessing. This further motivates an inelastic neutron scattering study, where both the energy and the wave-vector of the excitations can be probed.

3.5.2 Identification of the excitations

The inelastic neutron scattering experiments were performed on the V2/FLEX triple axis spectrometer at HMI, Berlin. The collimation was achieved by the ^{58}Ni neutron guide and three 60' collimators. The PG(002) monochromator was set to vertical focusing, while the analyser was kept flat. Energy transfers were achieved by keeping the final energy $E_f = 3.5$ meV ($k_f = 1.3$ Å^{-1}) constant and varying the incident energy. Higher order neutrons were removed by a Be filter. For energy transfers below 1.5 meV ($E_i < 5$ meV) Be filter was placed before the sample, for higher energy transfers it was moved to after the sample.

Originally, the scattering plane $(0, k, l)$ was used to investigate the excitation spectrum around $(0, 1, \frac{1}{2})$ where the minimum gap Δ_0 occur in zero field. But with the discovery of the elastic magnetic signal at $(\frac{1}{2}, 1, \frac{1}{2})$, a new experiment was performed probing the $(h, 2h, l)$ plane.

Excitations around $(0, 1, \frac{1}{2})$

For this experiment, the twinned crystal number 1 was mounted with b^* and c^* in the scattering plane. (Just to explain, crystal number 2 was not available at the

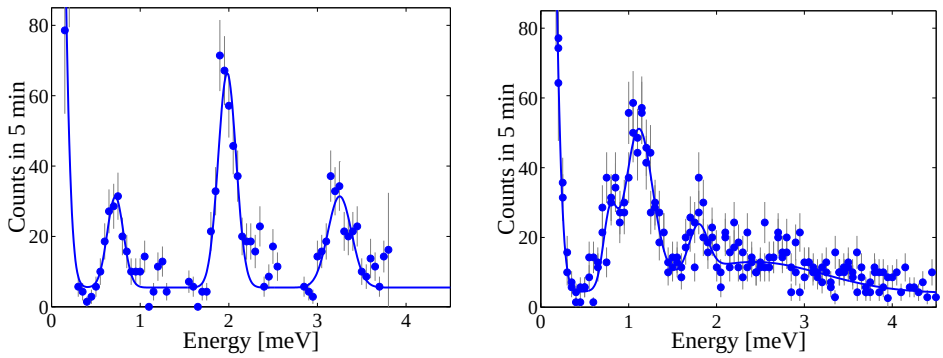

Figure 3.29. Energy scans with focused analyser at $(0, 1, \frac{1}{2})$ *for respectively 10* T *and 14.5* T.

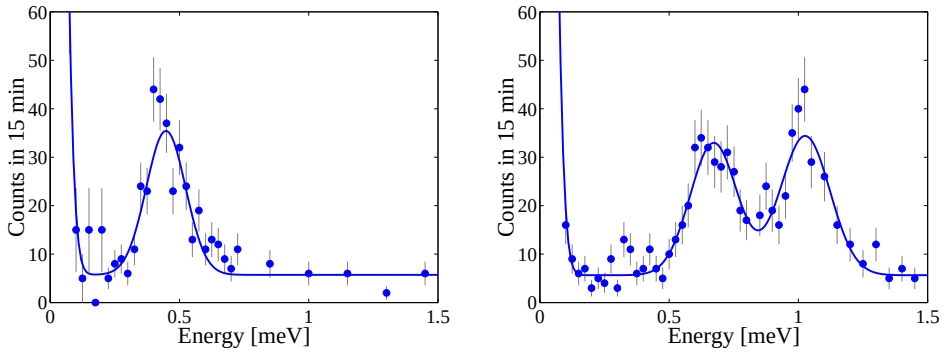

Figure 3.30. Energy scans with flat analyser at $(0, 1, \frac{1}{2})$ *for respectively 12* T *and 13* T.

time of this experiment.)

For the initial survey, a different configuration was used with the analyser set to horizontal focusing and the two corresponding 60' collimators removed. To make a connection to the existing work on the SP phase (Regnault *et al.*, 1996), a few scans were performed below H_c. Figure 3.29 shows energy scans at $(0, 1, \frac{1}{2})$ at 10 T and 14.5 T respectively. The former shows the three Zeeman split triplet modes at 2 meV and 2 ± 1.25 meV, while the latter displays a double peak around 1 meV and a broad feature at higher energies. The peak shapes with a sharp rise and a high energy tail is due to the resolution of the focusing analyser enhanced by the existence of a twin in the crystal.

Due to the twinning of the crystal, it is difficult to determine whether the broad feature above 1.6 meV in the 14.5 T scan is a real continuum, a damped remainder of the 2 meV triplet, or several weak peaks multiplied in in number by two due to the twin. Therefore focus was set on the sharp modes at lower energy which were investigated using the flat analyser configuration with two Be filters. A series of scans were taken as a function of applied field, of which two for 12 T and 13 T are shown in figure 3.30.

It is seen how the lower triplet mode at 12 T is replaced by two new modes at 13 T. A series of such scans were taken at fields from 8 T to 14.5 T, as summarized in figure 3.31a.

At 13 T the q-dependence was investigated by performing scans at $(0, 1, \frac{1}{2} + \Delta q)$. Care was taken in choosing the direction in which the second twin did not have any effect. The results are summarized in figure 3.31b. The intensity of both modes dies away on the scale of $\delta k_{sp} = 0.01$. There appears to be no or very little dispersion

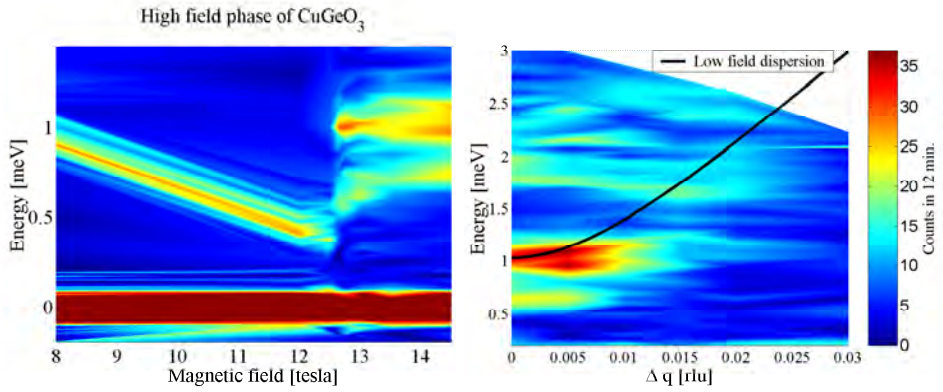

Figure 3.31. Pseudo color summary of the energy scans taken at different magnetic fields at $(0, 1, \frac{1}{2})$ *and at 13* T *as a function of* $(0, 1, \frac{1}{2} + \delta q)$*. For comparison the dispersion found in the SP phase has been indicated by the solid black line.*

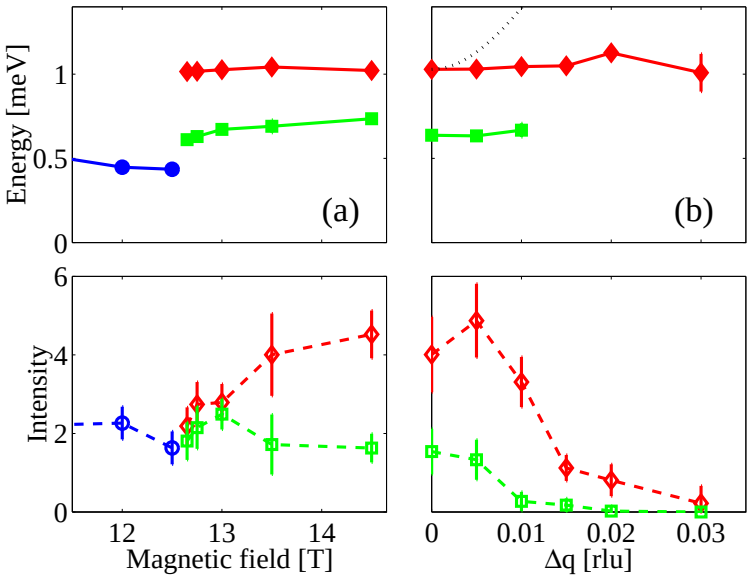

Figure 3.32. The position in energy and amplitude of the two modes for $q = (0, 1, \frac{1}{2})$ *as a function of field (left) and for* $q = (0, 1, \frac{1}{2} + \Delta q)$ *at 14.5* T.

of the modes.

From the raw data in figure 3.31, the position in energy and intensity of the modes was extracted and is depicted in figure 3.32. It is worth noticing that the lowest triplet mode does not become soft before the transition, and that it does not continuously evolve into the two new modes.

In the scans away from $(0, 1, \frac{1}{2})$, no sign of a soft incommensurate mode was observed. This search was of course limited to the window between the edge of the elastic background at 0.25 meV and the lower edge of the lowest commensurate mode at 0.5 meV.

Excitations around $(\frac{1}{2}, 1, \frac{1}{2})$

The discovery of magnetic satellite reflections at $(\frac{1}{2}, 1, \frac{1}{2} \pm \delta k_{sp})$ prompted for an investigation of the excitation spectrum around this point. These measurements were performed on the untwinned crystal number 2. In zero field, the triplet excitation has the energy 2.8-2.9 meV at $(\frac{1}{2}, 1, \frac{1}{2})$ due to the weak ferromagnetic

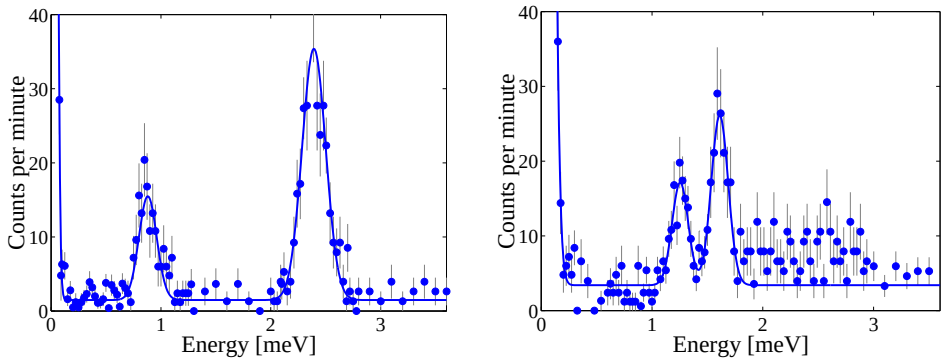

Figure 3.33. Energy scans at $(\frac{1}{2}, 1, \frac{1}{2})$ *for respectively 12* T *and 13* T.

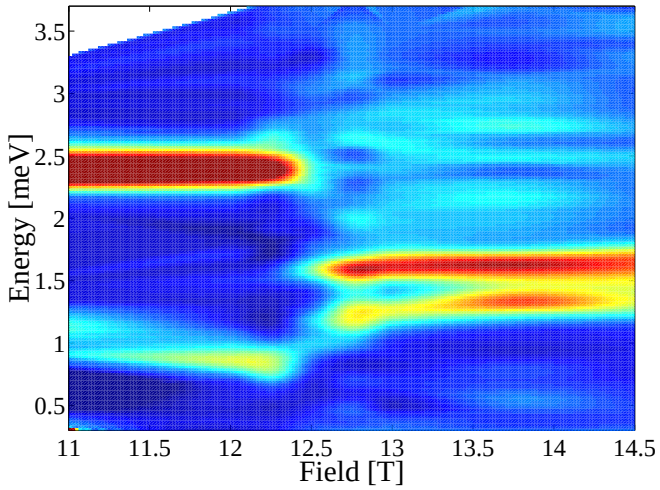

Figure 3.34. Pseudo color summary of the excitation spectrum at $(\frac{1}{2}, 1, \frac{1}{2})$.

coupling along a. As shown in figure 3.33, this remains qualitatively the same in an applied field, where the situation from $(0, 1, \frac{1}{2})$ is repeated, but at slightly higher energies. At H_c, the triplet modes disappear and two new modes evolve.

However, as evident from the 12 T scan, the energies of the Zeeman modes have softened by 0.4 meV. The middle mode, which should remain constant decreased by about 0.4 meV to 2.39 ± 0.01 meV. The lower mode decreased by 2 meV to 0.88 ± 0.01 meV, which corresponds to the Zeeman energy 1.6 meV plus additional 0.4 meV.

The evolution as a function of field is summarized in figures 3.34 and 3.35. What could have looked like a continuum in the investigation around $(0, 1, \frac{1}{2})$ looks in this untwinned crystal rather to be a broad remainder of the triplet modes.

Recalling the expectation in figure 3.4 from considering the fermion bands above H_c, the commensurate modes observed can be identified with the two transverse modes $\Delta_\pm$. These modes have also been deduced from numerical calculations, which have unfortunately only been performed for a few parameter choices that are not applicable to our experiment. Therefore a qualitative analysis must await the theoretical development.

From the fermion mode, also an incommensurate mode $\Delta_0 > \frac{1}{2}(\Delta_+ + \Delta_-)$ is expected, but no evidence for such a mode was found in the experiments. It is possible that the apparently weak dispersion of the Δ_+ mode is in fact due to

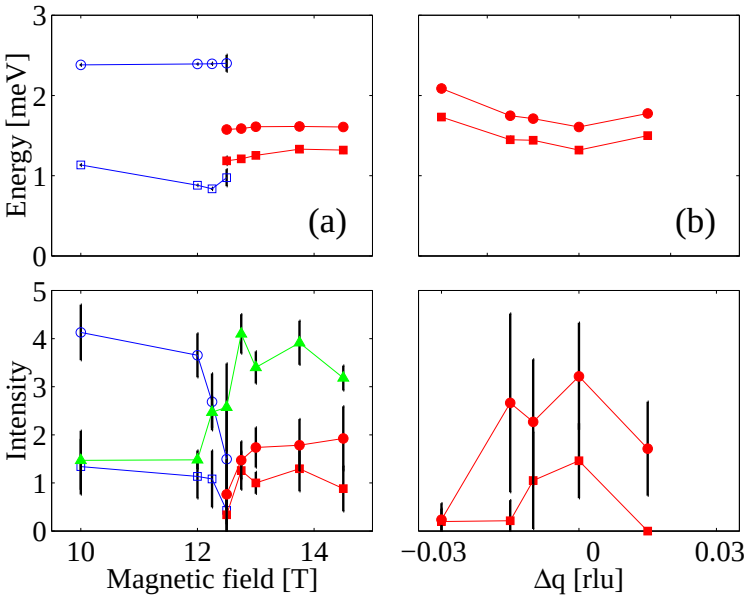

Figure 3.35. The position in energy and amplitude of the two modes for $q = (\frac{1}{2}, 1, \frac{1}{2})$ *as a function of field (left) and for* $q = (\frac{1}{2}, 1, \frac{1}{2} + \Delta q)$ *at 14.5 T. The data result from Gaussian fits with a constant background, which rose significantly above the transition as illustrated by the green triangles.*

incommensurate modes at $\frac{1}{2} \pm \delta k_{sp}$ with $\Delta_0 \sim \Delta_+$. If so, the longitudinal mode must have a lower amplitude than the transverse. An explanation for this could be that interchain interactions provide a mechanism for longitudinal excitations to decay into transverse fluctuations.

The phason mode

In addition to the magnetic excitations $\Delta_\pm$ and Δ_0, an incommensurate soft mode related to the phase of the modulation has been anticipated. The search for this mode was complicated by the inevitable fact that the condition for focusing of an acoustic excitation is at the same time the condition for picking up the resolution tail from an elastic Bragg peak. In figure 3.36, energy scans around $(\frac{1}{2}, 1, \frac{1}{2})$ are shown. The Bragg tails of the two satellite reflections $(\frac{1}{2}, 1, \frac{1}{2} \pm \delta k_{sp})$ are indicated by dashed lines, and it is seen how they disturb the low Q_l side of the data. This situation is worsened by an anomalous scattering effect due to inelastic scattering from the pyrolytic graphite monochromator and analyser (See Currat and Axe, 1978).

But on the high Q_l side there are no such spurion effects and a mode is clearly observed. It is seen to have a minimum in energy of 0.26 meV and a maximum in intensity at the incommensurate position $(\frac{1}{2}, 1, \frac{1}{2} + \delta k_{sp})$. At the commensurate position, the intensity has completely vanished.

This mode is interpreted as a gapped phason. As mentioned in section 3.4, a soft phason would cause zero point fluctuations, lowering the staggered soliton amplitude, m_s, from the value predicted by field theory, which does not take phasons into account. But since the neutron scattering determination of m_s is in good accord with field theory, this indirectly suggests that any phasons must be gapped. Thus elastic and inelastic neutron scattering leads to a consistent picture.

To reconcile this with the reduced staggered moment observed in NMR measurements, it must be realised that NMR is much slower probe than neutron scattering. It averages the spin configuration over time scales given by the NMR

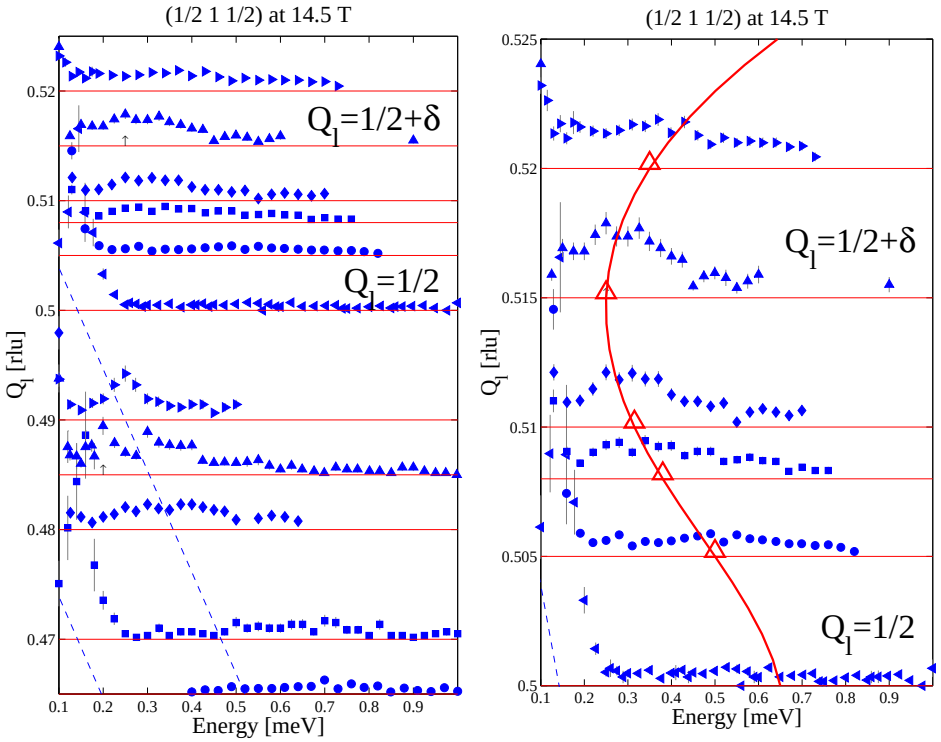

Figure 3.36. High resolution scans of the low-energy incommensurate mode. Left: At the low Q_l side, the resolution tails from the $(\frac{1}{2}, 1, \frac{1}{2} \pm \delta k_{sp})$ is indicated by the dashed lines. Right: The undisturbed high Q_l side reveals an incommensurate mode. The solid line and the open triangles are guides to the eye.

frequency $\sim$ 170 MHz. Therefore thermally excited phasons with frequencies $\sim$ 0.2 meV$\sim 5 \times 10^4$ MHz will affect the NMR signal but not the neutron scattering results. Most NMR measurements were performed at $T = 4$ K, where the observed mode at 0.26 meV$\sim$3 K would be considerably populated. At 1.3 K, the NMR line width and hence the deferred m_s was in fact seen to increase, albeit only with 5% (Horvatić *et al.*, 1999).

The reason that the phason is gapped is that the translational symmetry of the solitons is discrete and not continuous, as required for a Goldstone mode. This will be the case, if the is a small tendency towards pinning of the solitons relative to the lattice cites, which could also explain the hysteresis effects observed in the soliton phase.

3.5.3 Summary and outlook

In summary, the inelastic neutron scattering experiments in the soliton phase of $CuGeO_3$ have shown two commensurate modes around 1 meV and a low energy incommensurate mode around 0.26 meV. The commensurate modes have been identified with the transverse excitations expected from the fermion model for the spin dynamics. The IC mode is believed to be a phason, and the observation that it is gapped solves the apparent discrepancy for m_s in neutron and NMR measurements.

Though qualitatively understood, these findings call for a qualitative theoretical treatment of the excitations in the soliton phase. Experimentally, further characterization of the excitation has been planned and in particular a search for the longitudinal modes will be conducted.

Naturally, the excitations in a spin–Peierls system must be hybridizations of both spin and lattice fluctuations, and the next major task will be to identify and understand this hybridization. A useful method for separating the magnetic and nuclear neutron scattering is through polarization analysis. To date it is not practically feasible to perform polarization analysis in fields above 12.5 T, but when eventually new equipment is developed, a very interesting experiment will be to separate the components involved in the phason mode.

Chapter 4

$Cu(DCO_2)_2 \cdot 4D_2O$ — a 2D $S = \frac{1}{2}$ Heisenberg antiferromagnet

Correlations and fluctuations at finite temperature

This chapter describes experiments on $Cu(DCOO)_2 \cdot 4D_2O$, that aimed to investigate the properties of the 2D $S = 1/2$ Heisenberg antiferromagnet on a square lattice. The ($T = 0$) ground state exhibits long ranged Néel type order with spin-waves as the elementary excitations. At finite temperatures the system is characterized by an exponential decay of the correlation length with a concomitant damping of the fluctuations. Remarkably, the behaviour of this quantum ($S = 1/2$) system is well described by the classical model with the parameters renormalized due to quantum fluctuations.

The previous paragraph dealt with the description of a coherent (ordered) quantum ground state and the identification of the elementary excitations hereof. This paragraph focuses on the correlations and fluctuations that exist in a system that lacks long range order, namely the 2D Heisenberg antiferromagnet (HAF) at finite temperatures, as defined by the Hamiltonian

$$\mathcal{H} = \tfrac{1}{2} J \sum_{ij} \boldsymbol{S}_i \cdot \boldsymbol{S}_j \ . \tag{4.1}$$

In the study of critical properties such as correlations and fluctuations, 2D systems play a particular role on the borderline between order and disorder. In 3D, both the Ising, XY and Heisenberg antiferromagnet will obtain long ranged order at a finite temperature. On the other side, there can be no finite T phase transition in 1D. The 2D Ising system does have a finite transition temperature as found by Onsager's solution (Onsager, 1942). Mermin and Wagner (1966) showed that there can be no long range order at finite temperatures in the 2D Heisenberg and XY models. But for the later, Stanley and Kaplan (1966), Stanley (1968a,b), Berezinskii (1971, 1972), Berezinskii and Blank (1973), Kosterlitz and Thoules (1973) and Kosterlitz (1974) showed the occurrence of so-called topological order below a finite temperature T_{KT} called the Kosterlitz–Thouless temperature.

In addition to the long-standing interest from this location on the borderline between disordered 1D systems and ordered 3D systems, the 2D $S = 1/2$ HAF on a square lattice (2DQHAFSL) has attained particular attention, due to its relation to the high-T_c cuprate superconductors. The common feature of these materials are CuO_2 planes, where the Cu ions are arranged in square lattices connected by

oxygen ions. By non-stochiometric doping into the remaining crystal structure, the carrier concentration can be optimized to achieve superconductivity. In the undoped materials, the CuO_2 planes form 2D $S = 1/2$ Heisenberg antiferromagnets on square lattices (Vaknin *et al.*, 1987).

Several of the high-T_c materials such as $YBa_2Cu_3O_6$ and $Bi_2Sr_2CaCu_2O_8$ are in fact constituted of double layers of CuO_2 with a non-negligible coupling between the two layers. The effect hereof should eventually be addressed but so far, much attention has been devoted to the single layer materials La_2CuO_4 and $Sr_2CuCl_2O_2$.

The cuprates are characterized by very strong nearest neighbor coupling ($J \sim$ 1500 K) in the plane, which complicates studies of their properties on a comparable temperature scale. In addition, there is the specific limitation to neutron scattering studies that the wave-length and energy relation (4 Å$\sim$ 5 meV) of the neutrons are not well matched to the relevant scales in the cuprates ($a \sim 6$ Å, $J \sim 130$ meV).

Therefore, even if the motivation is to understand the cuprates, it is useful to extend the experimental efforts to other physical realizations of the 2DQHAFSL. Materials such as $KBa_2Cu(NO_2)_6$ and $Cu(DCO_2)_2 \cdot 4D_2O$ (CFTD) were known to be 2DQHAFSL well before the advent of high-T_c superconductivity, and deserve a reinvestigation with the developments and questions based on the cuprates. While $KBa_2Cu(NO_2)_6$ tends to grow in thin needle shaped crystals, it is fairly easy to grow large ($\sim cm^3$) single crystals of CFTD. This section describes neutron scattering studies of the properties of CFTD as a physical realization of a 2DQHAFSL. After a characterization of CFTD, the behaviour is presented in three sections covering respectively the zero temperature properties, the correlations at finite temperature and the dynamics at finite temperature.

4.1 Characterization of $Cu(DCO_2)_2 \cdot 4D_2O$

As the goal is not to understand $Cu(HCO_2)_2 \cdot 4H_2O$ (CFTH), but to gain experimental results concerning the 2DQHAFSL, it is important first to establish the extend to which CFTH represents the ideal model system. This section summarizes the knowledge of CFTH and the deuterated form $Cu(DCO_2)_2 \cdot 4D_2O$ (CFTD).

Deuteration for neutron and proton-NMR experiments

In neutron scattering studies, the existence of hydrogen in the samples is problematic due to the large incoherent scattering cross-section of hydrogen. This will give rise to a q independent elastic signal that in particular disturbs quasi-elastic studies such as those reported in section 4.3. Therefore, it is common practice to deuterate organic materials when performing neutron scattering studies.

Another reason for deuterating is found in proton NMR studies. By deuterating all but one crystallographic type of hydrogen in the material, the NMR signal can be related to only those positions in the crystal structure.

Deuteration seldom changes the overall crystal structure and therefore does not affect the magnetic properties qualitatively. There are however small changes in lattice and magnetic behaviour associated with deuteration, and the characterization and determination of the relevant parameters should be performed on the deuterated version of the system whenever possible. There are examples where deuteration has led to relevant changes in the magnetic Hamiltonian, as in the $S = 1$ chain material NENP, where the orthorombic anisotropy changes sign upon deuteration (Enderle *et al.*, 2000).

The preparation of deuterated CFTH (CFTD) is straight forward, but require skills and patience. Formic acid and water are commercially available in respectively 97% and 99.9% deuterated form. The crystal growth should then be performed without contact to the atmosphere, as this will cause substitution of H_2O and D_2O. It is estimated that the final samples are 97% deuterated, although this has not been checked. One method for measuring the degree of deuteration is by ion-irradiation (Broholm, 1999).

4.1.1 Crystallographic properties

The crystal structure of CFTH has been studied with X-ray (Kiriyama *et al.*, 1954) and neutron (Okada *et al.*, 1966, Kay, 1975) diffraction. While X-ray scattering provides good resolution for determining the lattice parameters and the positions of heavy atoms, the structure factors for neutron scattering are more sensitive to the hydrogen positions. The crystal structure is monoclinic with layers of copper formate in the ab-plane separated by layers of crystal bound water. At room temperature, the space group symmetry $P2_1/a$ and the lattice parameters are $a = 8.15$ Å, $b = 8.18$ Å and $c = 6.35$ Å with the non-orthogonal angle $\beta = 101.1°$.

At 236.1 K there is a para-electric to antiferroelectric phase transition, at which the water molecules order. The ordering of the water-molecules removes the center of symmetry and the unit cell is doubled along c, with a new space group symmetry $P2_1/n$ (Kiriyama *et al.*, 1954). The association of the phase transition with the ordering of the water molecules was confirmed by dielectric absorption (Kiriyama, 1962a, Okada and Sugie, 1968), NMR (Kiriyama, 1962b, Soda and Chiba, 1969) and Raman (Berger, 1975) studies. Also, the shift of the transition temperature: 236.1 K, 245.6 K and 246.1 K for respectively $Cu(HCOO)_2{\cdot}4H_2O$, $Cu(HCOO)_2{\cdot}4D_2O$ and $Cu(DCOO)_2{\cdot}4D_2O$ illustrates the role of the water molecules.

In the deuterated form, CFTD, the same structures and space group symmetries are found. The lattice parameters are $a = 8.184$ Å, $b = 8.137$ Å, $c = 6.323$ Å and

$\beta = 100.79°$ at 296 K and $a = 8.113$ Å, $b = 8.119$ Å, $c = 12.45$ Å and $\beta = 100.79°$ at 120 K.

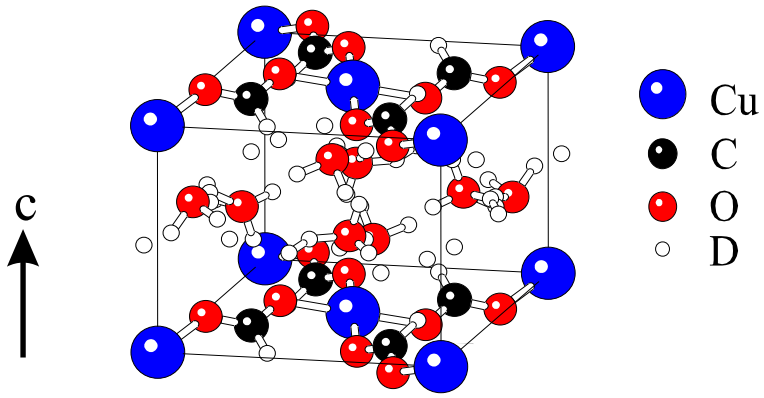

Figure 4.1. The crystal structure of CFTD with face-centered square ab-layers of copper formate separated by crystal bound water.

The crystal structure with the atomic positions is shown in figure 4.1. It can be described as face centered *ab*-planes of copper formate separated by the water molecules. The Cu^{2+} ions are coordinated by four formate-oxygen and two water-oxygen, giving an octahedron which is about 20% elongated along the Cu^{2+}–D_2O directions. The corresponding g-tensor is 2.4 along the Cu^{2+}–D_2O direction and 2.1 in the plane, with an average of 2.2. The two inequivalent Cu sites in the *ab* plane give a staggering of the g-tensor.

In both CFTH and CFTD, the *ab* plane is almost square, within 0.4% and 0.07% respectively. In the following, this difference will be neglected, and the basal plane treated as being square. In particular, as the Cu ions are placed in a face centered way, there is only one nearest neighbour distance $d = \frac{1}{2}\sqrt{a^2 + b^2} = 5.74$ Å. The monoclinic angle β means that adjacent *ab*-squares are shifted along the a direction. As this thesis deals with the 2D phase, where correlations between the planes can be neglected, the shift is irrelevant.

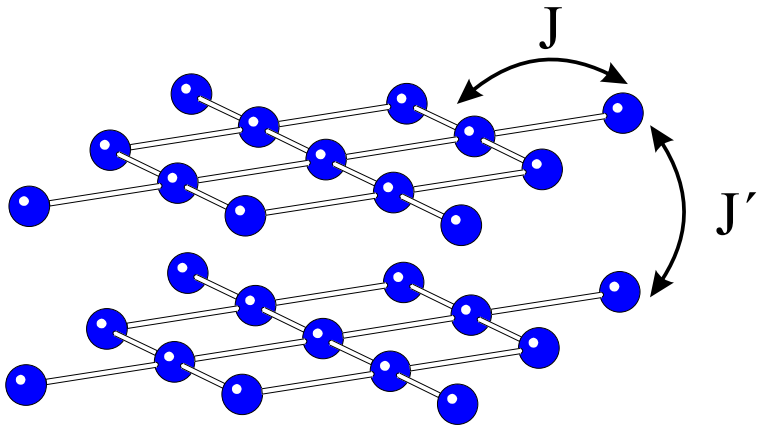

Figure 4.2. The magnetic lattice in CFTD with face-centered square ab-layers of copper spin 1/2 coupled within the plane through J and between the planes only through the weak interlayer coupling J'

The magnetic unit cell is spanned by the nearest neighbour vectors $\boldsymbol{x} = \frac{1}{2d}(\boldsymbol{a} - \boldsymbol{b})$ and $\boldsymbol{y} = \frac{1}{2d}(\boldsymbol{a} + \boldsymbol{b})$, defined in units of the nearest neighbour distance $d = 5.74$ Å. In reciprocal space, the 2D magnetic system is independent of the component

along $\boldsymbol{c}^*$ (perpendicular to the planes). For instance, the crystallographic lines $(1,0,l)$ and $(0,1,l)$ correspond to respectively $(\pi,-\pi)$ and (π,π).

From the crystal structure, it is natural to expect weak magnetic coupling between the copper formate planes. Provided a path for interactions within the planes, the system can be expected to be quasi two dimensional. The in-plane super-exchange between the Cu^{2+} ions is mediated by the formate ions, whose π-type orbitals are not localized at any part of the ion. If a π-electron is transferred to a Cu^{2+} ion, the orientation of the magnetic moment of the latter is transferred to the formate ion and can thus be transferred further to the neighbouring Cu^{2+} ion.

4.1.2 Magnetic properties

The 2D antiferromagnetic nature of CFTH was first realised through susceptibility measurements (Martin and Waterman, 1959, Flippen and Friedberg, 1963, Kobayashi and Haseda, 1963, Seehra, 1968, 1969). The measurements display both a 3D antiferromagnetic transition at $T_{\mathrm{N}} = 16.5$ K and a broad maximum around 65 K. Down to about 35 K, the susceptibility, including the 65 K maximum, is well described by the high-temperature series expansion for a 2D square lattice $S = 1/2$ Heisenberg antiferromagnet by Rushbrooke and Wood (1958):

$$\frac{Ng^2\mu_B^2}{\chi J} = 4t(1 + \frac{1}{t} + \frac{1}{2t^2} + \frac{1}{6t^3} + \frac{0.0156}{t^4} - \frac{0.0151}{t^5} + \frac{0.00002}{t^6} + \cdots) \ , \tag{4.2}$$

where $t = T/J$. From the position $T_{\max} = 0.91 \times J$ of the maximum, the coupling parameter J was found to be 71.5 ± 3.0 K.

The ordered phase below T_{N} has been studied with proton NMR on the partially deuterated material $Cu(HCOO)_2{\cdot}4D_2O$ such that only the hydrogen in the formate groups was probed (van der Leeden *et al.*, 1967, Dupas and Renard, 1970). An antiferromagnetic structure with a zero temperature staggered moment of only $0.53 \times S$ was derived. With a critical exponent of $\beta = 0.32 \pm 0.02$, the magnetization curve $m(T) \propto (T_{\mathrm{N}} - T)^{\beta}$ deviated from the mean field Brillouin function (Dupas and Renard, 1970). The low temperature part of $m(T)$ could be described by a Green's function calculation (Lines, 1969, 1970) introducing an uniaxial anisotropy $D = g\mu_B H_A/xJS = 4 \times 10^{-3}$, but as this method fails for higher T, it should not be used to determine the anisotropy of the system.

The magnetic structure was determined through neutron scattering by Burger *et al.* (1980). This study confirmed the zero-point reduction of the staggered moment being $(0.48 \pm 0.02) \times \mu_B$ per copper ion. The moments are aligned antiferromagnetically in the *ac* plane in a four sublattice structure that allows weak canting along *b* without giving a net magnetization, which was excluded by a polarized neutron scattering experiment. The ordering direction was found to be 8° from the *a* axis, away from the *c*-axis.

Electron spin resonance measurements have been used to estimate the magnetic Hamiltonian, including anisotropic perturbations (Seehra and Castner Jr., 1970). For this study, the spin-direction was found to be 8.5° from *a* towards the *c* direction. Without further investigations, it can only be concluded that the spins align in the *ac* plane, close to the *a* direction. The position of the ESR modes as a function of strength and direction of the applied field, was analysed in a model with exchange anisotropy and a symmetric *g*-tensor. The exchange anisotropy parameters were estimated to be 1-8$\times 10^{-4} \times J$ and 0.01-0.03$\times J$ for respectively the symmetric exchange anisotropy and an asymmetric Dzyaloshinskii–Moriya (DM) type interaction $\boldsymbol{D} \cdot (\boldsymbol{S}_i \times \boldsymbol{S}_j)$, which is allowed due to the low crystal symmetry. The DM vector was found to point mainly along the spin-direction.

The analysis was however based on a two-sublattice model rather than the four sublattice model found by neutron scattering.

Yamagata and Sakai (1980) and Yamagata *et al.* (1981) have analysed bulk magnetization curves using the four sublattice model. They consistently reach a DM interaction of strength $0.013 \times J$, but with a direction closer to c than to a. The symmetric exchange anisotropy was estimated to be $3\text{-}5\times10^{-5} \times J$, slightly lower than from ESR, but roughly consistent. Because of the four sublattices, it was possible also to estimate the inter-layer coupling to be $3 \times 10^{-5} \times J$.

One much used method for determining the exchange parameters in magnetic materials is by measuring and subsequently modeling the excitation spectrum. This procedure has led to the determination of the main exchange parameter $J = 73.2 \pm 0.2$ K in good agreement with the result from the paramagnetic susceptibility. Measurements of the spin-wave dispersion is described in section 4.2.2.

Effects of an applied field

To lowest order in the spin-wave expansion, the application of a magnetic field has the same effect as an easy-plane exchange anisotropy. A 2D system with such an anisotropy will develop a Kosterlitz–Thouless transition, at which the correlation length diverges. As an effect, the transition temperature will be pushed to higher temperatures. It is believed that future studies will bring interesting insight into the effect of this suppression on the correlations and fluctuations above T_{N}.

In a preliminary neutron scattering study, the intensity of the antiferromagnetic Bragg peak at (1,0,0) was studied as a function of temperature for different fields. In zero field, the transition to long range order at $T_{\mathrm{N}} = 16.5$ K is seen as a sharp onset of the peak. In applied fields, this onset is smeared out but also shifted towards higher temperatures. The extracted transition temperatures in fields up to 8 T are shown in figure 4.3.

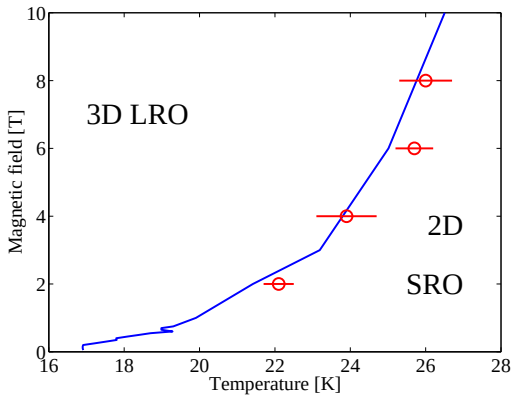

Figure 4.3. T_N as a function of applied field perpendicular to the 2D planes. The red points are extracted from neutron scattering measurements of the magnetic (1,0,0) reflection. The blue line is extracted from magnetization measurements as described below.

4.1.3 Magnetization study

This section reports the results from a magnetization study of CFTD. The measurements were performed with the help of Charles Dewhurst, using an Oxford Instrument MagLab vibrating sample magnetometer (VSM) at the University of Warwick. It was the purpose to measure the field dependence of the transition

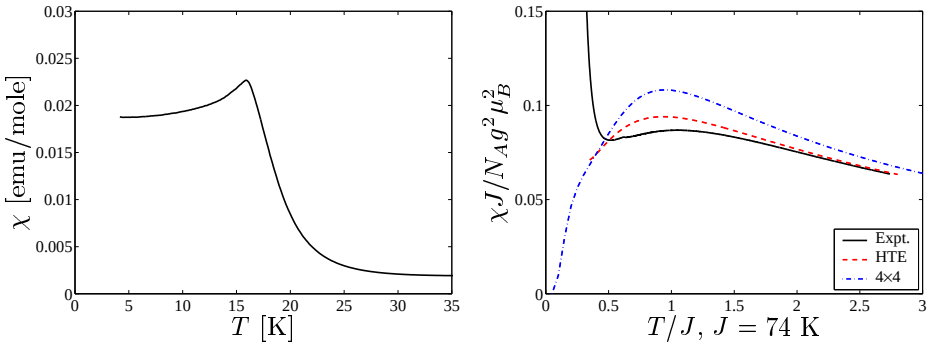

Figure 4.4. Temperature dependence of the susceptibility $\chi(T) \simeq m(T)/H$ in a field of 0.2 T *applied along the c^* direction of a 61.8* mg *sample of CFTD. The left panel shows the 3D transition to antiferromagnetic order at $T_N = 16.65$* K*. The right panel shows the broad peak above T_N, scaled to a coupling parameter $J = 73$* K*. It is compared to the results based on high-temperature expansion (Rushbrooke and Wood, 1958) and exact diagonalization of a 4×4 system (Lefmann* et al.*, 2000).*

temperature as well as supply a broad set of data both above and below T_N that can test the theoretical understanding of the system. The data have not yet been fully analysed, but are included for the case that subsequent studies of CFTD could benefit hereof.

An interesting observation was that if the samples were allowed to dehydrate (becoming pale blue), they gave rise to a ferromagnetic signal below 30 K. To avoid this, a 61.8 mg sample was fixed to the VSM sample stick by tight wrapping with PTFE tape.

The magnetization was measured both in temperature sweeps at a constant field and in field sweeps at constant temperatures. The field was applied along the $\boldsymbol{a}$, $\boldsymbol{b}$, $\boldsymbol{c}^*$ and $\boldsymbol{a} + \boldsymbol{b}$ directions. Except for well below T_N, all field directions gave similar results, reflecting that CFTD is close to being an isotropic Heisenberg antiferromagnet. In this brief summary only the results with the field along $\boldsymbol{c}^*$ are presented.

In a reasonably low field, the susceptibility can be approximated by $\chi \simeq m/H$. In figure 4.4 the temperature dependence of the magnetization, $m(T)$ in a field of 0.2 T is shown up to 200 K. The broad maximum due to short range 2D correlations as well as the sharp peak at T_N is seen. The low temperature part

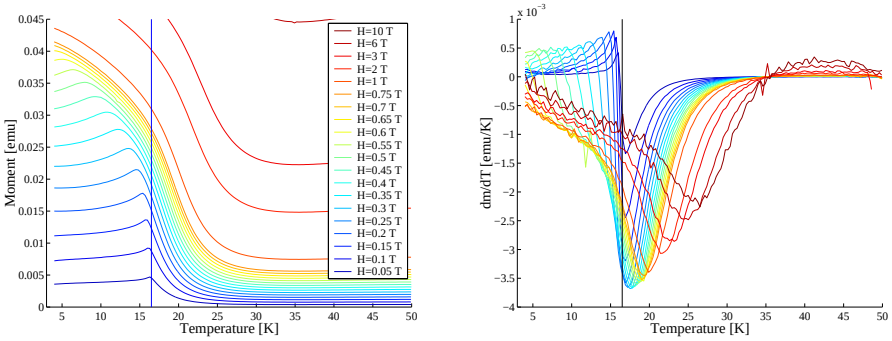

Figure 4.5. Temperature dependence of the magnetization (left), $m(T)$ and of $dm(T)/dT$ (right) at fields varying from 0.05 T to 10 T. The field was applied along the c^* direction of a 61.8 mg sample of CFTD.

of $m(T)$ and of $dm(T)/dT$ is shown for a series of fields between 0.05 T and

10 T in figure 4.5. In zero field the susceptibility displays a kink at the critical temperature $T_{\rm N}$, corresponding to a discontinuity in the derivative dm/dT. Upon increasing field, this sharp signature is smeared, but as seen in the left panel of 4.5 there is still a rounded kink that shifts towards $T = 0$. This feature corresponds to the maximum in $dm(T)/dT$, which in the right panel is seen to move towards $T = 0$ until 0.7 T where the maximum disappears.

However, the minimum in dm/dT, which for the smallest field almost coincides with the maximum, is seen to move towards higher temperatures. In figure 4.3 the location of the minimum is plotted as a function of field. It is seen to exactly correspond to the temperature where magnetic Bragg peaks developed in a neutron scattering study. It must therefore be concluded that the minimum in $dm(T)/dT$ gives T_N, while the maximum must correspond to a rearrangement of the weakly ordered moments. To understand this behaviour is a theoretical challenge requiring a theoretical treatment of the coupling between strongly fluctuating planes. The work of Berezinskii (1971, 1972) and Berezinskii and Blank (1973) can probably serve as a point of departure.

Recently, there has been some interest in the behaviour of the magnetization versus field in the 2DQHAFSL at zero or very low temperatures (See *e. g.* Zhitomirsky and Nikuni, 1998). Though these studies are mostly concerned with effects close to the saturation field $H_{\rm sat} = 8J/g\mu_B \sim 440$ T, the experimental results that extend only to 10 T are summarized in figure 4.6. For temperatures well above $T_{\rm N}$, the magnetization increases linearly with field. Below $T_{\rm N}$, dm/dH starts at a high slope corresponding to 0.12 emu/mole T, and then assumes the same linear dependence as for temperatures above $T_{\rm N}$. Further investigations of the magnetization

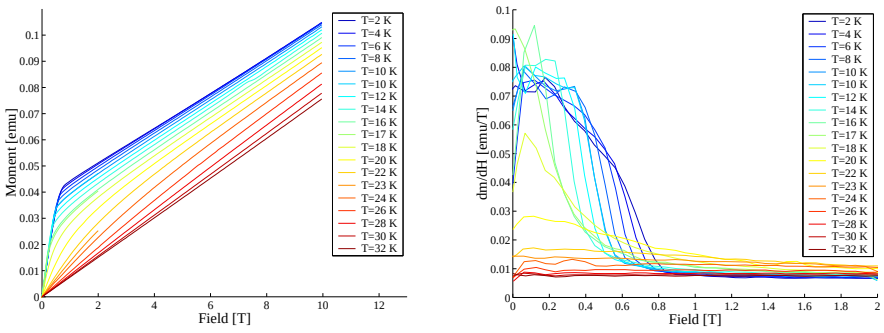

Figure 4.6. Field dependence of the magnetization (left), $m(H)$ and of $dm(H)/dH$ (right) at temperatures varying from 2 K *to 32* K*. The field was applied along the c^* direction of a 61.8* mg *sample of CFTD.*

curve will probably benefit from studies on systems with an even lower value of the coupling parameter J, for which the saturation field is actually feasible for experiments.

Summary and comparison with other 2DQHAFSL's

Possible candidates with lower values of J include materials like $K_2BaCu(NO_2)_6$ and $Nd_4CuPO_4{\cdot}D_2O$. Though they are currently only on the level where a thorough characterization of their ability to represent the model system is needed, these materials could in future complement the present results from CFTD.

As already mentioned, much of the revived interest in the 2DQHAFSL stems from the fact that this model to some extend describes the undoped parent compounds of the high-T_c cuprate superconductors. However, many of these systems have significant perturbations of the simple model. For instance, the compounds

$YBa_2Cu_3O_{6+x}$ and $Bi_2Sr_2CaCu_2O_{8+\delta}$ actually form double layers with considerable inter-double-layer coupling of the order $J/10$ (Andersen and Uimin, 1997). The two systems that most closely represent the 2DQHAFSL are La_2CuO_4 and $Sr_2CuCl_2O_2$, which have been studied to a large extent. From the point of view of understanding superconductivity, La_2CuO_2 has the advantage that it can be doped to continuously study the transition from an antiferromagnet to a superconductor. However, exactly this ability to develop carrier mobility signals that care should be taken when interpreting the undoped La_2CuO_4 as a completely localized spin model (See section 4.2.2).

In summary, CFTD can be considered a very good physical realization of the 2DQHAFSL, albeit with small perturbations. Most notably, the intraplane coupling J' causes 3D ordering at a finite transition temperature T_N. In table 4.1 the perturbative interactions in CFTD are compared to those in $Sr_2CuCl_2O_2$ and La_2CuO_4.

	CFTD	$Sr_2CuCl_2O_2$	La_2CuO_4
J [meV]	6.31 ± 0.02	125 ± 6	135
J_{anis}/J	$\sim 10^{-4}$	5×10^{-4}	6×10^{-4}
J_{DM}/J	~ 0.03	0	0.015
J'/J	$\sim 4 \times 10^{-5}$	$\sim 10^{-8}$	5×10^{-5}
J_{NNN}/J	$0.07 \pm 0.01^{\dagger}$	~ 0.08	$-0.10 \pm 0.04^{\dagger}$
T_N [K]	16.35	256 ± 6	325

Table 4.1. Comparison of the relevant magnetic coupling parameters for respectively CFTD, $Sr_2CuCl_2O_2$ (Keimer et al.*, 1992, Vaknin* et al.*, 1997) and La_2CuO_4 (Hayden* et al.*, 1991, Greven* et al.*, 1995, Birgeneau* et al.*, 1999, Coldea, 1999a). †Assuming that the zone-boundary dispersion is entirely due to NNN coupling, see section 4.2.2.*

4.2 Zero temperature properties

Though this investigation mainly deals with the behaviour at finite temperatures, it is useful to review the zero temperature properties of the 2DQHAFSL. In 1D, the ground state is disordered by quantum fluctuations. This is evident from the exact solution based on the Bethe ansatz (Bethe, 1931, Hulthén, 1938). No exact solutions exist for the ground state in higher dimensions, but it has been shown that in 3D the ground state does contain long ranged antiferromagnetic order (LRO) (Dyson *et al.*, 1978, Kennedy *et al.*, 1988). The order is destroyed by thermal fluctuations at a critical temperature. In 2D it has been proven that thermal fluctuations destroy LRO at any finite temperature (Mermin and Wagner, 1966). No rigorous results exist for the existence of LRO in the ground state at zero temperature, but some attempts come close. Considering easy plane anisotropy, $J(S_i^x S_j^x + S_i^y S_j^y + \alpha S_i^z S_j^z)$, it has been shown that the ground state has LRO for any value of α if $S \geq 1$ and for $0 \leq \alpha < 0.13$ and $\alpha > 1.78$ at $S = 1/2$ (Kubo, 1988). However, there exist a large amount of approximate approaches which combined form overwhelming evidence that the ground state is long range ordered. A review of both the $T = 0$ and finite temperature properties is given by Manousakis (1991).

4.2.1 Spin-wave theory

Knowing that the ground state is ordered, it makes sense to investigate its behaviour using the so-called spin-wave theory (SPW), which is a very successful method in the description of magnetism in ordered systems. As will be described in the following sections, the 2DQHAFSL is dominated by spin-wave excitations both at zero and at finite temperatures. As an introduction, the simple linear spin-wave theory for nearest neighbour (NN) interactions will be derived.

Linear spin-wave theory for nearest neighbour coupling

The following gives a short derivation of the linear spin-wave theory for a nearest neighbour antiferromagnet in d dimensions (i.e. linear chain, square, cubic or hyper-cubic lattice). The Hamiltonian is written as

$$\mathcal{H} = \frac{1}{2} J \sum_{r,\delta} S_r \cdot S_{r+\delta} \ , \tag{4.3}$$

where δ runs over the $z = 2d$ nearest neighbours.

The lattice is divided into two sublattices, A (up) and B (down), so that a spin belonging to A has neighbours on B and vice versa. Lattices where such a division is possible are called bipartite. For each of the two sublattices, the spin operators are transformed into boson operators through the Holstein–Primakoff transformation (Holstein and Primakoff, 1940)

$$\begin{array}{lll} S_A^z &= S - a^\dagger a & \\ S_A^+ &= \sqrt{2S} a^\dagger f(S) & \text{and} \\ S_A^- &= \sqrt{2S} f(S) a & \end{array} \qquad \begin{array}{lll} S_B^z &= b^\dagger b - S & \\ S_B^+ &= \sqrt{2S} f(S) b & \\ S_B^- &= \sqrt{2S} b^\dagger f(S) \ , & \end{array} \tag{4.4}$$

where $f(S) = \sqrt{1 - c^\dagger c / 2S}$ (c is either a or b). One major difference between the spin operator S^z and the boson operator $n = c^\dagger c$ is that while the former is bounded to a subspace of $2S + 1$ states, the later spans an infinite number of states. The operator $f(S)$ ensures the truncation to the physical subspace of $2S + 1$ states, but at the same time holds the complication of the problem. In the spin-wave approximation only terms up to a given power in the boson operators are kept. Expanding $f(S) \simeq 1 - c^\dagger c / 4S + \cdots$ leads to increasingly higher powers of $c^\dagger c / 2S$.

In linear spin-wave theory only the terms that are quadratic in the boson operators are retained in the Hamiltonian. To this order $f(S)$ is approximated by 1. Next order with $f(S) \simeq 1 - c^\dagger c/4S$ is then called first order (in $c^\dagger c/2S$). Remembering the definitions $S^\pm = S^x \pm iS^y$, their inverse $S^x = \frac{1}{2}(S^+ + S^-)$ and $S^y = \frac{1}{2i}(S^+ - S^-)$, the inner product becomes

$$S_A \cdot S_B \simeq -S^2 + S(a^\dagger a + b^\dagger b + a^\dagger b^\dagger + ab) \ . \tag{4.5}$$

The Hamiltonian couples bosons on different lattice sites, but exploiting the translational symmetry, it can be decoupled by Fourier transformation giving

$$\mathcal{H}^{(2)} = -\frac{z}{2}NJS^2 + zJS\sum_q [a_q^\dagger a_q + b_q^\dagger b_q + \gamma_q(a_q^\dagger b_q^\dagger + a_q b_q)] \ , \tag{4.6}$$

where $\gamma_q = \frac{1}{z}\sum_\delta e^{i\boldsymbol{q}\cdot\boldsymbol{\delta}}$ is introduced for shorter notation. The Fourier transformed Hamiltonian still couples the a_q and b_q operators, but can be diagonalised through a Bogoliubov transformation to new quasi-particles α_q and β_q

$$a_q^\dagger = u_q\alpha_q^\dagger - v_q\beta_q \qquad b_q^\dagger = -v_q\alpha_q + u_q\beta_q^\dagger \tag{4.7}$$

$$a_q = u_q\alpha_q - v_q\beta_q^\dagger \qquad b_q = -v_q\alpha_q^\dagger + u_q\beta_q \ , \tag{4.8}$$

which satisfy the commutation relation provided that $u_q^2 - v_q^2 = 1$, which is satisfied by the parameterization $u_q = \cosh\theta_q$ and $v_q = \sinh\theta_q$. Requiring that the Hamiltonian expressed in these operators should be diagonal (without any terms connecting α_q with β_q) leads to $\tanh 2\theta_q = \gamma_q$ and

$$\mathcal{H} = -\frac{z}{2}NJS(S+\eta) + zJS\sum_q \sqrt{1-\gamma_q^2}(\alpha_q^\dagger\alpha_q + \beta_q^\dagger\beta_q) \ , \tag{4.9}$$

where $\eta = \frac{2}{N}\sum_q 1 - \sqrt{1-\gamma_q^2} \simeq 0.158$ (here and below, the numerical values are for $d = 2$). The first term is the ground state energy, while the second gives the energy dispersion for the quasi-particles, which are called spin waves.

$$\omega_q = zJS\sqrt{1-\gamma_q^2} \tag{4.10}$$

The expansion in powers of $c^\dagger c$ is justified if

$$\epsilon \equiv \frac{1}{N}\sum_q \langle c_q^\dagger c\rangle \simeq 0.197 \ll 1 \ . \tag{4.11}$$

This number corresponds to the average number of spin waves per site or expressed differently, the staggered magnetization given by

$$m \equiv \frac{1}{N}\sum_r (-1)^r\langle S_r^z\rangle \simeq \frac{1}{2} - \epsilon = 0.303 \tag{4.12}$$

is reduced to about 61% of the classical value due to zero point motion of the spin-waves.

Similarly the other results can be thought of as renormalised due to quantum fluctuations. In this spirit, a number of renormalization constants are defined with respect to the classical values of the different parameters:

$$\begin{array}{rclrcl} v_s &=& Z_c v_s^{\rm cl} & v_s^{\rm cl} &=& 2\sqrt{2}SJa \\ \rho_s &=& Z_\rho \rho_s^{\rm cl} & \rho_s^{\rm cl} &=& S^2 J \\ \chi_\perp &=& Z_\chi \chi_\perp^{\rm cl} & \chi_\perp^{\rm cl} &=& \frac{1}{2zJ} \\ \chi_\perp(q,\omega) &=& Z_d\chi_\perp^{\rm cl}(q,\omega) & \chi_\perp^{\rm cl}(q,\omega_q) &=& \frac{S}{2}\sqrt{\frac{1-\gamma_q}{1+\gamma_q}}\delta(\omega-\omega_q). \end{array} \tag{4.13}$$

To first order in the spin-wave expansion, $Z_c = 1 + \eta = 1.158$, $Z_\rho = 2.99$, $Z_\chi = 1 - \eta - 2\epsilon = 0.448$ and $Z_d = 0.519$ The renormalization Z_c of the spin-wave velocity is actually only defined from the $q \to 0$ limit of the dispersion relation, but up to first order spin wave theory, it is uniformly renormalised over the entire q-range, $\omega_q = Z_c\omega_q^{\rm cl}$. The uniform and dynamic susceptibilities could be calculated by including a term $h\sum_r e^{i\omega t}S_r^x$ to the Hamiltonian, but they can also be extracted from the scattering functions via the fluctuation–dissipation theorem.

Scattering functions

The neutron scattering cross-section is given in terms of the correlation functions $\langle S_0^\alpha(0) S_r^\beta(t)\rangle$. Since the Hamiltonian commutes with $\sum_r S_r^z$, only the terms $\langle zz\rangle$, $\langle +-\rangle$ and $\langle -+\rangle$ will be non-zero. Defining $S_q = \frac{1}{\sqrt{N}} \sum_r e^{iqr} S_r$ the dynamic structure factor becomes

$$S^{\alpha\beta}(q,\omega) = \int e^{i\omega t} dt \langle S_{-q}^\alpha S_q^\beta(t)\rangle = \int e^{i\omega t} dt \sum_n \langle 0|S_{-q}^\alpha|n\rangle\langle n|S_q^\beta(t)|0\rangle \ , \quad (4.14)$$

where $|0\rangle$ denotes the ground state and the completeness relation $1 = \sum_n |n\rangle\langle n|$ has been inserted. Remembering that $S(t) = e^{-Ht/\hbar} S e^{Ht/\hbar}$, $e^{Ht/\hbar}|n\rangle = e^{E_N t/\hbar}|n\rangle$ and $\int e^{i\omega t} = \delta(\omega)$ this becomes

$$S^{\alpha\beta}(q,\omega) = \sum_n \langle 0|S_{-q}^\alpha|n\rangle\langle n|S_q^\beta|0\rangle \delta(\omega - E_n/\hbar + E_0/\hbar) \ . \quad (4.15)$$

Writing the spin operators in terms of the quasi-particle operators α_q and β_q and using the corresponding eigenstates, the dynamic structure factor can be evaluated. The transverse part is $S^\perp(q,\omega) = S^{xx}(q,\omega) = S^{yy}(q,\omega)$. Neglecting higher order excitations in $S^{zz}(q,\omega)$, the rotationally invariant dynamic structure factor $S(q,\omega) = \sum_\alpha S^{\alpha\alpha}(q,\omega)$ becomes

$$S(q,\omega) = S\left(\frac{1-\gamma_q}{1+\gamma_q}\right)^{1/2} \delta(\omega - \omega_q) \ . \quad (4.16)$$

The absorptive part of the susceptibility is then given by the fluctuation–dissipation theorem $2\hbar\chi''(q,\omega) = (1 - e^{-\beta\hbar\omega}) S(q,\omega)$, where for positive energies the exponential disappears at $T = 0$.

There exist different relations between the renormalization parameters. Noting that Z_c renormalizes the energy scale and that the susceptibility is in inverse energy units, it follows that $\chi_\perp(q,\omega) \equiv Z_d \chi_\perp^{\rm cl}(q,\omega) = Z_d \chi_\perp^{\rm cl}(q, Z_c\omega^{\rm cl}) = (Z_d/Z_c)\chi_\perp^{\rm cl}(q,\omega^{\rm cl})$. From this it is seen that $Z_\chi = Z_d/Z_c$. Another relation between the parameters is obtained from the prediction of hydrodynamics (Halperin and Hohenberg, 1969) that $\rho_s = v_s^2 \chi_\perp$. As this relation is satisfied by the classical result, it must also hold for the renormalization parameters: $Z_\rho = Z_c^2 Z_\chi$.

Effect of further neighbour, interlayer and anisotropic coupling

The spin-wave calculation can be generalized to more complicated couplings, by replacing $zJ\sqrt{1-\gamma_q^2}$ by $\sqrt{A_q^2 - B_q^2}$. Including second J' and third J'' neighbour and inter plane J_c coupling gives (Morr, 1998)

$$A_q = 2J + J_c - 2J'(1 - \cos qa \cos qb) - J''(2 - cos2qa - cos2qb) \quad (4.17)$$

$$B_q = J\cos qa + J\cos qb + J_c \cos qc \quad (4.18)$$

Since an antiferromagnetic NNN coupling leads to frustration, this increases the effect of the quantum fluctuations, as manifested in the staggered magnetization, which for $\alpha < 0.3$ decreases linearly according to $m \sim 0.303 - 0.2 \times \alpha$.

Higher order spin-wave theory

As seen above, linear spin-wave theory gives the dispersion $\omega_q^{(0)} = 4JS\sqrt{1-\gamma_q^2}$ and ground state energy per site $E_0^{(0)} = -2JS^2(1 + \eta/S)$, where $\eta = \frac{2}{N}\sum_k (1 - \sqrt{1-\gamma_q^2}) \simeq 0.158$. Keeping terms up to order $1/S$ in the expansion gives:

$$\mathcal{H} = E_0^{(1)} + \sum_q \omega_q^{(1)} (\alpha_q^\dagger \alpha_q + \beta_q^\dagger \beta_q) \quad (4.19)$$

$$+ \frac{2J}{N} \sum_{qq'} (1 - C_{qq'})(\alpha_q^\dagger \alpha_q \alpha_{q'}^\dagger \alpha_{q'} + \beta_q^\dagger \beta_q \beta_{q'}^\dagger \beta_{q'}) - 2(1 + C_{q'})\alpha_q^\dagger \alpha_q + \beta_{q'}^\dagger \beta_{q'} \ ,$$

where $E_0^{(1)} = -2JS^2N(1+\eta/2S)^2, \omega_q^{(1)} = \omega_q^{(0)}(1+\eta/2S)$ and $C_{qq'} = \sqrt{1-\gamma_q^2}\sqrt{1-\gamma_{q'}^2}$. It is worth noticing that the dispersion relation is uniformly renormalised by $1+\eta/2S$.

Going to second order becomes a considerable task of careful book keeping, leading to a number of summations that have to be evaluated numerically (Igarashi, 1992). The result for $m = 0.3069$, $Z_c = 1.1794$, $Z_\chi = 514$ and $Z_\rho = 0.724$ are close to the first order results, suggesting convergence of the expansion. The values are also in good accord with other methods. Remarkably, it was found that even to second order, the dispersion is uniformly renormalized with $\omega_q^{(2)} = Z_c\omega_q^{\rm cl}$.

Here a small remark is in place. Whether the second order SPW theory gives a uniform renormalization of the dispersion or not depends delicately on the treatment of Umklapp processes. Depending on how these are related, a small dispersion can actually occur along the zone boundary (Igarashi and Watabe, 1991). In a slightly different approach based on the Dyson–Maleev formalism Canali *et al.* (1992) and Canali and Wallin (1993) found that the second order correction is an increase of 4% at $(\frac{\pi}{2},\frac{\pi}{2})$ but only 2% at $(\pi,0)$.

Igarashi (1993) has also calculated the second order result with NNN interaction $J_{NNN} = \alpha J$ included. The first order corrections grow with increasing α, which reflects how frustration favors quantum fluctuations.

4.2.2 Spin-wave dispersion in CFTD

The excitation spectrum of CFTD has been measured at 4.3 K by Harrison *et al.* (1992) and Clarke *et al.* (1999) using inelastic neutron scattering. As expected for a 2D Heisenberg antiferromagnet, the spectrum is composed of a single spin-wave branch with no dispersion along c^*. However, there is a gap of $\Delta = 0.38\pm0.02$ meV at the zone center, which probably arises from a small anisotropy in the symmetric exchange $\delta = (J_{zz} - J_{xx})/J$, like a Dzyaloshinskii–Moriya interaction. The zone boundary energy along b^*, corresponding to $q = (\frac{\pi}{2},\frac{\pi}{2})$, is 14.8 ± 0.2 meV and the entire dispersion along b^* was well described by the dispersion relation

$$\hbar\omega_q = 4S\tilde{J}\sqrt{(\delta+1-\gamma_q)(1+\gamma_q)}\ , \tag{4.20}$$

with $\tilde{J} = 7.4 \pm 0.2$ meV and $\delta = 0.0007 \pm 0.0001$. The tilde indicates that $\tilde{J}$ corresponds to the classical spin-wave dispersion. Correcting for the quantum renormalization gives the real $J = \tilde{J}/Z_c$.

As will be described in section 4.4 the present time-of-flight neutron scattering study has also led to a measurement of the spin-wave dispersion along both $(1,1)$ and $(0,1)$. The analysis of these data are described in section 4.4.4 and the result is shown in figure 4.7.

It is first noted that the spin-wave velocity can be extracted directly from the data as the initial slope around (π,π). Due to the small gap in CFTD, the form $\omega_q = \sqrt{\Delta^2 + v_s^2q^2}$ should be employed, but with 5Δ as the lowest probed energy, the fits were insensitive to Δ, which was kept fixed at the value 0.38 meV determined by Clarke *et al.* (1999). Because of the poor statistics along $(1,0)$, only the $(1,1)$ data were included in the fit giving $v_s/d = 10.55 \pm 0.06$ meV.

The dispersion along (1,1) is in good agreement with the earlier measurements by Clarke *et al.* (1999) and can be fitted by the classical spin-wave result using $\tilde{J} = 7.46 \pm 0.02$ meV, corresponding to $J = 6.31 \pm 0.02$ meV. But along (1,0) the dispersion was found to exhibit a dip at the zone boundary $q = (\pi,0)$, making it 7% lower than at $(\frac{\pi}{2},\frac{\pi}{2})$. As shown by the dashed line, this can be accounted for by introducing a NNN coupling, giving $\tilde{J} = 8.00 \pm 0.08$ meV and $\alpha = 0.066 \pm 0.008$. At this value of α, the second order spin wave theory (Igarashi, 1993) predicts $Z_c = 1.201$ and $v_s = 1.117 \times \sqrt{2}Ja$, giving $J = 6.68 \pm 0.07$ meV.

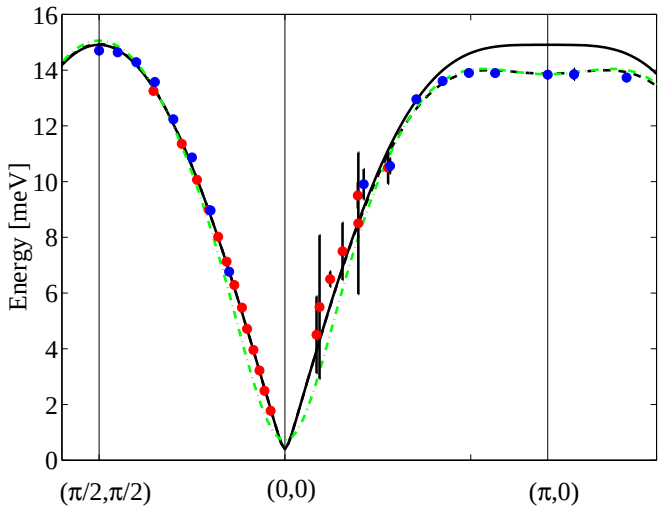

Figure 4.7. The spin-wave dispersion of CFTD along (1,1) and (1,0) at 8 K. *The solid and dashed lines are fits to linear spin-wave theory with parameter choices* $(\tilde{J}, \alpha = J'/J) = (7.46 \pm 0.02 \text{ meV}, 0)$ *and* $(8.00 \pm 0.08 \text{ meV}, 0.066 \pm 0.008)$ *respectively. The dot-dashed line is the series expansion result by Singh and Gelfand (1995) using* $J = \tilde{J}/Z_c = 6.31 \pm 0.02$ meV.

However, as explained below, there exist some indications that the uniform renormalization of the dispersion found in spin-wave theory is not correct at $q = (\pi, 0)$. In a series expansion from the Ising limit Singh and Gelfand (1995) found that the energy at this point of the zone boundary was lowered by 7%, which is exactly the value observed in CFTD. Apart from around $q = (\pi, \pi)$, where the series expansion is expected to fail, the predicted dispersion as depicted by the dot-dashed line in figure 4.7 is indistinguishable from the NNN result. It is therefore not possible on the basis of the dispersion alone to distinguish between the two possibilities, but the coincidence that the observed dip matches the one predicted by series expansion without any free parameters makes this explanation more attractive.

4.2.3 Beyond spin-wave theory

It is important to remember that the spin-wave expansion is really an expansion from the Néel state. In the 2DQHAFSL the staggered magnetization is reduced by 30% indicating that a significant part of the ground state expectation value lies in states that are neither of the two Néel states. Therefore, in spite of its success in describing the ground state parameters, the spin-wave expansion should be treated with an appropriate amount of scepticism and additional methods should be used to improve the credibility of its predictions.

Numerical calculations

Even with the large number of symmetries offered by the nearest neighbour Heisenberg antiferromagnet, numerical exact diagonalization is currently only possible on finite systems of up to about 36 spins. For finite $N \times N$ systems, only a discrete number of points exist in reciprocal space. To measure the dispersion at $(\pi, 0)$, N just has to be even, but to measure it at $(\frac{\pi}{2}, \frac{\pi}{2})$, N must be dividable by four.

Exact diagonalization of a 4×4 system has been feasible for a while (Chen *et al.*, 1992). Interestingly, this leads to exactly the same energy at both points $\hbar\omega(\pi, 0)/J = \hbar\omega(\frac{\pi}{2}, \frac{\pi}{2})/J = 2.710$. It is a very small system for which care should

be taken in attempts to extrapolate to infinite systems, but the fact that the two energies are exactly the same does insinuate that this would be a robust result.

Unfortunately the next N that is dividable by 4 is 8, and exact diagonalization of 64 spins will remain out of reach in a while despite of Moore's law for the growth of computational power. There is one improvement possible however, which is based on a clever choice of boundary conditions. Forming a square out of four 4×4 blocks, such that the two along each diagonal are copies of each other, gives a total of 32 inequivalent spins. The reciprocal space of the full 8×8 system is thereby depleted in a way that still enable calculation of the excitation energy at the two points of interest. Though still being far from $N=\infty$ it is indeed interesting to see if the lack of zone boundary dispersion persists, and the implementation of this scheme is in progress (Lefmann *et al.*, 2000).

Abandoning the goal of finding all the lowest lying eigenstates of the system, somewhat larger system sizes can be treated in Monte Carlo based calculations. For any 'trial' state $|\psi_T\rangle$, the ground state $|\psi_0\rangle$ can be produced by applying the evolution operator $e^{-\tau H}$ for sufficiently long imaginary time τ.

$$|\psi_0\rangle = \frac{e^{\tau E_0}}{\langle\psi_0|\psi_T\rangle} e^{-\tau H}|\psi_T\rangle \ , \tag{4.21}$$

which can be seen by applying $\langle\psi_0|$ on both sides of the equation. The basic idea of the projector- or Greens function Monte Carlo technique is to perform the imaginary time evolution in finite steps $\Delta\tau$ numerically, thereby reaching an approximation for the ground state. Since this technique operates only on a small subspace of the entire set of states, systems up to 16×16 have been studied. The results generally confirm the findings of SPW theory, but the extrapolation to $N\to\infty$ gives uncertainties that are too large to answer detailed questions like the possible existence of a 7% zone boundary dispersion (Trivedi and Ceperley, 1990).

Series expansion from the Ising limit

As an alternative to the spin-wave expansion, Singh and Gelfand (1995) have performed a series expansion in λ from the Ising limit ($\lambda=0$):

$$\mathcal{H} = -\frac{1}{2}\sum_{rr'} J[S_r^z S_{r'}^z + \lambda(S_r^x S_{r'}^x + S_r^y S_{r'}^y)] \ . \tag{4.22}$$

The series expansion for the spin-wave velocity is given below. A direct summation with $\lambda=1$ gives $v_s/Ja = 2.267$, which is far from the expected value of $1.18\times2\sqrt{2}S$. This is due to the poor convergence of the series, which can be improved by considering the Padé approximants (Cabannes, 1976).

A given function $f(x)$, can be approximate around $x=0$ either by the simple Lth order Taylor polynomial $T_L(x)=\sum_{n=1}^{L} t_n x^n$ or by the $[N,M]$ Padé approximant, which is defined as the ratio between two polynomia $P_N(x)/Q_M(x)$ of order respectively N and M. If the first L Taylor coefficients of a function are known, they can be used to calculate the Padé approximants for which $N+M\le L$. In general, the best approximants are found around the diagonal $N\sim M\sim L/2$. Astonishingly, it is in many cases found that the Padé approximants give a better approximation of the function than the Taylor expansion from which they were derived. However, it is difficult to assess the convergence of the Padé approximants, and sometimes it fails — this is the weakness of the Padé approximant method.

Since the series expansion above is in orders of λ^2, $L=5$ and the three most promising Padé approximants are [2,2], [2,3] and [3,2]. As seen in table 4.2 these three approximants agree within 0.3% and give $v_s = 1.67\times Ja$ corresponding to $Z_c = 1.18$ in good agreement with the spin-wave expansion and other results.

The series expansion for the dispersion relation is given in table 1 of Singh and Gelfand (1995). Specifically, for the three q-vectors $(0,0)$, $(\frac{\pi}{2},\frac{\pi}{2})$ and $(0,\pi)$, the series are:

$$(v_s/cJ)^2 = 4\lambda^2 - 2.30556\lambda^4 + 2.41051\lambda^6 - 3.06490\lambda^8 + 4.10055\lambda^{10} \qquad (4.23)$$

$$\omega(0,0) = 2 - 5/3\lambda^2 + 0.31713\lambda^4 - 0.41923\lambda^6 + 0.27100\lambda^8 - 0.38943\lambda^{10}$$

$$\omega(\tfrac{\pi}{2},\tfrac{\pi}{2}) = 2 + 1/3\lambda^2 + 0.05324\lambda^4 - 0.00907\lambda^6 + 0.00511\lambda^8 + 0.00208\lambda^{10}$$

$$\omega(0,\pi) = 2 + 1/3\lambda^2 - 0.09954\lambda^4 - 0.00169\lambda^6 - 0.02807\lambda^8 - 0.01062\lambda^{10}$$

The coefficients for $q = (0,0)$ are seen to remain large and alternating, thus warning about a poor convergence of the series. While $\omega(0,0)$ is expected to be zero, a direct summation gives 0.113. This result is not improved by a Padé analysis shown in table 4.2. It has in some cases proven advantageous to make the transformation $\lambda^2 = 2x - x^2$, which moves the competing discontinuity at $\lambda = -1$ to minus infinity. In this case however, there is no sign of improvement through such a trick. It will seem that the series expansion from the Ising limit is not able to reach the gapless zone-center energy of the Heisenberg model. This is understandable, as the existence of a gap in the Ising model poses a qualitative difference between the two models.

v_s^2	1	2	3	4	$\omega(0,0)$	1	2	3	4
1	2.537	3.066	2.553	3.082	1	0.560	0.077	0.451	-4.56
2	2.874	2.781	2.790		2	0.470	0.382	0.309	
3	2.759	2.789			3	0.396	1.576		
4	2.799				4	0.342			
$\omega(\frac{\pi}{2},\frac{\pi}{2})$	1	2	3	4	$\omega(\pi,0)$	1	2	3	4
1	2.397	2.401	2.380	2.385	1	2.257	2.235	2.220	2.197
2	2.379	2.381	2.383		2	2.232	2.394	2.160	
3	2.381	2.332			3	2.234	2.153		
4	2.386				4	2.187			

Table 4.2. Padé approximants $[N,M]$ (row and column) for v_2, $\omega(0,0)$, $\omega(\frac{\pi}{2},\frac{\pi}{2})$ and $\omega(\pi,0)$ with λ^2 as variable. The numbers re in units where $\hbar$, J and a are equal to unity. For $\omega(0,0)$, it is noticed how very few approximants are close to the expected value of zero.

The convergence looks more promising for the two zone-boundary points, where the coefficients become quite small for the λ^{10} term. The values obtained by direct summation are $\omega(\frac{\pi}{2},\frac{\pi}{2}) = 2.385$ and $\omega(0,\pi) = 2.193$, respectively. Approximately the same values are reached for the well-behaved Padé approximants. It is therefore reasonable to trust the two values, although it is of great importance to have them confirmed by other methods like QMC.

The important result is that while the dispersion along $[1,1]$ is uniformly renormalized by Z_c, the dispersion along $[0,1]$ shows a suppression of the excitation energy at $(0,\pi)$ by approximately 7%.

The physical origin of this non-uniform quantum correction has not yet been clearly explained, but a hint may be found in the flux-phase description of Hsu (1990). Using a resonating-valence-bond like ground state, which has the major fault that it has zero staggered magnetization, Hsu reaches a dispersion relation which is uniformly renormalized along $(1,1)$ but has a large suppression of the energy at $(0,\pi)$. In this work, the suppression is related to nesting of the Fermi-surface obtained after a quasi-particle transformation. It could be imagined that the true ground-state is a combination of the flux-phase and the spin-wave ground-

state — closer to the later, and that the dispersion is in some sense an average of the two.

It is worth noticing that the spin-wave dispersion obtained in the series expansion analysis corresponds to the spin-wave theory result, with nearest neighbour coupling $J_{\mathrm{NN}}^{\mathrm{eff}} \simeq 1.07 \times J$ and next nearest neighbour coupling $J_{\mathrm{NNN}}^{\mathrm{eff}} \simeq 0.06 \times J$. This could be an indication that an analytic calculation of the zone-boundary dispersion should be based on mapping the quantum effects that are neglected in spin-wave theory onto an effective NNN coupling. This is a challenging task that involves the part of the ground-state expectation value that is not found in the Néel state.

4.2.4 Summary of zero temperature properties

As described above, the zero temperature value of most physical quantities of the 2DQHAFSL have been established by comparing different approximative and numerical methods. In summary, the ground state of the 2DQHAFSL exhibits long range antiferromagnetic order and the $T = 0$ properties are therefore qualitatively described by the classical spin wave theory. Quantitatively, the parameters are renormalized due to quantum fluctuations: $m = 0.31$, $Z_c = 1.18$, $Z_\chi = 0.51$, $Z_\rho = 0.72$ and $Z_d = 0.61$.

While it should not be forgotten that only a few exact results exist and that the full nature of the ground state is still not known, it is fair to say that the zero temperature behaviour of the 2DQHAFSL is relatively well understood. One exception to this is the question of a possible zone-boundary dispersion, which needs to be clarified.

4.3 Correlations at finite temperature

In 1966 it was rigorously proven by Mermin and Wagner (1966) that at any non-zero temperature the one- and two-dimensional Heisenberg model with finite interactions cannot exhibit long ranged magnetic order. Their proof was inspired by Hohenberg and built on Bogoliubov's inequality

$$\frac{1}{2}\langle\{A, A^\dagger\}\rangle\langle[[B, H], B^\dagger]\rangle \leq k_B T|\langle[B, A]\rangle|^2 \ , \tag{4.24}$$

with $A = S^-(Q - q)$ and $B = S^+(q)$. For the antiferromagnet, $Q = (\pi, \pi)$, while $Q = 0$ for the ferromagnet.

This absence of long ranged order makes it necessary to modify methods based on a perturbative expansion from the Néel state or to invoke new methods that do not require knowledge of the ground state. At low temperatures, the spins are still strongly correlated, and the disorder is only visible on length scales larger than the correlation length $\xi(T)$. The present section reports measurements of $\xi(T)$ in CFTD, but first the theoretical foundation is reviewed.

Structure factor $S(q)$ and correlation length ξ

The correlations in a system are described by the time independent correlation function $\langle S(0)\cdot S(r)\rangle$ or by its Fourier transform $S(q)$, which is called the structure factor. Sometimes it is called the instantaneous structure factor to explicitly distinguish it from the dynamic structure factor $S(q, \omega)$. The two correlation functions are defined and related by

$$S(q, \omega) \equiv \int \sum_r e^{iq\cdot r - i\omega t}\langle S_0(0)\cdot S_r(t)\rangle dt \tag{4.25}$$

$$S(q) \equiv \sum_r e^{ik\cdot r}\langle S_0 \cdot S_r\rangle = \frac{1}{2\pi}\int S(q, \omega)d\omega \ . \tag{4.26}$$

In the absence of long range order, the correlation function will decay with r, and the correlation length is often defined as the long distance decay rate of the spin-spin correlation function $\langle S_0 \cdot S_r\rangle \propto e^{-|r|/\xi}$. If the correlation function follows precisely an exponential decay as a function of the distance r, the structure factor becomes a Lorentzian $S(q) \propto \frac{1}{1+q^2\xi^2}$, and the correlation length is the inverse of the half-width half-maximum (HWHM) of the structure factor. From a calculational point of view, it is useful to realize that i/ξ corresponds to the location of the pole in $S(i\xi)$ along the imaginary momentum axis (Elstner *et al.*, 1995a).

If the space and momentum dependences deviate from these ideal forms, the definition becomes ambiguous. Analytical theories often reach real-space behaviour $f(r)e^{-|r|/\xi}$, where $f(r)$ is some pre-exponential factor. For instance, three predictions for $S(q)$ that have been proposed in the litterature are the simple Lorentzian S_L and two scaling forms proposed by respectively Chakravarty *et al.* (1989) (CHN) and Chubukov *et al.* (1994) (CSY). These three options have the following real-space behaviour:

$$\begin{aligned}
S_{\text{L}} = S_0\frac{1}{1+q^2\xi^2} \quad &\overset{\mathcal{F}^{-1}}{\rightarrow} \quad e^{-\frac{|r|}{\xi}} \\
\tilde{S}_{\text{CHN}} = S_0\frac{\ln(1+q^2\xi^2)}{1+q^2\xi^2} \quad &\overset{\mathcal{F}^{-1}}{\rightarrow} \quad e^{-\frac{|r|}{\xi}}\ln\left(\frac{2\xi}{|r|e^{-\gamma}}\right) + \sqrt{\frac{2|r|}{\pi\xi}}K^{(1,0)}_{-\frac{1}{2}}\left(\frac{|r|}{\xi}\right) \\
S_{\text{CSY}} = S_0\frac{1}{\sqrt{1+q^2\xi^2}} \quad &\overset{\mathcal{F}^{-1}}{\rightarrow} \quad \frac{2K_0(|r|/\xi)}{\pi} \ ,
\end{aligned} \tag{4.27}$$

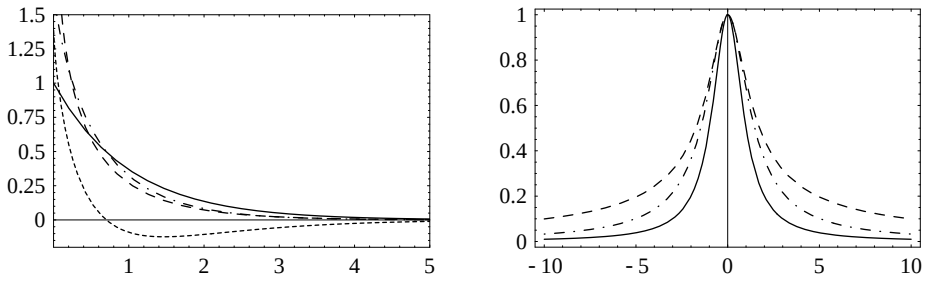

Figure 4.8. The real space (left) and reciprocal space (right) behaviour in units of r/ξ and $q\xi$ of three possible lineshapes for the correlation function: S_{L} (solid), S_{CHN} (short-dashed), S_{CSY} (dot-dashed) and in the left panel also $\tilde{S}_{\text{CHN}}$ (dotted)

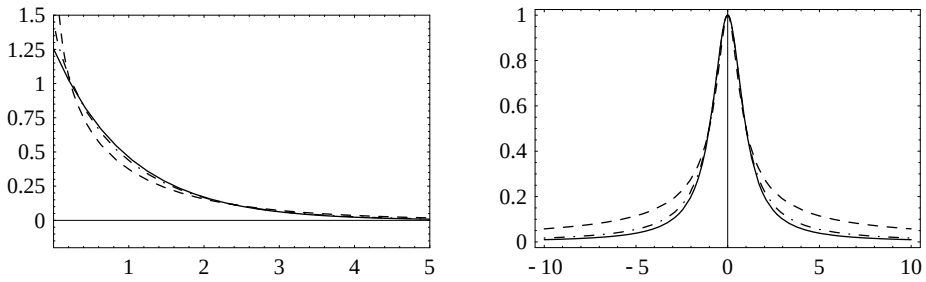

Figure 4.9. The real space (left) and reciprocal space (right) line shapes scaled to their respective FWHM.

where $S_0 = \xi\sqrt{2/\pi}$ ensures the normalization, $\gamma \simeq 0.577216$ is Euler's constant, $K_\nu(x)$ is the modified Bessel function of second kind and $K_\nu^{(1,0)} = \frac{\partial}{\partial\nu}K_\nu(x)$. The form $S_{\text{CHN}} = S_{\text{L}} + \frac{1}{2}B_f\tilde{S}_{\text{CHN}}$, where B_f is of the order of unity, is a slight generalization of the simple Lorentzian S_{L}. Respectively the real-space and reciprocal space shapes of the three forms are illustrated in figure 4.8.

Another used definition is through the second moment of the structure factor

$$\xi_M^2 = \frac{-1}{2S(q=0)}\left.\frac{\partial^2 S(q)}{\partial q^2}\right|_{q=0} . \tag{4.28}$$

This definition is often used in studies on finite lattices $L \times L$, where the structure factor is known only on a discrete lattice in units of $2\pi/L$, from which the derivative is then calculated. Analytic results for the three line shapes considered here give respectively $\xi_M = \xi$, $\xi_M = \xi\sqrt{1 - B_f/2}$ and $\xi_M = \xi/\sqrt{2}$.

Alternatively, discrete data for $S(q)$ can be fitted to a functional form like the Lorentzian, thereby extracting the correlation length and the amplitude S_0. Due to the statistical error in experiments, this is the only method that is applicable when analyzing neutron scattering data. Independent of the exact line-shape, this method will extract a correlation length which is close to the inverse HWHM. The HWHM for each of the three line shapes are $\text{HWHM}_{\text{L}} = \xi^{-1}$, $\text{HWHM}_{\text{CHN}} = \xi^{-1}\sqrt{B_f T_{-1}(e^{-2/B_f}/B_f) - 1}$ and $\text{HWHM}_{\text{CSY}} = \xi^{-1}\sqrt{3}$, where $T_n(x)$ is the nth order tree-generating function. For $0 \le B_f \le 1$, HWHM_{CHN} varies from 1 to 1.465 which is close to the result for ξ_M. In figure 4.9 the line-shapes have been plotted in units of $r\times$FWHM and q/FWHM using their respective values for FWHM. It is seen how apart from a difference in the 'background', which would not be easily identified in an experiment, the scaled line-shapes are very alike.

Defined as the long distance decay rate, the three line shapes considered here share the same correlation length ξ. However, as just demonstrated, numerical calculations evaluated through the second derivative or experimental results based

on fits would lead to differences of up to a factor of $\sqrt{3}$. It is therefore important that quantitative comparisons use consistent definitions for the correlation lengths or take the differences in the definitions properly into account.

4.3.1 Theoretical and numerical predictions

In the treatment of the short range ordered system, much attention has been focused on the correlation length. In addition to being one of the most important observables, the correlation length has attained status as a bench-mark because it provides a way to compare and test analytic, numerical and experimental results. A number of different approaches have been taken, including quasi-particle transformations, mapping onto the quantum non-linear σ model (QNLσM), high-temperature expansions, semiclassical methods and quantum Monte Carlo calculations.

Quasi-particle transformations

Various quasi-particle formulations, such as the Schwinger-boson (Schwinger, 1952, Arovas and Auerbach, 1988, Auerbach and Arovas, 1988, Kopietz, 1990), Dyson–Maleev (Dyson, 1956, Maleev, 1957, Takahashi, 1989) and Holstein–Primakoff (Holstein and Primakoff, 1940, Hirsch and Tang, 1989) transformations have been applied. They all lead to the same self-consistency equation for the parameters η and λ that renormalize the zero temperature spin-wave dispersion according to $\omega_q = \lambda\sqrt{1-\eta^2\gamma_q^2}$. In the low-temperature limit, these equations can be solved as

$$\eta = 1 - \frac{1}{2}(T/\lambda_0)^2 e^{-\frac{\pi\lambda_0(S-\epsilon)}{k_B T}}[1 + O(T/J)^2] \tag{4.29}$$

$$\lambda = \lambda_0 - \frac{16J}{\pi}(T/\lambda_0)^3 + O(T/\lambda_0)^5 \ , \tag{4.30}$$

where $\lambda_0 = 4SJZ_c$. The correlation function is then given by

$$(-1)^{||r||}\left(\frac{2T}{\lambda_0}\right)^2 \frac{\xi}{\pi|r|}e^{-|r|/\xi} \tag{4.31}$$

with the correlation length

$$\xi(T) = \frac{S\hbar v_s}{k_B T}e^{\frac{2\pi\rho_s}{k_B T}}[1 + O(T/2\pi\rho_s)^2] \ . \tag{4.32}$$

The exponential decay of $\xi(T)$ at increasing temperature is common to all theoretical predictions and has been verified experimentally. The prefactor $S\hbar v_s/k_B T$ is however subject to corrections.

The susceptibility acquires a term linear in temperature

$$\chi(T) = \frac{S-\epsilon}{12JZ_c} + \frac{k_B T}{2\pi JZ_c} + O(T^3) \ . \tag{4.33}$$

The factor of $\frac{2}{3}$ to the $T = 0$ result $\chi_\perp = \frac{S-\epsilon}{8JZ_c}$ is due to the loss of a well defined direction of the order parameter, by which χ is averaged over the three directions which at $T = 0$ give $\chi_{xx} = \chi_{yy} = \chi_\perp$ and $\chi_{zz} = 0$.

The quantum non-linear σ model

A much celebrated approach has been the mapping of the Heisenberg antiferromagnet onto the quantum non-linear σ model (QNLσM) (Haldane, 1983, Affleck, 1988b,a). Technically, the QNLσM can be obtained as the long-wavelength, large-S and low-temperature limit of the HAF by disregarding the so-called topological Berry phase term. The procedure will be outlined below.

The first step in reaching the field theoretical description is to introduce the notion of coherent states $|\boldsymbol{N}\rangle$ where $\boldsymbol{N}$ runs over the unit sphere. While $\{|-S\rangle, \cdots, |S\rangle\}$ form a minimal complete set of basis states, the coherent states are not orthogonal but do satisfy the completeness relation $\int |N\rangle\langle N| dN = 2\pi$. They are related to the original states by $\langle \boldsymbol{N}|\boldsymbol{S}|\boldsymbol{N}\rangle = S\boldsymbol{N}$, giving the relations $|S\rangle = |\boldsymbol{N} = (0,0,1)\rangle$ and $|\boldsymbol{N}\rangle = \exp(zS^+ - s^*S^-)|S\rangle$ with $z = -\frac{\theta}{2}\exp(-i\phi)$ in terms of the spherical coordinates of $\boldsymbol{N} = (\sin\theta\cos\phi, \sin\theta\sin\phi, \cos\theta)$.

By inserting an infinite number of the completeness relation into the partition function $Z = \mathrm{Tr}\,\exp(-\beta\mathcal{H}(S))$, the path-integral formulation is reached.

$$Z = \int \mathcal{D}\boldsymbol{N}(\tau) \exp\left\{ -\int_0^\beta d\tau \mathcal{H}(SN(\tau)) - iS\int_0^1 du N(\tau)\cdot\left(\frac{\partial N}{\partial u}\times\frac{\partial N}{\partial \tau}\right)\right\} \tag{4.34}$$

In the semiclassical limit, $N(r)$ becomes the direction of the spin at site r and can conveniently be written as $N(r) = (-1)^r n(r)\sqrt{1-a^{2d}l^2(r)} + a^d l(r)$, where a is the lattice constant, d the dimension, $n^2 = 1$ and $\boldsymbol{n}\cdot\boldsymbol{l} = 0$. At low temperatures where the correlation length is long (adjacent spins point in almost opposite directions) it can be assumed that n and l are slowly varying functions $\nabla n \ll a^{-1}$, $\nabla l \ll a^{-2}$ and $|l| \ll a^{-1}$. This is used to keep only terms up to the lowest (second) order in the action

$$\mathcal{S} = \frac{1}{2}\int_0^\beta d\tau \int d^d r \left\{ \rho_s^0 (\nabla n)^2 + \chi_\perp^{-1} l^2 + 2il\cdot\left(n\times\frac{\partial n}{\partial\tau}\right)\right\} + \theta\ , \tag{4.35}$$

where $\rho_s^0 = JS^2a^{2-d}$ and $\chi_\perp = 1/4dJa^d$. The term $\theta = iS\sum_n (-1)^n \int_0^\beta d\tau \int_0^1 du\, \boldsymbol{n}_{\boldsymbol{n}}\cdot\left(\frac{\partial n_n}{\partial u}\times\frac{\partial n_n}{\partial\tau}\right)$ is the topological part of the so-called Berry phase, which due to the factor $(-1)^n$ cannot easily be turned into a continuum description. However, under the smooth function assumption θ vanishes for the 2D model (Haldane, 1988). The field l can be integrated out to give

$$\mathcal{S} = \frac{1}{2}\int_0^\beta d\tau \int d^d r \rho_s^0 \left[(\nabla n)^2 + \frac{1}{v_s^2}(\partial_\tau n)^2\right]\ . \tag{4.36}$$

This action represents the so-called quantum non-linear sigma model (QNLσM) with $v_s = 2d^{1/2}SJa$. It can also be obtained in a more direct manner (Affleck, 1988b) by defining

$$\begin{aligned}
n(x+\tfrac{1}{2}, y+\tfrac{1}{2}) &= (S_{x,y} - S_{x+1,y} - S_{x,y+1} + S_{x+1,y+1})/(4\sqrt{S(S+1)}) \\
l(x+\tfrac{1}{2}, y+\tfrac{1}{2}) &= (S_{x,y} + S_{x+1,y} + S_{x,y+1} + S_{x+1,y+1})/4 \\
A_x(x+\tfrac{1}{2}, y+\tfrac{1}{2}) &= (S_{x,y} - S_{x+1,y} + S_{x,y+1} - S_{x+1,y+1})/(4\sqrt[4]{S(S+1)}) \\
A_y(x+\tfrac{1}{2}, y+\tfrac{1}{2}) &= (S_{x,y} + S_{x+1,y} - S_{x,y+1} - S_{x+1,y+1})/(4\sqrt[4]{S(S+1)})\ .
\end{aligned} \tag{4.37}$$

where x and y are even integers. Under the assumption of slow variation, they correspond to modes near (π,π), (0,0), $(\pi,0)$ and $(0,\pi)$ respectively. Knowing that for the 2DQHAFSL, the ground state has long range order, or in general, just assuming that n is well defined at all points in space and time, Haldane showed that in two dimensions, the Berry phase falls out (Haldane, 1988). In addition, the knowledge from spin-wave theory, that the excitation energy has minima only at (π,π) and (0,0), the two additional fields can be expected to become irrelevant, and the Hamiltonian density becomes

$$\mathcal{H}/v = \frac{1}{2}\rho_s^0 (\nabla n)^2 + \frac{1}{2\chi_\perp} l^2\ , \tag{4.38}$$

leading to the same action as derived above.

Renormalization group analysis

Several different approaches have been taken to study the QNLσM. In their seminal work, Chakravarty *et al.* (1989) (CHN) used a one-loop renormalization group method to reach results for the structure factor.

CHN starts by adding a source term $H\int_0^\beta d\tau \int dr\sigma(r,\tau)$, where $\sigma(r,\tau)$ is one component of the M dimensional field $\boldsymbol{n} = (\boldsymbol{\pi}, \sigma)$. Using the constraint $|\boldsymbol{n}| = 1$, $\sigma(r,\tau)$ is integrated out. The remaining field $\boldsymbol{\pi}(r,\tau)$ is then expanded in Fourier coefficients $\boldsymbol{\pi}(\boldsymbol{k},\omega_n)$. The integrals are regularized by introducing a momentum cutoff Λ and the space dimension is rescaled to this so that $k < 1$.

The renormalization procedure is achieved by integrating out the high momentum part $e^{-l} < k < 1$ to reach a new effective action. This is known as momentum-shell integration because only a shell of momentum space is integrated out. Defining new variables $k' = e^l$ and $\pi' = \pi/\eta$ the new effective action can be brought to the same form as the original provided that the parameters are rescaled according to

$$u' = ue^{-l} \tag{4.39}$$

$$(t')^{-1} = \eta^2 e^{-d-2l}\left(t^{-1} + I\right) \tag{4.40}$$

$$h'u' = \eta^2 e^{-dl}(hu + \frac{1}{2}hg(M-1)I)\ , \tag{4.41}$$

where $u_0 = \beta\hbar\Lambda v_s$, $g_0 = \hbar v_s \Lambda^{d-1}/\rho_s^0$, $t = g/u$, $t_0 = k_B T\Lambda^{d-2}/\rho_s^0$, $h_0 = H\Lambda^{-d-1}/(\hbar v_s)$ and $I = \sum_n \sum_{e^{-l}<k<1}(k^2 + \omega_n^2 + hg)^{-1}$. The spin rescaling η is determined by the requirement that the the Zeeman energy h'/η and temperature scales in the same way ($h'u'/\eta = hu$), giving $\eta = e^{dl}(1 - \frac{1}{2}t(M-1)I)$. From the rescaling scheme the following flow equations are achieved

$$\frac{dg}{dl} = (1-d)g + \frac{K_d}{2}(M-2)g^2\coth(g/2t) \tag{4.42}$$

$$\frac{dt}{dl} = (2-d)t + \frac{K_d}{2}(M-2)gt\coth(g/2t)\ , \tag{4.43}$$

where $K_d = 2^{1-d}\pi^{-d/2}/\Gamma(d/2)$, and Γ is the Euler gamma function. In two dimensions with $M = 3$ there is a $T = 0$ fixed point at $g_c = 1/(4\pi)$, while there is no finite temperature fixed point. The flow equations are integrated until the renormalized correlation length equals the lattice constant $e^{-l^*}\xi = a$. Though this is not an exact determination, it gives the leading order of the temperature dependence

$$\xi^{-1} = \frac{2}{a\Lambda}\frac{k_B T}{\hbar v_s}\sinh^{-1}\left[\sinh(g_0/2t_0)e^{1-2\pi/t_0}\right]\ . \tag{4.44}$$

There are three regions for which limiting results for ξ can be written out

$$\xi = 0.74 \times a\Lambda\frac{\hbar v_s}{k_B T}\exp\left(\frac{2\pi\rho_s}{k_B T}\right) \qquad g < g_c - t \tag{4.45}$$

$$\xi = 1.14 \times a\Lambda\frac{\hbar v_s}{k_B T} \qquad g = g_c \tag{4.46}$$

$$\xi = \frac{ag/2}{g - g_c\left(1 - \frac{k_B T}{2\pi\rho_s^0}\exp(8\pi\rho_s/T)\right)} \qquad g > g_c + t\ , \tag{4.47}$$

where $\rho_s = \rho_s^0(1 - g_0/g_c)$ is the quantum renormalised spin-wave stiffness.

The three regions are sketched in figure 4.10. For $g < g_c$ the correlation length diverges exponentially towards a long range ordered ground state, and the low temperature properties are described by a renormalization of the parameters. This is called the *renormalised classical* (RC) region. Above g_c the ground state is *quantum disordered* (QD) in what can be denoted a quantum fluid, where the correlation length is only weakly temperature dependent and stays finite as $T \to 0$. At

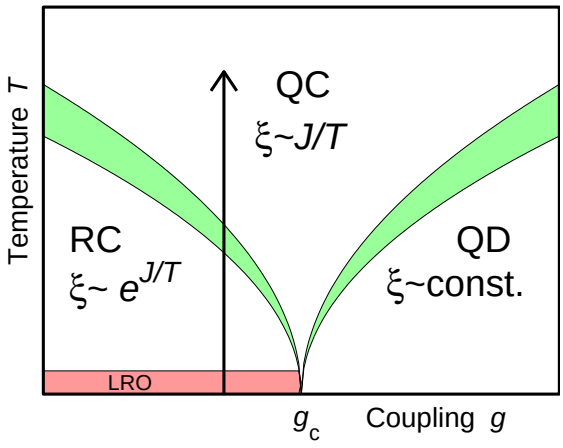

Figure 4.10. Schematic phase diagram of the QNLσM as a function of temperature T and the coupling parameter g. The leading temperature dependence of the correlation length ξ is indicated for each of the three regions RC, QC and QD. At $T = 0$ there is long range order for $g < g_c$. The arrow illustrates the location of the 2DQHAFSL when mapped onto the QNLσM.

the critical point g_c the correlation length is inversely proportional to temperature, and this *quantum critical* (QC) behaviour will influence the region above the RC and the QD until it is eventually taken over by ordinary classical behaviour at high temperatures. As described in section 4.2, it is well established that the ground state of the 2DQHAFSL is long range ordered, which means that the low temperature properties should be described by the RC prediction.

It is seen that this one loop calculation reproduces the result from the quasiparticle approaches. But the method can be improved by summing over all nonzero Matsubara frequencies (instead of performing a momentum-shell integration). This leads to an effective action $S = \frac{1}{2t_{cl}} \int d^2r (\nabla \hat{n})^2$ corresponding to the classical NLσM. In this model, the correlation length has been determined as (Hasenfratz *et al.*, 1990) and Hasenfratz and Niedermayer (1990)

$$\xi = \frac{e}{8} \frac{k_B T t_{cl}}{2\pi v_s} \exp\left(\frac{2\pi}{t_{cl}}\right) \left(1 + \frac{t_{cl}}{8\pi} + \cdots\right) . \tag{4.48}$$

The renormalization procedure of CHN led to an estimate for t_{cl} that depends logarithmically on the momentum cutoff Λ. Instead it was proposed to calculate a long-distance property in both the classical and the quantum models. The effective coupling constant t_{cl} is then determined by matching the two results. Choosing as a variable the change $f(h) - f(0)$ of the free energy as a function of the chemical potential, Hasenfratz *et al.* (1990), Hasenfratz and Niedermayer (1990) reached $2\pi/t_{cl} = \frac{2\pi\rho_s}{k_B T} - \frac{3}{4}\frac{k_B T}{2\pi\rho_s}$, leading to

$$\xi = \frac{e}{8} \frac{v_s}{2\pi\rho_s} \exp\left(\frac{2\pi}{k_B T}\right) \left[1 - \frac{1}{2}\frac{k_B T}{2\pi\rho_s} + O\left(\frac{k_B T}{2\pi\rho_s}\right)^2\right] . \tag{4.49}$$

Recently this approach has been improved further by comparing $f(h) - f(0)$ of the NLσM with the result obtained directly from the 2DQHAFSL using a spin-wave expansion (Hasenfratz, 1999). This procedure circumvents the cutoff-effects that occur when going from the 2DQHAFSL to the QNLσM. The result is that ξ

in 4.49 is multiplied by a factor $\exp(-C(\gamma))$, where $\gamma = 2JS/T$ and

$$C(\gamma) = \frac{\pi}{2} + \ln 8\gamma + 2\pi\gamma 2 \int \frac{d^2k}{(2\pi)^2} \frac{s_k}{\eta_k} \frac{\eta_k \exp(-\eta_k) - 1 + \exp(\eta_k)}{\eta_k(1 - \exp(-\eta_k))} \ , \tag{4.50}$$

where $\eta_k = \gamma \left(\sum_{ij} (1 - \cos k_i)(1 - \cos k_j) \right)^{1/2}$. The function $C(\gamma)$ has been tabulated by Hasenfratz (1999). It has been pointed out by Beard *et al.* (1999) that that the same spin-wave theory also gives part of the $O\left(\frac{k_B T}{2\pi\rho_s}\right)^2$ term namely $3^3(k_B T)^2/2^3(4\pi\rho_s)^2$.

Within the momentum-shell renormalization scheme the structure factor is renormalized according to

$$S(q, t_0) = \exp\left[2l - \frac{n-1}{2\pi} \int_0^l t(l')dl' \right] S(e^l q, t(l)) \ , \tag{4.51}$$

which with the matching condition $\xi^2(t_0) + q^{-2} = e^{2l}$ leads to the scaling form

$$S(q) = S_0 f(q\xi) \quad , \quad f(x) = \frac{1 + \frac{1}{2} B_f \ln(1 + x^2)}{1 + x^2} \tag{4.52}$$

with $S_0 = S(q = 0) = \frac{B_S \xi^2}{(2\pi\rho_s / k_B T + 1)^2}$, where B_f and B_s are constants that cannot be determined within the renormalization approach. The one loop renormalization approach gives $B_f = 1$ (Chakravarty *et al.*, 1989), but higher order corrections are believed to give a value closer to zero (Tyč *et al.*, 1989, Makivić and Jarrell, 1992).

In addition to the renormalization group approach, the QNLσM has been treated in an expansion from the large-M limit, where M is the dimensionality of the field (Sachdev and Ye, 1992, Sachdev, 1992, Chubukov and Sachdev, 1993, Chubukov *et al.*, 1994). This approach reproduces most of the renormalization group results, but showed that the numerator of the scaling function $f(q\xi)$ only contains the logarithmic term for moderately large $q\xi > 1$, while $f(q\xi) \simeq (1 + 0.022 q^2\xi^2)/(1 + q^2\xi^2)$ for $q\xi \to 0$. This result shows that there is only a very small difference between ξ and the correlation length ξ_∂ defined from the second moment of $S(q)$. The same conclusion was reached in an $1/M$ expansion for ξ_∂/ξ, where the difference was found to be only 0.3% (Chubukov and Starykh, 1999). This reflects that the line-shape is in fact very close to a Lorentzian.

Quantum criticality

It was realized by CHN that the QNLσM had a critical value g_c of the effective coupling constant, above which the ground state was quantum disordered. Since the ground state of the 2DQHAFSL has long range order, it must correspond to a value of g below g_c. In comparison, the frustrated triangular lattice system is believed to have a quantum disordered ground state corresponding to $g > g_c$. But even for the square lattice, $\rho_s = 0.181J$ is considerably smaller than J, signaling that the system is not too far from the critical point.

Chubukov *et al.* (1994) have derived scaling forms for a number of physical observables including the instantaneous and dynamics structure factors. They are valid for a 2D quantum Heisenberg antiferromagnet in the vicinity of a quantum phase transition from a Néel ordered state to a spin fluid state. These general scaling considerations lead to the same linear temperature dependence of ξ^{-1} as in equation 4.46.

The QNLσM was treated in an expansion in powers of $1/M$. This led to results similar to the RG treatment of CHN, with a prediction for ξ in the QC regime

$$\xi = 0.962 \hbar c (T - 0.3098 \times 2\pi\rho_s)^{-1} \ . \tag{4.53}$$

For a g smaller than but close to g_c, the correlation length was expected to cross over from the RC prediction to the QC prediction. In the 2DQHAFSL, such a cross-over would be expected around $0.5J$, but a very important question is whether the mapping of the 2DQHAFSL onto the QNLσM is still valid at this temperature.

Elstner *et al.* (1995a) used high temperature expansions (HTE) for the instantaneous structure factor $S(q)$ and susceptibility $\chi(q)$ to address the question of such a cross-over. They suggested to consider the *spin wave mass* $m = v_s/\chi$ for the two respective models. The lowest $(1/M)$ order QC prediction is $m_{\rm QC}/T = 1.04$. For the RC prediction, they used the CHN-HN prediction modified by a renormalization group argument $m_{\rm RC} = \frac{16\pi\rho_s}{e} e^{-2\pi\rho_s/T}(1 - T/4\pi\rho_s)^{-1}$, and showed how the HTE result crossed over from $m_{\rm RC}$ to $m_{\rm RC}$ around $0.6J$. This is illustrated in figure 4.11. It would therefore be natural to conclude, that there is a cross-over in

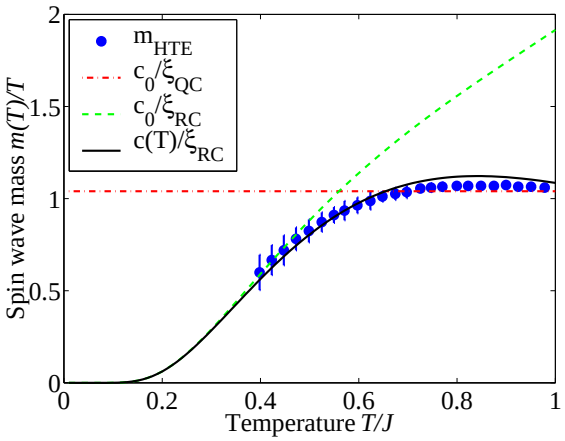

Figure 4.11. The temperature dependence of the spin wave mass $m(T) = c(T)/\xi(T)$ divided by temperature for respectively a high temperature expansion (HTE), the QC prediction and the RC prediction using either the zero temperature spin wave velocity c_0 or the temperature dependent spin wave velocity $c(T)$.

the spin wave mass from RC to QC behaviour. However, the RC prediction may also be plotted using the temperature dependent spin wave velocity

$$v_s(T) = v_s^0 \left(1 + \frac{\zeta(3)}{8\pi S}\left(\frac{T}{SJ}\right)\right)^{-1} \tag{4.54}$$

calculated by Kaganov and Chubukov (1988). In this case, which is the solid line in figure 4.11, the RC prediction is seen to follow almost exactly the HTE calculation. This illustrates that in discussing cross-over effects, care should be taken that all quantities are calculated to the same order in the approximations involved.

High-temperature expansion

The mapping onto the QNLσM is an approximation based on the assumption of low temperatures. High-temperature expansion (HTE) provides results in the other limit. To lowest order the correlation length becomes $\xi(T) = 1/\ln(T/JS^2)$, which has been shown by quantum Monte Carlo calculations to perform well down to $T \sim 2J$ (Manousakis and Salvador, 1989). HTE have been performed up to 14th order for the structure factor $S(q)$ of the two dimensional square lattice Heisenberg antiferromagnet for spin values between $S = 1/2$ and $S = 5/2$ (Elstner *et al.*, 1995a,b). The correlation length was extracted from the second moment definition. This study confirmed the experimental observations that the

second order result by Hasenfratz and Niedermayer (1991) failed for higher values of the spin. The explanation for this is that the cutoff in the NLσM calculation is approximately given by $\Lambda \sim ST/\rho_s a$. When Λ exceeds the Brillouin zone, it ceases to have effect and the integrals become equivalent to those of the classical model.

Pure-quantum self-consistent harmonic approximation

The connection with the classical model was also exploited in a so-called *pure-quantum self-consistent harmonic approximation* (PQSCHA) (Cuccoli *et al.*, 1995, 1996, 1997, 1998), where the quantum fluctuations integrated out in a Gaussian approximation leaving an effective classical model in which the Hamiltonian and the effective operators are functions of T and S. Defining an effective temperature T_{eff} the effective Hamiltonian is brought to the same form as that of the classical antiferromagnet. The correlation length is then given by $\xi(T) = \xi_{\text{cl}}(T_{\text{eff}})$, where the classical correlation length can be calculated by classical Monte Carlo methods. The validity of this approach is similar to that of the HTE with the advantage that any physical quantity that can be calculated in the classical model can be obtained within the PQSCHA and the calculation can easily be extended to include perturbative terms like a magnetic field, anisotropy or inter-plane coupling in the Hamiltonian.

Quantum Monte Carlo calculations

With analytic results for respectively the low and the high temperature limit, results obtained by quantum Monte Carlo (QMC) calculations have in combination with experimental data played a crucial role in establishing how the two limits connect (Lee *et al.*, 1984, Gomez-Santos *et al.*, 1989, Manousakis and Salvador, 1988, 1989, Ding and Makivić, 1990, Makivić and Ding, 1991, Kim *et al.*, 1997, Kim and Troyer, 1998, Harada *et al.*, 1998, Beard *et al.*, 1998, 1999, Keller-Marxer, 1999).

In QMC calculations, finite lattices of size $N \times N$ are considered and the analysis proceeds by increasing N until it the results converge. Obviously, aN has to be considerably larger than the correlation length, which sets a lower temperature limit for the applicability of the method. On increasing N the demand on the computational power increases drastically, and hence the system sizes have increased steadily with the development of faster computers. Today systems of $N = 1000$ have been studied down to temperatures where $\xi = 120$ (Kim and Troyer, 1998).

As a compensation for the limited system sizes, advanced methods for extrapolating the results to larger system sizes and towards $N \to \infty$ have been developed, by which reliable results have been obtained for ξ up to 10^5 (Caracciolo *et al.*, 1995, Beard *et al.*, 1998, 1999). These results illustrate how the CHN-HN prediction fails due to cutoff effects for ξ below 10^5 while the cutoff-corrected result by Hasenfratz (1999) holds down to $\xi \sim 100$.

Summary of theoretical predictions

In figure 4.12 the results of the different methods are summarized.

It is instructive to divide out the leading exponential temperature dependence, on which all approaches agree. In the right panel the results have been divided by the third order result by Hasenfratz and Niedermayer (1991). It is seen how upon increasing temperature first the CHN, then the HN and finally the Hasenfratz (1999) predictions depart from the QMC data at $T \sim 0.4 \times J$. But at that temperature the HTE and PQSCHA take over.

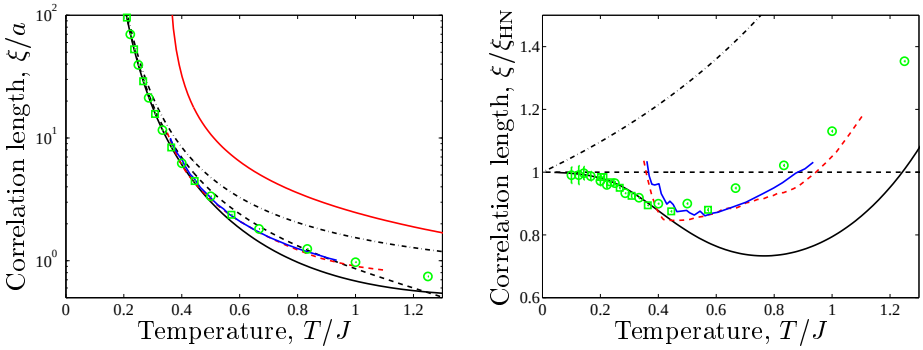

Figure 4.12. The theoretical and numerical predictions for the correlation length $\xi(T)$. In black lines the NLσM results (Chakravarty et al.*, 1989, dot-dashed), (Hasenfratz and Niedermayer, 1991, dashed) and (Hasenfratz, 1999, solid). In red the QC scaling (Chubukov* et al.*, 1994, solid) and the PQSCHA (Verrucchi, 1999, dashed). The HTE by Elstner* et al. *(1995b) is shown in blue, the green symbols are QMC data from (Kim and Troyer, 1998, squares) and (Beard* et al.*, 1998, circles) In the right panel, the predictions are plotted relative to the Hasenfratz and Niedermayer (1991) result.*

In summary, the panoply of methods that have been applied combine to a consistent description of the time independent properties as exemplified by the correlation length. The mapping of the 2DQHAFSL onto the NLσM is valid outside of the renormalised classical region, but only if the cutoff effects are properly taken into account when determining the relations between the parameters of the two models.

4.3.2 Experiments on cuprate 2DQHAFSLs

The instantaneous spin correlations in the cuprate materials La_2CuO_4 (Yamada *et al.*, 1989, Keimer *et al.*, 1992, Birgeneau *et al.*, 1995, 1999) and $Sr_2CuCl_2O_2$ (Greven *et al.*, 1994a,b, 1995) have been studied intensely using the energy integrating neutron scattering method that will be described below. By progressive improvements on the experiments, the correlation length $\xi(T)$ in these materials have now been measured in the temperature ranges $0.2 < T/J < 0.5$ for La_2CuO_4 and $0.2 < T/J < 0.4$ for $Sr_2CuCl_2O_2$.

For both materials i $\xi(T)$ in good accord with the prediction from the QNLσM and with QMC calculations. But the upper temperaure limit of these data is approximately where the different theoretical methods meet (*c.f.* figure 4.12). It would therefore be desirable to extend the experimentally probed temperature range beyond this limit. However, due to the high value of $J \sim 1500$ in these materials, it has proved difficult to improve the measurements further. Instead, the following sections present measurements on CFTD, where the much lower value of $J = 73$ K allowed determination of $\xi(T)$ up to $T \sim J$.

4.3.3 Energy integrating correlation length measurements

The neutron scattering cross-section is proportional to the dynamic structure factor $S(q, \omega)$, and therefore has to be integrated over energy ω in order to reach $S(q)$. In principle, this could be done by measuring $S(q, \omega)$ and then integrating the data over energy. However, as the signal is weak compared to the intrinsic background, this method is not feasible in practice. Instead, the low dimensionality is exploited in a 2-axis configuration, where the integration is performed directly.

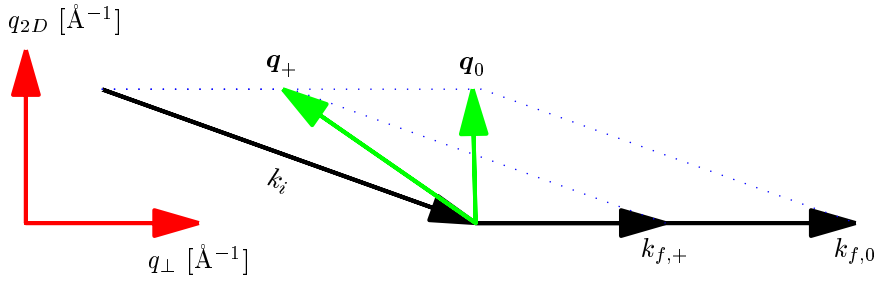

Figure 4.13. Illustration of the 2D energy integrating configuration for E_i = 10 meV when q is lying on the $(0,1,l)$ line. All values of $|k_f|$ are accepted, but only two are shown. They are $k_{f,0}$ corresponding to zero energy transfer and $k_{f,+}$ corresponding to $\hbar\omega = 5$ meV. It is seen how all possible q correspond to the same in-plane component q_{2D}.

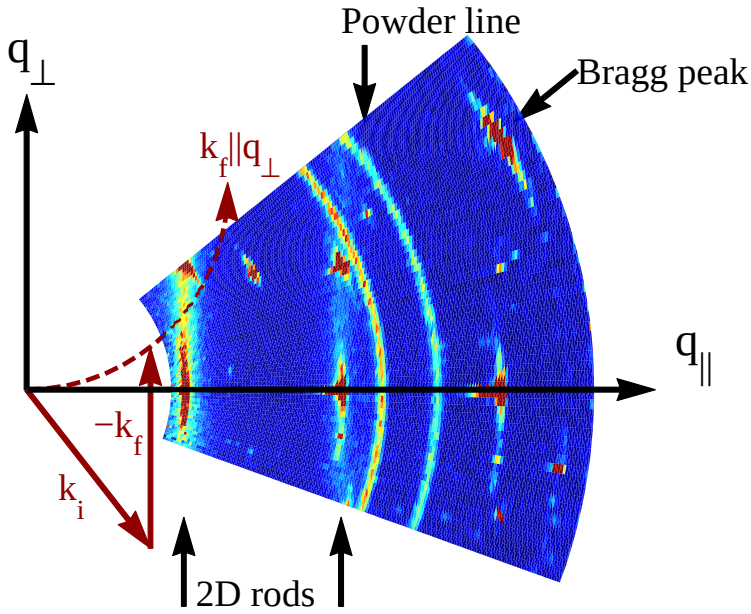

Figure 4.14. Direct measurement of the 2D rods in the $S = 5/2$ honeycomb antiferromagnet $MnPS_3$ obtained at a time-of-flight spectrometer by Wildes et al. *(1998a) (see also Wildes* et al. *(1994, 1998b) and Rønnow* et al. *(2000)). The zero energy transfer locus of an energy integrating scan is shown with the dashed line, illustrating the importance of choosing the incident energy so that the mosaic tails from the Bragg peaks are avoided.*

For low dimensional systems, the scattering will be independent of any momentum transfer in the 'missing' directions. In the 2D system, only the momentum transfer q_{2D} in the plane is important. By placing the planes perpendicular to the outgoing neutron wave-vector, q_{2D} becomes independent of the length of k_f (*c.f.* figure 4.13). By counting all neutrons scattered into this direction, the signal integrates over energy transfer corresponding to one particular q_{2D}.

In reality, the signal is only approximately equal to the instantaneous structure factor, but is rather given by:

$$\left.\frac{d^2\sigma}{d\Omega d}\right|_{2D} \propto \int_{-\infty}^{E_i} \frac{k_f}{k_i} \left|\tfrac{1}{2} g f(q)\right|^2 S(q_{2D},\omega) d\omega \simeq S(q_{2D}) \ , \tag{4.55}$$

where the factor $k_f/k_i = \sqrt{2m(E_i - \hbar\omega)}/k_i$ normalizes the incoming and outgoing

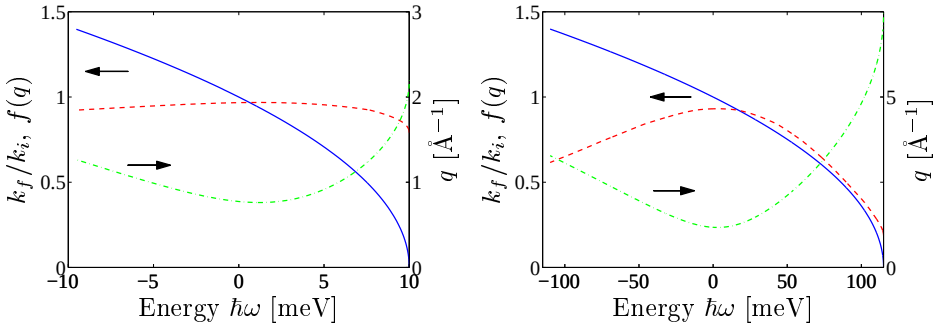

Figure 4.15. The scattering vector q (dot-dashed) and prefactors k_f/k_i (solid) and $|f(q)|^2$ (dashed) as a function of energy transfer, when the spectrometer is set to $q_{2D} = (\pi, pi)$ for respectively the measurements on CFTD (left) and on La_2CuO_4 (right).

flux and $f(q)$ is the form factor, which in this work is taken to be that of free Cu^{2+}.

For the integration to work, the excitation spectrum must be confined to an energy interval, in which the factor $\frac{k_f}{k_i}|f(q)|^2$ does not vary too much. In the experiments on CFTD, an incident energy of $E_i = 10$ meV$\simeq \frac{3}{2}J$ was used. In comparison, similar experiments on La_2CuO_4 and $Sr_2CuCl_2O_2$ used incident energies up to J and $J/3$ respectively. In the following, it is addressed how good the energy integration is for this choice of incident energy, and how corrections can be made for an imperfect integration.

For a given 2D momentum transfer, *e.g.* $q_{2D} = (\pi, \pi)$, the absolute length of q becomes a function of the energy transfer as shown in figure 4.15. Also the factors k_f/k_i and $|f(q)|^2$ are depicted. It is seen that in the interval $-E_i < \omega < E_i$, the longest q vector is equal to k_i, which for CFTD gives $|f(k_i)|^2 = 0.79$ and for La_2CuO_4 (with $E_i = 115$ meV) $|f(k_i)|^2 = 0.19$. Whereas $f(q)$ is almost constant for CFTD, the $k_f/k_i = \sqrt{1 - \hbar\omega/E_i}$ factor does vary, and its influence on the measurements should be taken into account.

An elastic filter to remove incoherent background

Despite the deuteration, the sample still provided a significant incoherent background, which became a problem as the peak in $S(q)$ broadened and weakened with increasing temperature. To circumvent this problem, a special kind of filter was constructed. By placing crystals of pyrolytic graphite (PG) in the outgoing beam (between sample and detector) and tuning them to Bragg scatter neutrons with $E_f = E_i$, an elastic filter was realized. The idea was that while the magnetic signal is distributed over energy, the incoherent signal stays elastic, hence the filter will mainly discard the incoherent with only moderate effects on the magnetic scattering.

In practice there are several technical aspects that need consideration. Firstly, due to the finite resolution of the front end of the spectrometer, there will be a distribution of incident energies around the nominal E_i. For the filter to successfully suppress all elastically scattered neutron, it must have a relaxed Bragg-scattering condition with at least the same energy width as the incoming beam. On the other hand, it should not exceed this width as the magnetic signal should remain as little affected as possible. Such a matching of the energy width can be achieved by using several crystals each with a fairly small mosaicity. By slightly misaligning the individual crystals, the total energy width can be controlled.

The second important point is that if the individual crystals are placed too closely after each other, the neutrons scattered out of the beam by one crystal can be scattered back into the beam by the previous crystal. This will reduce the

reduction factor of N crystals with individual transmission t from t^N to $\frac{t}{N(1-t)}$. This can be avoided by placing the crystals far enough apart that the rejected neutrons can escape at the side of the filter as illustrated in figure 4.16.

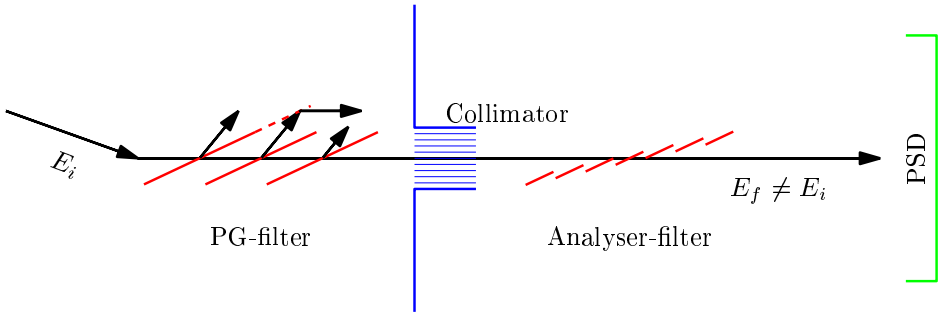

Figure 4.16. Schematic drawing of the elastic filter with 3 1"×2" crystals and the 7 analyser blades rejecting the neutrons that have been elastically scattered at the sample.

The filter was composed of 3 1"×2" crystals before the collimator at the entry of the detector tank. These were aligned by hand as to minimize the count rate in the background. The fine-tuning of the total transmission function was achieved with the analyser block with its 7 individually turnable blades. This is a good example of how a flexible instrument design facilitates specialized experiments. The analyser block was oriented such that effectively 2 blades were encountered along any neutron path to the detector.

Once calibrated to expel 10 meV neutrons, the transmission function $T(\omega)$ of the filter was determined by scanning the incident energy as shown in figure 4.17. The transmission function was best described by a sum of two Gaussians as defined to the right of the figure.

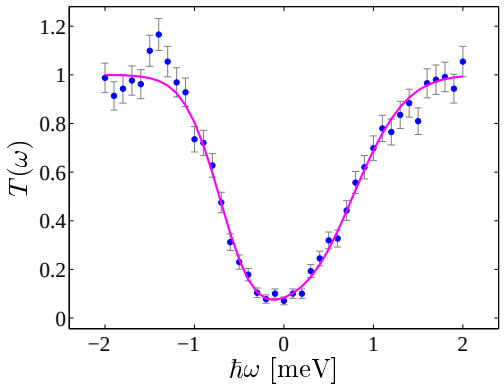

$$T(\omega) = 1 - \sum_n a_n e^{-\frac{1}{2}\frac{(\omega-\omega_n)^2}{\sigma_n}}$$

n	a_n	ω_n	σ_n
1	0.37	-0.46 meV	0.34 meV
2	0.81	0.20 meV	0.58 meV

Figure 4.17. The measured transmittance $T(\omega)$ through the elastic filter around the filtering energy of 10 meV. *The solid line is a fit to a double Gaussian shape as defined to the right.*

Corrections for non-perfect integration

The error contained in the actual integration of $\int_{-\infty}^{E_i} \frac{k_f}{k_i}|f(q)|^2 S(q,\omega)T(w)d\omega$ compared to the definition $S(q) = S(q,\omega)$ can be estimated by assuming a functional form for $S(q,\omega)$. The behaviour of $S(q,\omega)$ at finite temperatures is discussed in section 4.4. For the present purpose, the prediction from RG and scaling arguments based on the QNLσM mapping is used.

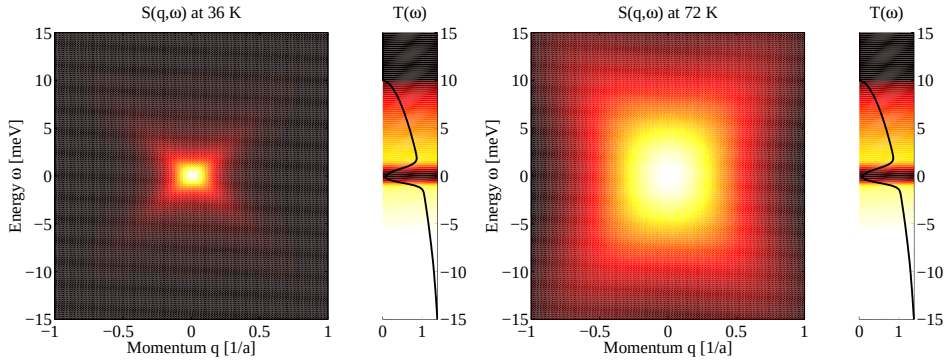

Figure 4.18. The dynamic structure factor $S(q,\omega)$ at 36 K *and at 70* K *in the scaling prediction (Tyč* et al.*, 1989). The panels to the right illustrate the experimental integration factor $\frac{k_f}{k_i}|f(q)|^2T(\omega)$. Black is zero and white is maximum.*

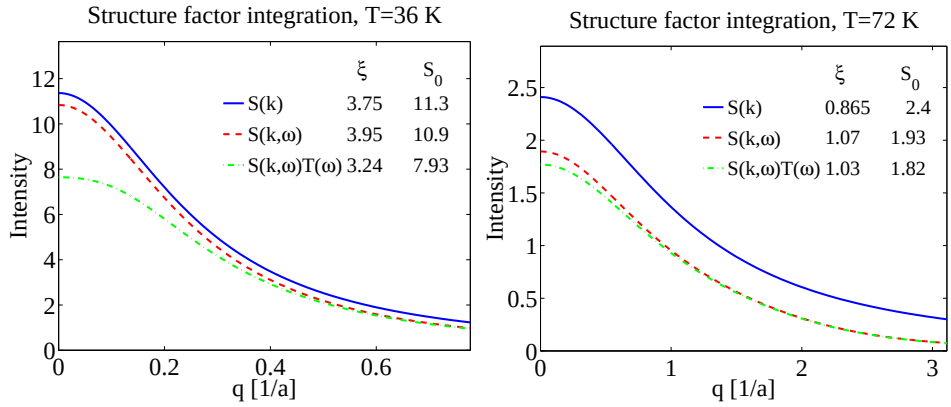

Figure 4.19. The line-shapes at 36 K *and at 72* K *obtained respectively by correct integration (solid blue), actual integration without (dashed red) and with the elastic filter (dot-dashed green). The ξ and S_0 obtained by Lorentzian fits are listed.*

In figure 4.18 pseudocolour plots of $S(q,\omega)$ are shown for $T = J/2 = 36$ K and $T = J = 72$ K. The integration factor is illustrated as colour bars on the right side of the plots. At 36 K the spectral weight is confined to a few meV around 0, over which the integration factor does not vary much. This is no longer the case at 72 K, where the spectral weight has been distributed over an energy range similar to the integration range. On the other hand, the elastic filter has most effect at low temperatures, which is also realized when considering the line-shapes expected respectively without and with filter.

Three different line-shapes were calculated by numerical integration of the line-shapes for respectively the true $S(q)$, the integration range affected result $\int_{-\infty}^{E_i} \frac{k_f}{k_i}|f(q)|^2 S(q,\omega)d\omega$ and the result that would be obtained with an elastic filter $\int_{-\infty}^{E_i} \frac{k_f}{k_i}|f(q)|^2 S(q,\omega)T(w)d\omega$. These line-shapes were fitted to Lorentzians, giving values for ξ and S_0 as shown in figure 4.19. The difference between $S(q)$ and $S_x(q)$ is illustrated for 36 K and 72 K in figure 4.19.

Being able to calculate the ratio between the ξ and S_0 that will be extracted from an experiment and the real values, makes it possible to correct for the imperfect integration. The experimentally determined parameters should be divided by this ratio, which is shown as a function of temperature in figure 4.20.

It is seen how below $T \sim J/2$, the integration range means little to the result, while the elastic filter drastically lowers the measured values for both ξ and S_0.

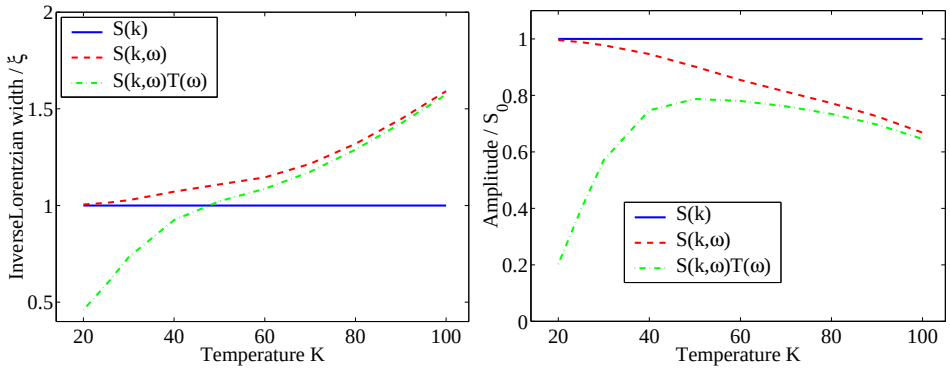

Figure 4.20. Correction factors for the correlation length ξ and the amplitude S_0, respectively without (dashed red) and with the elastic filter (dot-dashed green).

Above $T \sim J/2$, the elastic filter has less effect, but the integration range starts to have influence. As long as the correction factors remain fairly small, they are rather insensitive to the precise form of the assumed $S(q,\omega)$, but beyond 100 K, the correction factors become so large that the result becomes biased by the choice of $S(q,\omega)$. In order to perform measurements beyond this temperature, the incident energy should be raised.

4.3.4 Experimental details

The energy integrating neutron scattering measurements were performed using the RITA (re-invented triple axis) spectrometer at Risø. A schematic drawing of the instrument is shown in figure 2.2 of chapter 2. The features of this instrument makes it particularly suitable for studies of low-dimensional systems. The premonochromating velocity selector suppresses higher order contamination in the beam by a factor of 10^3 at 10 meV. This is important because it allows a free choice of incident energy to optimize the resolution, (q,ω) range or in this case the energy integration without being restricted to the energies suitable for filters such as BeO, Be or PG. The front-end is equipped with a vertically focusing monochromator and focusing neutron guides, giving a high flux at the sample position. Often, measurements on low-dimensional systems are limited by the intensity and not by the resolution. The analyser consists of 7 individually turnable blades, allowing a custom modeling of the resolution in (q,ω). For this experiment, the analyser was removed and the detector placed in the two-axis position.

The 17×12 cm^2 position sensitive detector (PSD) can in combination with the 7-blade analyser be used to image planes in (q,ω) space. This experiment employed a simpler but very powerful use of the PSD. By inspecting the distribution of counts over the detector, so-called spurion intensity due to for instance coincidental failure of the shielding for particular arrangements of the spectrometer can be recognized. An example of such spurion intensity is shown in figure 4.21. By masking out the part of the detector that suffers from spurion intensity, the otherwise problematic apparently q dependent noise can be removed. Often, the center of the detector will hold the best signal to noise ratio, so by integrating the counts in a window of the detector, the signal to noise ratio can be improved. At the same time, however, the absolute number of counts decreases, and there will be an optimum detector-size, where the background intensity and statistical scatter contribute equally to the standard error when the data are fitted during analysis. The important point about the PSD is that all this masking and windowing can be performed during the process of analysis, after the experiment has taken place.

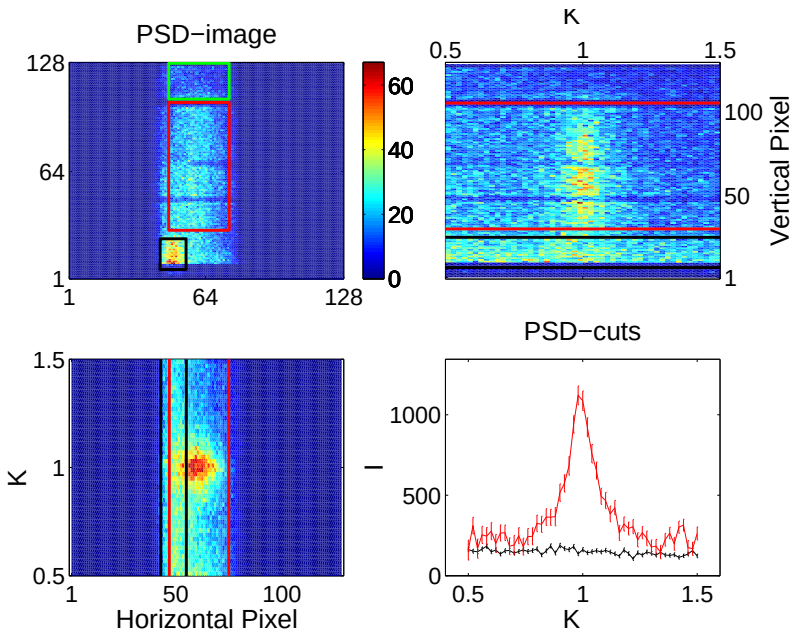

Figure 4.21. Visualization of the counts in the PSD during a scan through the $(0, 1, l)$ *rod. Upper left: the sum over all scan point for each pixel in the detector. The three windows that have been selected contain respectively signal (red), uniform background (green) and a spurion (black). Upper right: The data summed over the horizontal pixels. It is seen how the signal peaks at the scan center, while the spurion increases in intensity with decreasing scattering angle (*K*) all the way. Lower left: The data summed over the vertical direction. In the horizontal direction, the signal is much more concentrated, which is because the spectrometer only employs horizontal collimation — in fact the spectrometer is vertically focusing. Lower right: the counts in respectively the signal window and the spurion window. It is seen how masking of the spurion reduces the background by more than 50%.*

Convolution with the experimental resolution

As explained above, scans through the $(0, 1, l)$ rod are expected to measure S(q) convoluted by the experimental resolution. Since the correlation length $\xi(T)$ decreases exponentially, $S(q)$ will go from being narrow to being broad. To accommodate this, three different resolutions were employed. The instrument resolution can most easily be controlled by insertion of collimators. At the lowest temperatures, a collimation of 15' was used to give sufficient resolution to measure the narrow width of $S(q)$. At higher temperatures, this gave unnecessarily good resolution with a concomitant loss in intensity. Therefore also 30' and 60' collimations were used. Finally, for the highest temperatures also the elastic filter was used in combination with 60' collimation.

In each configuration, the resolution was determined experimentally, by performing grid scans of the (0,1,0) and (0,1,1) Bragg peaks as shown in figure 4.22. The principal axes and orientation of the resolution ellipse were extracted by fitting a Gaussian function to the grid-data. The vertical resolution was determined by tilting the sample. The resolution is given by $\Delta q = Q\Delta\lambda$, where λ is the angle of $\boldsymbol{Q}$ perpendicular to the scattering plane.

Having determined the resolution, the experimental data were analysed by fitting it to the theoretical scattering cross-section (a Lorentzian in this case) convoluted with the resolution function. The convolution was performed using an adaptive algorithm to ensure convergence.

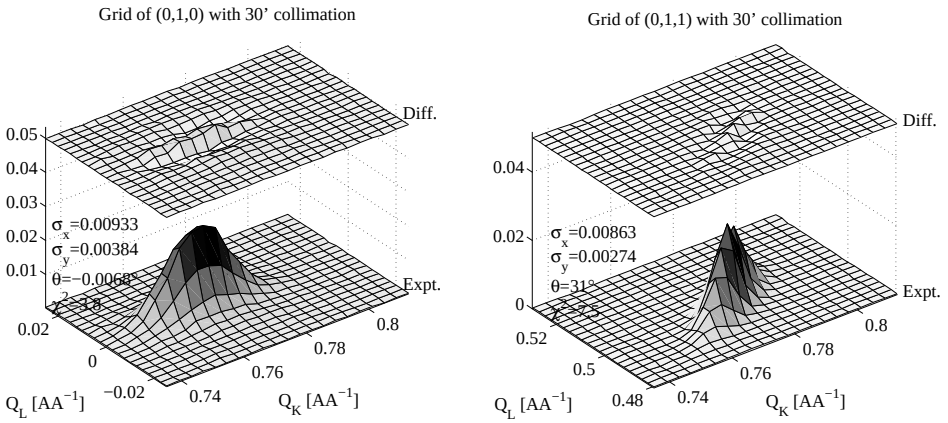

Figure 4.22. The instrument resolution was determined by grid scans of the (0,1,0) and (0,1,1) Bragg peaks. Both the measured intensity and the remainder after fits to Gaussian functions are shown.

Sample and cryostat

The $12 \times 12 \times 4$ mm^3 single crystal of CFTD was grown by Andrew Harrison and Douglas I. D. Youngson by slow dedeuteration of $Cu_2CO_3(OD)_2{\cdot}D_2O$ in a solution of d_2-formic acid in D_2O. It was mounted on a cadmium coated aluminum pin and lowered in a helium flow cryostat (Orange type) with a base temperature of 1.6 K. The reciprocal axes b^* and c^* were in the scattering plane, so that scans could be performed through the $(0, 1, l)$ rod with $c^*||k_f$.

Data

Scans were recorded at a series of temperatures ranging from $T_N = 16.5$ K to 100 K using the four different instrument configurations mentioned above. In figure 4.23, typical data for each of the four configurations are shown. The right panel illustrates how the use of the elastic filter changed the signal to noise ratio from 1/10 to 2/1. This allowed data to be taken up to 90 K as seen in figure 4.24. The signal still allows a quite accurate fit to the peak, but above this temperature, the integration range required progressively larger correction factors. Because the correction factors rely on an assumption about $S(q, \omega)$, analysis of data beyond this temperature would not be unbiased.

Analysis

The experimental data were well described by Lorentzians and were insufficient to distinguish between other possible lineshapes. The data were therefore fitted to a Lorentzian line shape convoluted by the full experimental resolution. At each point of the scan, the resolution was found by interpolating between the two measured resolution ellipses. Since $S(q)$ does not depend on the momentum transfer perpendicular to the planes, the resolution ellipse was projected down along this direction. In the two remaining directions, the convolution was carried out numerically by an adaptive algorithm to ensure convergence. The results of these fits can be seen as the solid lines in figure 4.23 and 4.24.

4.3.5 Results for $\xi(T)$ and $S_0(T)$

The experimental data for $\xi(T)$ as summarized in figure 4.25 covers the temperature range $0.2 \times J < T < 1.25 \times J$ and two orders of magnitude in ξ. It is seen that there is good agreement between the data for each of the four configurations in the

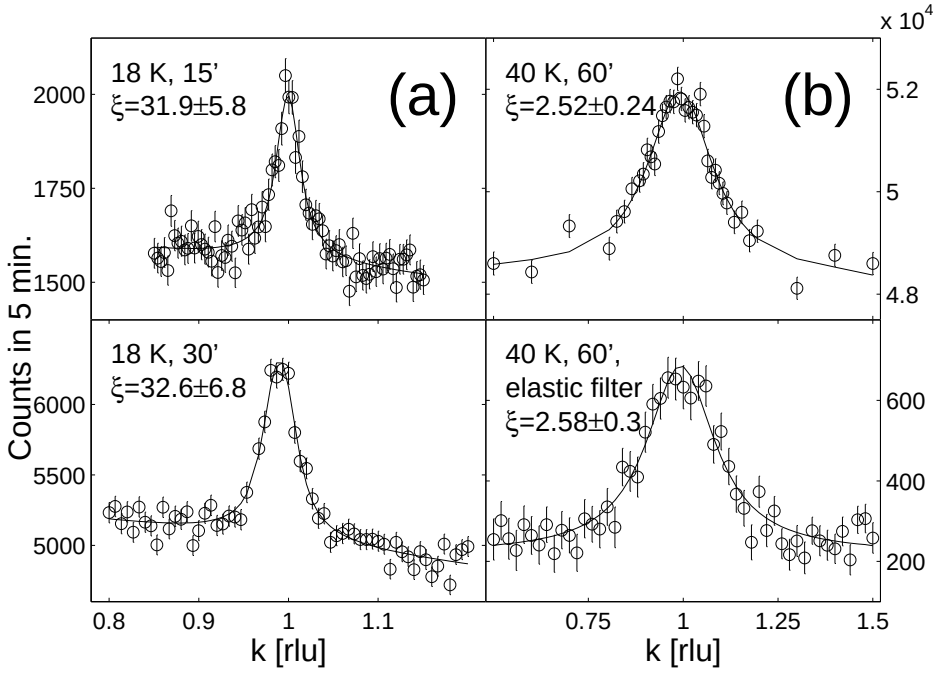

Figure 4.23. Typical scans through the $(0,1,l)$ *rod. (a) Data taken at 18* K *with respectively 15' and 30' collimation. (b) Data taken at 40* K *with 60' collimation with and without the elastic filter. It is seen how the different configurations of the spectrometer gave consistent values for the correlation length* ξ*.*

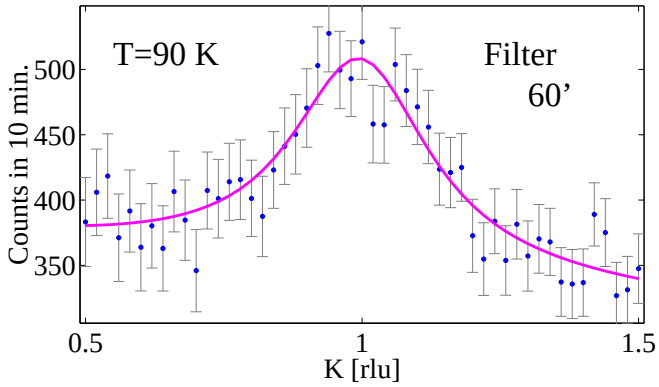

Figure 4.24. Scan taken at 90 K *with the elastic filter.*

region of overlap. At the lowest temperatures, the coarse resolution configurations underestimate ξ. At these temperatures the peak width is about a tenth of the coarse resolution, which makes the determination vulnerable to systematic error due to imperfect determination of the resolution. Thus for low temperatures, most emphasis should be put on the data taken with 30' and 15' collimation.

In the lower panel where the data are plotted relative to the HN prediction it is seen that $\xi_{\mathrm{expt}}/\xi_{\mathrm{HN}}$ changes from 1 to about 0.8 at $T = J/2$ and increases above 1 for higher temperatures. Although the error bars and scatter of the data are unsatisfactorily large in this presentation, the behaviour is seen to be consistent with Hasenfratz (1999) and the PQSCHA results. Thus for the first time has the behaviour in the region where the different theoretical approaches meet been tested experimentally.

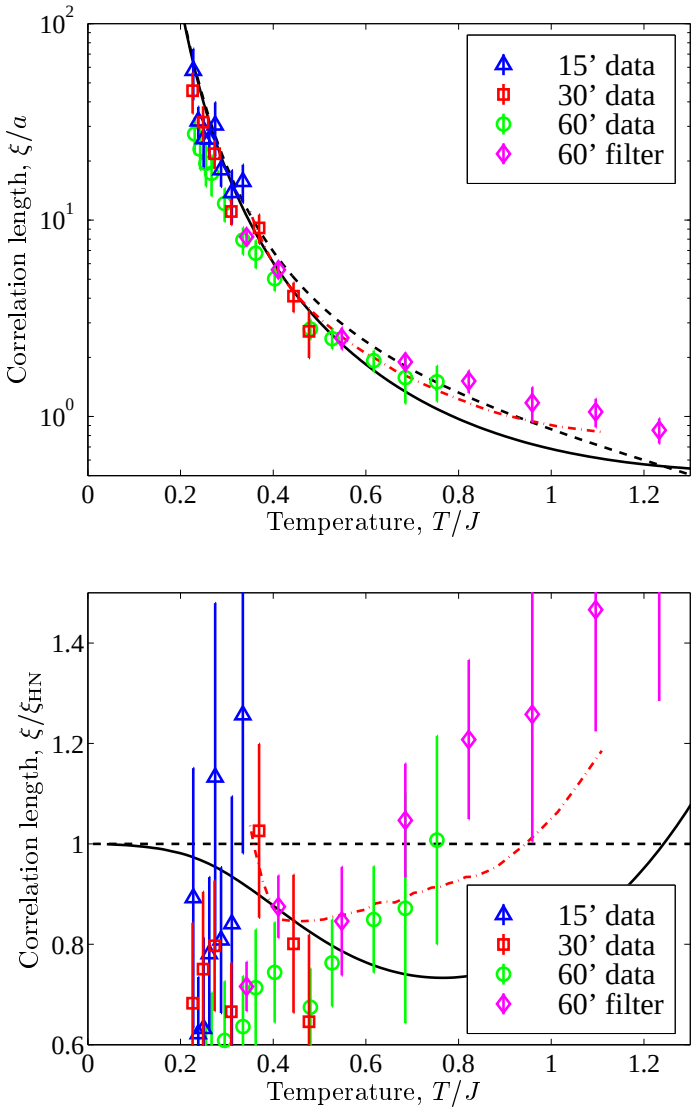

Figure 4.25. The measured correlation length $\xi(T)$ for each of the four configurations. The data are compared to the NLσM predictions (Hasenfratz and Niedermayer, 1991, dashed black) and (Hasenfratz, 1999, solid black) and the PQSCHA result (dot-dashed red).

Although most emphasis has been on the correlation length, the experiment in principle also gives a determination of the amplitude S_0 of the structure factor. In this case, however, the lack of an absolute normalization of the data complicates a decisive interpretation of the data. In figure 4.26 the data for the different configurations have been normalized to each other in the regions of overlap. It is seen that it is possible in this manner to collapse the data on one curve which covers more than two orders of magnitude. At temperatures above $0.8 \times J$ the amplitude becomes more or less constant, in apparent agreement with the NLσM result. However, as seen from the correlation length it is questionable whether the NLσM result should be given any significance above $J/2$.

The NLσM prediction for S_0 has actually been questioned even for $T < J/2$ on the basis of data from $Sr_2CuCl_2O_2$, where a constant value for S_0/ξ^2 was reported (Greven *et al.*, 1995). This question is addressed in the lower panel, where S_0/ξ^2 is shown as a function of temperature. Though it is difficult to draw conclu-

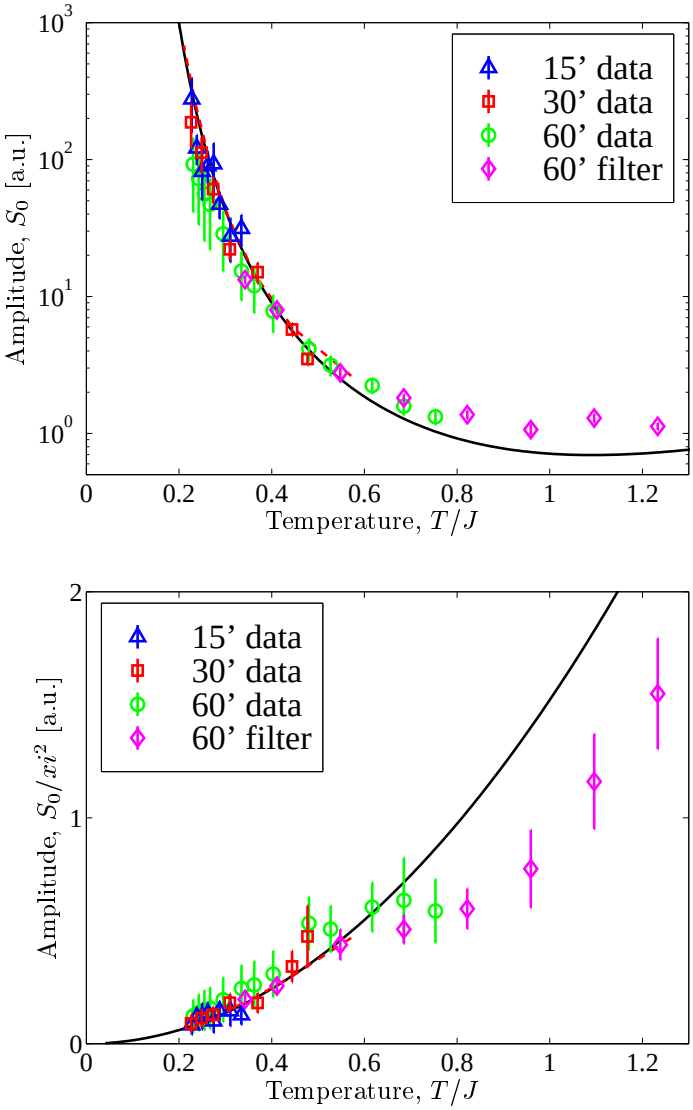

Figure 4.26. The measured amplitude $S_0(T)$ for each of the configurations have been scaled to agree within the regions of overlap. Similarly has the predictions from the NLσM (solid black) and the QMC (Kim and Troyer, 1998, dashed red).

sions about the functional form it is clear that there is a significant temperature dependence.

4.3.6 Consolidation of the time independent properties

Recently, these results have been complemented by a proton NMR study on $Cu(HCO_2)_2{\cdot}4D_2O$ (Carretta *et al.*, 2000). By analyzing the relaxation rate through a mode-coupling approach, the correlation length has been extracted in a temperature interval similar to the present study. Though the determination of $\xi(T)$ is less direct than for the neutron scattering data, the analysis reaches a consistent conclusion.

In summary, the introduction of CFTD as a physical realization of the 2DQHAFSL has added to the cuprate based investigations by allowing measurements over the temperature region where there was a gap between the different theoretical approaches (Rønnow *et al.*, 1999). Subsequently this gap has been closed by extend-

ing the QMC calculations (Beard *et al.*, 1999) and by performing a more correct treatment of the cutoff effects when mapping the 2DQHAFSL onto the QNLσM. It is therefore fair to say that the time independent behaviour of the 2DQHAFSL has been understood on a detailed quantitative level.

4.4 Fluctuations at finite temperature

This section describes a time-of-flight neutron scattering experiment on CFTD. The purpose was to address the behaviour of the excitation spectrum at finite temperatures, where the correlation length decreases exponentially with temperature. The experiment showed that even at $T \sim J/2$, where $\xi \sim 3a$, the excitation spectrum contains well defined spin-waves albeit damped and softened considerably. The temperature dependence of both the damping and the softening was found to be consistent with theoretical predictions, but additional efforts are needed both theoretically and experimentally, before the dynamic behaviour of the 2DQHAFSL can be consolidated.

Having understood the instantaneous correlations in the 2DQHAFSL, we now turn to the dynamic behaviour. Again, most of the physics is compiled in a pair-correlation function

$$S(q,\omega) = \int dt\, e^{-i\omega t} \sum_{RR'} e^{iq\cdot(R'-R)} \langle S_0(0) \cdot S_R(t) \rangle \tag{4.56}$$

known as the dynamic structure factor.

Most descriptions of excitation spectra in many-body physics build on the notion of quasi-particles that are elementary excitations from a certain ground state. At $T = 0$, the elementary excitations in the antiferromagnetically ordered ground state of the 2DQHAFSL are spin-waves. At finite temperature, the ground state is no longer ordered but the existence of large correlated regions enables spin-wave like excitations to persist.

Very few experimental results exist on the finite temperature excitation spectrum of the 2DQHAFSL. In a triple-axis neutron scattering study of CFTD, Clarke (1991) and Clarke *et al.* (1999) measured scans along both energy and q at temperatures up to $T \sim 0.4 \times J$. Above $T_{\rm N}$ they observed spin-wave peaks that were broadened and lowered in energy as the temperature was increased. Using time-of-flight (TOF) neutron scattering, the full $S(q,\omega)$ along $(1,1)$ and $(1,0)$ has been measured for temperatures up to $T \sim J/2$. The excitation spectrum is still composed of spin-waves, albeit damped and softened due to the loss of long range order at finite T.

The following lists the available theoretical predictions for the finite temperature dynamics, then describes the TOF experiment and its analysis and discusses the results. According to my knowledge, literature contains no reports of direct measurements of the spin-wave damping in the 2DQHAFSL. I believe that the present measurements on CFTD will stimulate a convergence of the theoretical predictions and aid to a better understanding of excitations in short range ordered systems.

4.4.1 Theories of excitations at finite temperatures

At $T = 0$ the excitation spectrum contains well defined spin-waves. Due to the negative curvature of the dispersion relation, energy and momentum conservation prevents a single-magnon from spontaneously decaying into multi-magnon excitations. At finite T there are two mechanisms for decay of a magnon excitation; i) it can be scattered against other thermally excited magnons and ii) due to the finite correlation length $\xi(T)$ a propagating spin-wave will eventually be scattered against the 'boundary' of the region where its polarization matches that of the order parameter. The finite life-time, τ, of the spin-wave excitations results in a line-width, $\Gamma = 1/\tau$, of the excitation spectrum.

A number of articles deal with the finite temperature excitation spectrum using a variety of different approaches. With the first experimental results at hand it is time to reach a coherent picture of the problem. In the following, a short

review is given of the reported results. No attempt is made to asses the validity of the approximations used in the different approaches. Instead, the results are compared to the experimental data in an attempt to reach a conclusion or at least guide further theoretical efforts towards consensus. We begin, though, by some considerations over what functional form is adequate to describe the excitation spectrum in the presence of finite life-times.

Lifetimes and line-shapes

The excitation spectrum is contained in the dynamic structure factor $S(q,\omega)$, which is the Fourier transform in space and time of the spin-spin correlation function $\langle S_0(0)S_R(t)\rangle$. An excitation mode with a characteristic frequency ω_q and a finite life-time τ_q, will give rise to a peak in $S(q,\omega)$ at approximately ω_q and with width approximately $\Gamma_q = 1/\tau_q$. If $\Gamma_q \ll \omega_q$, this picture holds precisely, but as the damping factor Γ_q becomes comparable to the frequency, the excitation spectrum develops a non-trivial line-shape.

The line-shape problem has been discussed by Fåk and Dorner (1992, 1997) in the case of phonons in solids and liquids. Much of their discussion can be generalized to magnetic excitations, as it is based on the linear response theory. The dynamic structure factor is related to the imaginary parts of the generalized susceptibility and the retarded Green's function as:

$$S(q,\omega) = \frac{1}{\pi}\frac{-1}{1-e^{-\omega/T}}\chi''(q,\omega) = \frac{1}{\pi}\frac{-1}{1-e^{-\omega/T}}Z_q G''(q,\omega)\ , \tag{4.57}$$

where Z_q is a normalization factor.

For well defined excitations with infinite life-time, the retarded Green's function is given by

$$G_0(q,\omega) = \frac{1}{\omega-\omega_q+i\varepsilon} - \frac{1}{\omega+\omega_q+i\varepsilon}\ , \tag{4.58}$$

where ε is a positive infinitesimal number and ω_q the frequency of the excitation. The imaginary part is

$$\mathrm{Im}\{G_0(q,\omega)\} = -\pi[\delta(\omega-\omega_q) - \delta(\omega+\omega_q)]. \tag{4.59}$$

The full Green's function (including damping terms) can be derived through Dyson's equation

$$G(q,\omega) = \frac{1}{G_0^{-1}(q,\omega)-\Sigma_q(\omega)} = \frac{2\omega_q}{\omega^2-\omega_q^2-2\omega_q\Delta_q(\omega)+2i\omega_q\Gamma_q(\omega)}\ , \tag{4.60}$$

where the self-energy $\Sigma_q(\omega) = \Delta_q(\omega) - i\Gamma_q(\omega)$ has to be calculated *e.g.* through a diagramatic expansion. The real part describes the energy shift relative to the zeroth order dispersion relation ω_q, while the imaginary part $\Gamma_q(\omega)$ is related to the inverse life-time.

It is desirable to parameterize the general function in a way that experimental data can be fitted to a small number of parameters. Often it will be the case, that the unperturbed dispersion relation ω_q can be derived from theory with just a few parameters entering the functional form. On the other hand, the functions $\Delta_q(\omega)$ and $\Gamma_q(\omega)$ will only in special cases be calculable. Instead, it is practical to keep only the first terms in a power expansion. The real part of the self energy is an even function of energy and can be approximated by $\Delta_q(\omega) \simeq \Delta_q$, while the imaginary part is an odd function that will be approximated by $\Gamma_q(\omega) \simeq \Gamma_q\omega/\omega_q$. The approximation is good for small ω, but not necessarily for larger energies.

The resulting Green's function

$$G(q,\omega) = \frac{2\omega_q}{\omega^2-\Omega_q^2+2i\omega\Gamma_q} \tag{4.61}$$

with $\Omega_q^2 = \omega_q^2 + 2\omega_q\Delta_q$, corresponds to the result for a damped harmonic oscillator. It is important to realize that the perturbations of or interactions among the excitations in general lead to both a damping Γ_q and a shift of the excitation energy from ω_q to $\Omega_q \simeq \omega_q + \Delta_q$.

The dynamic structure factor can be written in several mathematically equivalent forms

$$S(q,\omega) = \frac{1}{\pi}\frac{1}{1-e^{\omega/T}} Z_q' \frac{4\omega\Omega_q\Gamma_q}{(\omega^2-\Omega_q^2)^2 + 4\omega^2\Gamma_q^2} \tag{4.62}$$

$$= \frac{1}{\pi}\frac{1}{1-e^{\omega/T}} Z_q'' \left[\frac{\Gamma_q}{(\omega-w_q)^2+\Gamma_q^2} - \frac{\Gamma_q}{(\omega+w_q)^2+\Gamma_q^2}\right] , \tag{4.63}$$

where $Z_q' = Z_q\omega_q/\Omega_q$, $w_q^2 = \Omega_q^2 - \Gamma_q^2$ and $Z_q'' = Z_q\omega_q/w_q$.

For $\Gamma_q \gg \Omega_q$ it is essentially a single Lorentzian at $\omega = 0$. For $\Gamma_q < \Omega_q$ the scattering is very close to the sum of two Lorentzians located at $\omega \pm \omega_q$, which is an often used line-shape

$$S(q,\omega) = \frac{1}{\pi}\frac{1}{1-e^{\omega/T}} Z_q\omega \left[\frac{\Gamma_q}{(\omega-\omega_q)^2+\Gamma_q^2} + \frac{\Gamma_q}{(\omega+\omega_q)^2+\Gamma_q^2}\right] . . \tag{4.64}$$

However, there exist few (if any) examples where the double-Lorentzian with a plus-sign comes out as a theoretical line-shape. It has the unphysical properties that the zeroth and first moments diverge at zero temperature. The first moment also diverges in the high temperature limit. The inadequacy of the sum of two Lorentzians is discussed in the context of the 2DHAFSL by Wysin and Bishop (1990).

Ideally, the neutron scattering cross-section should off course be compared to the true $S(q,\omega)$ when calculable, but in terms of reducing the data to a set of parameters which can be compared to theory, the above considerations are useful and add only the two parameters Δ_q and Γ_q to the parameters involved in ω_q.

Tyč, Halperin and Chakravarty (89)

Using a combination of hydrodynamics, scaling and RG analysis, Tyč *et al.* (1989) (CHN-Tyč) reached a scaling relation

$$S(q,\omega) = \omega_0^{-1} S(q)\Phi(q\xi, \omega/\omega_0) \tag{4.65}$$

$$\omega_0 = \frac{v_s}{\xi(T)}\sqrt{\frac{T}{2\pi\rho_s}} , \tag{4.66}$$

where $S(q)$ is the equal time correlation function, $\xi(T)$ is the correlation length at temperature T and v_s is the zero temperature spin-wave velocity. As a dynamic scaling function they use the simple sum of two Lorentzians

$$\Phi(q,v) = \frac{\gamma_q}{(v-v_q)^2+\gamma_q^2} + \frac{\gamma_q}{(v+v_q)^2+\gamma_q^2} , \tag{4.67}$$

with the dimensionless spin-wave frequency v_q and damping factor γ_q given by:

$$v_q = \sqrt{\frac{3}{2}}q\sqrt{\delta + \frac{1}{2}\ln(1+q^2)} \tag{4.68}$$

$$\gamma_q = \frac{\gamma_0\sqrt{1+\mu k^2\xi^2}}{[1+\frac{1}{2}\Theta\ln(1+k^2\xi^2)]^{3/2}} , \tag{4.69}$$

where *classical rotor simulations* were fitted to give $\delta = 1.7$, $\gamma_0 = 0.8$, $\mu = 2.0$ and $\Theta = 0.15$ or $\delta = 1.05$, $\gamma_0 = 0.86$, $\mu = 1.4$ and $\Theta = 0.08$.

The $q \to 0$ limit of the spin-wave frequency $\omega_q(T) = \omega_0 v_q$ gives the finite temperature spin-wave velocity $v_s(T) = \omega_o \xi \sqrt{\frac{3\delta}{2}} = v_s(0)\sqrt{\frac{3\delta}{2}}\sqrt{\frac{T}{2\pi\rho_s}}$. The factor of $\sqrt{\frac{3}{2}}$ comes from $\chi_\perp(T) \simeq \frac{2}{3}\chi_\perp(0)$, due to the absence of broken symmetry at finite T.

Tyč and Halperin (90)

Tyč and Halperin added a microscopic calculation of spin wave collisions within the Dyson-Maleev formalism (Tyč and Halperin, 1990). They give 4 different k regions: A, B, C and D:

$$A: \qquad \Gamma_q = J\frac{ze(q)\tau^2}{2\pi S}\left(\ln(\frac{2\pi S^2}{\tau^2}) + C_A\right) \tag{4.70}$$

$$B: \qquad \Gamma_q = J\frac{ze(q)\tau^2}{2\pi S}\left(\ln(\frac{\tau}{q}) + C_B\right) \tag{4.71}$$

$$C: \qquad \Gamma_q = J\frac{7z\zeta(\frac{5}{2})}{8(2\pi)^{3/2}S}\left(e(q)\tau^5\right)^{1/2} \tag{4.72}$$

$$D: \qquad \Gamma_q = J\frac{3z\zeta(3)}{8\sqrt{2}\pi S e(q)\sqrt{f(\hat{q})}}\tau^3 \ , \tag{4.73}$$

where $\tau = 2T/JzS$, $z = 4$ is the number of neighbors and $e(q) = \sqrt{1-\gamma_q^2}$ is the normalized dispersion. The regions are separated by:

$$q_{\min} \ll q_A \ll \tau^3/2\pi S^2 \ll q_B \ll \tau \ll q_C \ll \tau^{1/3} \ll q_D \ll 1 \ . \tag{4.74}$$

Following the spirit of CHN mapping, they rewrite the result in terms of spin-wave velocity c and spin wave stiffness ρ_s.

$$A: \qquad \Gamma_q = \frac{\pi cq}{2}(T/2\pi\rho_s)^2(2\ln(2\pi\rho_s/T) + \ln(2/\pi) + u_A) \tag{4.75}$$

$$B: \qquad \Gamma_q = \frac{\pi cq}{2}(T/2\pi\rho_s)^2(\ln(T/\hbar cq) + u_B) \tag{4.76}$$

$$C: \qquad \Gamma_q = \frac{0.662\pi}{2}(Tcq/\hbar)^{1/2}(T/2\pi\rho_s)^2 \tag{4.77}$$

$$D: \qquad \Gamma_q = \frac{1.80\pi}{2}(T/2\pi\rho_s)^2\frac{T}{\hbar qa\sqrt{f(\hat{q})}} \ , \tag{4.78}$$

where u_A and u_B are constants of order unity and $f(\hat{q}) \simeq \frac{1}{5}$ is a function varying slowly on the direction of q. The constants u_A and u_B are fixed by fits to the *classical rotor simulations*. The requirements on q are as follows:

$$q_{\min} \ll q_A \ll \left(\frac{T}{\rho_s}\right)^2\frac{T}{8\pi\hbar c} \ll q_B \ll \frac{T}{\hbar c} \ll q_C \ll \left(\frac{TS}{2\rho_s}\right)^{1/3}\frac{1}{a} \ll q_D \ll \frac{1}{a} \ . \tag{4.79}$$

To make comparisons to classical rotor simulations, they also derive the result for the classical limit:

$$A_{cl}: \qquad \Gamma_q = \frac{\pi cq}{2}(T/2\pi\rho_s)^2(2\ln(2\pi\rho_s/T) + \ln(2/\pi) + u_A) \tag{4.80}$$

$$B_{cl}: \qquad \Gamma_q = \frac{\pi cq}{2}(T/2\pi\rho_s)^2(\ln(1/qa) + \ln(\sqrt{32}e^{\pi/2}) + u_B) \ , \tag{4.81}$$

where the two regions are separated by $q_A \ll e^{\pi/2}(T/\rho_s)^2/(\sqrt{2}\pi) \ll q_B$. They get fair agreement with classical rotor simulations using $u_A = 0$ and $u_{B_{cl}} = -0.9$ or $u_A = -1$ and $u_{B_{cl}} = -1$.

As shown in Fig. 2 of Tyč and Halperin (1990), both the RG scaling result and the A-limit of the analytical calculations obey the scaling behaviour $\Gamma_q/\omega_q = f(q\xi(T))$. For higher temperatures, the classical rotor simulation data also follow this behaviour, although they do not agree with either of the theoretical curves.

Wysin and Bishop (90)

Wysin and Bishop (1990) have performed classical MC/molecular dynamics on the 2DHAFSL directly (not on the classical rotor model. They find quite good agreement with the scaling predictions by CHN-Tyč but with parameters $\delta = 2.5$, $\gamma_0 = 1.7$, $\mu = 1.7$ and $\Theta = 0.7$. They state, though, that there is considerable freedom in choosing the parameters. The investigation covers temperatures up to $T/JS^2 = 0.85$. This article also gives a nice discussion of different possible line-shapes.

The spin-wave frequency $\omega_q(T)$ is in this work adopted from the scaling analysis (Tyč *et al.*, 1989).

Auerbach and Arovas (88)

In a Schwinger boson mean-field appoach Auerbach and Arovas (1988) reached scaling functions for $S(q)$ and $S(q,\omega)$. Later Kopietz (1990) performed a Brillouin-zone integration occurring in the result analytically, thereby allowing a comparison to other theories as a function of q and T. While the scaling function for $S(q)$ was reasonably close to the CHN-Tyč result, the damping was found to be $\Gamma_q/\omega_q \propto 1/q\xi$. While in disagreement with CHN-Tyč, this result was also obtained by Takahashi (1989) for the quantum ferromagnet.

Makivić and Jarrell (92)

Makivić and Jarrell (1992) have performed quantum Monte Carlo calculations of the imaginary-time spin correlation function $S(q,\tau) = \frac{1}{2\pi}\int_{-\infty}^{\infty} e^{-\omega\tau} S(q,\omega)d\omega$. For the discrete and noisy QMC data-set they invert the Laplace transform by the maximum entropy method. They deduce the spin-wave frequency ω_q and damping $\gamma_q = \langle\omega^2\rangle - \omega_q^2$ from the first and second moments of the relaxation function. They find that for small q, $S(q,\omega)$ does follow the scaling proposed by CHN-Tyč. However, the scaling frequency $\omega_0(T)$ was found to exhibit a different temperature dependence than $\omega_0 \propto \sqrt{T}/\xi$ proposed by CHN-Tyč. For $0.35 \times J < T < 0.4 \times J$, they find $\omega_0\xi \simeq 1.8$, while the product decreases to 1.52 at $T = 0.5 \times J$. This result disagrees with CHN-Tyč and is closer to the results from Schwinger-boson and modified spin wave theories by Auerbach and Arovas (1988) and Takahashi (1989) respectively. In the scaling function for $S(q) \propto \frac{1+\frac{1}{2}B_f \ln(1+q^2\xi^2)}{1+q^2\xi^2}$, the parameter B_f had the value in the original RG scaling analysis, but was later shown to be reduced by higher-loop corrections (0.23 (Makivić and Jarrell, 1992) or even 0.1 (Tyč *et al.*, 1989)). Similarly, Makivić and Jarrell find it necessary to introduce the parameter $A = 0.1$ in $\omega_q/\omega_0(T) \simeq \sqrt{3/2}q\xi(\delta + \frac{1}{2}A\ln(1+q^2\xi^2))^{1/2}$. The other parameters were found to be $\delta = 0.25$, $\gamma_0 = 1$, $\mu = 0.85$ and $\theta = 0.115$. For ω_q, the scaling is valid for $q\xi < 5$; at higher $q\xi$, ω_q/ω_0 decreases with temperature. The same behaviour is seen for γ_q/γ_0, but here the scaling breaks down already at $q\xi \sim 3$.

In addition to the spin-wave velocity, which is the initial slope of ω_q, figures 2 and 4 of Makivić and Jarrell (1992) also give the spin-wave frequency out towards the zone boundary, which is reproduced in figure 4.27. The zone boundary energy

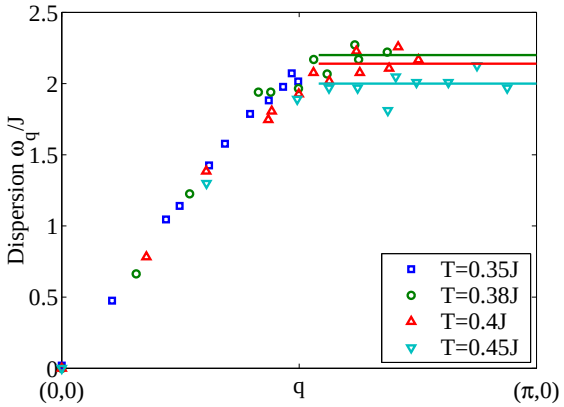

Figure 4.27. The spin-wave frequency for four different temperatures digitized from reference (Makivić and Jarrell, 1992). The zone-boundary energies indicated with solid lines correspond to Z_c =1.17, 1.15, 1.12 and 1.06 for increasing temperatures.

corresponds to $4SJZ_c(T)$, where Z_c =1.17, 1.15, 1.12 and 1.06 respectively for T/J =0.35, 0.38, 0.40 and 0.45.

Unfortunately, the temperature range $0.35 < T/J < 0.5$ covered is rather limited and it is therefore difficult to conclude to what extend the scaling functions would be valid over a larger range. With the improvement in computational capabilities, it would be very interesting to see the work extended to lower (and higher) temperatures.

Wang, Li and Gong (97)

have developed a self-consistent correlation theory of the relaxation function (Wang *et al.*, 1997). With this, they can calculate most physical observables including the spin wave dispersion and the damping (defined from moments of the relaxation function) for $0.4 < T/J < 1.8$. They show that a gap develops at (π, π) and that the zone-boundary energy softens. At the zone center, the damping increases with temperature from 0 to $\gamma_q \sim J$ at $T = 2J$. At $T = 0.4 \times J$ their result is in very close agreement with QMC (cf. figure 7 of Wang *et al.* (1997) and figure 4 of Makivić and Jarrell (1992)). Figure 4.28, which is adapted from Wang *et al.* (1997), shows the results at relatively high temperatures. The zone boundary energies correspond to $Z_c(T)$ =1.05, 0.98, 0.88, 0.79, 0.74 and 0.70 for T/J =0.4, 0.6, 0.8, 1.0, 1.2 and 1.8 respectively.

Nagao and Igarashi (98)

worked with a variant of the mode-mode coupling theory (Nagao and Igarashi, 1998). They do not show any graphs of the spin-wave damping, but it is contained in their results — just needs to be digged out. As seen in their figure 5, they predict a much more rapid softening than the QMC result. At $T = 0.4 \times J$ they estimate $Z_c \simeq 0.91$.

Winterfeldt and Ihle (99)

have developed a Green's-function theory for the short-range ordered system (Winterfeldt and Ihle, 1997, 1999). They fix some parameters (α_1 and α_2) of the theory by trying to match the ground state energy per spin u, staggered magnetization m and uniform static susceptibility χ. This is not simultaneously possible, and instead, they work with a couple of different parameter choices. For $\alpha_1 = \alpha_2$ they reproduce the $T = 0$ SPW dispersion from linear SPW theory. However, once they

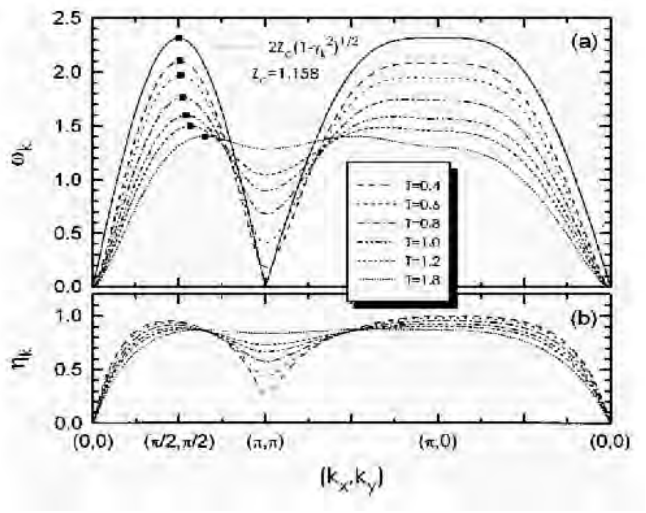

Figure 4.28. Spin-wave frequency and damping for $0.4 < T/J < 1.8$. *Figure is adapted from Wang* et al. *(1997).*

allow $\alpha_1 \neq \alpha_2$ the dispersion develops a minimum at $q = (0, \pi)$, much resembling the linear SPW result in the presence of NNN interactions.

The damping factor γ_q is found to be in fair agreement with the QMC data, albeit slightly underestimated. This is interpreted as a result of considering only 2-magnon processes. The spin-wave frequency ω_q is calculable within the approach, but no values are reported.

Chubukov, Sachdev and Ye (94)

There is also a prediction for the quantum critical regime. CSY reports a result for the generalized susceptibility $\chi(q, \omega)$, which through the fluctuation dissipation theorem gives $S(q, \omega)$:

$$S(q,\omega) = \frac{2}{1 - e^{-\beta\omega}} \chi''(q,\omega) \ . \tag{4.82}$$

Since the temperature factor is brought in explicitly, there is no problem with the principle of detailed balance. The form for $\chi(q,\omega)$, which is similar to the damped harmonic oscillator is given by:

$$\chi(q,\omega) = \frac{2}{3} \frac{\hbar^2 c_q^2}{\rho_s} \frac{\rho_s^q}{\rho_s} \frac{1}{\epsilon_q^2 - (\omega + i\gamma_{q,\omega})^2} \tag{4.83}$$

$$\epsilon_q = \hbar c_q \sqrt{1 + q^2\xi^2}/\xi \tag{4.84}$$

$$c_q^2 = \rho_s^q / \chi_\perp^q \tag{4.85}$$

$$\rho_s^q = \frac{1}{2\pi\beta}(\delta + \frac{1}{2}\ln(1 + q^2\xi^2)) \tag{4.86}$$

$$\chi_\perp^q = \rho_s / c^2 (\frac{2}{3} + (\frac{\rho_s^q}{\rho_s})^3) \tag{4.87}$$

$$\gamma_{q,\omega} = \frac{\pi}{2} c_q q \bar{\eta}_{q,\omega} (2\pi\rho_s^q\beta)^{-2} (2\ln(2\pi\rho_s^q\beta) + \Gamma) \ , \tag{4.88}$$

where $\bar{\eta}_{q,\omega}$ and the parameters δ and Γ are of order unity. However when plotted out this form also has a problem in that when the damping $\gamma_{q,\omega}$ becomes finite, $S(q,\omega)$ develops a dip at $q = 0$. Strictly speaking the CSY form is only valid for $q\xi \ll 1$ which is not the case when we measure around $q = 0$.

Summary of the different approaches

All of the mentioned approaches agree that well defined spin-wave like excitations persist at finite temperatures even though long range order is lost. They also share the result that the dispersion softens and the spectrum is progressively broadened due to damping. The scaling form by CHN-Tyč was found to describe well the results from several numerical studies. But, with quite different values for the 5 parameters and with different scaling of $\omega_0(T)\xi(T)$. Probably, this merely reflects that 5 parameters plus ω_0 are sufficient to describe the behaviour.

The recent works (Wang *et al.*, 1997, Nagao and Igarashi, 1998, Winterfeldt and Ihle, 1997, 1999) appear very promising, but all involve self-consistent equations that are solved numerically, which complicates their evaluation. In this thesis, only the results that could be directly read of the references are included.

4.4.2 Time-of-flight excitation spectrum measurements

When the excitation spectrum is broadened to occupy a significant part of (q, ω) space, the time-of-flight (TOF) neutron scattering technique acquires its full adequacy. The inherited weakness due to the restriction of probing along paraboloids in $\boldsymbol{q}$ and ω is resolved as more of the probed space becomes relevant. This section describes how TOF neutron scattering was used to measure the dynamic structure factor in CFTD for temperatures up to $T \sim J/2$.

2D configuration

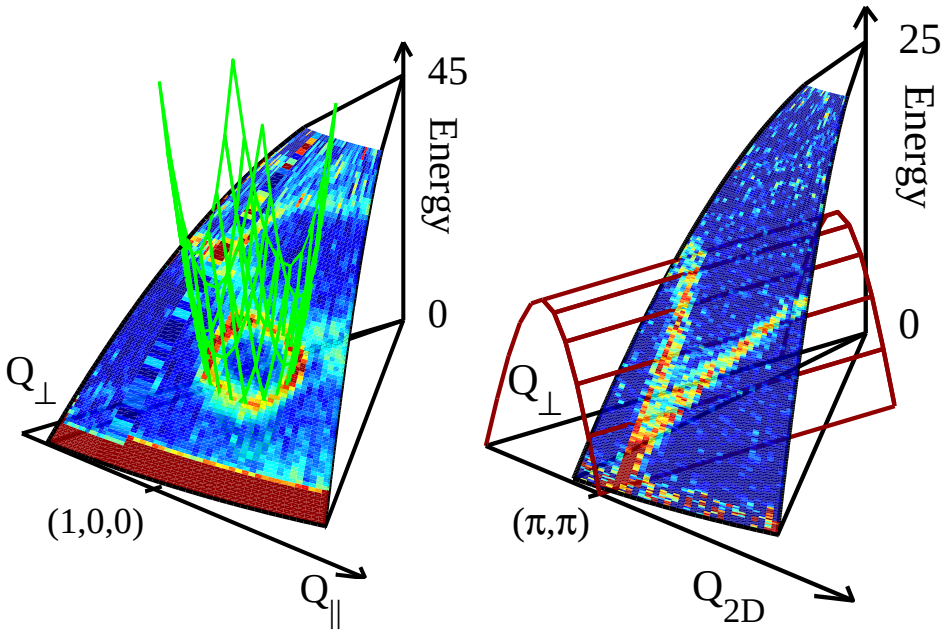

Figure 4.29. Illustration of how the TOF-paraboloid intersects respectively the dispersion cone of the ferromagnetic spin-wave excitations in the colossal magnetoresistance material $La_{0.7}Pb_0.3MnO_3$ *(Perring* et al.*, 1996) (left) and the spin-wave dispersion of a 2D Heisenberg antiferromagnet with the planes perpendicular to* $\boldsymbol{k}_i$*. (right)*

Due to the energy and momentum relation, a TOF experiment probes a paraboloid

in (q, ω) space defined by

$$\omega = \frac{\hbar}{2m}(k_i^2 - k_f^2) = \frac{\hbar}{2m}(\boldsymbol{k}_i - \boldsymbol{k}_f) \cdot (\boldsymbol{k}_i + \boldsymbol{k}_f) = \frac{\hbar}{2m}(2\boldsymbol{q} \cdot \boldsymbol{k}_i - q^2) \ . \qquad (4.89)$$

Scattering will be detected, where this paraboloid extroverts the dispersion manifold $\omega_{\boldsymbol{q}}$ of the sample.

Figure 4.29a illustrates how the dispersion cone of an acoustic excitation is intersected, forming a ring of intensity in the data-set. To measure the dispersion relation along some direction in reciprocal space, the incident energy is varied to place the intersections at different energies. In a 2D system, the lack of dispersion perpendicular to the planes can be exploited to measure the entire dispersion along some direction in one run. By placing the planes perpendicular to $\boldsymbol{k}_i$, the data can be projected down onto the $q_{2D} \perp \boldsymbol{k}_i$ plane as illustrated in figure 4.29b. By placing the direction of interest in the scattering plane spanned by the detector-bank, the entire dispersion was recorded along this direction.

4.4.3 Experimental details

The measurements were performed on the TOF spectrometer HET described in chapter 2. The weak scattering from a 2D $S = 1/2$ system required as much flux as possible. Therefore the most relaxed resolution (3S corresponding to the 'sloppy' chopper rotating at 3 times the pulse frequency) was chosen. This gave a flux of 1.5×10^4 neutrons $\mathrm{cm}^{-2}\mathrm{s}^{-1}$. The resolution was 1.1 meV FWHM at zero energy transfer, decreasing to 0.4 meV at 25 meV transfer.

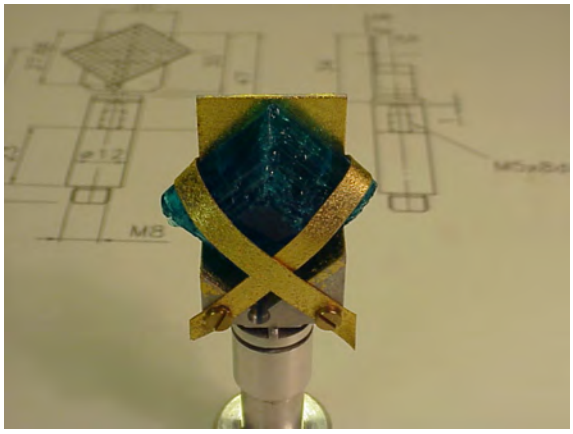

Figure 4.30. The sample mount used for the HET experiment. The neutrons travel through the back-plate of 1 mm aluminum, which is gold-plated to avoid chemical interaction with the sample.

A CFTD sample of 3.71 g was mounted as shown in figure 4.30 with $\boldsymbol{c}^* || \boldsymbol{k}_i$ and $\boldsymbol{b}^*$ in the horizontal plane. This placed a^* 11° from vertical and the 2D planes perpendicular to $\boldsymbol{k}_i$. Neglecting the small difference (0.07%) between a and b, the horizontal and vertical banks all cover equivalent directions $q_{2D} || (\pm 1, \pm 1)$ in the magnetic reciprocal space. Correspondingly, the four diagonal banks give the scattering along $(1, 0)$ type directions. This allows us to add the banks, thus obtaining a factor of 4 in counting rates. The added data-set are shown in figure 4.31.

The data contain several different features. The spin-wave dispersion is clearly visible along both directions. Also visible is a band of scattering around 20 meV as well as 'blobs' around 7 meV that are confined at certain q positions. Finally, a large elastic signal mainly due to incoherent scattering from the sample is seen.

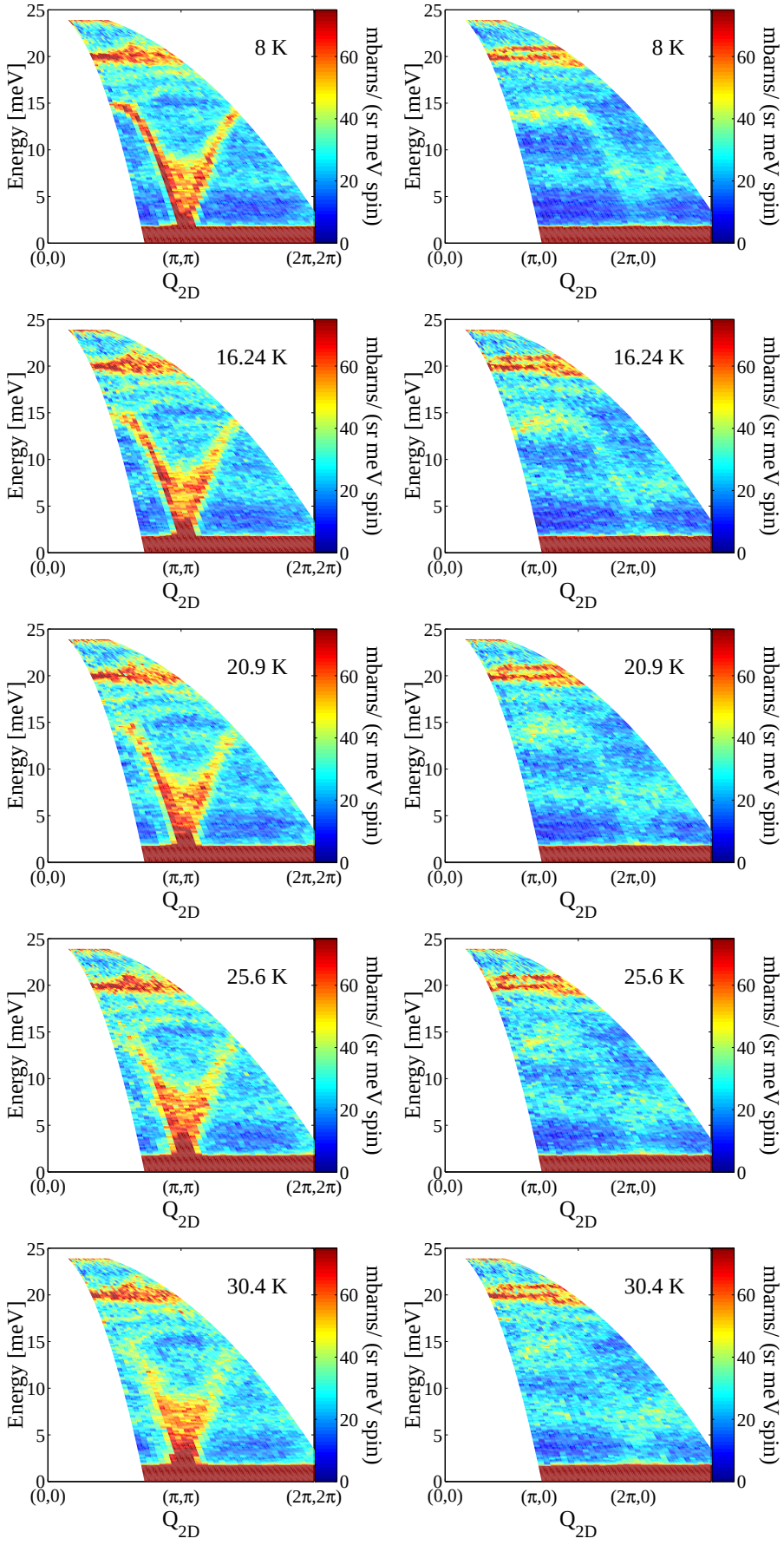

Figure 4.31 continues on next page.

Figure 4.31 continued from previous page.

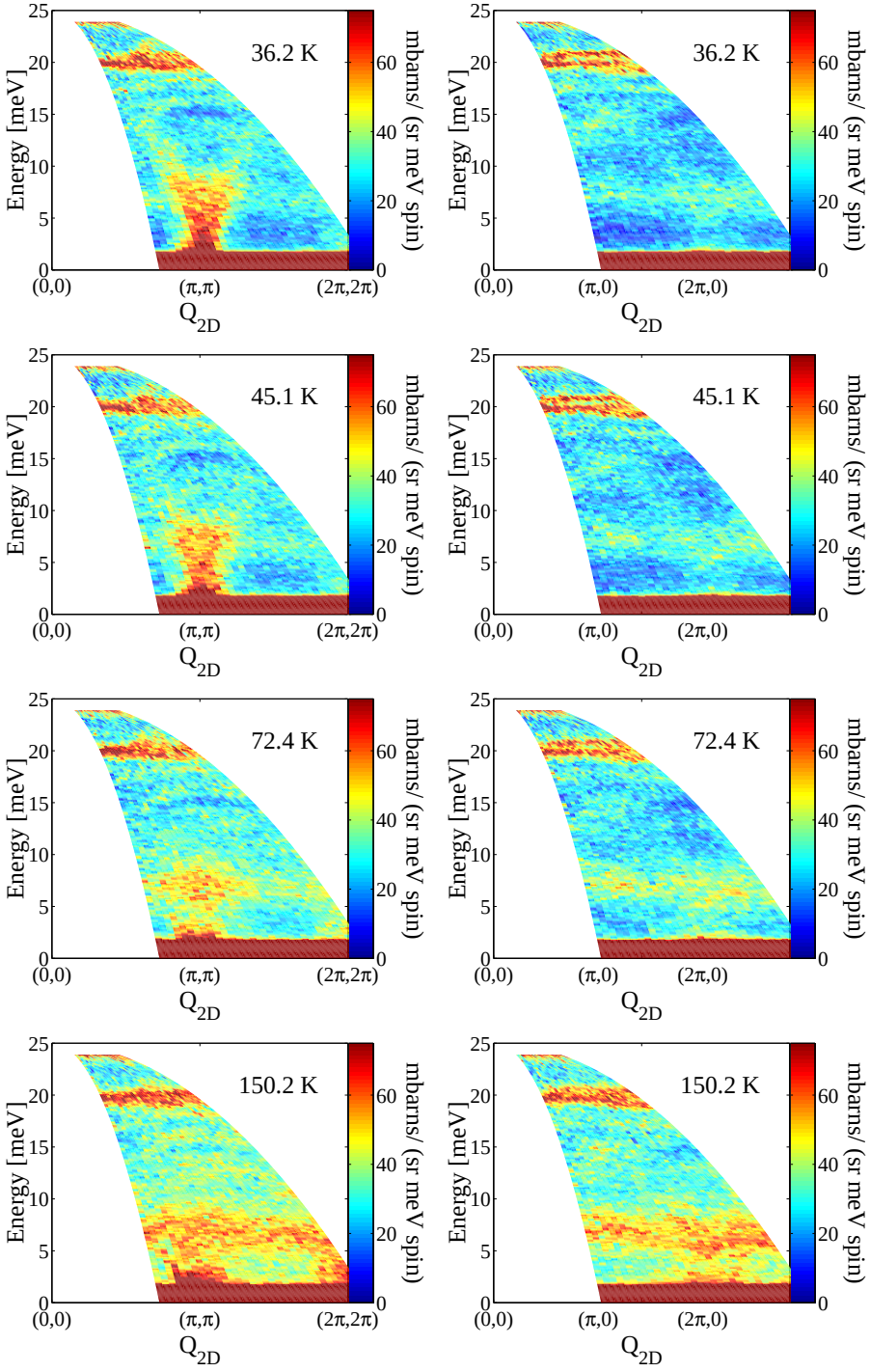

Figure 4.31. The measured scattering along $(1,1)$ *(left) and* $(1,0)$ *(right) obtained by adding four equivalent detector-banks in each case.*

The band around 20 meV is believed to be related to the motion of the D_2O molecules, which order at 236 K$\simeq$20.3 meV. These local modes should have little q-dependence. The apparent additional scattering at $\omega \sim 7$ meV around $q = (\pi, \pi)$ and $q = (2\pi, 0)$ is interpreted as acoustic phonons emanating from the crystallographic (1,0,1) and (1,1,1) Bragg-reflections. This becomes clear when looking at the 72 K and 150 K data, where the phonon scattering is dominant. There, it is seen how the 20 meV band and 7 meV 'blob' persist and grow in

intensity with the bose-factor.

4.4.4 Analysis

The analysis proceeds as follows:

1. From cuts along q and along energy in the 8 K data, the dispersion-relation and hence the coupling parameter are extracted.
2. Through spin-wave theory, the magnetic contribution was simulated and subtracted from the 8 K data to get a background data set, which was then subtracted from the remaining data-set.
3. Cuts along energy of the background corrected data-set were fitted to a dispersion broadened with a damped harmonic oscillator line-form, to extract the spin-wave damping and softening.

Cuts and fits

The output from detector-corrections and vanadium normalization is the resolution convoluted scattering cross-section shown in figure 4.31 in units of mbarns sr^{-1} spin^{-1}, where 1 barn= 10^{-24} cm^2 and sr is steradians (the full sphere is 4π sr).

If the full theoretical cross-section including magnetic and nuclear scattering was known or at least expressible in terms of a number of parameters, it could be convoluted by the instrument resolution and fitted to the experimental data. In practice this is almost impossible and seldom practical. Instead, it is very useful to select limited sub-sets of the data (called cuts) and fit these individually. By considering small enough sub-sets, the approximation of a constant background is often valid. And the sets of fit parameters (one set for each cut) can then be considered and interpreted to understand the physics of the system.

For the HET data, cuts are made using the MATLAB based program MSLICE (Coldea, 1999b). The data are in form of a 2D array spanned by the number of detectors and the number of energy bins for each detector, along with the information about the solid angle element $\Delta\Omega$ and energy interval ΔE covered by each data-bin in the array. In this thesis, the data-sets are shown in graphs, where the x-axis has been converted from detector-number to the q_{2D} value they represent.

A cut defines a set of bins of equal width and length as illustrated in figure 4.32. The data-bins that lie within the cut-bins are included, keeping not only the intensity but also the information of the total solid angle element contributed to each cut-bin. In other words, a cut is merely a sub-set of the data-bins, selected and grouped according to their position in $(\boldsymbol{q}, \omega)$.

Fitting the data requires a parameterized model for the scattering cross-section, which can be convoluted by the experimental resolution for each data-bin. The parameters are then determined by a least-squares procedure. The resolution convolution is accomplished by the program TOBYFIT (Perring, 1999) which calls the Multi-frills (Osborn and Perring, 1999) package for fitting. The scattering cross-section used to fit the CFTD data was that obtained from spin-wave theory:

$$\frac{d^2\sigma}{d\Omega dE_f} = A\frac{k_f}{k_i}|f(q)|^2\frac{1}{1-e^{-\beta\hbar\omega}}\sqrt{\frac{1-\gamma_q}{1+\gamma_q}}f(\omega,\omega_q)\ , \tag{4.90}$$

where $\omega_q = 4S\tilde{J}\sqrt{1-\gamma_q^2}$. The line shape $f(\omega,\omega_q)$ was chosen to be a delta-function $\delta(\omega-\omega_q)$ at 8 K and that of a damped harmonic oscillator

$$f(\omega,\omega_q) = \frac{4}{\pi}\frac{\Gamma_q\omega_q\omega}{(\omega^2-\omega_q^2)^2+4\Gamma_q^2\omega^2} \tag{4.91}$$

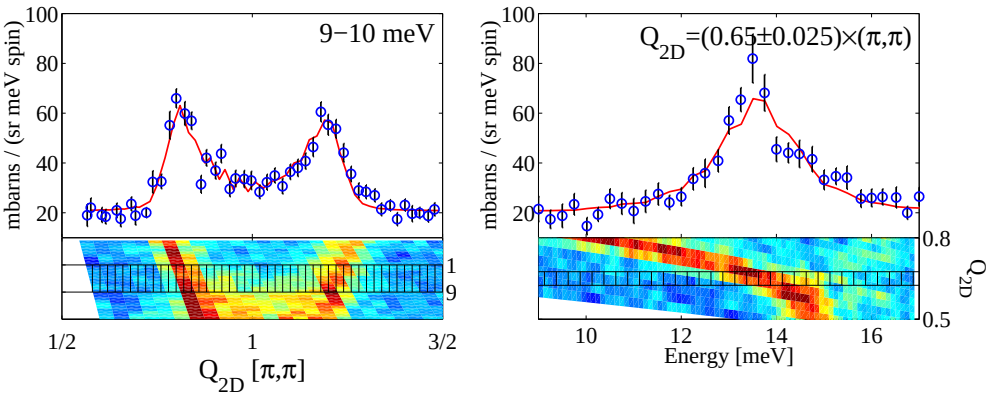

Figure 4.32. Cuts in the 8 K *data along q of width 9 meV to 10 meV. The data-bins that fall within each cut-bin are summed to make one point on the graph. The solid line is a fit to linear spin-wave theory convoluted by the full experimental resolution.*

for $T \leq T_N$. The variable parameters were the effective coupling parameter $\tilde{J}$ [meV], the spin-wave damping Γ_q [meV] and the overall amplitude A [mbarns sr^{-1} spin^{-1}]. The solid lines in figure 4.32 show the result of such fits.

The spin-wave dispersion at 8 K

The effective coupling parameter $\tilde{J}$ should for each cut be interpreted as the value that through linear spin-wave theory gives the right energy $\omega_q = 4S\tilde{J}\sqrt{1-\gamma_q^2}$. If due to anisotropy, further neighbor interactions or quantum corrections the dispersion from linear spin-wave theory is not correct, then the value of $\tilde{J}$ will differ for different cuts.

To establish the dispersion relation at 8 K, the $\tilde{J}$ values were for each cut converted to a point on the dispersion curve, which was shown in section 4.2.2, figure 4.7. For a cut along energy at a constant $q \pm \delta q$ like in figure 4.32b, a point $\omega_q = 4S\tilde{J}\sqrt{1-\gamma_q^2}$ is produced on the dispersion curve (blue points in figure 4.7). The standard error is directly obtained as $\sigma\omega_q = \sigma(\tilde{J})4S\sqrt{1-\gamma_q}$. For a cut along q at a constant energy $E \pm \delta E$ the corresponding q is found by inverting $E = 4s\tilde{J}\sqrt{1-\gamma_q^2}$. Rather than assigning an error in q, the points from q cuts (red points in figure 4.7) are assigned a standard error in energy. Though technically equivalent this facilitates fitting the dispersion data to a more general expression for the dispersion relation. The interpretation of figure 4.7 is described in section 4.2.2. The main results are that the dispersion along (1,1) is given by renormalized linear spin-wave theory $4SZ_cJ\sqrt{1-\gamma_q^2}$ with $Z_c = 1.18$ and $J = 6.31 \pm 0.02$ meV, while the zone boundary energy around $(\pi, 0)$ is suppressed 7% by quantum fluctuations.

Background subtraction

The overall amplitude for cuts along (1,1) varied only within the standard error from each fit, giving an average value of 57 ± 2 mbarns sr^{-1} spin^{-1}. Using the fitted values for A and $\tilde{J} = Z_c \times 6.31$ meV, the spin-wave contribution to the scattering cross-section from equation 4.90 was convoluted with the instrument resolution for each data-bin, giving the result in figure 4.33a. This simulated magnetic scattering was subtracted from the 8 K data, leaving a background-set shown in figure 4.33b.

The remainder is constituted by the intrinsic background, the elastic scattering and the phonon contribution. The intrinsic background of the instrument is due to detection of fast neutrons that have made it through the shielding, detector-noise

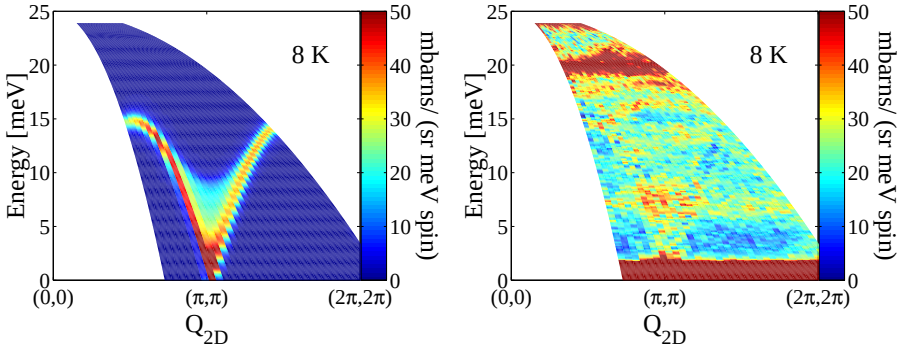

Figure 4.33. The calculated magnetic contribution (left) and the background data-set (right) at 8 K.

etc. At low temperatures, this is the dominating signal at low energies, since there are no excitations that can loose energy to the neutron. The large elastic signal is mainly due to incoherent scattering from the sample, which is not perfectly deuterated and therefore contains a small amount of hydrogen.

Scaled to the appropriate temperature factor, this background data-set was subtracted from the data taken at higher temperatures, thus leaving effectively only the magnetic scattering. The background corrected data are shown in figure 4.34.

It is seen how the background correction successfully removes the 20 meV phonon band. This gives confidence that also the 7 meV 'blob' is treated correctly. (Since the 7 meV 'blob' is superimposed on the magnetic scattering, it is difficult to verify this directly.) The corrected data show that the spin-wave dispersion persists, gradually broadened up to 45 K. At 72 K, the data are essentially flat an feature-less. At this temperature, the excitation spectrum is expected to be very broad, weak and perhaps gapped (Wang *et al.*, 1997). The statistical scatter combined with the error from the background subtraction make interpretation of the 72 K and 150 K data impossible.

The background corrected data from T_N to 45 K were analyzed as described for the 8 K data, but including a damping Γ_q in form of a DHO line-shape. Constant-q cuts along energy were found to provide the most stable fits. At low temperatures cuts of width and spacing $0.05 \times (\pi, \pi)$ were used. As the signal broadened with the concomitant weakening, some fit became unstable. For these q's the width was increased to $0.1 \times (\pi, \pi)$. Eventually, even some of the broad cuts gave unstable fits. In the following results, only the stable fits have been included.

4.4.5 Results

The outcome for each temperature was a set of parameters A_q, $\tilde{J}_q$ and Γ_q for a number of q's between $(\frac{\pi}{2}, \frac{\pi}{2})$ and $(\frac{3\pi}{2}, \frac{3\pi}{2})$. Because of the symmetry around (π, π), the results are presented in a reduced q measured from this point.

Absolute amplitude

The amplitude A makes it possible to determine the renormalization factor Z_χ defined in section 4.2. According to the definitions of the renormalization constants, $S(q,\omega) = Z_d S^{\mathrm{cl}}(q, Z_c\omega^{\mathrm{cl}}) = Z_\chi S^{\mathrm{cl}}(q,\omega^{\mathrm{cl}})$, where it is used that $Z_\chi = Z_d/Z_c$ and that $S^{\mathrm{cl}}(q,\omega^{\mathrm{cl}})$ given in equation 4.16 is in units of inverse energy. Linear spin-wave theory assumes order along a given direction which is denoted the z direction. For 1-magnon scattering the dynamic structure factor becomes $S_{\alpha\beta}(q,\omega) = 0$ when $\alpha = z$ or $\alpha \neq \beta$ and $S(q,\omega) = S_{xx}(q,\omega) + S_{yy}(q,\omega) + S_{zz}(q,\omega) = 2S_{xx}(q,\omega)$. Above

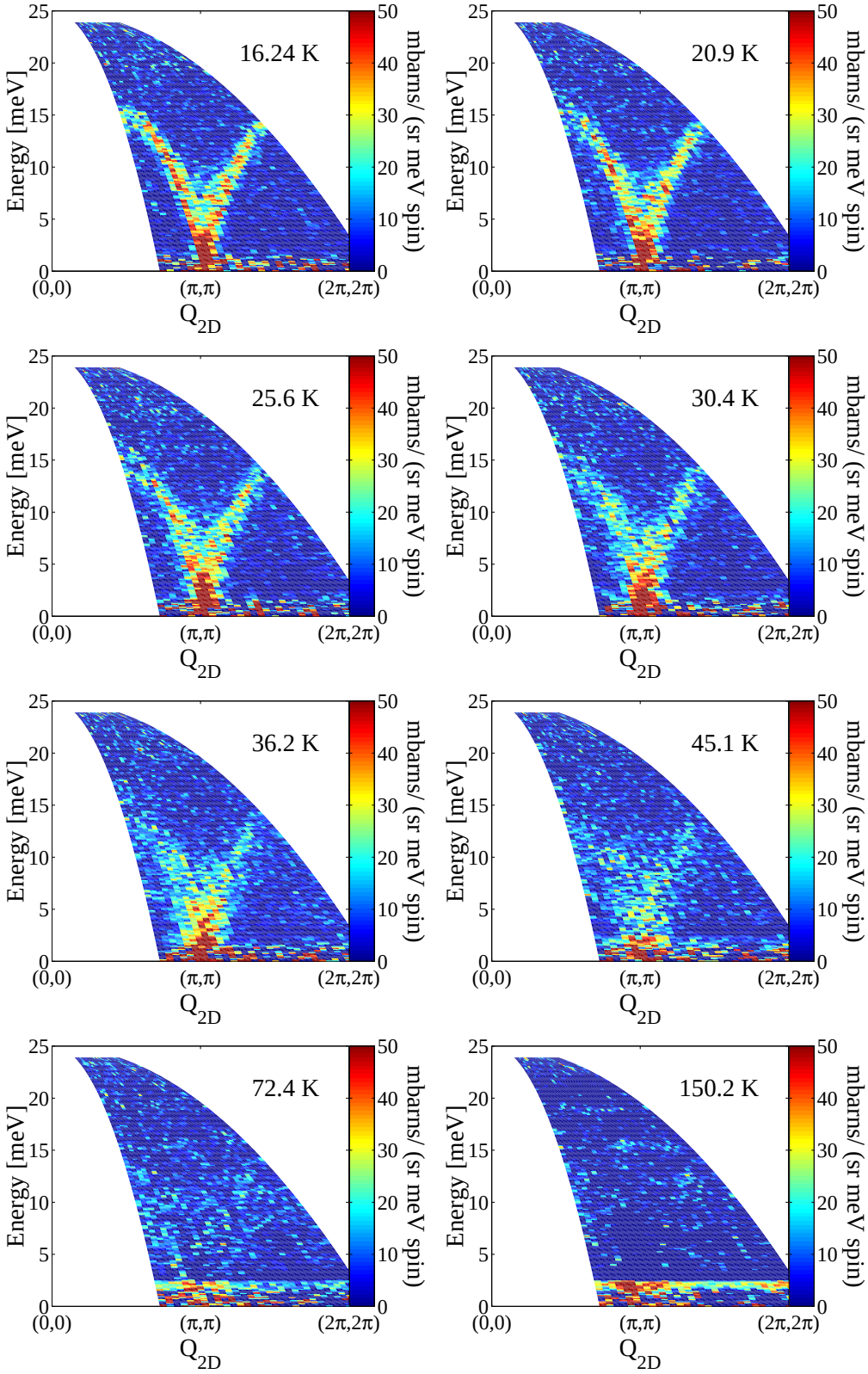

Figure 4.34. The background corrected data along $(1,1)$.

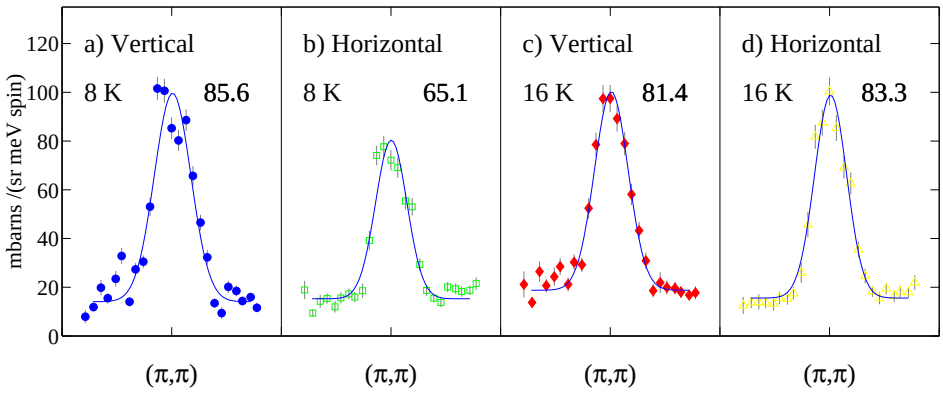

Figure 4.35. Cuts along q for 2-4 meV of vertical 8 K *data (a), horizontal 8* K *data (b), vertical 16.24* K *data (c) and horizontal 16.24* K *data (d). In each case, the amplitude is given in* mbarns sr^{-1} spin^{-1}.

T_N where the direction of the order parameter fluctuates in space and time, there is no preferred z direction. In this isotropic case, $S_{xx}(q,\omega) = S_{yy}(q,\omega) = S_{zz}(q,\omega) = \frac{1}{3}S(q,\omega)$, where $S(q,\omega)$ is still given by equation 4.16.

Neutron scattering measures the geometrical average

$$\sum_{\alpha\beta}(1-\hat{q}_\alpha\hat{q}_\beta)S_{\alpha\beta}(q,\omega)\ , \tag{4.92}$$

which above T_N gives $\frac{2}{3}S(q,\omega)$. Below T_N the spins align in the ac plane (perpendicular to b) and almost along a. For the horizontal detector banks, q is perpendicular to a and hence approximately perpendicular to the spins and the geometric factor gives $\frac{1}{2}S(q,\omega)$. For the vertical banks, the geometric factor becomes q_{2D} dependent with maximum $S(q,\omega)$, where q is parallel to the ordering direction. In figure 4.35 cuts along q for 2 meV$< E <$4 meV are shown for 8 K (a,b) and for 16.24 K. It is seen how at 16.24 K$\simeq T_N$ there is no difference between the amplitudes in the vertical (c) and horizontal (d) detector banks, which reflects that there is no preferred orientation of the moments so that in both cases, the geometric factor is $\frac{2}{3}$. At 8 K, the geometric factor for the horizontal detector banks (b) is $\frac{1}{2}$, and the ratio $83.3/65.1 = 1.28$ is close to the expected $\frac{2}{3}/\frac{1}{2} \simeq 1.33$. The amplitude in the vertical banks (a) is energy dependent, and will not be considered, as there is sufficient statistics in the horizontal banks. By comparing the fitting form to the spin-wave prediction, it is seen that above T_N, $A = \frac{2}{3}(\gamma r_e)^2 Z_\chi S$. Below T_N, using only the horizontal detector banks, $A = \frac{1}{2}(\gamma r_e)^2 Z_\chi S$.

For each temperature, A was found to be independent of q within the statistical scatter. This means that the structure factor found in spin-wave theory remains valid even in the short range ordered region. To find the renormalization factor Z_χ, the average A was computed for each temperature. At 8 K only the horizontal banks were used to find A. The result for $Z_\chi(T)$ is listed in table 4.3.

The low temperature value $Z_\chi = 0.50 \pm 0.02$ is in very good agreement with the theoretical prediction $Z_\chi = 0.51$ (Igarashi, 1992, Singh and Gelfand, 1995). In comparison, the value measured in La_2CuO_4 was $Z_\chi = 0.39 \pm 0.1$, which is still consistent within the standard error (Hayden *et al.*, 1998).

Spin wave softening

As the temperature is increased, the spin-waves soften so that the energy of the dispersion is lowered. This results in a lower value of the effective coupling parameter $\tilde{J}_q(T)$ used in the fits. As described for the 8 K dispersion, $\tilde{J}_q(T)$ can be converted back to a dispersion curve. It is instructive however to consider directly

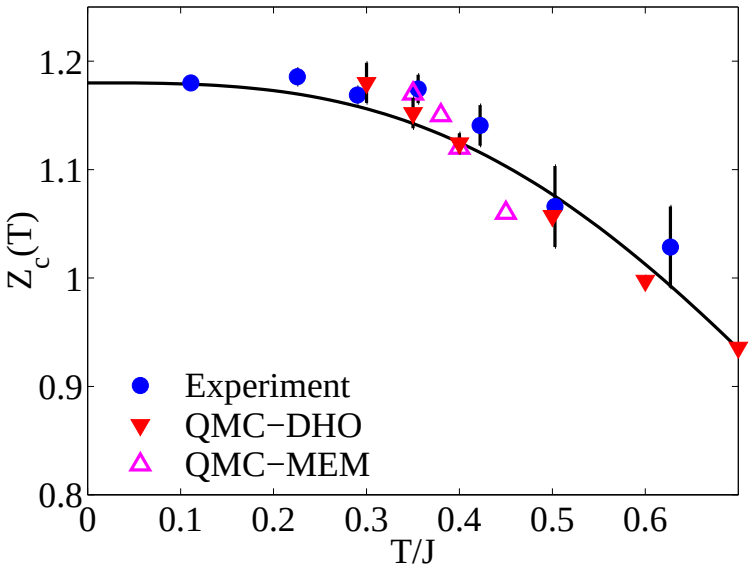

Figure 4.36. The spin wave-softening in CFTD as a function of T, obtained by averaging over q. The QMC results are by Makivić and Jarrell (1992) (MEM) and Syljuåsen and Rønnow (2000a) (DHO), while the solid line is an analytic prediction by Kaganov and Chubukov (1988) and Elstner et al. *(1995a)*

$\tilde{J}_q(T)$, where the q dependence from spin-wave theory is divided out. This value was evenly scattered around an average value $\bar{J}(T)$, meaning that along (1,1) the dispersion shape remains described by spin-wave theory. The softening can therefore be expressed in terms of a temperature dependent renormalization factor $Z_c()$. The average values $\bar{J}(T)$ and the corresponding renormalization factors are listed in table 4.3 and depicted in figure 4.36.

In figure 4.36 the renormalization factor $Z_c(T) = \bar{J}(T)/J(0) = Z_c(0)\overline{\omega_q(T)/\omega_q(0)}$ is compared to the QMC predictions by Makivić and Jarrell (1992) (MEM) and Syljuåsen and Rønnow (2000a) (DHO) and to the simple spin-wave result of Kaganov and Chubukov (1988) and Elstner *et al.* (1995a).

$$Z_c(T) = Z_c(0)\left(1 + \frac{\zeta(3)}{4\pi}\left(\frac{T}{JS}\right)^3\right)^{-1} \tag{4.93}$$

It is seen that there is good consistency between the data, the QMC results and the analytic prediction.

In comparison, the spin-wave velocity in La_2CuO_4 has been found to decrease from 850 meV Åat 4 K to 750 meV Åat 300 K, corresponding to $Z_c(T = 0.2J) = 1.04$, which is a much more rapid decrease. This must be taken as another indication that La_2CuO_4 is not ideally described by the simple 2DQHAFSL model system.

Spin wave damping

Concomitant with the softening, the finite correlation length leads to a damping of the spin waves. This was modeled by a DHO line shape in the fits. The results for $\Gamma_q(T)$ are depicted in figure 4.37. The CHN-Tyc scaling prediction 4.69 is represented as shaded areas bounded by the two different choices of parameters (Tyč *et al.*, 1989) (lower) and (Makivić and Jarrell, 1992) (upper). At 25 K, also the QMC result as extracted from Makivić and Jarrell (1992) is shown as a solid red line. Except at 45 K, where the fits are rather loosely confined, the results

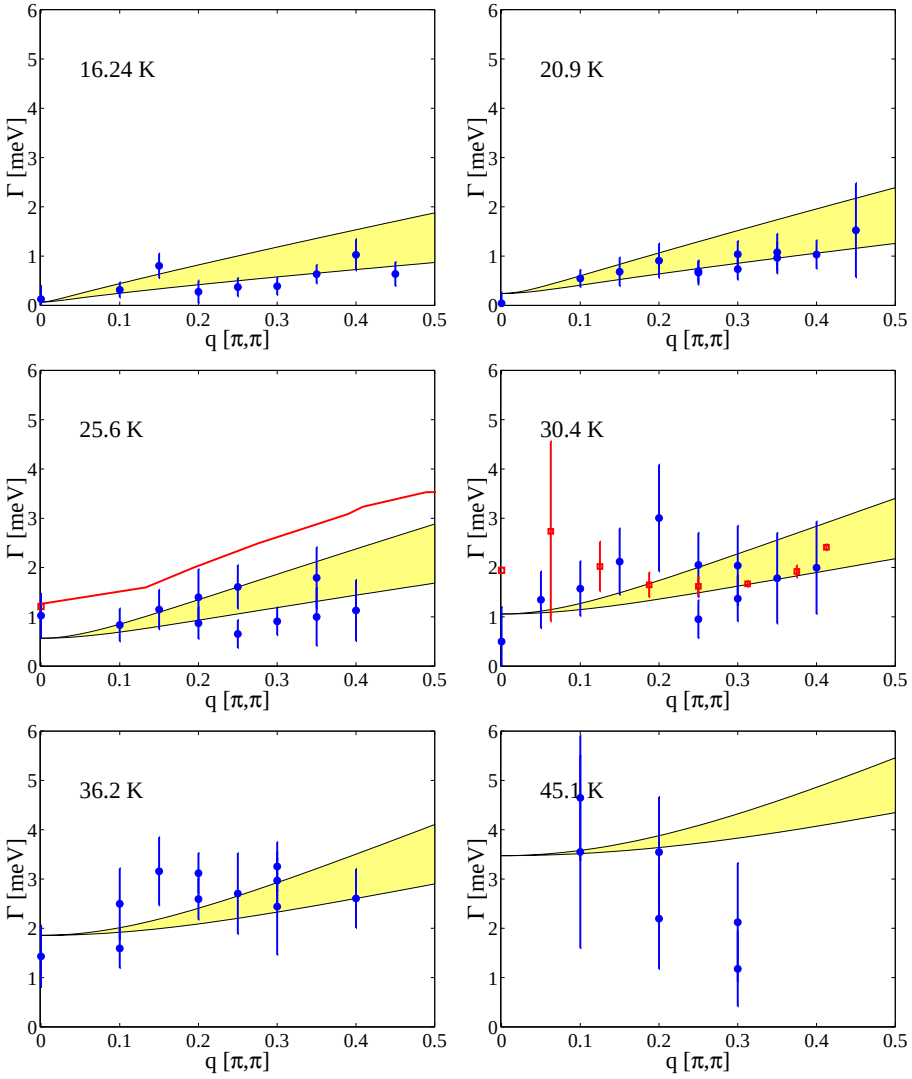

Figure 4.37. The spin wave-damping in CFTD as a function of q for each T, obtained by fitting constant-q cuts of the background corrected data in figure 4.34. The shaded region represents the scaling prediction as discussed in the text. For 25.6 K and 30.4 K the red line and squares shows the results from QMC calculations by respectively Makivić and Jarrell (1992) and Syljuåsen and Rønnow (2000a).

show that Γ_q increases with q, albeit with considerable scatter and relatively large standard errors. The quality of the data does not permit a discussion of the functional form of the q dependence, but it is roughly consistent with the scaling prediction. To address the temperature dependence, the average value $\bar{\Gamma}(T)$ is considered and depicted in figure 4.38. The average $\bar{\Gamma}(T)$ should lie within the limiting values at $q = (0,0)$ and $q = (\frac{\pi}{2}, \frac{\pi}{2})$, which bound the shaded regions in figure 4.38. The CHN-Tyč scaling prediction is shown using the parameters from Makivić and Jarrell (1992) (yellow), while the QMC result has been digitized directly from Makivić and Jarrell (1992) (pink). Up to $T = 0.5J$, the data lie within the scaling prediction, which however only only imposes a very weak constraint. The QMC results of Makivić and Jarrell (1992) overestimates the damping by almost a factor of 2.

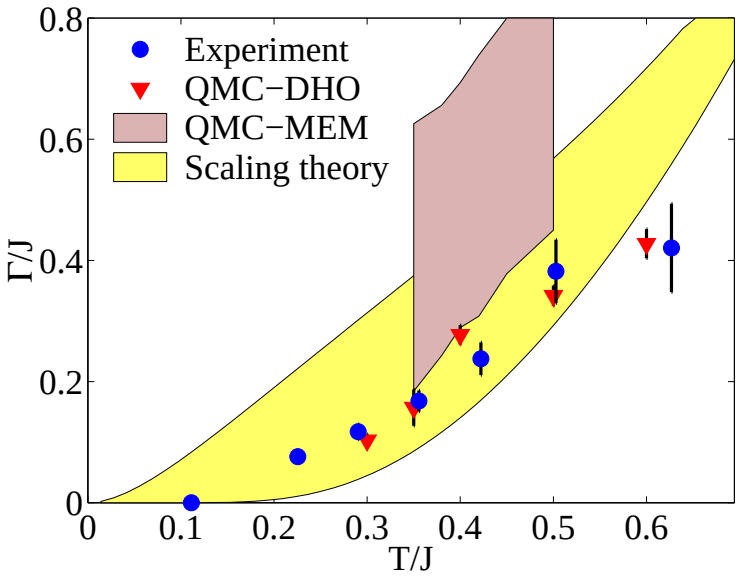

Figure 4.38. The spin wave-damping in CFTD as a function of T, obtained by averaging over q. The shaded region represents the predictions from scaling analysis (yellow) and QMC calculations (Makivić and Jarrell, 1992) (pink) as discussed in the text. The triangles are new QMC results of Syljuåsen and Rønnow (2000a)

New quantum Monte Carlo results To understand the discrepancy between the experiment and the QMC results, a new QMC investigation has been undertaken (Syljuåsen and Rønnow, 2000a,b). The QMC method calculates the correlation functions in imaginary time τ, which gives the Laplace transform of $S(q,\omega)$.

$$S(q,\tau) = \int_0^\infty d\omega e^{-\omega\tau} S(q,\omega) \tag{4.94}$$

The analytic continuation by which $S(q,\omega)$ is obtained corresponds to inverting the Laplace transform. Since the QMC data are discrete and contain statistical errors, this inversion is not straightforward. Following the maximum entropy method (MEM) employed by Makivić and Jarrell (1992), identical results were obtained.

The advantage of the MEM is that no assumptions for the line shape of $S(q,\omega)$ are needed, but it is seldom possible to estimate its validity. As an alternative to the MEM, a definite assumption for the line shape was taken. By Laplace transforming the assumed line shape, the imaginary time QMC data were fitted directly. Using a damped harmonic oscillator (DHO) line shape, the resulting spin-wave damping as shown in figure 4.38 was approximately halved compared to using the MEM method.

It is seen that the QMC results obtained using the DHO method are in almost exact agreement with the experiment. The consistency of the new QMC results is presently being checked by studying different choices of line shapes and trying to understand why the MEM apparently fails (Syljuåsen and Rønnow, 2000a).

Using the same method, the zone boundary energies at respectively $(\frac{\pi}{2},\frac{\pi}{2})$ and $(\pi,0)$ were calculated for $T > 0.5J$. The temperature dependence of $\omega(\frac{\pi}{2},\frac{\pi}{2})$ is depicted in figure 4.36, while $\omega(\pi,0)$ was consistently found to be slightly lower as depicted in the insert of figure 4.39. The extrapolated $T = 0$ difference is around 6% in close agreement with the measurement and the series expansion result of Singh and Gelfand (1995). From this, it is concluded that the zone boundary dispersion is a true quantum effect in the pure nearest neighbour model.

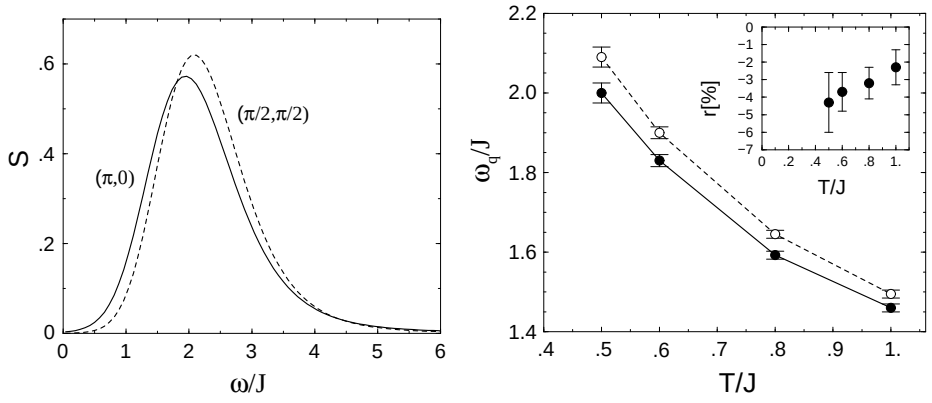

Figure 4.39. Left: $S(q,\omega)$ for $q = (\pi, 0)$ (solid) and $(\frac{\pi}{2}, \frac{\pi}{2})$ (dashed) at $T0.5J$ from a $L \times L = 32 \times 32$ lattice. Right: The extrapolated $L \to \infty$ peak positions for $(\pi, 0)$ (filled circles) and $(\frac{\pi}{2}, \frac{\pi}{2})$ (open circles). Insert: The relative difference $(\omega(\pi, 0) - \omega(\frac{\pi}{2}, \frac{\pi}{2}))/\omega(\frac{\pi}{2}, \frac{\pi}{2})$ in percent.

4.4.6 Conclusion and outlook

In summary, a TOF neutron scattering experiment on CFTD has shown that up to $T \sim J/2$, well defined spin-wave excitations persist. Fitting cuts through the data has supplied information on the zone-boundary dispersion, the temperature dependent renormalization of respectively amplitude and energy of the excitations, as well as the temperature and in part q dependence of the spin-wave damping. The results are summarized in table 4.3. There is generally good consistency between the results and the prediction based on the combined picture from different theoretical and numerical approaches.

T [K]	8	16.24	20.9	25.6	30.4	36.2	45.1
A	37 ± 3	47 ± 2	49 ± 2	48 ± 3	41 ± 3	57 ± 4	40 ± 8
$Z_\chi \times 100$	51 ± 4	49 ± 2	51 ± 2	49 ± 2	42 ± 3	58 ± 5	41 ± 8
$\bar{J}$ [meV]	7.45(2)	7.48(4)	7.38(5)	7.41(8)	7.2(1)	6.7(2)	6.5(2)
Z_c	1.18	1.19(1)	1.17(1)	1.17(1)	1.14(2)	1.07(4)	1.03(4)
$\bar{\Gamma}$ [meV]	0.00(2)	0.48(7)	0.74(8)	1.06(9)	1.5(2)	2.4(3)	2.7(5)

Table 4.3. The q averaged results from fits to the TOF-data at 7 temperatures from 8 K to 45 K. The susceptibility renormalization factor Z_χ was determined from the absolute amplitude A in units of mbarn sr^{-1} fu^{-1}. *The renormalization factor for the spin-wave velocity Z_c was determined from $\omega_q(T)/(4SJ)$, where $J = 6.31$ meV was determined at 8 K. The spin wave damping Γ_q gave the width of the damped harmonic oscillator line-shape used in the fits.*

It would be interesting to improve the experimental data, which should be possible. Some improvement could be achieved simply by increasing the counting time, by which the statistical uncertainty is reduced. If the same or a different spectrometer could supply more flexibility in the choice of resolution and incident energy, while still imaging the dispersion relation in the detector banks, this would enable a more rigorous phonon correction. Finally, as part of the full picture, the damping and possible opening of a gap at the zone-center could be probed on a triple axis type spectrometer, which gives much more flexibility in optimizing the resolution and incoherent background.

On the theoretical side, it is hoped that the present results will stimulate an effort to converge the predictions from different approaches in order to consolidate a picture like it has recently happened for the time-independent problem.

Chapter 5

$LiHoF_4$ — an Ising ferromagnet in a transverse field

Excitations around the quantum critical point

$LiHoF_4$ is a well characterized rare-earth ferromagnet, which in a field of 5 T *applied perpendicular to the easy axis undergoes a quantum phase transition to a polarized paramagnet. This chapter presents a neutron scattering study of the excitations around this quantum critical point. The behaviour of the excitations is well understood by a mean-field random-phase-approximation, although a few quantitative details need to be addressed. The existence of a well controlled quantum phase transition in a system with a completely characterized Hamiltonian opens possibilities for detailed investigations of pure quantum critical behaviour.*

There exist materials, where the strength of the quantum fluctuations can be controlled in such a way that the system can be taken from an ordered ground state to a disordered ground state at $T = 0$. Such a transition is called a quantum phase transition (QPT) and the universal behaviour around the quantum critical point (QCP) is of great current interest. Recent years have seen significant advances in the theoretical treatment of quantum critical behaviour (Sachdev, 1999).

Experimentally, the situation is rather difficult, as there is the need for some external parameter that can control the quantum fluctuations through the QCP. Examples are the pressure, chemical composition or an applied magnetic field. By applying pressure it is possible to introduce minute changes in the crystal structure, thereby changing the coupling parameters (see *e. g.* Carter *et al.*, 1991, Bogenberger and v. Löhneysen, 1995). However, only a very limited region around the QCP is available and the method seldom gives a very accurate handle on the phase transition. Changes in the chemical composition can potentially take the system between very different states. But at the same time, non-stochiometric compositions introduce a randomness, which can have severe influence on the behaviour of the system. Also, as new or modified samples have to be used for each point along the phase transition, the possibility of studying the critical behaviour is limited. Much better access to the QCP is provided in systems, where it is an external magnetic field that drives the transition. With modern magnets, the magnetic field can quickly be changed with an accuracy that is several orders of magnitude smaller than its absolute value. Such a magnetic field driven QPT occurs in the transverse field Ising ferromagnet, which is the subject of the present

chapter.

Here inelastic neutron scattering study of $LiHoF_4$ is presented. In $LiHoF_4$ the crystal field generates an effective two-level system corresponding to an Ising system, and the experiment aimed to observe the characteristic behaviour of the excitations around the QCP in a transverse field Ising model.

As an introduction, a single mean-field and random-phase treatment of the Ising model will be presented, followed by a description of $LiHoF_4$. The inelastic neutron scattering experiment and its interpretation will then lead to a conclusion about the perspectives for further studies of $LiHoF_4$ as a model QCP.

5.1 The transverse field Ising ferromagnet

The transverse field Ising model defined by the Hamiltonian

$$\mathcal{H} = -\frac{1}{2}\sum_{ij} J_{ij} S_i^z S_j^z - \Gamma \sum_i S_i^x \tag{5.1}$$

was actually first proposed by de Gennes (1963) to model hydrogen-bonded ferroelectrics. It generally describes a system of particles that can tunnel between two identical states with a probability determined by Γ and an interaction given by J. Because most applications of the model have not been directly related to a ferromagnet in a transverse field, the symbol Γ is used rather than $g\mu_B H_\perp$, but the term transverse field will be used synonymously.

The simplest theoretical approaches to the model are the mean field theory and the random phase approximations (de Gennes, 1963, Brout *et al.*, 1966, Wang and Cooper, 1968) which are expected to work well as long as the coordination number z is large or if the interactions are long ranged. Other methods include series expansions (Elliott *et al.*, 1970), the Blume–Hubbard method, Monte Carlo (Creswick *et al.*, 1988, de Oliveira and Chiappin, 1997), local magnetic field distributions (Thomsen, 1986), renormalization group calculations (Burkhardt and Gunton, 1974), $1/z$ expansions (Stinchcombe, 1973a,b) and correlated-basis-function analysis (Ristig and Kim, 1996).

The mean field (MF) approximation is achieved by writing $S_i^z = \langle S^z\rangle + (S_i^z - \langle S^z\rangle)$ and neglecting the term that is quadratic in the fluctuations

$$\begin{aligned}\frac{1}{2}\sum_{ij} J_{ij} S_i^z S_j^z &= \frac{1}{2}\sum_{ij} J_{ij}(\langle S^z\rangle + (S_i^z - \langle S^z\rangle))(\langle S^z\rangle + (S_j^z - \langle S^z\rangle)) \\ &\simeq N J_0 \langle S^z\rangle^2 + J_0 \sum_i S_i^z \langle S\rangle \ , \end{aligned} \tag{5.2}$$

where $NJ_0 = \sum_{ij} J_{ij}$ and $\langle S^z\rangle$ is the mean expectation value of S^z. This approximation decouples the Hamiltonian into noninteracting spins coupled only through the self consistent field $\boldsymbol{\gamma} = (\Gamma, 0, J_0\langle S^z\rangle)$.

$$\mathcal{H} = -\sum_i \boldsymbol{\gamma}\cdot\boldsymbol{S}_i \tag{5.3}$$

The eigenvalues of the MF Hamiltonian are $\pm\frac{1}{2}\gamma$ and the average spin vector is $\langle \boldsymbol{S}\rangle = (\sin\theta, 0, \cos\theta) \times \frac{1}{2}\tanh\frac{1}{2}\beta\gamma$, where θ is the angle between $\boldsymbol{z}$ and $\boldsymbol{\gamma}$ such that $\sin\theta = \Gamma/\gamma$ and $\cos\theta = J_0\langle S^z\rangle/\gamma$. The selfconsistency equation is then given as

$$\langle S^z\rangle = \frac{J_0\langle S^z\rangle}{\sqrt{\Gamma^2 + J_0^2\langle S^z\rangle^2}} \frac{1}{2}\tanh\frac{1}{2}\beta\sqrt{\Gamma^2 + J_0^2\langle S^z\rangle^2} \ , \tag{5.4}$$

but is more transparently expressed in terms of γ and $\cos\theta$

$$\gamma\cos\theta = \tfrac{1}{2}J_0\cos\theta\tanh\tfrac{1}{2}\beta\gamma \ . \tag{5.5}$$

In the ordered state, where $\cos\theta$ is nonzero, the equation reduces to

$$\gamma = \tfrac{1}{2}J_0\tanh\tfrac{1}{2}\beta\gamma \ . \tag{5.6}$$

Outside the ordered region, $\gamma = \Gamma$, and in both cases the components of the average moment are given by:

$$|\langle \boldsymbol{S}\rangle| = \frac{1}{2}\tanh\frac{1}{2}\beta\gamma \tag{5.7}$$

$$\langle S^z\rangle = \frac{\sqrt{\gamma^2 - \Gamma^2}}{J_0} \tag{5.8}$$

$$\langle S^x\rangle = \frac{\Gamma}{\gamma}\frac{1}{2}\tanh\frac{1}{2}\beta\gamma \ . \tag{5.9}$$

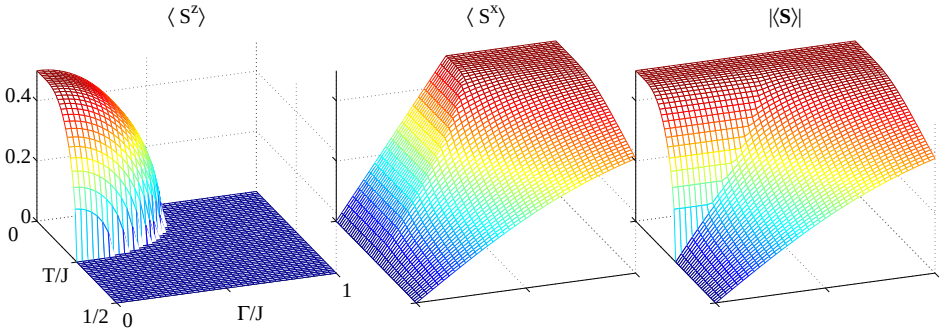

Figure 5.1. The mean field solution for the longitudinal and transverse components of the average moment as a function of temperature and transverse field.

The behaviour as a function of T and Γ is depicted in figure 5.1. The region with nonzero $\langle S^z \rangle$ is the spontaneously ordered ferromagnet, while the nonzero value of $\langle S^x \rangle$ is just the field induced polarization of the paramagnetic moments. The critical temperature β_c is determined from where γ becomes equal to Γ

$$\Gamma = \tfrac{1}{2} J_0 \tanh \tfrac{1}{2} \beta_c \Gamma \ . \tag{5.10}$$

In zero transverse field, $T_c = J_0/4$, while T_c vanishes for a critical transverse field $\Gamma_c = J_0/2$. This is the quantum critical point, where at zero temperature the system goes from being ordered to disordered as the transverse field is increased beyond Γ_c. The solution for T_c is single valued and can be turned around to give the value of the critical field as a function of temperature $\Gamma_c(T)$.

The excitation spectrum can be derived through the random phase approximation (RPA), which gives the susceptibility

$$\chi_q^{\alpha\beta}(\omega) = \chi_0^{\alpha\beta}(\omega) + \sum_{\gamma\epsilon} \chi_0^{\alpha\gamma}(\omega) J_q^{\gamma\epsilon} \chi_q^{\epsilon\beta}(\omega) \ , \tag{5.11}$$

in terms of the Fourier transformed coupling J_q and the MF single ion susceptibility

$$\chi_0^{\alpha\beta}(\omega) = \lim_{\epsilon \to 0^+} \sum_{nm} \frac{\langle n|S^\alpha|m\rangle\langle m|S^\beta|n\rangle}{E_m - E_n - \omega - i\epsilon} (n_n - n_m) \ , \tag{5.12}$$

where $|n\rangle$ are the eigenstates of the MF Hamiltonian. For simplicity, the following considerations are restricted to $T = 0$ and neglect the elastic part. In this case the single ion susceptibility becomes

$$\chi_0^{\alpha\beta}(\omega) = \lim_{\epsilon \to 0^+} c_{\alpha\beta} \frac{2\gamma}{\gamma^2 - (\omega + i\epsilon)^2} \ , \tag{5.13}$$

where $c_{\alpha\beta} = \langle n|S^\alpha|m\rangle\langle m|S^\beta|n\rangle$. In particular, $c_{zz} = \Gamma^2/\gamma^2$. For the Ising system, where only $J_q^{zz} \equiv J_q$ is nonzero, substitution into the RPA equation gives

$$\begin{aligned}
\chi_q^{xx} &= \chi_0^{xx} + \frac{J_q |\chi_0^{xz}|^2}{1 - J_q \chi_0^{zz}} &&= \frac{2\gamma c_{xx}}{\gamma^2 - \omega^2} + \frac{4 J_q \gamma^2 |c_{xz}|^2}{(\gamma^2 - \omega^2)(\omega_q^2 - \omega^2)} \\
\chi_q^{xz} &= \frac{\chi_0^{xz}}{1 - J_q \chi_0^{zz}} &&= \frac{2\gamma c_{xz}}{\omega_q^2 - \omega^2} \\
\chi_q^{zz} &= \frac{\chi_0^{zz}}{1 - J_q \chi_0^{zz}} &&= \frac{2\gamma c_{zz}}{\omega_q^2 - \omega^2} \ , \ ,
\end{aligned} \tag{5.14}$$

where the limit $\epsilon \to 0^+$ has been taken. All three susceptibilities give rise to an excitation with dispersion

$$\omega_q^2 = \gamma^2 - 2 J_q \Gamma^2 / \gamma \ , \tag{5.15}$$

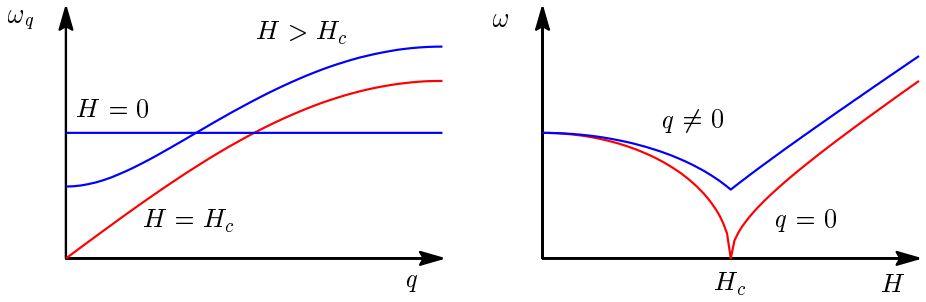

Figure 5.2. Schematic illustration of the dispersion ω_q around the QCP.

while for χ_q^{xx} there is an additional excitation at the single ion energy $\omega_0 = \gamma$.

Assuming a sinusoidal Fourier transform of the coupling $J_q = a\cos(q)$, the behaviour of ω_q as a function of q and field is sketched in figure 5.2. It is seen that at the transition, the dispersion softens for $q = 0$. The remainder of this chapter describes an attempt to establish an experimental demonstration of this softening at the QCP in $LiHoF_4$.

5.2 $LiHoF_4$

The current interest in the properties around quantum critical points have promoted a resurgence of interest in $LiHoF_4$. This material is known to be a nearly ideal 3D Ising ferromagnet and as such undergoes a QPT in a transverse field of 5 T.

5.2.1 The rare earth Hamiltonian

The appealing feature of $LiHoF_4$ is that the understanding of magnetism in rare-earth (RE) systems has been developed to a very advanced level (See *e.g.* Jensen and Mackintosh, 1991). The unfilled shell of $4f$ electrons couples according to Hund's rules, forming a total angular momentum J. This has resulted in a standard rare-earth Hamiltonian.

$$\mathcal{H} = \sum_i V_{\rm cf}(\boldsymbol{J}_i) + \sum_i A\boldsymbol{I}_i \cdot \boldsymbol{J}_i - \sum_i g_L\mu_B \boldsymbol{H}\cdot\boldsymbol{J}_i - \frac{1}{2}\sum_{ij}\boldsymbol{J}_i\boldsymbol{\mathcal{J}}_{ij}\boldsymbol{J}_j \qquad (5.16)$$

The crystal field $V_c(\boldsymbol{J})$, is due to the electronic environment felt by the different $4f$ orbitals that form the angular momentum J. This lifts the $2J+1$ degeneracy within the multiplet. An *ab initio* calculation of the crystal field operator requires a detailed knowledge of the electronic states in the system and is seldom sufficiently precise. However, when the symmetry of the crystal structure is taken into account, only a few parameters need to be determined. In $LiHoF_4$ only six parameters are needed.

The hyperfine coupling A between the electronic moments J and the spin $I = 7/2$ of the holmium nuclei cause an additional splitting of each crystal field level. This splitting will be seen to have substantial effects on the behaviour around the QCP.

The Zeeman energy $-g_L\mu_B bsH\cdot\boldsymbol{J}$ is given by the Landé factor $g_L = \frac{3}{2} + \frac{S(S+1)-L(L+1)}{2J(J+1)}$ equaling $\frac{5}{4}$ for holmium.

The coupling tensor $\mathcal{J} = \mathcal{J}_{\rm ex} + \mathcal{J}_{\rm dip}$ has contributions both from exchange mediated coupling and from direct coupling between the dipole moments. In $LiHoF_4$ it is believed to be dominated by the dipole coupling, as it is the case in $LiTbF_4$ (Als-Nielsen *et al.*, 1974, Holmes *et al.*, 1975, Als-Nielsen, 1976). The dipole coupling can be calculated both in real space and in reciprocal space using the method of Bowden and Clark (1981).

$$\mathcal{J}_{ij}^{\alpha\beta} = \frac{\mu_0}{4\pi}(g_L\mu_B)^2 \frac{3r_{ij}^{\alpha}r_{ij}^{\beta} - \delta_{\alpha\beta}r_{ij}^2}{r_{ij}^5} \ , \tag{5.17}$$

where r_{ij} is the vector separating the moments J_i and J_j. The fact that the dipole coupling is long ranged, proportional to $1/|r-r'|^3$ has important consequences, as will be described below.

Apart from the dipole coupling and the Zeeman energy, attempts of *ab initio* calculations of the parameters entering rare-earth Hamiltonians have only reached limited success so far. However, as there are only a limited number of parameters in the Hamiltonian, these can be determined experimentally. By collecting a sufficiently broad set of data (magnetization, magnetic structure, excitation spectrum *etc.*) the parameters can be determined in a way that they correctly describes the existing data. Once this is achieved, new measurements can be compared to theoretical predictions without any free parameters. In the following, the existing measurements and knowledge of the rare-earth Hamiltonian for $LiHoF_4$ are described.

Existing experimental data

The magnetic properties of $LiHoF_4$ have been characterized through a series of experimental techniques. Magnetization and susceptibility measurements have been performed by Hansen *et al.* (1975). At $T_c = 1.53$ K the system orders ferromagnetically with saturation moments of $6.9\mu_B$ along the c direction. By fitting $\chi_{||}(T)$ and $\chi_{\perp}(T)$, the crystal field parameters were determined. The resulting crystal field energy levels were roughly consistent with direct measurements hereof by polarized absorption and Raman spectroscopy (Christensen, 1979, Salaün *et al.*, 1997b,a). The temperature dependence of $H_c(T)$ close to T_c was found proportional to the square root of the reduced temperature $t = 1 - T/T_c$ with a logarithmic correction $H_c = 1.53 \times \ {\rm T} \times t^{1/2}(\ln 0.483/t)^{1/3}$ consistent with predictions from renormalization group considerations (Christensen, 1979). Electron spin resonance (ESR) measurements by Magariño *et al.* (1980) revealed a hyperfine structure of the resonance due to coupling $A = 0.032$ K to the eight states of the $I = 7/2$ nuclear spin. The value of A was confirmed in a specific heat study of Mennenga *et al.* (1984a,b), who also estimated the first three coupling parameters $\mathcal{J}_1 = 4.6$ mK, $\mathcal{J}_2 = -7.4$ mK and $\mathcal{J}_3 = 0.69$ mK.

The phase diagram as depicted in figure 5.5 was determined from susceptibility measurements by Bitko *et al.* (1996), who also found that the critical exponent of the susceptibility equals the mean-field prediction $\gamma = 1$ both at the classical phase transition in zero field and at the quantum phase transition at zero temperature. The phase boundary was successfully described by a mean-field solution to the rare-earth Hamiltonian with an effective coupling $\mathcal{J}_0 = \sum_n \mathcal{J}_n = 0.027$ K and the transverse g-factor, $g_\perp = 0.74$, as fitting parameters. It should be noted, that the substitution of $g_\perp$ for the Landé factor g_L while retaining the crystal field operator is not a consistent approach. The crystal field limits the available orbitals at low temperatures, thereby causing an effective g-tensor. In a simple model, the crystal field operator can be neglected by introducing an effective g-tensor, but they should not be used simultaneously. In the approach of Bitko *et al.* (1996), $g_\perp$ is simply a rescaling of the field in order to match the experimentally observed phase boundary.

There can be several reasons, why such a rescaling is necessary. The mean-field approximation neglects the correlation between fluctuations, which in general leads to an overestimation of the ordered region. In the related material HoF_3, the corrections to the mean-field result have been calculated to first order in a $1/z$ expansion by Jensen (1994) (z is the coordination number). The correction to *e.g.* the transition temperature was 11%. Though more than usual for three-dimensional systems, this correction is still far from the 40% discrepancy for the critical field in $LiHoF_4$. The dipole coupling for the x and y components of the moments is in fact antiferromagnetic, which will act to reduce the effect of a transverse field. In the calculations described below, the full dipole coupling has been included, but the effect hereof is much too small to account for the critical field. In principle an exchange contribution could aid the dipole coupling, but it would have to be two orders of magnitude larger than what was estimated from the specific heat measurements, which seems highly unlikely.

The most plausible explanation for the failure to predict the right critical field is that the estimated crystal field is not completely correct. Starting from the parameters of Hansen *et al.* (1975), it is not possible to get a notably better fit of the susceptibility and the measured crystal field levels. It can however not be excluded that there exists a different set of crystal field parameters that generate a similar scheme of crystal field levels but with different eigenstates. The possible parameter-space is however limited by the fact that the current parameters reproduce the correct saturated moments, which means that the ground state is correctly modeled.

5.2.2 The effective Ising model

Though in principle, all calculations and comparison to experiments could be performed in terms of the rare-earth Hamiltonian, it is instructive to consider the effective Ising model, which motivated the study.

The Ising model is characterized by the matrix elements $\langle\uparrow|S^z|\uparrow\rangle = -\langle\downarrow|S^z|\downarrow\rangle = \frac{1}{2}$ and $\langle\uparrow|S^x|\downarrow\rangle = \langle\uparrow|S^x|\downarrow\rangle = \frac{1}{2}$ which multiply respectively J and Γ. The corresponding matrix elements in the RE model are $\langle g|J^z|g\rangle = -\langle e|J^z|e\rangle \equiv M$ and $\langle g|J^x|e\rangle = \langle e|J^x|g\rangle = A$, where $|g\rangle$ and $|e\rangle$ are the two lowest lying states. The parameters of the effective Ising model are therefore $J_{\mathrm{Ising}} = 4M^2\mathcal{J}_0$ and $\Gamma = 2g\mu_B H_x A$.

Also in the RE model, it is the transverse field that produces the splitting $2Ag_L\mu_B H_x$ which is therefore readily identified with the splitting Γ in the Ising model. In zero field, the two lowest eigenstates are formed by the J^z eigenstates $\{|-5\rangle, |-1\rangle, |3\rangle, |7\rangle\}$ and $\{|-7\rangle, |-3\rangle, |1\rangle, |5\rangle\}$ respectively. Therefore J^x cannot couple directly between the two. But in a transverse field, the term $g_L\mu_B H_x J^x$ mixes a component proportional to H_x of the next level into the two lowest. As this level is formed by $|\pm 6\rangle, |\pm 2\rangle$, it gives J^x a nonzero matrix element proportional to H_x. As a consequence, the splitting Γ of the two lowest lying states starts by being proportional to H_x^2 as shown in the right panel of figure 5.3. The matrix element of J^z is on the other hand only mildly affected by the transverse field as depicted in the left panel of figure 5.3.

5.2.3 Doped $LiY_xHo_{-x}F_4$

In addition to the easy control of the QPT through the transverse field, the holmium ions can be substituted by non-magnetic yttrium. Reich *et al.* (1986, 1990), Wu *et al.* (1991, 1993), Rosenbaum (1996) and Bitko (1997) have performed a systematic study of the effects of doping in $LiY_xHo_{-x}F_4$. For low concentrations, x, of yttrium, the effect of depleting the magnetic system is simply to reduce T_N

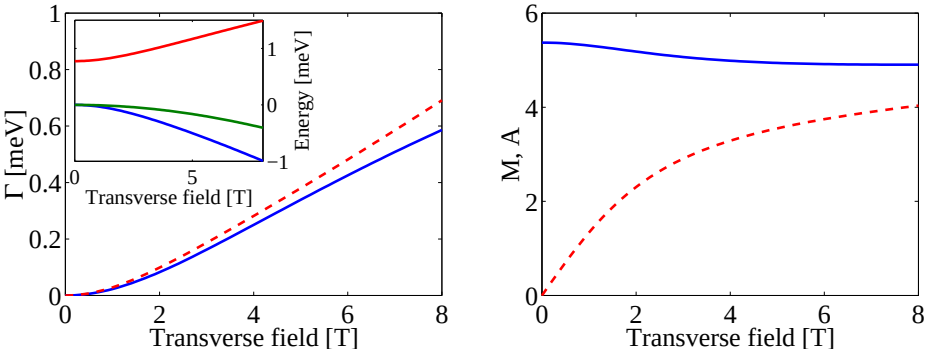

Figure 5.3. Left: In solid, the splitting Γ *of the two lowest levels as a function of the transverse field. The result* $2Ag_L\mu_B H_x$ *from considering just the 3 lowest states is shown by the dashed line. The insert displays the absolute energies of the 3 lowest modes. Right: The matrix elements* M *and* A *as a function of field.*

proportional to $(1-x)$. But around $x = 0.5$, the system has become an assembly of randomly placed dipoles, which due to the spatial dependence of the dipole coupling will be both ferro- and antiferromagnetically coupled. In effect, the system behaves like a spin glass. The ability to use the transverse field to lower the barriers for tunneling between the two Ising states of each ion opens for very interesting experiments, where the spin glass is relaxed through quantum annealing rather than normal thermal annealing (Brooke *et al.*, 1999).

5.3 Excitations around the quantum phase transition

As seen in section 5.1 the elementary excitation of the transverse field Ising model is expected to soften at the quantum critical point. This is an essential ingredient, which is responsible for much of the physics that is characteristic to the quantum phase transition. An inelastic neutron scattering investigation was performed in order to establish to which extent the behaviour in $LiHoF_4$ is given by this simple picture.

5.3.1 Experimental details

To follow the decreasing excitation energy towards the critical point, the experiments required relatively tight resolution. For this, the cold neutron triple axis spectrometer TAS7 at Risø National Laboratory was used. With incident energies of 2.7 meV, 3 meV and 4.2 meV, resolutions between 0.06 meV and 0.21 meV (FWHM) were achieved depending on the choice of collimation.

The sample was a single crystal of dimensions $12.3 \times 10.3 \times 5.6$ mm^3, the short dimension being the Ising direction. The sample was mounted with the reciprocal axes $(1,0,0)$ and $(0,0,1)$ in the scattering plane. To manage the significant torque that a ferromagnet suffers in a transverse field, the sample was embedded in a copper coffin as shown in figure 5.4. By making the coffin 0.3% larger than the sample, the difference in thermal contraction upon cooling ensured a tight mounting at low temperatures without crushing the crystal. The holder was made from oxygen free copper to provide sufficient thermal conduction at low temperatures.

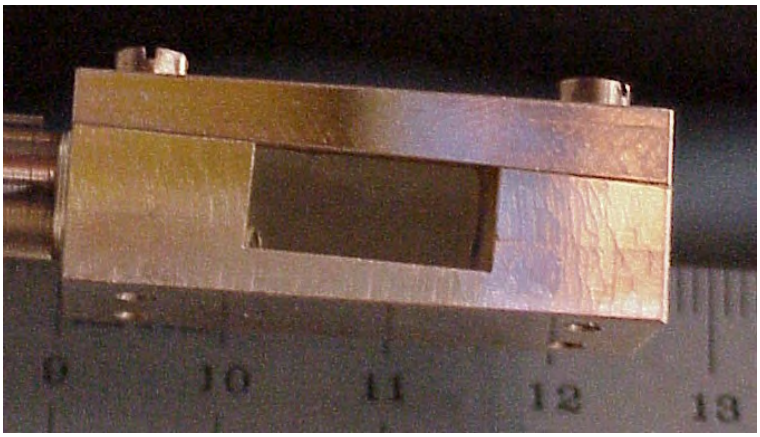

Figure 5.4. The $LiHoF_4$ sample embedded in a coffin of oxygen free copper.

The magnetic field was provided by a 9 T vertical field cryomagnet from Oxford Instruments. Due to the importance of having the field strictly transverse to the Ising axis, some efforts were made to estimate the accuracy of the field alignment. By rotating a Hall-probe inside the magnet core, it was found that the field axis was within 0.2° of the cryostat axis. Once aligned on the spectrometer, the alignment of the sample with respect to the cryostat was found by observing the Bragg reflections while tilting the cryostat. Since the sample was aligned within 0.15° of the cryostat axis, the magnetic field was at maximum 0.35° away from the Ising axis.

The low temperatures were achieved with a dilution refrigerator insert also from Oxford Instruments. From the mixing chamber, the sample is suspended on

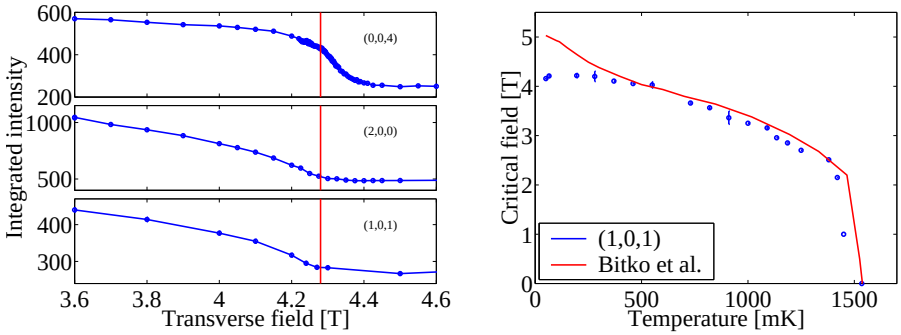

Figure 5.5. Left: Field dependence of the integrated intensity of the magnetic Bragg reflections (1,0,1), (2,0,0) and (0,0,4) at the base temperature. Right: The phase boundary between the ordered and the paramagnetic phases in $LiHoF_4$. The symbols represent the result from observing the intensity of the (1,0,1) Bragg peak, while the solid line was obtained by Bitko et al. *(1996) from susceptibility measurements.*

a 20 cm long Ø12 mm oxygen free copper rod into the core of the magnet. The temperature was measured at the mixing chamber with a base temperature of 50 mK. While the heat transport through the copper rod is usually sufficient to keep the sample temperature close to the measured, neutron-activation of the sample may have caused a higher temperature. In future experiments, a thermometer should be placed in the direct vicinity of the sample.

5.3.2 Summary of results

Phase diagram and order parameters The phase boundary between the ordered and the paramagnetic phases was found by observing the intensity of the magnetic Bragg reflections as a function of field and temperature. In the left panel of figure 5.5 the field dependence of the three magnetic Bragg peaks (1,0,1), (2,0,0) and (0,0,4) at the base temperature is depicted. The two Bragg peaks (2,0,0) and (1,0,1) behave similarly, with a well defined onset at 4.24 T. By performing scans of the (1,0,1) reflection at increasing temperatures, the phase boundary as shown in the right panel of figure 5.5 was obtained. One surprising feature was the absence of the enhancement of H_c due to the hyperfine coupling below 0.4 K. One possible explanation for this is that the activation of the sample due to the irradiation with neutrons heated the sample. Unfortunately, the thermometer was located at the mixing chamber separated from the sample by a 20 cm copper rod. It is therefore not unlikely that there could be a temperature gradient between sample and mixing chamber. Comparing to the phase boundary of Bitko *et al.* (1996), it is therefore concluded that the actual temperature of the sample was around 0.4 K. In the calculations below, this temperature will be used.

The intensity at (0,0,4) is seen to behave differently with a tail above what seems to be H_c for (2,0,0) and (1,0,1). First, it is remembered that the system has both electronic moments J and nuclear moments I. However, the nuclear spin scattering cross-section for holmium $\left(\frac{b_+ - b_-}{2I+1}\right)^2 = 0.0018 \times 10^{-24}$ cm^2 is so much smaller than the magnetic cross-section $(\gamma r_0)^2 = 0.29 \times 10^{-24}$ cm^2, that it can be neglected. Thus, the intensity of the (0,0,4) reflection should be proportional to $\langle J^x \rangle^2$, which as seen in figure 5.1, $\langle J^x \rangle$ increases linearly with the field belw H_c, and is almost constant at the saturation value above H_c. This behaviour, which is also seen in the RE MF calculations, is almost opposite to the intensity of the (0,0,4) reflection, which therefore remains a puzzle.

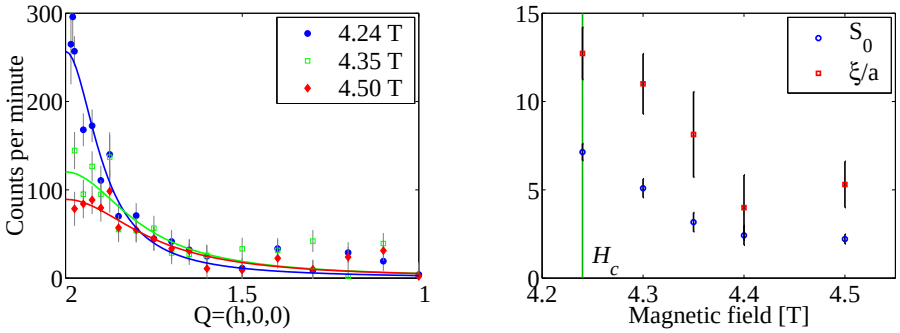

Figure 5.6. The quasi-elastic critical scattering around (2,0,0). Left: Scans along $(h,0,0)$ *at zero energy transfer for 4 different fields. The background scan at 6* T *has been subtracted in order to remove the Bragg peak at (2,0,0). Right: Correlation length* ξ *and amplitude* S_0 *of the critical scattering above* H_c*.*

Excitations The excitation spectrum was investigated by performing energy scans at constant values of q along $(h,0,0)$, $(1,0,l)$ and $(h,0,1)$. The spectrum was recorded at the three magnetic fields 3.6 T, 4.24 T and 6 T chosen respectively below, at and above the critical field $H_c = 4.24$ T. The data are summarized in figure 5.7.

There are several important features to be observed in figure 5.7. It should first be noted that the sharp ellipse around zero energy transfer is the resolution convolution of the (2,0,0) Bragg peak. Along $(h,0,0)$ a quasi-elastic signal is observed. Part of this is incoherent background scattering, but there is also a q-dependent component, which at 4.24 T is seen to be more intense and narrower confined around (2,0,0). This is the so-called central peak associated with the transition, which was also investigated by scans along $(h,0,0)$ for zero energy transfer as presented in figure 5.6. The scan at 6 T was almost completely dominated by the sharp nuclear (2,0,0) reflection. This data-set was subtracted from the scans taken at lower temperatures as shown in the left panel of figure 5.6. Below H_c the Bragg peak gained a field dependent magnetic contribution, which complicates analysis of the critical scattering severely. Therefore only the scans above H_c are considered in figure 5.6, where the background corrected data have been fitted to a Lorentzian line-shape $S(q) = S_0/(1+q^2\xi^2)$.

Though the quasi-elastic component containing the time independent correlations of the system is an important piece in a full description, the present experiment was focused on the behaviour of the excitations that have been mapped out in figure 5.7. It is seen that the qualitative features of the excitation spectrum are unaffected by the quantum phase transition. There is one low-energy mode, which disperses along $(h,0,0)$ but shows little dispersion along $(1,0,l)$. Along $(1,0,l)$ and $(h,0,1)$ only limited energy ranges have been mapped out, but individual scans throughout the range showed that no additional low-energy modes exist.

5.4 The random phase approximation

The excitations, were modeled by a random-phase approximation (RPA) of the RE Hamiltonian. The details of this approach have been described by Jensen and Mackintosh (1991), Leask *et al.* (1994), Rønnow (1996).

As discussed above, there were certain indications that the true sample temperature during the neutron scattering experiment was in fact closer to 0.4 K than to the nominal temperature of ∼50 mK. To make a comparison between the calculations and the experiment, the temperature in the calculations was set to 0.4 K and

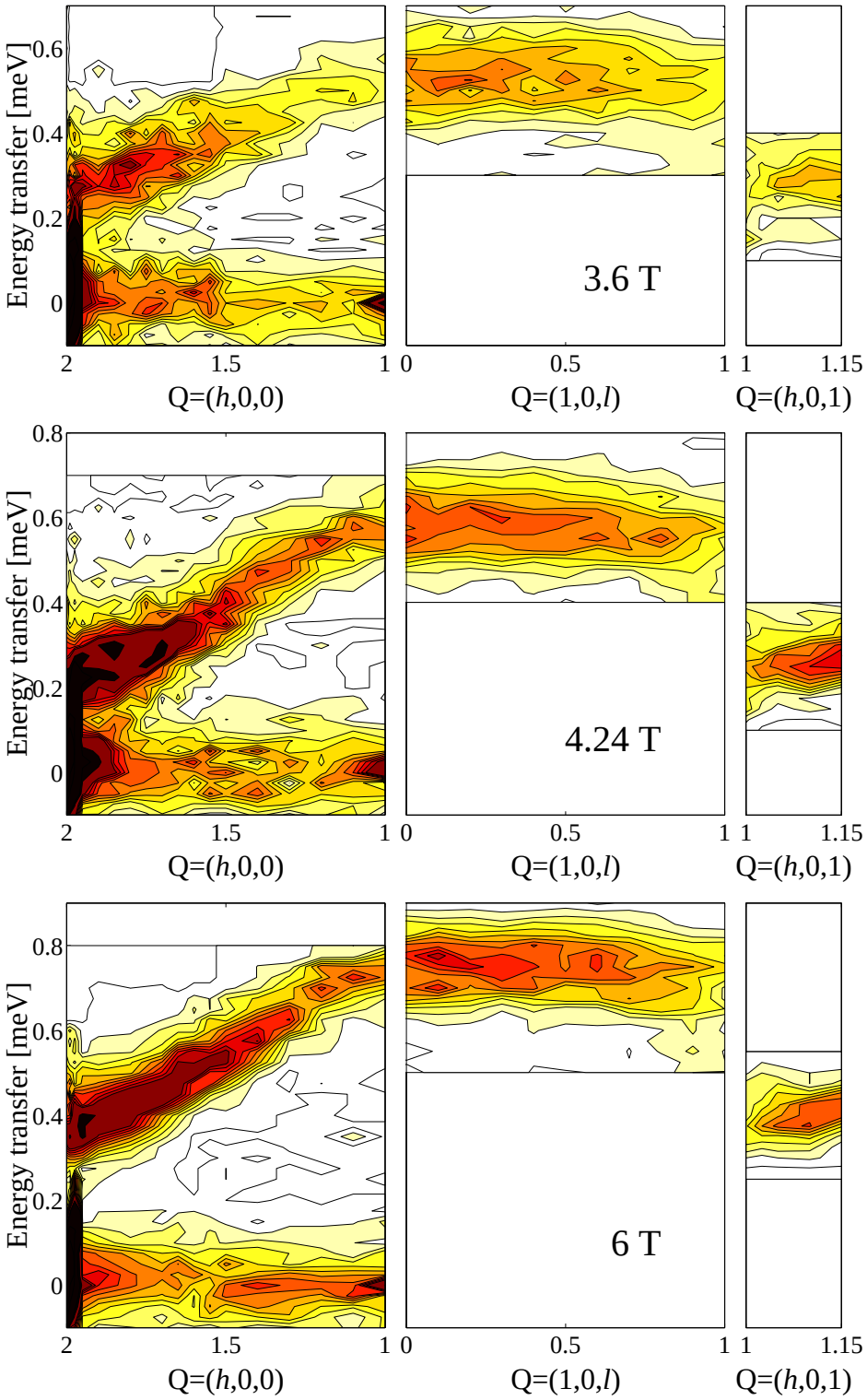

Figure 5.7. Pseudocolor plots of the intensity in energy scans along $(h, 0, 0)$, $(1, 0, l)$ *and* $(h, 0, 1)$ *at three different fields respectively below, at and above the critical field of* $H_c = 4.24$ T.

a critical field of 4.24 T was imposed. Because the field has to be rescaled to meet this requirement, it is difficult to make a direct connection between the actual field strength in the experiments and that entering the calculations — except at H_c which is well defined in both cases. Therefore the following analysis is mainly

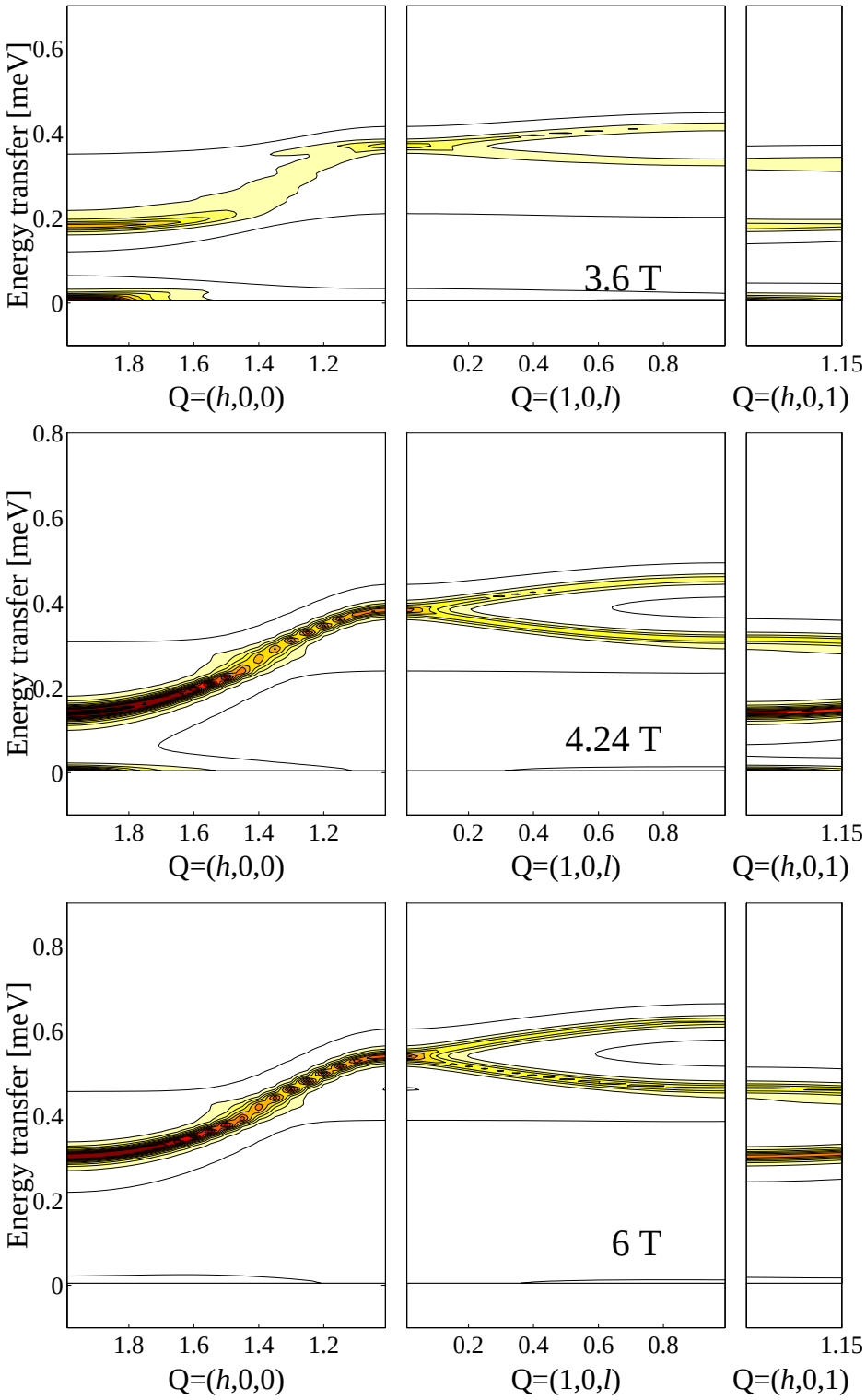

Figure 5.8. Summary of the excitation spectrum obtained by an RPA calculation with $T = 0.4$ K and $\lambda_H = 0.59$.

restricted to this field.

It is seen how the qualitative behaviour is in good agreement with the experimental data in figure 5.7, although the absolute energy scale is somewhat off. The spectral weight is concentrated around (2,0,0) where the dispersion has a minimum. Just as it was seen in the experiment, the calculation shows that the mode

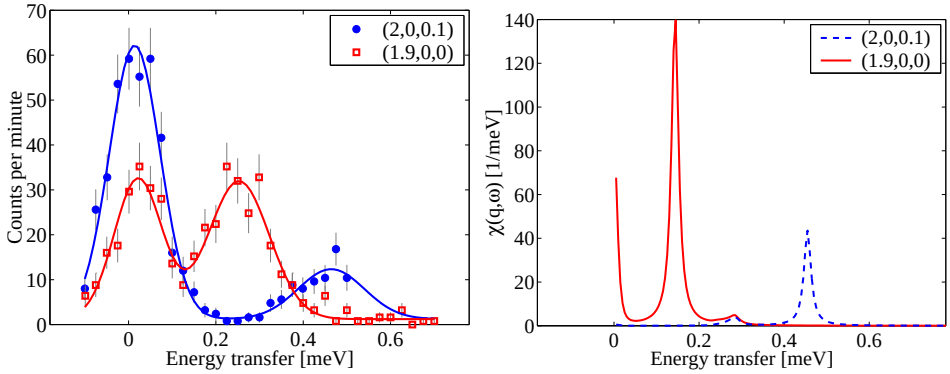

Figure 5.9. Right: Energy scans around (2,0,0) at $H_c = 4.24$ T, illustrating how the dispersion relation jumps from 0.25 ± 0.01 meV at (1.9,0,0) to 0.46 ± 0.02 meV at (2,0,0.1). Left: RPA calculation of the dynamics susceptibility at the same two q vectors, with peak positions 0.15 meV and 0.46 meV respectively. The width of the resonances is given by a small imaginary number $\epsilon = 0.01$ meV introduced to avoid the divergence of the susceptibility at the resonance.

only goes through a minimum around H_c.

By comparing the experimental data to the calculation, it is realised that the apparent broadening of the mode observed experimentally between (1,0,0) and (1,0,1) is in fact because the observed peak is constituted by two individual modes lying close in energy. The calculated splitting is, however, too large compared to the experimental energy width.

Due to the long ranged nature of the dipole coupling, there are discontinuities in its Fourier transform at the reciprocal space points. This can be seen in figures 5.7 and 5.8, where the spectral weight jumps to a lower energy from $q = (1, 0, 1 - \epsilon^+)$ to $(1+\epsilon^+, 0, 1)$. The same situation is present around (2,0,0) as illustrated in figure 5.9.

The dispersion and integrated intensity along $(h, 0, 0)$ have been extracted and is shown in figure 5.10. As shown by the solid lines, the dispersion is reasonably well described by a simple sinusoidal q dependence.

As already apparent from the summary in figure 5.7, the excitation does not soften at H_c, as would be expected from the simple theory presented in section 5.1. This is further demonstrated in figure 5.11, where the limiting excitation energy at $(1 + \epsilon, 0, 1)$ for $\epsilon \to 0$ is extracted as a function of the magnetic field around the QCP. It is seen that the gap goes through a minimum at H_c in what could be called an incomplete softening. This incomplete softening at H_c is due to the hyperfine coupling, which splits the ground state by $\Delta_{\mathrm{hf}} \sim 2AIJ = 0.188$ meV. This has been illustrated in figure 5.11 where the dashed line has been calculated without the hyperfine coupling. In this case, the gap closes at H_c.

In fitting the phase boundary, Bitko *et al.* (1996) had to introduce a scaling of the magnetic field. By replacing $g_L = \frac{5}{4}$ by $g_\perp = 0.74$, the field was effectively multiplied by $\lambda_H = \frac{5}{4} g_\perp = 0.59$. But as this scaling was introduced to compensate for an inaccurate crystal field operator, it should not be expected to successfully describe the excitations. One minimal generalization of this approach was attempted by introducing a second scaling parameter λ_{cf} multiplying the field operator. The two scaling parameters were chosen such that the correct critical field was predicted. However, it was found that varying λ_{cf} gave only minor changes in the excitation energies, and an unreasonably large value was required to match the calculation to the experimentally observed dispersion.

In summary, the experimental data on $LiHoF_4$ are in general well understood

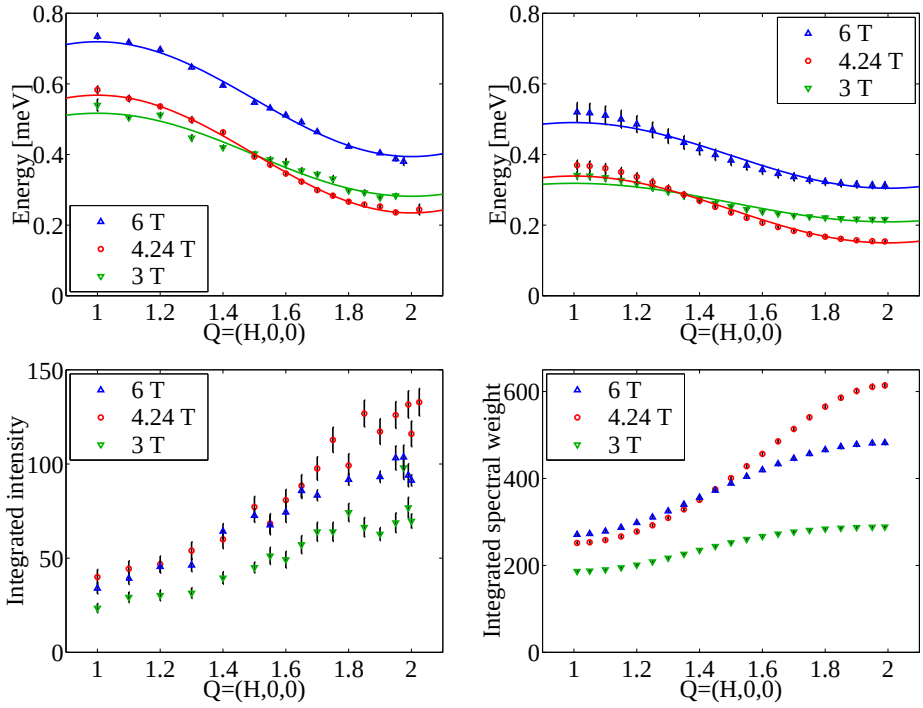

Figure 5.10. Right: Measured dispersion and integrated intensity of the excitation along $(h,0,0)$ at three different fields respectively below, at and above the critical field. Left: extracted dispersion and integrated spectral weight from the RPA results shown in 5.8. The solid lines are fits to simple sinusoidal dispersions.

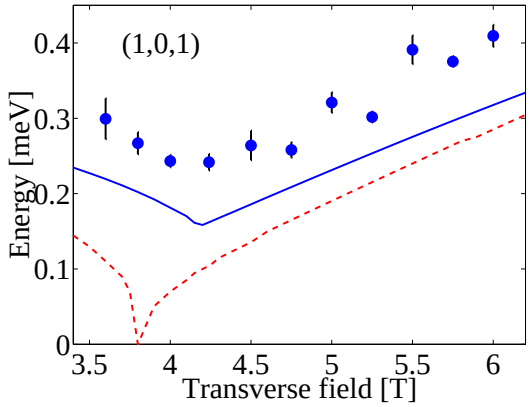

Figure 5.11. Field dependence of the limiting excitation energy at $(1+\epsilon,0,1)$ for $\epsilon \to 0$. The solid line is an RPA calculation using the full RE Hamiltonian, while the dashed line is without the hyperfine coupling.

on the basis of a standard rare-earth Hamiltonian. A quantitative analysis of the magnetization, susceptibility, specific heat and single ion crystal field levels have been used to fix the parameters of the Hamiltonian. The phase diagram and the excitation spectrum is qualitatively described by the RE model, but as these observables depend more critically on the exact eigenstates and eigenvalues of the crystal field, there are slight discrepancies in the absolute value of the critical field and of the excitation energies. It is believed that by using the presented neutron scattering data, these inconsistencies can be reconciled by a careful revision of the model parameters.

5.5 Conclusion and perspectives

The two previous chapters reported experimental results that directly provided new insight into the model systems they were meant to study. The outcome of the present experiment on $LiHoF_4$ does not directly address the physics of the QPT that motivated the study.

Instead it has been demonstrated that the effects around what have been denoted "the worlds simplest quantum critical point" (See *e. g.* Aeppli and Rosenbaum, 1998) are in fact complicated by hyperfine coupling to the nuclear moments. But it has also been shown that measurements of the excitation spectrum are qualitatively understood within the RE model, and can be used to fix the few undetermined parameters herein.

Even though its Hamiltonian is a bit more complicated than the simple Ising model, it is one of the few materials where the microscopic Hamiltonian is known, which can be driven continuously through the QCP. It may not be the simplest QCP, but as it is very well characterized, it opens possibilities for detailed and quantitative investigations of a quantum phase transition.

Chapter 6

Outlook

In summary, this thesis has presented neutron scattering studies of materials that exemplify three different aspects of quantum magnetism. It has been demonstrated how this technique provides direct information about the observables of interest. For $CuGeO_3$ and CFTD new insight was obtained not only into the behaviour of the specific materials but also about the model systems they represent. For $LiHoF_4$ the outcome has been a bit more modest, but the study has demonstrated the potential for future studies.

In the following, I have proposed a number of measurements, sub-projects and complimentary studies. Some of them could possibly provide answers to fundamental questions in quantum magnetism. Others are experimental demonstrations of accepted theoretical predictions. Except for the faint risk that established theories are overthrown, they just serve to please a physicist' mind. Finally, a few experiments aim to clarify aspects of the specific materials. The list is intended both to reflect my own ambitions and to inspire any colleagues in the field. Anyone should feel free and encouraged to work along these suggestions, but it may be useful to contact me and make sure that the given experiment has not already been performed or is in progress.

6.1 $CuGeO_3$

The study of the soliton phase is only one corner of the vast interest in this material. The initial puzzle of why $CuGeO_3$ is a spin–Peierls material at all, has lately been answered in terms of hard phonon coupling, but the large body of experimental data on the spin–Peierls transition and the theoretical developments still need to be combined in a quantitative description. One really interesting aspect which has so far only briefly been touched upon is the hybridization between spin and lattice excitations. As mentioned in chapter 2, the neutron scattering cross-section holds the potential to probe correlations between the spin and lattice degrees of freedom. Experimental studies of the spin–lattice excitations could provide important progress in the understanding of composite particle systems. Concerning the soliton phase, the coexistence and hysteresis effects at the C–IC transition have not been completely described, but more importantly, the excitation spectrum needs to be better characterized before an attempt of a theory can be properly tested. The four experiments that I would propose are therefore

- Polarized neutron scattering investigation of the hybridized spin–lattice excitations.
- Measurement of the dispersion, polarization and field dependencies of the phason mode.

- Measurement of the dispersion along b and c of the $\Delta\pm$ modes in the soliton phase.
- Search for the longitudinal, incommensurate Δ_0 modes.

6.2 CFTD

Where $CuGeO_3$ is in fact rather far from the simple ideal spin–Peierls model, CFTD has proven to be a very good realization of the 2DQHAFSL. The $T = 0$ properties of this model are generally well understood, but the experimental demonstration of the zone boundary dispersion calls for a theoretical understanding of its origin. An additional test of theory would be to see if the spin-wave amplitude also behaves anomalously around $(\pi, 0)$.

Combined with studies on systems with higher values of the spin, the measurements on CFTD have led to a conclusive determination of the correlation length in the 2D square lattice Heisenberg antiferromagnet. The situation for the amplitude S_0 is not equally good. An improvement hereof will either require improvement of the integration range in a two-axis measurement or better control over the phonon background in a time-of-flight measurement.

The measurements of the finite temperature dynamics are among the first that have been reported. Though the temperature dependence of the spin-wave damping was successfully determined, it is desirable to determine its q-dependence. Since the signal remains even at quite high damping rates, there is a posibility that the actual line shape of the damped excitations can be determined.

Finally, there is an entire branch open to studies of the system in applied magnetic fields. To begin with, the cross-over in the correlation length to diverge at the Kosterlitz–Thouless temperature could be investigated.

- Determination of the spin-wave amplitude around $(\pi, 0)$.
- Measurement of S_0 over a wide temperature range.
- Measurement of q-dependence and line shapes of the spin-waves.
- Complementary triple axis measurements of the damping and pseudo gap around $\omega = 0$.
- Application of a magnetic field, correlation length, T_{KT} *etc.*

6.3 $LiHoF_4$

The measurements on $LiHoF_4$ aimed to get a 'text book' picture of the softening around the quantum critical point. The situation turned out to be more complex due to the hyperfine coupling and the dipole interaction. Still, the behaviour of the system is understood through the rare-earth Hamiltonian. If the final details of the model could be adjusted to get a complete description, it would allow for a parameter free analysis of the studies of the yttrium doped systems.

- Precise determination of the lowest crystal field levels in zero field, including their amplitude, which will provide information on the matrix elements.
- Investigation of the quasi-elastic signal containing the hyperfine splitting.
- Parameter free modeling of the randomization effects in the dilute systems.

Acknowledgements

The results reported in this thesis are the outcome of fruitful collaborations with a number of people, whose company I have enjoyed both professionally and socially. The main collaborators have been Mechtild Enderle, Andrew Harrison, Gabe Aeppli and Raghuveer Parthasarathy, but help on these and other projects have also been given by Andrew Wildes, Andrew Wills, Douglas Youngson, Olav Syljuåsen and Charles Dewhurst.

This is an experimental thesis, and I must regard myself as an experimentalist. But to me the real fascination of physics lies on the borderline where measurements and theory meet. Being unable to comprehend all theory myself, I am grateful for the open hearted answers and discussions I have had with Roger Cowley, Robert Birgeneau, Sudip Chakravarty, Subir Sachdev, Andrey Chubukov, Mathias Troyer and Rajiv Singh. In particular, I would like to thank Paola Verrucchi, Valerio Tognetti and their group in Florence for their hospitality during a visit.

The time-of-flight measurements on CFTD at ISIS were performed with the help of Radu Coldea and Toby Perring. The experiments on $CuGeO_3$ were performed at HMI, with support from EC through TMR–LSF contract ERBFMGECT950060. The assistance from A. Hoser, P. Vorderwisch, K. Prokes, H. Schneider, P. Smeibidl and M. Meiner made the visits a pleasure.

The Ph.D. project was financed by The Danish Research Academy (Forskerakademiet) and Risø National Laboratory. The Department of Condensed Matter Physics and Chemistry has been an ideal base for my Ph.D. studies. I have felt privileged with few duties and easy access to beam time combined with good support for experiments and conferences abroad. I have benefited from our skilled technicians, who always met my crazy design directions despite tight time constraints. The atmosphere in the department has made it a pleasure to work there. I thank all of you for some pleasant years. In particular, I have enjoyed the company of my office mates — Thomas Frello for his views on physics, Katrine Nørgaard and Birgitte Jacobsen for views in general.

Throughout the project, I have been guided by my supervisors Jens Jensen and Des McMorrow. Since the university years, I have been able to rely on Jens to clarify many of my questions. Des has taught me the methods of experimental physics and I owe him my feeling for *good data*. I thank him for giving me well balanced measures of space and pace.

Since the early days, where we measured the friction of spheres falling in stairways and derived from basic principles the proportionality constant $\Xi = 1$, I have benefited from my friendship with Niels Asger Mortensen — the work on this thesis has been no exception.

My family in general have had little direct influence on my project, but indirectly their company in weekends and on vacations has refueled me after periods with travels and experiments. Most of all, I owe the completion of this thesis to my beloved wife. During the periods of long experiments, you have tolerated my absence while in relaxed periods you have sweetened my presence. You have comforted me at occasional frustration and shared my joy for seemingly meaningless manifestations of what I call quantum magnetism.

References

Below the references given in the text are listed separately for each of the chapters. The list may at a first glance seem rather comprehensive, but this is in line with the overall ambition that this thesis should serve as a guide to researchers entering one of the fields covered. Though far from complete, the list should be regarded as a compilation of the important contributions on each subject.

Own Publications

M. Enderle, L.-P. Regnault, C. Broholm, D. Reich, I. Zaliznyak, M. Sieling, H. M. Rønnow and D. F. McMorrow (2000a),
High-field spin dynamics of antiferromagnetic quantum spin chains,
Physica B , in press.

M. Enderle, H. M. Rønnow, D. F. McMorrow, L.-P. Regnault, G. Dhalenne, A. Revcolevschi, P. Vorderwich, H. Schneider, P. Smeibidl and M. Meißner (2000b),
Inelastic neutron scattering study of the magnetic excitations in the high-field incommensurate phase of $CuGeO_3$,
In preparation.

K. Lefmann, D. F. McMorrow, H. M. Rønnow, K. Nielsen, K. N. Clausen, B. Lake and G. Aeppli (2000),
Added flexibility in triple axis spectrometers: The two RITAs at Risø,
Physica B , in press.

N. A. Mortensen, H. M. Rønnow, H. Bruus and P. Hedegård (2000),
The magnetic neutron scattering resonance of high-T_c superconductors in external magnetic fields: an SO(5) study,
Submitted to Phys. Rev. B.

H. M. Rønnow, M. Enderle, D. F. McMorrow, L.-P. Regnault, G. Dhalenne, A. Revcolevschi, A. Hoser, P. Vorderwich and H. Schneider (2000a),
Neutron scattering study of the incommensurat high field phase of $CuGeO_3$,
Physica B **276-278**, 678.

H. M. Rønnow, M. Enderle, D. F. McMorrow, L.-P. Regnault, G. Dhalenne, A. Revcolevschi, A. Hoser, P. Vorderwich and H. Schneider (2000b),
Neutron scattering study of the field-induced soliton lattice in $CuGeO_3$,
Phys. Rev. Lett. **84**,
to appear in May.

H. M. Rønnow, D. F. McMorrow, R. Coldea, A. Harrison, G. Aeppli and O. F. Syljuåsen (2000c),
Quantum effects on the spin dynamics of a model 2D Heisenberg antiferromagnet,
In preparation.

H. M. Rønnow, D. F. McMorrow and A. Harrison (1999),
High-Temperature Magnetic Correlations in the 2D $S = 1/2$ Antiferromagnet Copper Formate Tetradeuterate,
Phys. Rev. Lett. **82**, 3152.

H. M. Rønnow, R. Parthasarathy, T. F. Rosenbaum, D. F. McMorrow and G. Aeppli (2000d),
Dynamics at the quantum critical point of the Ising ferromagnet $LiHoF_4$ in a transverse field,
In preparation.

H. M. Rønnow, A. R. Wildes and S. T. Bramwell (2000e),
Magnetic correlations in the 2D $S = 5/2$ honeycomb antiferromagnet $MnPS_3$,
Physica B **276-278**, 676.

O. F. Syljuåsen and H. M. Rønnow (2000),
Quantum renormalization of the excitations in the Heisenberg model,
Submitted.

Chapter 1

A. S. Borovik-Romanov and S. K. Sinha (eds.) (1988),
Spin waves and magnetic excitations,
vol. 22 of *Modern problems in condensed matter sciences*,
North-Holland.

N. D. Mermin and H. Wagner (1966),
Absence of ferromagnetism or antiferromagnetism in one- or two-dimensional isotropic Heisenberg models,
Phys. Rev. Lett. **17**, 1133.

Chapter 2

G. E. Bacon (1975),
Neutron diffraction,
Oxford University Press.

C. Broholm (1996),
Proposal for a doubly focusing cold neutron spectrometer at NIST,
Nuc. Instr. and Meth. A **369**, 169.

P. J. Brown (1992),
Magnetic form factors,
in *International tables for crystallography*, edited by A. J. C. Wilson,
vol. C,
chap. 4.4.5 and 6.1.2. Kluwer Academic.

R. S. Eccleston, R. Osborn and R. I. Bewley (1998),
The HET mini-manual,
RAL report RAL-94-117,
see also `www.isis.rl.ac.uk/excitations/het/het.html`.

FRM-II (2000),
The FRM-II home page,
`www.frm2.tu-muenchen/d/instrumente/damf/rahmen.html`.

A. Hiess (1999),
The millennium programme, Proposals for ILL's 5-year development programme,
Tech. Rep. SC 99-1,
ILL Report.

L. Koester, H. Rauch and E. Seymann (1991),
Neutron scattering lengths: a survey of experimental data and methods,
Atomic Data and Nuclear Data Tables **49**, 65.

K. Lefmann, D. F. McMorrow, H. M. Rønnow, K. Nielsen, K. N. Clausen, B. Lake and G. Aeppli (2000),
Added flexibility in triple axis spectrometers: The two RITAs at Risø,
Physica B , in press.

S. W. Lovesey (1984),
Theory of neutron scattering from condensed matter,
Oxford Science Publications,
Clarendon Press.

T. E. Mason, K. N. Clausen, G. Aeppli, D. F. McMorrow and J. K. Kjems (1995),
RITA: The reinvented triple axis spectrometer,
Can. J. Phys. **73**, 697.

NIST and ILL (2000),
For some reactor-based TOF instruments see:,
`www.ncnr.nist.gov/instruments/dcs/dcs.html` and
`www.ll.fr/YellowBook/instr\_gr/tof.html`.

V. F. Sears (1992),
Neutron scattering lengths and cross sections,
Neutron News **3**, 26.

G. L. Squires (1978),
Introduction to the theory of thermal neutron scattering,
Cambridge University Press,
Available from Dover Publications 1996, ISBN 0-486-69447-X.

J. R. Stehn, M. D. Goldberg, B. . Magurno and R. Wiener-Chasman (1964),
Neutron cross sections,
Bnl 325,
Brookhaven Ntional Laboratory.

Chapter 3

I. Affleck (1990),
Field theory methods and quantum critical phenomena,
in *Fields, Strings and Critical Phenomena*, edited by E. Brézin and J. Zinn-Justin,
p. 563. North-Holland,
Amsterdam.

M. Aïn, J. E. Lorenzo, L. P. Regnault, G. D. A. Revcolevschi, B. Hennion and T. Jolicoeur (1997),
Double gap and solitonic excitations in the spin–Peierls chain $CuGeO_3$,
Phys. Rev. Lett. **78**, 1560.

M. Arai, M. Fujita, M. Motokawa, J. Akimitsu and S. M. Bennington (1996),
Quantum Spin Excitations in the Spin-Peierls System $CuGeO_3$,
Phys. Rev. Lett. **77**, 3649.

N. W. Ashcroft and N. D. Mermin (1976),
Solid state physics,
Saunders company.

D. Augier, D. Poilblanc, E. Sørensen and I. Affleck (1998),
Dynamical effects on soliton binding in spin–Peierls systems,
Phys. Rev. B **58**, 9110.

D. Augier, D. Poilblanc, E. Sørensen and I. Affleck (1999),
Dynamical effects of phonons on soliton binding in quasi-one-dimensional spin–Peierls systems,
Physica B **259-261**, 1015.

T. Barnes, J. Riera and D. A. Tennant (1999),
$S = \frac{1}{2}$ alternating chain using multiprecision methods,
Phys. Rev. B **59**, 11384.

H. A. Bethe (1931),
Zur Theorie der Metalle I. Eigenwerte und Eigenfunktionen der linearen Atomkette,
Z. Phys. **71**, 205.

S. M. Bhattacharjee, T. Nattermann and C. Ronnewinkel (1998),
Incommensurate phase of the pure and doped spin–Peierls system $CuGeO_3$,
Phys. Rev. B **58**, 2658.

S. J. Blundell, F. L. Pratt, P. A. Pattenden, M. Kurmoo, K. H. Chow, S. Takagi, T. Jestädt and W. Hayes (1997),
Spin dynamics in the organic spin–Peierls system $MEM(TCQN)_2$ studied using muon-spin relaxation,
J. Phys. C **9**, L119.

J. C. Bonner and M. E. Fisher (1964),
Linear magnetic chains with anisotropic coupling,
Phys. Rev. **135**, A640.

J. P. Boucher and L. P. Regnault (1996),
Inorganic Spin–Peierls Compound $CuGeO_3$,
J. Phys. I **6**, 1939.

G. Bouzerar, O. Legeza and T. Ziman (1999),
Minimal model to describe the magnetism in $CuGeO_3$,
Phys. Rev. B **60**, 15278.

M. Braden, B. Hennion, P. Pfeuty, G. Dhalenne and A. Revcolevschi (1999),
High-energy magnetic excitation in $CuGeO_3$,
Phys. Rev. Lett. **83**, 1858.

M. Braden, B. Hennion, W. Reichardt, G. Dahlenne and A. Revcolecschi (1998a),
Spin–Phonon Coupling in $GuGeO_3$,
Phys. Rev. Lett. **80**, 3634.

M. Braden, E. Ressouche, B. Büchner, R. Keßler, G. Heger, G. Dahlenne and A. Revcolecschi (1998b),
Anharmonic structural behaviour in $GuGeO_3$,
Phys. Rev. B **57**, 11497.

M. Braden, G. Wilkendorf, J. Lorenzana, M. Aïn, G. J. McIntyre, M. Behruzi, G. Hger, G. Dhalenne and A. Revcolevschi (1996),
Structural analysis of $CuGeO_3$: Relation between nuclear structure and magnetic interaction,
Phys. Rev. B **54**, 1105.

J. W. Bray (1978),
Magnetic field dependence of the spin-Peierls transition,
Solid State Commun. **26**, 771.

J. W. Bray, L. V. Interrante and J. C. Bonner (1983),
The Spin–Peierls Transition,
in *Extended Linear Chain Compounds*, edited by J. S. Miller,
p. 353. Plenum,
New York.

J. W. Bray, H. r. Hart, L. V. Interrante, L. V. Jacobs, I. S. Kasper, G. D. Watkins, S. H. Wee and J. C. Bonner (1975),
Observation of a spin-Peierls transition in a Heisenberg antiferromagnetic linear-chain system,
Phys. Rev. Lett. **35**, 744.

W. Brenig (1997),
Magnetic excitations in quasi-two-dimensional spin–Peierls systems,
Phys. Rev. B **56**, 14441.

T. M. Brill, J. P. Boucher, J. Voiron, G. Dahlenne, A. Revcolevschi and J. P. Renard (1994),
High-field electron resonance and magnetization in the dimerized phase of $CuGeO_3$,
Phys. Rev. Lett. **73**, 1545.

C. Broholm, D. H. Reich, G. Aeppli, S.-H. Lee, D. C. Dender, P. R. Hammar, G. Xu, J. F. Ditusa and A. P. Ramirez (1998),
Neutron scattering studies of non-metallic low-dimensional quantum antiferromagnets,
in *Dynamical Properties of Unconventional Magnetic Systems*, edited by A. T. Skjeltorp and D. Sherrington,
p. 123. Kluwer Academic Publishers,
Dordrecht.

B. Büchner, U. Ammerdahl, T. Lorenz, W. Brenig, G. Dhalenne and A. Revcolevschi (1996),
Magnetic frustration induced formation of the spin–Peierls phase in $CuGeO_3$: Experimental evidence,
Phys. Rev. Lett. **77**, 1624.

B. Büchner, H. Fehske, A. P. Kampf and G. Wellein (1999),
Lattice dimerization in the spin–Peierls compound $CuGeO_3$,
Physica B **259-261**, 956.

L. N. Bulaevskii, A. I. Buzdin and D. I. Khomskii (1978),
Spin-Peierls transition in magnetic field,
Solid State Commun. **27**, 5.

R. J. Bursill, R. H. McKenzie and C. J. Hammer (1999),
Phase diagram of a Heisenberg spin–Peierls model with quantum phonons,
Phys. Rev. Lett. **83**, 408.

A. I. Buzdin, M. L. Kulić and V. V. Tugushev (1983),
Spin–Peierls systems in magnetic field: Phase transition fromdimerized to soliton lattice state,
Solid State Commun. **48**, 483.

G. Castilla, S. Chakravarty and V. J. Emery (1995),
Quantum Magnetism of $CuGeO_3$,
Phys. Rev. Lett. **75**, 1823.

R. Chitra, S. Pati, H. R. Krishnamurthy, D. Sen and S. Ramasesha (1995),
Desity-matrix renormalization-group studies of the spin-1/2 Heisenberg system with dimerization and frustration.,
Phys. Rev. B **52**, 6581.

D. S. Chow, P. Wzietek, D. Fogliatti, B. Alavi, D. J. Tantillo, C. A. Merlic and S. E. Brown (1998),
Singular behaviour in the pressure-tuned competition between spin–Peierls and antiferromagneti ground states of $(TMTTF)_2PF_6$,
Phys. Rev. Lett. **81**, 3984.

M. J. Cooper and R. Nathans (1967),
The resolution function in neutron diffractometry I. The resolution function of a neutron diffractometer and its application to phonon measurements,
Acta Cryst. **23**, 357.

R. A. Cowley, B. Lake and D. A. Tennant (1996),
Models of excitations in $CuGeO_3$,
J. Phys. C **8**, L179.

M. C. Cross (1979),
Effect of magnetic fields on a spin–Peierls transition,
Phys. Rev. B **20**, 4606.

M. C. Cross and D. S. Fisher (1979),
A new theory of the spin–Peierls transition with special relevanc to the experiments on TTFCuBDT,
Phys. Rev. B **19**, 402.

R. Currat and J. D. Axe (1978),
Spurious peaks due to accidental Bragg scattering,
Brookaven National Laboratory research memo G-106.

J. Deisz (1992),
Spin and dimer correlations for $S = 1$ biliniear-biquadratic antiferromagnetic Heisenberg chains,
Phys. Rev. B **46**, 2885.

D. C. Dender, P. R. Hammar, D. H. Reich, C. Broholm and G. Aeppli (1997),
Direct observation of field-induced incommensurate fluctuations in a one-dimensional $S = 1/2$ antiferromagnet,
Phys. Rev. Lett. **79**, 1750.

J. des Cloizeaux and J. J. Pearson (1962),
Phys. Rev. **128**, 2131.

A. Dobry and D. Ibaceta (1998),
Domin excitations in spin–Peierls systems,
Phys. Rev. B **58**, 3124.

A. Dobry and J. Riera (1995),
Soliton width in the incommensurate phase of spin-Peierls systems,
Phys. Rev. B **56**, R2912.

R. S. Eccleston, T. Barnes, J. Brody and J. W. Johnson (1994),
Inelastic neutron scattering from the pin ladder compound $(VO)_2P_2O_7$,
Phys. Rev. Lett. **73**, 2626.

S. Eggert, I. Affleck and M. Takahashi (1994),
Susceptibility of the spin 1/2 Heisenberg antiferromagnetic chain,
Phys. Rev. Lett. **73**, 332.

G. Els, G. S. Uhrig, P. Lemmens, H. Vonberg, P. H. M. van Loosdrecht, G. Güntherodt, O. Fujita, J. Akimitsu, G. Dhalenne and A. Revcolevschi (1998),
Dopant-bound spinons in $Cu_{1-x}Zn_xGeO_3$,
Eur. Phys. Lett. **43**, 463.

M. Enderle (1999),
Quantum spin chains — The macroscopic quantum ground states of Haldane and spin–Peierls chains,
Habilitationsschrift,
Universität des Saarlandes.

M. Enderle, H. M. Rønnow, D. F. McMorrow, L. P. Regnault, G. Dhalenne, A. Revcolevschi, P. Vorderwisch, H. Schneider, P. Smeibidl and M. Meiner (2000),
Inelastic neutron scattering study of the magnetic excitations in the high-field incommensurate phase of $CuGeO_3$,
In preparation .

H. Eskes and J. H. Jefferson (1993),
Superexchange in the cuprates,
Phys. Rev. B **48**, 9788.

K. Fabricius, A. Klümper, U. Löw, B. Büchner, T. Lorenz, G. Dhalenne and A. Revcolevschi (1998),
Reexamination of the microscopic coupling of the quasi-one-dimensional antiferromagnet $CuGeO_3$,
Phys. Rev. B **57**, 1102.

Y. Fagot-Revurat, M. Horvatić, C. Berthier, J. P. Boucher, P. Ségransan, G. Dahlenne and A. Revcolevschi (1997),
^{63,65}Cu NMR investication of $CuGeO_3$ single crystals: The uniform and the dimerized spin–Peierls phase,
Phys. Rev. B **55**, 2964.

Y. Fagot-Revurat, M. Horvatić, C. Berthier, P. Ségransan, G. Dahlenne and A. Revcolevschi (1996),
NMR Evidence for a Magnetic Soliton Lattice in the High-Field Phase of $CuGeO_3$,
Phys. Rev. Lett. **77**, 1861.

X.-J. Fan and C.-D. Gong (1999),
The spin–Peierls phase transition in the quasi-one-dimensional spin-1/2 Heisenberg model,
Eur. Phys. J. B **7**, 233.

A. E. Feiguin, J. A. Riera, A. Dobry and H. A. Ceccatto (1997),
Numerical study of the incommensurate phase in spin–Peierls systems,
Phys. Rev. B **56**, 14607.

S. Feldkemper and W. Weber (1998),
Generalized calculation of magnetic coupling constants for Mott–Hubbard insulators: Application to ferromagnetic Cr compounds,
Phys. Rev. B **57**, 7755.

S. Feldkemper and W. Weber (1999),
Superexchange via cluster states: calculations of spin–phonon coupling constants for $CuGeO_3$,
cond-mat/9909134 .

A. Fledderjohann and C. Gros (1997),
Spin dynamics of dimerized Heisenberg chains,
Eur. Phys. Lett. **37**, 189.

Y. Fudamoto, K. M. Kojima, M. Larkin, G. M. Luke, J. Merring, B. Nachumi, Y. J. Uemura, M. Isobe and Y. Ueda (1999),
Static spin freezing in NaV_2O_5 detected by muon spin relaxation,
Phys. Rev. Lett. **83**, 3301.

M. Fujita and K. Machida (1984),
Spin-Peierls Transition in Magnetic Fields — Thermodynamic Properties of a Soliton Lattice State —,
J. Phys. Soc. Jpn. **53**, 4395.

M. Fujita and K. Machida (1988),
Magnetic structure in a soliton lattice state of a spin–Peierls system under applied fields,
J. Phys. C **21**, 5813.

W. Geertsma and D. Khomskii (1996),
Influence of side groups on 90° superexchange: A modification of the Goodenough–Kanamori–Anderson rules,
Phys. Rev. B **54**, 3011.

J. B. Goodenough (1963),
Magnetism and Chemical Bond,
Interscience.

B. Grenier, L. P. Regnault, J. E. Lorenzo, J. Voiron, J. Bossy, J. P. Renard, G. Dhalenne and A. Revcolevschi (1998),
Neutron-scattering study of the commensurate-incommensurate transition under field in Si-doped $CuGeO_3$ spin-Peierlse systems,
Eur. Phys. Lett. **44**, 511.

B. Grenier, J. P. Renard, P. Veillet, L. P. Regnault, J. E. Lorenzo, C. Paulsen, G. Dhalenne and A. Revcolevschi (1999),
Universal phase diagram of Si-, Zn, Mg- and Ni-doped $CuGeO_3$: spin–Peierls order and antiferromagnetism,
Physica B **259-261**, 954.

R. B. Griffiths (1964),
Magnetization curve at zero temperature for the antiferromagnetic Heisenberg linear chain,
Phys. Rev. **133**, A768.

Q. J. Harris, Q. Feng, R. J. Birgeneau, K. Hirota, K. Kakurai, J. E. Lorenzo, G. Shirane, M. Hase and K. Uchinokura (1994),
Thermal contraction at the spin–Peierls transition in $CuGeO_3$,
Phys. Rev. B **50**, 12606.

M. Hase, I. Terasaki and K. Uchinokura (1993a),
Observation of the Spin–Peierls Transition in Linear Cu^{2+}(Spin-$\frac{1}{2}$) Chains in an Inorganic Compound $CuGeO_3$,
Phys. Rev. Lett. **70**, 3651.

M. Hase, I. Terasaki, K. Uchinokura, M. Tokunaga, N. Kiura and H. Obara (1993b),
Magnetic phase diagram of the Spin–Peierls cuprate $CuGeO_3$,
Phys. Rev. B **48**, 9616.

T. W. Hijmans, H. B. Brom and L. J. de Jongh (1985),
Evidence for an Incommensurate High-Field Phase in the Spin-Peierls System Tetrathiafulvalene-$AuS_4C_4(CF_3)_4$,
Phys. Rev. Lett. **54**, 1714.

K. Hirota, R. J. Birgeneau, M. Hase, H. Kojima, J. E. Lorenzo, Y. Shibuyma, G. Shirane, I. Tanaka, J. M. Tranquada and K. Uchinokura (1995),
Lattice-dynamics and spin-excitations in the spin–Peierls compound $CuGeO_3$,
Physica B **213&214**, 284.

K. Hirota, D. E. Cox, J. E. Lorenzo, G. Shirane, J. M. Tranquada, M. Hase, K. Uchinokura, H. Kojima, Y. Shibuya and I. Tanaka (1994),
Dimerization of $CuGeO_3$ in the Spin-Peierls State,
Phys. Rev. Lett. **73**, 736.

M. Honda, T. Shibata, K. kindo, S. Sugai, T. Takeuchi and H. Hori (1996),
Electron Spin Resonance in One-Diemensional Antiferromagnet $CuGeO_3$,
J. Phys. Soc. Jpn. **65**, 691.

H. Hori, M. Furusawa, S. Sugai, M. Honda, T. Takeuchi and K. Kindo (1995),
High-field magnetization and ESR measurement in $CuGeO_3$,
Physica B **211**, 180.

M. Horvatić, Y. Fagot-Revurat, C. Berthier, G. Dahlenne and A. Revcolevschi (1999),
NMR Imaging of the Soliton Lattice Profile in the Spin-Peierls Compound $CuGeO_3$,
Phys. Rev. Lett. **83**, 420.

S. Huizinga, J. Kommandeur, G. A. Sawatzky, B. T. Thole, K. Kopinga, W. J. M. de Jonge and J. Roos (1979),
Spin-Peierls transition in N-methyl-N-ethyl-morpholinium -ditetracyanoquinodimethanide (MEM-$(TCNQ)_2$),
Phys. Rev. B **19**, 4723.

L. Hulthén (1938),
Über das Austauschproblem eines Kristalles,
Arkv. Mat. Astron. Fys. **26A**.

S. Inagaki and H. Fukuyama (1983a),
Spin-Peierls State vs Neel State: I. Small Ising Anisotropy,
J. Phys. Soc. Jpn. **52**, 2504.

S. Inagaki and H. Fukuyama (1983b),
Spin-Peierls State vs Neel State: II. Interchain Exchange Interaction,
J. Phys. Soc. Jpn. **52**, 3620.

S. Inagaki and H. Fukuyama (1984),
Spin-Peierls State vs Antiferromagnetic State. III. Effects of Magnetic Field,
J. Phys. Soc. Jpn. **53**, 4386.

M. Isobe and Y. Ueda (1996),
Magnetic susceptibility of quasi-one-dimensional compound α'-NaV_2O_5 — Possible spin–Peierls compound with high critical temperature of 34 K,
J. Phys. Soc. Jpn. **65**, 1178.

I. S. Jacobs, J. W. Bray, H. R. Hart, L. V. Interrante, J. S. Kasper, G. D. Watkins, D. E. Pober and J. C. Bonner (1976),
Spin-Peierls transitions in magnetic donor-acceptor compounds of tetrathiafulvalene (TTF) with bisdithiolene metal complexes,
Phys. Rev. B **14**, 3036.

J. B. Jamali, N. Wada, Y. Shimboe, N. Achiwa, S. Kuwajima, Y. Soejima and K. Mukai (1998),
The effect of non-magnetic impurities on the spin–Peierls transition of 3-(4-cyanophenyl)-1,5-dimethyl-6-oxoverdazyl radical, *p*-CyDOV,
Chem. Phys. Lett. **292**, 661.

D. C. Johnston, J. W. Johnson, D. P. Goshorn and A. J. Jacobson (1987),
Magnetic susceptibility of $(VO)_2P_2O_7$: A one-dimensional spin-1/2 Heisenberg antiferromagnet with a ladder configuration and a single ground state,
Phys. Rev. B **35**, 219.

O. Kamimura, M. Terauchi, M. Tanaka, M. Fujita and J. Akimitsu (1994),
Electron Diffraction Study of an Inorganic Spin-Peierls System $CuGeO_3$,
J. Phys. Soc. Jpn. **63**, 2467.

D. Khomskii, W. Geertsma and M. Mostovoy (1996),
Elementary excitations, exchange interaction and spin-Peierls transition in $CuGeO_3$,
Czech. J. Phys. **46**, 3239.

V. Kiryukhin and B. Keimer (1995),
Incommensurate lattice modulation in the spin–Peierls system $CuGeO_3$,
Phys. Rev. B **52**, 704.

V. Kiryukhin, B. Keimer, J. P. Hill, and A. Vigliante (1996a),
Soliton Lattice in Pure and Diluted $CuGeO_3$,
Phys. Rev. Lett. **76**, 4608.

V. Kiryukhin, B. Keimer, J. P. Hill, S. M. Coad and D. M. Paul (1996b),
Synchrotron x-ray scattering study of magnetic-field-induced transitions in $Cu_{1-x}(Zn,Ni)_xGeO_3$,
Phys. Rev. B **54**, 7269.

V. Kiryukhin, B. Keimer and D. E. Moncton (1995),
Direct observation of a magnetic field induced commensurate–incommensurate transition in a spin–Peierls system,
Phys. Rev. Lett. **74**, 1669.

C. Kittel (1953-1996),
Introduction to solid state physics,
John Wiley and Sons.

A. Klümper, R. Raupach and F. Schönfeld (1999),
Finite temperature density-matrix-renormalization-group investigations of the spin–Peierls transition in $CuGeO_3$,
Phys. Rev. B **59**, 3612.

S. Kokado, N. Nojiri and N. M. andN. Suzuki (1998),
Exchange splitting of EPR spectra in $CuGeO_3$ under ultra-high magnetic fields — theoretical analysis,
Physica B **246-247**, 238.

K. Kuboki and H. Fukuyama (1987),
Spin–Peierls transition with competing interactions,
J. Phys. Soc. Jpn. **56**, 3126.

B. Lake (1999),
Private cmmunication.

B. Lebech and M. Nielsen (1975),
Intensity and resolution of a general scan in reciprocal space,
in *Proceedings of the Neutron Diffraction Conference*,
p. 466,
Petten, The Netherlands.

K. Lefmann and C. Rischel (1996),
Dynamical correlation functions of the $S = 1/2$ nearest-neighbor and Haldane–Shastry Heisenberg antiferromangetic chains in zero and applied fields,
Phys. Rev. B **54**, 6340.

K. Lefmann and C. Rischel (1998),
Users manual to the spin diagonalization program RLexact,
Risø National Labratory,
4000 Roskilde, Denmak.

H. Q. Lin and D. K. Cambell (1991),
Spin–spin correlations in the one-dimensional spin 1/2 antiferromagnetic Haesenberg chain,
J. Appl. Phys. **69**, 5947.

Y. Liu, J. E. Drumheller and R. D. Willet (1995),
Low-temperature susceptibilities of the quasi-one-dimensional spin-1/2 Heisenberg antiferromagnets (6MAP)$CuCl_3$ and (3MAP)$CuCl_3$: Spin–Peierls transition versus broken-chain effects,
Phys. Rev. B **52**, 15327.

I. Loa, S. Gronemeyer, C. Thomsen and R. K. Kremer (1996),
Low-energy magnetic excitations in the dimerized and incommensurate phase of $CuGeO_3$,
Solid State Commun. **99**, 231.

I. Loa, S. Gronemeyer, C. Thomsen and R. K. Kremer (1999),
Low-energy magnetic excitations in the dimerized and incommensurate phase of $CuGeO_3$,
Solid State Commun. **111**, 181.

T. Lorenz, B. Büchner, P. H. M. van Loosdrecht, F. Schönfeld, G. Chouteau, A. Revcolecschi and G. Dahlenne (1998),
Incommensurate Phase of $CuGeO_3$: rom Solitons to Sinusoidal Modulation,
Phys. Rev. Lett. **81**, 148.

J. E. Lorenzo, K. Hirota, G. Shirane, J. M. Tranquada, M. Hase, K. Uchinokura, H. Kojima, I. Tanaka and Y. Shibuya (1994),
Soft longitudinal modes in spin-singlet $CuGeO_3$,
Phys. Rev. B **50**, 1278.

J. E. Lorenzo, L. P. Regnault, J. P. Boucher, B. Hennion, G. Dhalenne and A. Revcolenschi (1999),
Anisotropy of the spin interactions in the spin–Peierls compound $CuGeO_3$: A new magnetic excitation branch,
Eur. Phys. Lett. **45**, 619.

J. E. Lorenzo, L. P. Regnault, B. Hennion, M. Aïn, F. Bourdarot, J. Kulda, G. Dhalenne and A. Revcolenschi (1997),
Spin dynamics in the spin–Peierls compound $CuGeO_3$,
J. Phys. C **9**, L211.

M. D. Lumsden and B. D. Gaulin (1999),
Critical phenomena at te spin–Peierls transition in $MEM(TCQN)_2$,
Phys. Rev. B **59**, 9372.

J. G. Lussier, S. M. Coad, D. F. McMorrow and D. M. Paul (1995),
Observation of the Neel state in doped $CuGeO_3$,
J. Phys. C **7**, L325.

J.-G. Lussier, S. M. Coad, D. F. McMorrow and D. M. Paul (1996),
The temperature dependence of the spin–Peierls energy gap in $CuGeO_3$,
J. Phys. C **8**, L59.

A. Luther and I. Peschel (1975),
Calculation of critical exponents in two dimensions from quantum field theory in one dimension,
Phys. Rev. B **12**, 3908.

K. Machida and M. Fujita (1984),
Soliton lattice structure of incommensurate spin–density waves: Application to Cr and Cr-rich Cr-Mn and Cr-V alloys,
Phys. Rev. B **30**, 5284.

T. Masuda, I. Tsukada, K. Uchinokura, Y. J. Wang, V. Kiryukhin and R. J. Birgeneau (1999),
The first-order transition between dimerized-antiferromagnetic and uniform-antiferromagnetic phases in $Cu_{1-x}M_xGeO_3$,
cond-mat/9906130 .

L. F. Mattheiss (1994),
Band picture of the spin–Peierls transition in the spin-1/2 linear-chain cuprate $CuGeO_3$,
Phys. Rev. B **49**, 14050.

Y. Meurdesoif and A. Buzdin (1999),
Soliton structure in spin–Peierls systems,
Phys. Rev. B **59**, 11165.

Y. Mizuno, T. Tohyama, S. Maekawa, T. Osafune, N. Motoyama, H. Eisaki and S. Uchida (1998),
Electronic states and magnetic properties of edge-sharin Cu-O chains,
Phys. Rev. B **57**, 5326.

D. E. Moncton, R. J. Birgeneau, L. V. Interrante and F. Wudl (1977),
X-ray scattering study of spin–lattice dimerization in a quasi one-dimensional Heisenberg antiferromagnet,
Phys. Rev. Lett. **39**, 507.

N. A. Mortensen and H. M. Rønnow (2000),
In progress.

K. Mukai, N. Wada, J. B. Jamali, N. Achiwa, Y. Narumi, K. Kindo, T. Kobayashi and K. Amaya (1996),
Magnetic properties of 1,5-dimethyl-6-oxoverdazyl radical crystals. Observation of a spin–Peierls transition in 3-(4-cyanophenyl)-1,5-dimethyl-6-oxoverdazyl radical, *p*-CyDOV,
Chemical Physics Letters **257**, 538.

G. Müller, H. Thomas, H. Beck and J. C. Bonner (1981),
Quantum spin dynamics of the antiferromagnetic linear chain in zero and nonzero magnetic field,
Phys. Rev. B **24**, 1429.

V. N. Muthukumar, C. Gros, R. Valentí, M. Weiden, C. Geibel, F. Steglich, P. Lemmens, M. Fisher and G. Güntherodt (1997),
J_1-J_2 model revisited: Phenomenology of $CuGeO_3$,
Phys. Rev. B **55**, 5944.

T. Nakano and H. Fukuyama (1980),
Solitons in spin-Peierls systems and applications to polyacetylene,
J. Phys. Soc. Jpn. **49**, 1679.

T. Nakano and H. Fukuyama (1981),
Dimerization and Solitons in One-Dimensional XY-Z Antiferromagnets,
J. Phys. Soc. Jpn. **50**, 2489.

M. Nishi, O. Fujita and J. Akimitsu (1994),
Neutron-scattering study of the spin–Peierls transition in a quasi-one-dimensional magnet $CuGeO_3$,
Phys. Rev. B **50**, 6508.

M. Nishi, O. Fujita and J. Akimitsu (1995),
Inelastic neutron scattering study of the lattice dynamics in $CuGeO_3$,
Physica B **210**, 149.

M. Nishi, K. Kakurai, Y. Fujii, S. Katano, J. Akimutsu, M. Yethiraj and J. A. Fernandez-baca (1999),
New aspects of the b^*-LA phonon of $CuGeO_3$,
J. Phys. Chem. Solids **60**, 109.

H. Nojiri, H. Ohta, N. Nimura and M. Motokawa (1998a),
Study of spin–Peierls $CuGeO_3$ by high-field ESR,
Physica B **246-247**, 16.

H. Nojiri, Y. Shimamoto, N. Miura, M. Hase, K. Uchinokura, H. Kojima, I. Tanaka and Y. Shibuya (1998b),
Exchange splitting in $CuGeO_3$ under ultrahigh magnetic fields,
Phys. Rev. B **57**, 10276.

H. Nojiri, H. T, O. Fujita and J. Akimitsu (1998c),
ESR study of the field-induced mgnetic phase of spin–Peierls $CuGeO_3$ and $MEM(TCNQ)_2$,
J. Magn. Magn. Mater **177-181**, 687.

K. Nomura and M. Yamada (1991),
Thermal Bethe-ansatz study of the correlation length of the one-dimensional $S = 1/2$ Heisenberg antiferromagnet,
Phys. Rev. B **43**, 8217.

H. Ohta, S. Imagawa, H. Ushiroyama, M. Motokawa, O. Fujita and J. Akimitsu (1994),
Electron Spin Resonance of Spin-Peierls Material $CuGeO_3$,
J. Phys. Soc. Jpn. **63**, 2870.

W. Palme, G. Ambert, J. P. Boucher, G. Dahlenne and A. Revcolevschi (1996),
Hysteresis in the Incommensurate Phase of the Spin–Peierls Compound $CuGeO_3$: Electron Spin resonance in High Field,
Phys. Rev. Lett. **76**, 4814.

B. Pilawa (1997),
Anisotropy of the electron spin-resonance linewidth of $CuGeO_3$,
J. Phys. C **9**, 3779.

D. Poilblanc, J. Riera, C. A. Hayward, C. Berthier and M. Horvatić (1997),
Spin dynamics of the spin–Peierls compound $CuGeO_3$ under a magnetic field,
Phys. Rev. B **55**, R11941.

M. Poirier, P. Fertey, J. Jegoudez and A. Revcolevschi (1999),
Dielectric behaviour and charge ordering in NaV_2O_5,
Phys. Rev. B **60**, 7341.

M. Popovici (1975),
On the resolution of slow-neutron spectrometers. IV. The triple-axis spectrometer resolution function, spatial effects included,
Acta Cryst. **A31**, 507.

J. P. Pouget, L. P. Regnault, M. Aïn, B. Hennion, J. P. Renard, P. Veillet, G. Dhalenne and A. Revcolevschii (1994),
Structural evidence for a spin–Peierls ground state in the quasi-one-dimensional compound $CuGeO_3$,
Phys. Rev. Lett. **72**, 4037.

E. Pytte (1974),
Peierls instability in Heisenberg chains,
Phys. Rev. B **10**, 4637.

R. Raupach, A. Klümper and F. Schönfeld (1999),
Pressure dependence and non-universal effects of the microscopic couplings on the spin–Peierls transition in $CuGeO_3$,
cond-mat/9908407 .

L. P. Regnault, M. Aïn, B. H. an G. Dahlenne and A. Revcolevschi (1996),
Inelastic-neutron-scattering investigation of the spin-Peierls system $CuGeO_3$,
Phys. Rev. B **53**, 5579.

L. P. Regnault, J. P. Renard, G. Dhalenne and A. Revcolevschi (1995),
Coexistence of dimerization and antiferromagnetism in Si-doped $CuGeO_3$,
Eur. Phys. Lett. **32**, 579.

G. Rémenyi, S. Sahling, J. C. Lasjaunias, N. Hegman, J. P. Brison, A. I. Buzdin, G. Dhalenne and A. Revcolevschi (1997),
Specific heat at the spin–Peierls transition in $CuGeO_3$ under magnetic fields up to 22 tesla,
J. Low Temp. Phys. **107**, 243.

A. Revcolevschi, U. Ammerahl and G. Dhalenne (1999),
Crystal growth of pure and substituted low-dimensionality cuprates $CuGeO_3$, La_2CuO_4, $SrCuO_2$, Sr_2CuO_3 and $Sr_14Cu_24O_41$ by the floating zone and travelling solvent zone methods,
Crystal Growth **198/199**, 593.

J. Riera and A. Dobry (1995),
Magnetic susceptibility in the spin–Peierls system $CuGeO_3$,
Phys. Rev. B **51**, 16098.

M. Saint-Paul, G. Reményi, N. Hegman, P. Monceau, G. Dhalenne and A. Revcolevschi (1997),
Phonon-soliton interaction in the incommensurate phase of the spin–Peierls compound $CuGeO_3$,
Phys. Rev. B **55**, 6121.

A. W. Sandvik and D. K. Campbell (1999),
Spin–Peierls transition in the Heisenberg chain with finite-frequency phonons,
Phys. Rev. Lett. **83**, 195.

Y. Sasago, N. Koide, K. Uchinokura, M. C. Martin, M. Hase, K. Hirota and G. Shirane (1996),
New phase diagram of Zn-doped $CuGeO_3$,
Phys. Rev. B **54**, R6835.

J. P. Schoeffel, J. P. Pouget, G. Dhalenne and A. Revcolevschi (1996),
Spin–Peierls lattice fluctuations of pure and Si- and Zn-substituted $CuGeO_3$,
Phys. Rev. B **53**, 14971.

F. Schönfeld, G. Bouzerar, G. S. Uhrig and E. Müller-Hartmann (1998),
On the incommensurate phase in modulated Heisenberg chains,
Eur. Phys. J. B **5**, 521.

H. J. Schulz (1986),
Phase diagrams and correlation exponents for quantum spin qhains of arbitrary spin quantum number,
Phys. Rev. B **34**, 6372.

G. Shirane (1999),
Magnetism of doped $CuGeO_3$,
J. Phys. Chem. Solids **60**, 1031.

H. L. Skriver (1984),
The LMTO Method: Muffin tin orbitals and electronic structure,
Springer-Verlag.

Ž. V. Šljivančanin, Z. S. Popović and F. R. Vukajlović (1997),
Band picture of the spin–Peierls cuprate $CuGeO_3$,
Phys. Rev. B **56**, 4432.

E. Sørensen, I. Affleck, D. Augier and D. Poilblanc (1998),
Soliton approach to spin–Peierls antiferromagnets: Large-scale numerical results,
Phys. Rev. B **58**, R14701.

M. Steiner, J. Villain and C. G. Windsor (1976),
Theoretical and experimental studies on one-dimensional magnetic systems,
Advances in Phyics **25**, 87.

K. Takehana, T. Takamasu, M. Hase, G. Kido and K. Uchinokura (1998),
Magnetostriction measurements of $CuGeO_3$ in high magnetic fields,
Physica B **246-247**, 246.

K. Takehana, T. Takamasu, M. Hase, G. Kido and K. Uchinokura (1999),
Far-infrared spectroscopy in spin–Peierls compound $CuGeO_3$ under high magnetic fields,
cond-mat/9905325 .

D. A. Tennant and D. F. McMorrow (1996),
Rescal,
Part of the mFit suite for Matlab, see `www.ill.fr/tas/matlab/doc`.

D. A. Tennant, S. E. Nagler, Q. W. Garrett, T. Barnes and C. C. Torardi (1997),
Excitation spectrum and superexchange pathways in the spin dimer $VODPO_4 \cdot \frac{1}{2}D_2O$,
Phys. Rev. Lett. **78**, 4998.

H. Terauchi, N. Sakamoto and I. Shirotani (1976),
Lattice instability near monomer-dimer phase transition temperature,
J. Chem. Phys. **64**, 437.

S. Tornow, O. Entin-Wohlman and A. Aharony (1999),
Anisotropic superexchange for nearest and next-nearest coppers in chain, ladder, and lamellar cuprates,
Phys. Rev. B **60**, 10206.

M. Troyer, H. Tsunetsugu and D. Würtz (1994),
Thermodynamics and spin gap of the Heisenberg ladder calculated by the look-ahead Lanczos algorithm,
Phys. Rev. B **50**, 13515.

A. Tucciarone, H. Y. Lau, L. M. Corliss, A. Delapalme and J. M. Hastings (1971),
Quantitative analysis of inelastic scattering in two-crystal and three-crystal neutron spectrometry; critical scattering from $RbMnF_3$,
Phys. Rev. B **4**, 3206.

G. S. Uhrig (1997),
Symmetry and dimension of the magnon dispersion of inorganic spin–Peierls systems,
Phys. Rev. Lett. **79**, 163.

G. S. Uhrig (1998),
Nonadiabatic approach to spin–Peierls transitions via flow equations,
Phys. Rev. B **57**, 14004.

G. S. Uhrig (1999),
Modulated phases in spin–Peierls systems,
in *Advances in solid state physics*, edited by B. Kramer,
vol. 39,
p. 291. Vieweg Verlag,
Braunschweig,
cond-mat/9904387.

G. S. Uhrig, F. Schönfeld and J. P. Boucher (1998),
A magnetic model for the incommensurate I phase of spin-Peierls systems,
Eur. Phys. Lett. **41**, 431.

G. S. Uhrig, F. Schönfeld, J.-P. Boucher and M. Horvatić (1999a),
Soliton lattices in the incommensurate spin–Peierls phase: Local distortions and magnetizations,
Phys. Rev. B **60**, 9468.

G. S. Uhrig, F. Schönfeld, M. Laukamp and E. Dagotto (1999b),
Unified quantum mechanical picture for confined spinons in dimerized and frustrated spin $S = 1/2$ chains,
Eur. Phys. J. B **7**, 67.

G. S. Uhrig and H. J. Schulz (1996),
Magnetic excitation spectrum of dimerized antiferromagnetic chains,
Phys. Rev. B **54**, R9624.

B. van Bodegom, B. C. Larson and H. A. Mook (1981),
Diffuse X-ray and inelastic neutron scattering study of the spin Peierl's transition in N-methyl-N-ethyl-morpholinium bistetracyanoquinodimethane ($MEM(TCNQ)_2$),
Phys. Rev. B **24**, 1520.

P. H. M. van Loosdrecht (1998),
Optical spectroscopy on the spin–Peierls compound $CuGeO_3$,
Solid State Phenomena **61-62**, 19.

P. H. M. van Loosdrecht, J. P. Boucher, G. Martinez, D. Dhalene and A. Revcolevschi (1996a),
Inelastic Light Scattering from Magnetic Fluctuations in $CuGeO_3$,
Phys. Rev. Lett. **76**, 311.

P. H. M. van Loosdrecht, S. Huant, G. Martinez, D. Dhalene and A. Revcolevschi (1996b),
Dynamics in the dimerized and the high-field incommensurate pase of $CuGeO_3$,
Phys. Rev. B **54**, R3730.

H. Völlenkle, A. Wittmann and H. Nowotny (1967),
Monatsh. Chem. **98**, 1352.

Y. J. Wang, V. Kiryukhin, R. J. Birgeneau, T. Masuda, I. Tsukada and K. Uchinokura (1999),
Structural critical scattering study of Mg-doped $CuGeO_3$,
Phys. Rev. Lett. **83**, 1676.

R. E. Watson and A. J. Freeman (1961),
Hartree-Fock Atomic Scattering Factors for the Iron Transition Series,
Acta Cryt. **14**, 27.

T. S. Wei, A. J. Heeger, M. B. Salamon and G. E. Delker (1977),
Specific heat studies of the spin-Peierls transition,
Solid State Commun. **21**, 595.

A. Weiße and H. Fehske (1998),
Peierls instabillity and optical response in the one-dimensional half-filled Holstein model of spinless fermions,
Phys. Rev. B **58**, 13526.

A. Weiße, G. Wellein and H. Fehske (1999),
Quntum lattice fluctuations in a frustrated Heisenberg spin–Peierls chain,
Phys. Rev. B **60**, 6566.

G. Wellein, H. Fehske and A. P. Kampf (1998),
Peierls dimerization with nonadiabatic spin–Phonon coupling,
Phys. Rev. Lett. **81**, 3956.

R. Werner, C. Gros and M. Braden (1999),
Microscopic spin–phonon coupling constants in $CuGeO_3$,
Phys. Rev. B **59**, 14356.

S. R. White (1992),
Density matrix formulation for quantum renormalization groups,
Phys. Rev. Lett. **69**, 2863.

S. R. White (1993),
Density-matrix algorithms for quantum renormalization groups,
Phys. Rev. B **48**, 10345.

S. R. White (1998),
Strongl correlated electron systems and the density matrix renormalization group,
Physics Reports **301**, 187.

H. Winkelmann, E. Gamper, B. Büchner, B. Braden, A. Revcolevschi and G. Dahlenne (1995),
Giant anomalies of the thermal expansion at the spin–Peierls transition in $CuGeO_3$,
Phys. Rev. B **51**, 12884.

I. Yamada, M. Nishi and J. Akimitsu (1996),
Electron paramagnetic resonance governed by the Dzyaloshinsky-Moriya antisymmetric exchange interaction in $CuGeO_3$,
J. Phys. C **8**, 2625.

W. Yu and S. Haas (1999),
Excitation spectra of structurally dimerized and spin–Peierls chains in a magnetic field,
cond-mat/9909093 .

S. Zagoulaev and I. I. Tupitsyn (1997),
Electronic structure and magnetic properties of the spin–Peierls compound $CuGeO_3$,
Phys. Rev. B **55**, 13528.

J. Zang, A. R. Bishop and D. Schmeltzer (1995),
Frustrated spin–Peierls chains,
Phys. Rev. B **52**, 6723.

J. Zang, S. Chakravarty and A. R. Bishop (1997),
Interchain coupling effects and solitons in $CuGeO_3$,
Phys. Rev. B **55**, R14705.

H. Zheng (1997),
Quantum lattice fluctuations in the ground state of an XY spin–Peierls chain,
Phys. Rev. B **56**, 14414.

Chapter 4

I. Affleck (1988a),
Field theory methods and quantum critical phenomena,
in *Fields, strings and critical phenomena*, edited by E. Brezin and J. Zinn-Justin,
p. 563. NATO-ASI,
North-Holland.

I. Affleck (1988b),
Spin gap and symmetry breaking in CuO_2 layers and other antiferromagnets,
Phys. Rev. B **37**, 5186.

N. H. Andersen and G. Uimin (1997),
Model for the low-temperature magnetic phases observed in doped $YBa_2Cu_3O_6 + x$,
Phys. Rev. B **56**, 10840.

D. P. Arovas and A. Auerbach (1988),
Functional integral theories of low-dimensional quantum Heisenberg models,
Phys. Rev. B **38**, 316.

A. Auerbach and D. P. Arovas (1988),
Spin dynamics in the square-lattice antiferromagnet,
Phys. Rev. Lett. **61**, 617,
See also comment by Kopietz (1990).

B. B. Beard, R. J. Birgeneau, M. Greven and U.-J. Wiese (1998),
Square-Lattice Heisenberg Antiferromagnet at Very Large Correlation Lengths,
Phys. Rev. Lett. **80**, 1742.

B. B. Beard, V. Chudnovsky and P. Keller-Marxer (1999),
Reconciling the correlation length for high-spin Heisenber antiferromagnets,
cond-mat/9910291 .

V. L. Berezinskii (1971),
Destruction of long-range order in one-dimensional and two-dimensional systems having a continuous symmetry group I. Classical systems,
Sov. Phys. JETP **32**, 493.

V. L. Berezinskii (1972),
Destruction of long-range order in one-dimensional and two-dimensional systems having a continuous symmetry group II. Quantum systems,
Sov. Phys. JETP **34**, 610.

V. L. Berezinskii and Y. Y. Blank (1973),
Thermodynamics of layerd isotropic magnets at low temperature,
Sov. Phys. JETP **37**, 369.

J. Berger (1975),
The Raman spectra and the antiferroelectric phase transition of copper formate tetrahydrate,
J. Phys. C **8**, 2903.

H. A. Bethe (1931),
Zur Theorie der Metalle I. Eigenwerte und Eigenfunktionen der linearen Atomkette,
Z. Phys. **71**, 205.

R. J. Birgeneau, A. Aharony, N. R. Belk, F. C. Chou, Y. Endoh, M. Greven, S. Hosoya, M. A. Kastner, C. H. Lee, Y. S. Lee, G. Ahirane, S. Wakimoto, B. O. Wells and K. Yamada (1995),
Magnetism and magnetic fluctuations in $La_{2-x}Sr_xCuO_4$ for $x = 0$ (2D antiferromagnet), 0.04 (3D spin glass) and $x = 0.15$ (superconductor),
J. Phys. Chem. Solids **56**, 1913.

R. J. Birgeneau, M. Greven, M. A. Kastner, Y. S. Lee, B. O. Wells, Y. Endoh, K. Yamada and G. Shirane (1999),
Instantanous spin correlations in La_2CuO_4,
Phys. Rev. B **59**, 13788.

C. Broholm (1999),
Private communication.

N. Burger, H. Fuess and P. Burlet (1980),
Neutron Diffraction Study of the Antiferromagentic Phase of Copper Formate Tetradeuterate,
Solid State Commun. **34**, 883.

H. Cabannes (ed.) (1976),
Padé approximants method and its applications to mechanics,
vol. 47 of *Lecture Notes in Physics*,
Springer-Verlag.

C. M. Canali, S. M. Girvin and M. Wallin (1992),
Spin-wave velocity renormalization in the two-dimensional Heisenberg antiferromagnet at zero temperature,
Phys. Rev. B **45**, 10131.

C. M. Canali and M. Wallin (1993),
Spin-spin correlation functions for the square-lattce Heisenberg antiferromagnet at zero temperature,
Phys. Rev. B **48**, 3264.

S. Caracciolo, R. G. Edwards, A. Pelissetto and A. D. Sokal (1995),
Asymptotic scaling in the two-dimensional O(3) σ model at correlation length 10^5,
Phys. Rev. Lett. **75**, 1891.

P. Carretta, T. Ciabattoni, A. Cuccoli, E. Mognaschi, A. Rigamonti, V. Tognetti and P. Verrucchi (2000),
Spin dynamics and magnetic correlation length in two-dimensional quantum Heisenberg antiferromagnets,
Phys. Rev. Lett. **84**, 366.

S. Chakravarty, B. I. Halperin and D. R. Nelson (1989),
Two-dimensional quantum Heisenberg antiferromagnet at low temperatures,
Phys. Rev. B **39**, 2344.

G. Chen, H.-Q. Ding and W. A. Goddard III (1992),
Elmentary excitations for the two-dimensional quantum Heisenberg antiferromagnet,
Phys. Rev. B **46**, 2933.

A. V. Chubukov and S. Sachdev (1993),
Universal magnetic properties of $La_{2-\delta}Sr_{\delta}CuO_4$ at intermediate temperatures,
Phys. Rev. Lett. **71**, 169.

A. V. Chubukov, S. Sachdev and J. Ye (1994),
Theory of two-dimensional quantum Heisenberg antiferromagnets with a nearly critical ground state,
Phys. Rev. B **49**, 11919.

A. V. Chubukov and O. A. Starykh (1999),
On the behaviour of a 2D Heisenberg antiferromagnet at very low temperatures,
J. Phys. C **11**, L169.

S. J. Clarke (1991),
An experimental study of some two-dimensional quantum antiferromagnets,
Ph.D. thesis,
St. John's College, University of Oxford.

S. J. Clarke, A. Harrison, T. E. Mason and D. Visser (1999),
Characterisation of spin-waves in copper(II) deuteroformate tetradeuterate: a square $S = 1/2$ Heisenberg antiferromagnet,
Solid State Commun. **112**, 561.

R. Coldea (1999a),
Private communication.

R. Coldea (1999b),
mSlice,
Rutherford Appleton Laboratory,
Chilton, Oxfordshire, UK.

A. Cuccoli, R. Giachetti, V. Tognetti, R. Vaia and P. Verrucchi (1995),
The effective potential and effictive Hamiltonian in quantum statistical mechanics,
J. Phys. C **7**, 7891.

A. Cuccoli, V. Tognetti, R. Vaia and P. Verrucchi (1996),
Temperature and Spin Dependent Correlation Length of the Quantum Heisenberg Antiferromagnet on the Square Lattice,
Phys. Rev. Lett. **77**, 3439,
ibid **79**, 1583 and 1584 (1997).

A. Cuccoli, V. Tognetti, R. Vaia and P. Verrucchi (1997),
Reply to comment on previous letter,
Phys. Rev. Lett. **79**, 1584.

A. Cuccoli, V. Tognetti, P. Verrucchi and R. Vaia (1998),
Heisenberg antiferromagnet on the square lattice for $S \leq 1$,
Phys. Rev. B **58**, 14151.

H.-Q. Ding and M. S. Makivić (1990),
Spin Correlations of 2D Quantum Antiferromagnet at Low Temperatures and a Direct Comparison with Neutron-Scattering Experiments,
Phys. Rev. Lett. **64**, 1449.

A. Dupas and J.-P. Renard (1970),
Zero-point deviation and spontaneous sublattice magnetization in the two-dimensional antiferromagnet $Cu(HCOO)_2 \cdot 4D_2O$,
Phys. Lett. A **33**, 470.

F. J. Dyson (1956),
Phys. Rev. **102**, 1217,
ibid **102**, 1230 (1956).

F. J. Dyson, E. H. Lieb and B. Simon (1978),
Phase transitions in quantum spin systems with isotropic and nonisotropic interactions,
J. Stat. Phys. **18**, 335.

N. Elstner, R. L. Glenister, R. R. P. Singh and A. Sokol (1995a),
Scaling regimes, crossovers, and lattice corrections in two-dimensional Heisenberg antiferromagnets,
Phys. Rev. B **51**, 8984.

N. Elstner, A. Sokol, R. R. P. Singh, M. Greven and R. J. Birgenau (1995b),
Spin Dependence of Correlations in Two-Dimensional Square-Lattice Quantum Heisenberg Antiferromagnets,
Phys. Rev. Lett. **75**, 938.

M. Enderle, L.-P. Regnault, C. Broholm, D. Reich, I. Zaliznyak, M. Sieling, H. M. Rønnow and D. F. McMorrow (2000),
High-field spin dynamics of antiferromagnetic quantum spin chains,
Physica B , in press.

B. Fåk and B. Dorner (1992),
On the interpretation of phonon line shapes and excitation energies in neutron scatterin experiments,
ILL Report No. 92FA008S.

B. Fåk and B. Dorner (1997),
Phonon line shapes and excitation energies,
Physica B **234**, 1107.

R. B. Flippen and S. A. Friedberg (1963),
Low-Temperature Susceptibilities of Some Hydrated Formates of Cu^{++} and Mn^{++},
J. Chem. Phys. **38**, 2652.

G. Gomez-Santos, J. D. Joannopoulos and J. W. Negele (1989),
Monte Carlo study of the quantum spin-$\frac{1}{2}$ Heisenberg antiferromagnet on the square lattice,
Phys. Rev. B **39**, 4435.

M. Greven, R. J. Birgenau, Y. Endoh, M. A. Kastner, B. Keimer, M. Matsuda, G. Shirane and T. R. Thurston (1994a),
Spin correlations in $Sr_2CuO_2Cl_2$,
Physica B **199&200**, 642.

M. Greven, R. J. Birgenau, Y. Endoh, M. A. Kastner, M. Matsuda and G. Shirane (1995),
Neutron scattering study of the two-dimensional spin $S = \frac{1}{2}$ square-lattice Heisenberg antiferromagnet $Sr_2CuO_2Cl_2$,
Z. Phys. B **96**, 465.

M. Greven, R. J. Birgenau, Y. Endoh, M. A. Kastner, M. Matsuda, G. Shirane and T. R. Thurston (1994b),
Spin Correlations in the 2D Heisenberg Antiferromagnet $Sr_2CuO_2Cl_2$: Neutron Scatterin, Monte Carlo Simulation and Theory,
Phys. Rev. Lett. **72**, 1096.

F. D. M. Haldane (1983),
Continuum dynamics of the 1-D Heisenberg antiferromagnet: Identification with the $O(3)$ nonlinear sigma model,
Physics Letters **93A**, 464.

F. D. M. Haldane (1988),
O(3) nonlinear σ model and the topological distinction between integer- and half-integer-spin antiferromagnets in two dimensions,
Phys. Rev. Lett. **61**, 1029.

B. I. Halperin and P. C. Hohenberg (1969),
Phys. Rev. **188**, 898.

K. Harada, M. Troyer and N. Kawashima (1998),
The two-dimensional $S = 1$ quantum Heisenberg antiferromagnet at finite temperatures,
J. Phys. Soc. Jpn. **67**, 1540.

A. Harrison, S. J. Clarke, T. E. Mason and D. Visser (1992),
Dispersion of spin-waves in the $S = 1/2$ square Heisenberg antiferromagnet $Cu(CuD_2O)_2{\cdot}4D_2O$,
J. Magn. Magn. Mater **104-107**, 557.

P. Hasenfratz (1999),
The correlation length of the Heisenberg antiferromagnet with arbitrary spin S,
cond-mat/9901355 To be published in Europhys. J. B.

P. Hasenfratz, M. Maggiore and F. Niedermayer (1990),
The exact mass gap of the O(3) and O(4) non-linear sigma-models in $d = 2$,
Physics Letters B **245**, 522.

P. Hasenfratz and F. Niedermayer (1990),
The exact mass gap of the O(N) sigma -model for arbitrary $N \geq 3$ in $d = 2$,
Physics Letters B **245**, 529.

P. Hasenfratz and F. Niedermayer (1991),
The exact correlation length of the antiferromagnetic $d = 2 + 1$ Heisenberg model at low temperatures,
Physics Letters B **268**, 231.

S. M. Hayden, G. Aeppli, P. D. an H. A. Mook, T. G. Perring, S.-W. Cheong, Z. Fisk, F. Doğan and T. E. Mason (1998),
Absolute measurements of the high frequency magnetic dynamics in high-T_c superconductors,
Physica B **241-243**, 765.

S. M. Hayden, G. Aeppli, R. Osborn, A. D. Taylor, T. G. Perring, S.-W. Cheong and Z. Fisk (1991),
High-energy spin wavew in La_2CuO_4,
Phys. Rev. Lett. **67**, 3622.

J. E. Hirsch and S. Tang (1989),
Spin-wave theory of the quantum antiferromagnet with unbroken sublattice symmetry,
Phys. Rev. B **40**, 4769.

T. Holstein and H. Primakoff (1940),
Phys. Rev. **58**, 1048.

T. C. Hsu (1990),
Spin waves in the flux-phase description of the $S = 1/2$ Heisenberg antiferromagnet,
Phys. Rev. B **41**, 11379.

L. Hulthén (1938),
Über das Austauschproblem eines Kristalles,
Arkv. Mat. Astron. Fys. **26A**.

J. Igarashi (1992),
$1/S$ expansion for thermodynamic quantities in a two-dimensional Heisenberg antiferromagnet at zero temperature,
Phys. Rev. B **46**, 10763.

J. Igarashi (1993),
$1/S$ expansion in a two-dimensional frustrated Heisenberg antiferromagnet,
J. Phys. Soc. Jpn. **62**, 4449.

J. Igarashi and A. Watabe (1991),
Dynamics of a two-dimensioal antiferomagnet at zero temperature,
Phys. Rev. B **43**, 13456.

M. I. Kaganov and A. V. Chubukov (1988),
Spin waves in magnetic dielectrics. Current status of the theory,
in *Spin waves and magnetic excitations*, edited by A. S. Borovik-Romanov and S. K. Sinha,
vol. 22.2,
p. 1. North-Holland.

M. I. Kay (1975),
A refinement of the paraelectric phase of copper formate tetrahydrate from neutron diffraction data,
Ferroelectrics **9**, 171.

B. Keimer, N. Belk, R. J. Birgenau, A. Cassanho, C. Y. Chen, M. Greven and M. A. Kastner (1992),
Magnetic excitations in pure, lightly doped, and weakly metallic La_2CuO_4,
Phys. Rev. B **46**, 14034.

P. Keller-Marxer (1999),
The antiferromagnetic square-lattice O(3) quanrum Heisenberg model for spins $S = 1/2 - 5/2$ *at low temperatures*,
Ph.D. thesis,
Universität Bern.

T. Kennedy, E. H. Lieb and B. S. Shastry (1988),
Existence of Neel order in some spin-1/2 Heisenberg antiferromagnets,
J. Stat. Phys. **53**, 1019.

J.-K. Kim, D. P. Landau and M. Troyer (1997),
Temperature Dependent Correlation Length for the $S = \frac{1}{2}$ Quantum Heisenberg Antiferromagnet on the Square Lattice,
Phys. Rev. Lett. **79**, 1583.

J.-K. Kim and M. Troyer (1998),
Low Temperature Behaviour and Crossovers of the Square Lattice Quantum Heisenberg Antiferromagnet,
Phys. Rev. Lett. **80**, 2705.

H. Kiriyama (1962a),
Bull. Chem. Soc. Japan **35**, 1199.

H. Kiriyama (1962b),
Bull. Chem. Soc. Japan **35**, 1205.

R. Kiriyama, H. Ibamoto and K. Matsuo (1954),
Acta Crystallogr. **7**, 482.

H. Kobayashi and T. Haseda (1963),
J. Phys. Soc. Jpn. **18**, 541.

P. Kopietz (1990),
Comment on "Spin dynamics in the square-lattice antiferromagnet",
Phys. Rev. Lett. **64**, 2587,
Comment to Auerbach and Arovas (1988).

J. M. Kosterlitz (1974),
The critical properties of teh two-dimensional xy model,
J. Phys. C **7**, 1046.

J. M. Kosterlitz and D. J. Thoules (1973),
Ordering, metastability and phase transitions in two-dimensional systems,
J. Phys. C **6**, 1181.

K. Kubo (1988),
Existence on long-range order in the XY model,
Phys. Rev. Lett. **61**, 110.

D. H. Lee, J. D. Joannopoulos and J. W. Negele (1984),
Monte Carlo solution of antiferromagnetic quantum Heisenberg spin systems,
Phys. Rev. B **30**, 1599.

K. Lefmann, C. Rischel and H. M. Rønnow (2000),
In progress.

M. E. Lines (1969),
Magnetism in two dimensions,
J. App. Phys. **40**, 1352.

M. E. Lines (1970),
The quadratic-layer antiferromagnet,
J. Phys. Chem. Solids **31**, 101.

M. Makivić and M. Jarrell (1992),
Low-Temperature Dynamics of the 2D Spin-$\frac{1}{2}$ Heisenberg Antiferromagnet: A Quantum Monte Carlo Study,
Phys. Rev. Lett. **68**, 1770.

M. S. Makivić and H.-Q. Ding (1991),
Two-dimensianal spin-$\frac{1}{2}$ Heisenberg antiferromagnet: A quantum Monte Carlo study,
Phys. Rev. B **43**, 3562.

S. V. Maleev (1957),
Zh. Eksp. Teor. Fiz. **30**, 1010.

E. Manousakis (1991),
The spin-$\frac{1}{2}$ Heisenberg antiferromagnet on a square lattice and its applications to the cuprous oxides,
Rev. Mod. Phys. **63**, 1.

E. Manousakis and R. Salvador (1988),
Long-range correlations in the two-dimensional spin-$\frac{1}{2}$ antiferromagnetic heisenberg model: A quantum Monte Carlo study,
Phys. Rev. Lett. **60**, 840.

E. Manousakis and R. Salvador (1989),
Monte Carlo study of the two-dimensional spin-$\frac{1}{2}$ quantum Heisenberg model: Spin correlations in La_2CuO_4,
Phys. Rev. B **39**, 575.

R. L. Martin and H. Waterman (1959),
J. Chem. Soc. p. 1359.

N. D. Mermin and H. Wagner (1966),
Absence of ferromagnetism or antiferromagnetism in one- or two-dimensional isotropic Heisenberg models,
Phys. Rev. Lett. **17**, 1133.

D. K. Morr (1998),
Effect of next-nearest-neighbor hopping on the spin dynamics in antiferromagnets,
Phys. Rev. B **58**, R587.

T. Nagao and J. Igarashi (1998),
Spin Dynamics in Two-Dimensional Quantum Heisenberg Antiferromagnets,
J. Phys. Soc. Jpn. **67**, 1029.

K. Okada, M. I. Kay, D. T. Cromer and I. Almodovar (1966),
Crystal Structure by Neutron Diffraction and the Antiferroelectric Phase Transition in Copper Formate Tetrahydrate,
J. Chem. Phys. **44**, 1648.

K. Okada and H. Sugie (1968),
Experimental study of antiferroelectric copper formate tetrahydrate and its deuterium substitute,
J. Phys. Soc. Jpn. **25**, 1128.

L. Onsager (1942),
Phys. Rev. **65**, 117.

R. Osborn and T. G. Perring (1999),
Multi-Frills, An interactive least-squares fitting package,
Rutherford Appleton Laboratory,
Chilton, Oxfordshire, UK,
www.isis.rl.ac.uk/excitations/Manuals/Multi_Frills/frameset.html.

T. G. Perring (1999),
Tobyfit version 2.0, Least-Squares Fitting to sincle crystal data on HET, MARI and MAPS,
Rutherford Appleton Laboratory,
Chilton, Oxfordshire, UK.

T. G. Perring, G. Aeppli, S. M. Hayden, S. A. Carter, J. P. Remeika and S.-W. Cheong (1996),
Spin waves throughout the Brillouin zone of a double-exchange ferromagnet,
Phys. Rev. Lett. **77**, 711.

H. M. Rønnow, D. F. McMorrow and A. Harrison (1999),
High-Temperature Magnetic Correlations in the 2D $S = 1/2$ Antiferromagnet Copper Formate Tetradeuterate,
Phys. Rev. Lett. **82**, 3152.

H. M. Rønnow, A. R. Wildes and S. T. Bramwell (2000),
Magnetic correlations in the 2D $S = 5/2$ honeycomb antiferromagnet $MnPS_3$,
Physica B **276-278**, 676.

G. S. Rushbrooke and P. J. Wood (1958),
Mol. Phys. **1**, 257.

S. Sachdev (1992),
Quantum antiferromagnets in two dimensions,
in *Low dimensional quantum field theories for condensed matter physicists*,
edited by S. Lundqvist, G. Morandi and Y. Lu,
vol. 6 of *Series on modern condensed matter physics*,
p. 553. World Scientific,
Singapore.

S. Sachdev and J. Ye (1992),
Universal Quantum-Critical Dynamics of Two-Dimensional Antiferromagnets,
Phys. Rev. Lett. **69**, 2411.

J. Schwinger (1952),
On Angular Momentum,
Rpt. nyo-3071,
U. S. Atomic Energy Commission,
reprinted in L. Biedenharn and H. Van Dam (eds.): *Quantum Theory of Angular Momentum* (Academic, NewYork 1965).

M. S. Seehra (1968),
Rev. Sci. Instr. **39**, 1044.

M. S. Seehra (1969),
Two-dimensional magnetic behavior of copper formate tetrahydrate,
Phys. Lett. A **28**, 754.

M. S. Seehra and T. G. Castner Jr. (1970),
Study of the ordered magnetic state of copper formate tetrahydrate by antiferromagnetic resonance,
Phys. Rev. B **1**, 2289.

R. R. P. Singh and M. P. Gelfand (1995),
Spin-wave excitation spectra and spectral weights in square lattice antiferromagnets,
Phys. Rev. B **52**, R15695.

G. Soda and T. Chiba (1969),
Deuteron magnetic resonance study of cupric formate tetrahydrate $Cu(DCOO)_2{\cdot}4D_2O$,
J. Phys. Soc. Jpn. **26**, 249.

H. E. Stanley (1968a),
Critical properties of isotropically interacting classical spins constrained to a plane,
Phys. Rev. Lett. **20**, 150.

H. E. Stanley (1968b),
Dependence of critical properties on dimensionality of spins,
Phys. Rev. Lett. **20**, 589.

H. E. Stanley and T. A. Kaplan (1966),
Possibility of a phase transition fo the two-dimensional Heisenberg model,
Phys. Rev. Lett. **17**, 913.

O. F. Syljuåsen and H. M. Rønnow (2000a),
Finite temperature excitation spectrum of the 2D Heisenberg antiferormagnet: A quantum Monte Carlo study,
In preparation.

O. F. Syljuåsen and H. M. Rønnow (2000b),
Quantum renormalization of the excitations in the Heisenberg model,
Submitted.

M. Takahashi (1989),
Modiefied spin-wave theory of a square-lattice antiferromagnet,
Phys. Rev. B **40**, 2494.

N. Trivedi and D. M. Ceperley (1990),
Ground-state correlations of quantum antiferromagnets: A Green-function Monte Carlo study,
Phys. Rev. B **41**, 4552.

S. Tyč and B. I. Halperin (1990),
Damping of spin waves in a two-dimensional Heisenberg antiferromagnet at low temperatures,
Phys. Rev. B **42**, 2096.

S. Tyč, B. I. Halperin and S. Chakravarty (1989),
Dynamic Properties of a Two-Dimensional Heisenberg Antiferromagnet at Low Temperatures,
Phys. Rev. Lett. **62**, 835.

D. Vaknin, L. L. Miller, J. L. Zarestky and D. C. Johnston (1997),
Elastic and quasielastic neutron scattering study of the spin-1/2 square lattice antiferromagnet $Sr_2CuO_2Cl_2$,
Physica C **274**, 331.

D. Vaknin, S. K. Sinha, D. E. Moncton, D. C. Johnston, J. M. Newsam, C. R. Safiya and H. E. King Jr. (1987),
Antiferromagnetism in $La_2CuO_4 - y$,
Phys. Rev. Lett. **58**, 2802.

P. van der Leeden, P. A. van Dalen and W. J. M. de Jonge (1967),
Investigation of the magnetic state of $Cu(COOH)_2{\cdot}4H_2O$ and $Cu(COOH)_2{\cdot}4D_2O$ at 4.2° K by a proton resonance study,
Physica **33**, 202.

P. Verrucchi (1999),
Private communication.

Y.-J. Wang, M.-R. Li and C.-D. Gong (1997),
Relaxation function theory of the quantum spin-$\frac{1}{2}$ Heisenberg antiferromagnets at finite temperatures,
Phys. Rev. B **56**, 10982.

A. R. Wildes, M. J. Harris and K. W. Godfrey (1998a),
Two-dimensional critical fluctuations in $MnPS_3$,
J. Magn. Magn. Mater **177-181**, 143.

A. R. Wildes, S. J. Kennedy and T. J. Hicks (1994),
True two-dimensional magnetic ordering in $MnPS_3$,
J. Phys. C **6**, L335.

A. R. Wildes, B. Roessi, B. Lebech and K. W. Godfrey (1998b),
Spin waves and the critical behaviour of the magnetization in $MnPS_3$,
J. Phys. C **10**, 6417.

S. Winterfeldt and D. Ihle (1997),
Theory of antiferromagnetic short-range order in the two-dimensional Heisenberg model,
Phys. Rev. B **56**, 5535.

S. Winterfeldt and D. Ihle (1999),
Spin dynamics and antiferromagnetic short-range order in the two-dimensional Heisenberg model,
Phys. Rev. B **59**, 6010.

G. M. Wysin and A. R. Bishop (1990),
Dynamic correlations in a classical two-dimensional Heisenberg antiferromagnet,
Phys. Rev. B **42**, 810.

K. Yamada, K. Kakurai, Y. Endoh, T. R. Thurston, M. A. Kastner, R. J. Birgeneau, G. Shirane, Y. Hidaka and T. Murakami (1989),
Spin dynamics in the two-dimensional quantum antiferromagnet La_2CuO_4,
Phys. Rev. B **40**, 4557.

K. Yamagata, Y. Kozuka and T. Morita (1981),
Magnetization Process of Nearly 2-Dimensional $Cu(HCOO)_2{\cdot}4H_2O$ and $Cu(HCOO)_2{\cdot}2(NH_2)_2CO{\cdot}2H_2O$. II Estimation of Magnetic Parameters,
J. Phys. Soc. Jpn. **50**, 421.

K. Yamagata and T. Sakai (1980),
Magnetization Process of Nearly 2-Dimensional $Cu(HCOO)_2{\cdot}4H_2O$ and $Cu(HCOO)_2{\cdot}2(NH_2)_2CO{\cdot}2H_2O$. I Mechanism of the Field-Induced Transition,
J. Phys. Soc. Jpn. **49**, 2165.

M. E. Zhitomirsky and T. Nikuni (1998),
Magnetization curve of a swuare-lattice Heisenberg antiferromagnet,
Phys. Rev. B **57**, 5013.

Chapter 5

G. Aeppli and T. F. Rosenbaum (1998),
Quantum critical points — experiments,
in *Dynamical properties of unconventional magnetic systems*, edited by A. T. Skjeltorp and D. Sherrington,
vol. 349 of *Series E*,
p. 107,
Dordrecht. NATO ASI,
Kluwer Academic Publishers.

J. Als-Nielsen (1976),
Experimental test of renormalization group theory on the uniaxial, dipolar coupled ferromagnet $LiTbF_4$,
Phys. Rev. Lett. **37**, 1161.

J. Als-Nielsen, L. M. Holmes and H. J. Guggenheim (1974),
Wave-vector–Dependent Susceptibility at $T > T_c$ in a Dipolar Ising Ferromagnet,
Phys. Rev. Lett. **32**, 610.

D. Bitko (1997),
Ph.D. thesis,
University of Chicago.

D. Bitko, T. F. Rosenbaum and G. Aeppli (1996),
Quantum Critical Behaviour for a Model Magnet,
Phys. Rev. Lett. **77**, 940.

B. Bogenberger and H. v. Löhneysen (1995),
Tuning of non-Fermi-liquid behaviour with pressure,
Phys. Rev. Lett. **74**, 1016.

G. J. Bowden and R. G. Clark (1981),
Fourier transforms of dipole–dipole interactions using Ewald's method,
J. Phys. C **14**, L827.

J. Brooke, D. Bitko, T. F. Rosenbaum and G. Aeppli (1999),
Quantum Annealing of a Disordered Magnet,
Science **284**, 779.

R. Brout, K. A. Müller and H. Thomas (1966),
Solid State Commun. **4**, 507.

T. W. Burkhardt and J. D. Gunton (1974),
Critical behaviour of an Ising model of classical spins in a transverse field,
Phys. Rev. A **9**, 2802.

S. A. Carter, T. F. Rosenbaum, J. M. Honig and J. Spalek (1991),
New phase boundary in highly correlated, barely metallic V_2O_3,
Phys. Rev. Lett. **67**, 3440.

H. P. Christensen (1979),
Spectroscopic analysis of $LiHoF_4$ and $LiErF_4$,
Phys. Rev. B **19**, 6564.

R. J. Creswick, H. A. Farach, J. M. Knight and C. P. P. Jr. (1988),
Monte Carlo method for the Ising model in a transverse field,
Phys. Rev. B **38**, 4712.

P. G. de Gennes (1963),
Solid State Commun. **1**, 132.

M. J. de Oliveira and J. R. N. Chiappin (1997),
Monte Carlo simulation of the quantum transverse Ising model,
Physica A **238**, 307.

R. J. Elliott, P. Pfeuty and C. Wood (1970),
Ising model with a transverse field,
Phys. Rev. Lett. **25**, 443.

P. E. Hansen, T. Johansson and R. Nevald (1975),
Magnetic properties of lithium fluorides: Ferromagnetism in $LiErF_4$ and $LiHoF_4$ and crystal-field parameters at the rare-earth and Li sites,
Phys. Rev. B **12**, 5315,
Note that the authors use different crystal field operators $\tilde{B}$ related to the usual Steven's operators B as: $B_2^0 = (1/2)\alpha_2\tilde{B}_2^0 = -0.0648$ meV, $B_4^0 = (1/8)\alpha_4\tilde{B}_4^0 = 0.426 \times 10^{-3}$ meV, $B_4^4(c) = -(\sqrt{70}/8)\alpha_4\tilde{B}_4^4 = 0.00453$ meV, $B_6^0 = (1/16)\alpha_6\tilde{B}_6^0 = 0.1 \times 10^{-6}$ meV, $B_6^4(c) = -(3\sqrt{14}/16)\alpha_6\tilde{B}_6^4(R) = 0.855 \times 10^{-4}$ meV, $B_6^4(s) = -(3\sqrt{14}/16)\alpha_6\tilde{B}_6^4(I) = 0.169 \times 10^{-4}$ meV, where their values for holmium has been inserted.

L. M. Holmes, J. Als-Nielsen and H. J. Guggenheim (1975),
Dipolar and nondipolar interactions in $LiTbF_4$,
Phys. Rev. B **12**, 180.

J. Jensen (1994),
$1/z$ renormalization of the mean-field behaviour of the dipole-coupled singlet-singlet system HoF_3,
Phys. Rev. B **49**, 11833.

J. Jensen and A. R. Mackintosh (1991),
Rare earth magnetism — structures and excitations,
Oxford Science Publications,
Clarendon Press.

M. J. M. Leask, M. R. Wells, R. C. C. Ward, S. M. Hayden and J. Jensen (1994),
Magnetic excitations in the dipole-coupled singlet-singlet system HoF_3,
J. Phys. C **6**, 505.

J. Magariño, J. Tuchendler, P. Beauvillain and I. Laursen (1980),
EPR experiments in $LiTbF_4$, $LiHoF_4$ and $LiErF_4$ at submillimeter frequencies,
Phys. Rev. B **21**, 18.

G. Mennenga, L. J. de Jongh and W. J. Huiskamp (1984a),
Field dependent specific heat tudy of the dipolar ising ferromagnet $LiHoF_4$,
J. Magn. Magn. Mater **44**, 59,
The coupling parameters in this article are in units that should be multiplied by $2(g_L/g_{||})^2$ to compare with the rare-earth Hamiltonian.

G. Mennenga, L. J. de Jongh, W. J. Huiskamp and I. Laursen (1984b),
A comparative study of the magnetic ordering specific heats of four $S = \frac{1}{2}$ dipolar magnets $LiFF_4$ (R=Er, Dy, Ho, Tb),
J. Magn. Magn. Mater **44**, 48.

D. H. Reich, B. Ellman, J. Yand, T. F. Rosenbaum, G. Aeppli and D. P. Belanger (1990),
Dipolar magnets adn glasses: Neutron-scattering, dynamical, and calorimetric studies of randomly distributed Ising spins,
Phys. Rev. B **42**, 4631.

D. H. Reich, T. F. Rosenbaum, G. Aeppli and H. J. Guggenheim (1986),
Ferromagnetism, glassiness and metastability in a dilute dipolar-coupled magnet,
Phys. Rev. B **34**, 4956.

M. L. Ristig and J. W. Kim (1996),
Correlated-basis-function analysis of the transverse Ising model,
Phys. Rev. B **53**, 6665.

H. M. Rønnow (1996),
Magnetic properties of Holmium–Erbium Alloys,
Master's thesis,
Niels Bohr Institute, University of Copenhagen,
ISBN 87-550-2221-9.

T. F. Rosenbaum (1996),
Quantum magnets and glasses,
J. Phys. C **8**, 9759.

S. Sachdev (1999),
Quantum phase transitions,
Physics World p. 33.

S. Salaün, A. Bulou, M. Rousseau, B. Hennion and J. Y. Gesland (1997a),
Lattice dynamics of fluoride sheelites: II. Inelastic neutron scattering in $LiYF_4$ and modelization,
J. Phys. C **9**, 6957.

S. Salaün, M. T. Fornoni, A. Bulou, M. Rousseau, P. Simon and J. Y. Gesland (1997b),
Lattice dynamics of fluoride sheelites: I. Raman an infrared study of $LiYF_4$ and $LiLnF_4$ (Ln=Ho, Er, Tm and Yb),
J. Phys. C **9**, 6941.

R. B. Stinchcombe (1973a),
Ising model in a transverse field: I. Basic theory,
J. Phys. C **6**, 2459.

R. B. Stinchcombe (1973b),
Ising model in a transverse field: II. Spectral fnctions and damping,
J. Phys. C **6**, 2484.

M. Thomsen (1986),
Transverse susceptibility for Ising systems: Direct calculation from the local field distribution,
Phys. Rev. B **34**, 4762.

Y.-L. Wang and B. R. Cooper (1968),
Collective excitations and magnetic ordering in materials with singlet crystal-field ground state,
Phys. Rev. **172**, 539.

W. Wu, D. Bitko, T. F. Rosenbaum, G. Aepli and D. H. Reich (1993),
Quenching of the nonlinear susceptibility at a $T = 0$ spin glass transition,
Phys. Rev. Lett. **71**, 1919.

W. Wu, B. Ellman, T. F. Rosenbaum, G. Aepli and D. H. Reich (1991),
From classical to quantum glass,
Phys. Rev. Lett. **67**, 2076.

Bibliographic Data Sheet **Risø–R–1180(EN)**

Title and author(s)

Aspects of Quantum Magnetism in One, Two and Three Dimensions

Henrik Moodysson Rønnow

ISBN	ISSN
87–550–2693–1; 87–550–2695–8 (internet)	0106–2840

Dept. or group	Date
Condensed Matter Physics and Chemistry Department	March 2000

Groups own reg. number(s)	Project/contract No.

Pages	Tables	Illustrations	References
180	5	89	387

Abstract (Max. 2000 char.)

The study of *quantum magnetism* remains at the forefront of condensed matter physics. Spin models provide a large class of many-body systems, in which cooperative quantum phenomena can be studied in a controlled way. In addition, the *neutron scattering* technique offers a near-ideal tool to probe the state of magnetic materials. This thesis presents neutron scattering studies of three selected materials, each representing an important aspect of quantum magnetism.

- $CuGeO_3$ is a quasi one-dimensional $S = 1/2$ spin–Peierls material. This is an example of a system that has a *quantum ground state* with no classical analogue. The spins dimerize to form a coherent non-magnetic singlet, where the expectation value of each individual spin is zero, as if they were 'hidden'. As a consequence, the *excitations* (called solitons) are different from the spin waves of a classical system. In a high magnetic field, the solitons can be condensed to form a periodic lattice. Through neutron scattering measurements, the structure of this soliton lattice has been determined, and the excitations in the soliton phase have been identified.
- $Cu(DCOO)_2{\cdot}4D_2O$ is a two-dimensional $S = 1/2$ Heisenberg antiferromagnet on a square lattice. The $T = 0$ ground state of this system has long range order similar to the classical system. But the order parameter is reduced by *quantum fluctuations*, and the physical observables are *renormalized*. In particular, it was found that the spin wave dispersion is non-uniformly renormalized. At finite temperatures long range order is destroyed by thermal and quantum fluctuations, which act together. Still, there are strong *correlations*, which on short length and time scales resembles the long range order. The temperature dependence of the correlation length and the excitation spectrum has been measured using two specialized neutron scattering methods.
- $LiHoF_4$ is a three-dimensional Ising ferromagnet, in which the magnetic order can be destroyed even at $T = 0$ by applying a large magnetic field transverse to the Ising axis. Ordinary phase transitions occur as a function of temperature, when the thermal fluctuations become strong enough to destroy the order. At $T = 0$ there are no thermal fluctuations and the transition is driven by quantum fluctuations, which are controlled by some external parameter,in this case the magnetic field. It is important to understand the universal behaviour of such *quantum phase transitions*, as several novel phenomena in solid state physics may be related to the proximity of a *quantum critical point*. Using inelastic neutron scattering the behaviour of the excitations around the quantum critical point in $LiHoF_4$ has been investigated.

This thesis was submitted in partial fulfillment of the requirements for a Ph.D. in physics at the University of Copenhagen. The work presented was carried out in the Department of Condensed Matter Physics and Chemistry at Risø National Laboratory, Denmark. The supervisors were Des McMowrrow from Risø and Jens Jensen from the University of Copenhagen.

Available on request from:
Information Service Department, Risø National Laboratory
(Afdelingen for Informationsservice, Forskningscenter Risø)
P.O. Box 49, DK–4000 Roskilde, Denmark
Phone (+45) 46 77 46 77, ext. 4004/4005 · Fax (+45) 46 77 40 13
E-mail: infserv@risoe.dk